Dissertation

submitted to the

Combined Faculties of the Natural Sciences and Mathematics

of the Ruperto-Carola-University of Heidelberg. Germany

for the degree of

Doctor of Natural Sciences

Put forward by

Marco Salathe

born in Seltisberg, Switzerland

Oral examination on November 25, 2015

Study on modified point contact germanium detectors for low background applications

Referees:

Prof. Dr. Manfred Lindner

Prof. Dr. Norbert Herrmann

Studie eines modifizierten Germaniumdetektors mit punktförmigem Auslesekontakt für Anwendungen bei einem tiefen Untergrund

Germaniumdetektoren mit einer punktförmigen Ausleseelektrode (PCGe) spielen bei der Erforschung von Themen wie dem neutrinolosen doppelten Betazerfall, der direkten Wechselwirkung von dunkler Materie, dem magnetischen Moment des Neutrinos und der kohärenten Streuung von Neutrinos am Atomkern, eine zentrale Rolle. Diese Doktorarbeit präsentiert eine experimentelle Untersuchung von zwei kommerziell erhältlichen, fast identischen PCGe-Detektoren mit großem Volumen ($\sim 760\,\mathrm{g}$). Die punktförmige Ausleseelektrode wurde, mit Hilfe von spezifischen Simulationen vom elektrischen Feld im Detektor, schrittweise verändert. Die Verkleinerung der fast punktförmigen Ausleseelektrode verbesserte sowohl die Unterdrückungseffizienz von Untergrundsignalen durch die Analyse der Signalform bei einigen MeV wie auch das elektronische Rauschen. Der tiefste Anteil vom Rauschen an der Energieauflösung war $(299 \pm 2)\,\mathrm{eV}$ und $(336 \pm 2)\,\mathrm{eV}$ (Halbwertsbreite) für die beiden Detektoren. Die bessere der beiden Auflösungen entspricht einer Energieschwelle von $1\,\mathrm{keV}$ für ein Experiment mit einem niedrigen Untergrund. Eine Sensitivitätsstudie kam zu der Schlussfolgerung, dass eine Auflösung von mindestens $150-180\,\mathrm{eV}$ nötig ist, um die kohärente Streuung von Neutrinos an Germaniumatomkernen in der Nähe eines Atomreaktors zu messen. Das ist ein Faktor zwei besser als das, was bisher erreicht wurde.

Zusätzlich, wurde mit zwei verschiedenen Ansätzen der Fano-Faktor bestimmt. Beide finden ein konsistentes Ergebnis, das bessere Ergebnis ist 0.1076 ± 0.0005. Damit diese optimierten Resultate erreicht werden konnten, war es wichtig, drei verschiedene Pulsformfilter (der cusp Filter mit abgerundetem Maximum, der trapezoidale Filter mit abgerundetem Maximum und der gaußförmige Filter) zusammen mit einer Korrekturmethode für das ballistische Defizit, zu evaluieren. Danach wurden die als ideal befundenen Filter benutzt, um die Auswertung durchzuführen.

Study on modified point contact germanium detectors for low background applications

Point contact germanium (PCGe) detectors play a vital role in research such as, neutrinoless double beta decay, direct dark matter detection, the neutrino magnetic moment and coherent neutrino-nucleus scattering. This dissertation presents an experimental investigation of two commercially available, almost identical large volume PCGe detectors ($\sim 760\,\mathrm{g}$). Their point contact size was stepwise modified according to specified simulations of the electric field in the detectors. The reduction of the point contact size improved both, the pulse shape discrimination efficiency of background signals at a few MeV and the noise from electronics. The lowest contribution of noise to the energy resolution was $(299 \pm 2)\,\mathrm{eV}$ and $(336 \pm 2)\,\mathrm{eV}$ (FWHM) for the two detectors, respectively. The better value translates to an energy threshold of $1\,\mathrm{keV}$ for an experiment with a low background level. A sensitivity study concluded that a resolution of less than $150 - 180\,\mathrm{eV}$ is required to detect the coherent neutrino-nucleus scattering near nuclear reactors. This is a factor of two better than the currently obtained value.

Additionally, two different approaches have been used to determine the Fano factor. They both yielded consistent results, the better result is 0.1076 ± 0.0005. Before the most optimal results could be obtained, an evaluation of three shaping filters (the rounded-top cusp, rounded-top trapezoidal and Gaussian filter) and a ballistic deficit correction was performed. Once completed the most ideal combinations of filters were used to procure the dissertation's findings.

Contents

1 Introduction

The origin of germanium detector technologies reaches back over half a decade. Although tremendous advances have been made in the meantime, technological developments take place at a rather slow pace. Particularly in the initial years intensive efforts were undertaken to understand these detectors that are currently used in a large range of different fields that stretch from nuclear physics and safeguard to fundamental research in particle physics. This thesis should help paving the way, so that this technology can also be used for many new exciting applications in the future. In order to do so, a particular, relatively new type of germanium detector will be studied – point contact germanium (PCGe) detectors.

1.1 Point contact germanium detectors

PCGe detectors, are cylindrical detectors that have been produced from germanium. On one base of the cylinder they have a circular electrode (contact) embedded. The contact radius is usually kept small – close to point like – which explains the name.

These detectors are the central subject of this thesis. Compared to previous studies, this thesis tries to take a more systematic approach in studying these detectors. The central question that should be answered is how these detectors are affected by changes in their geometry. In order to answer this question, special care will be given to the application and implementation of old and new computational methods so that the best performance can be obtained. Signal processing will therefore be a recurring subject that is nearly as important as the geometrical study itself. The study will additionally address several physics related topics. A material property, the Fano factor in germanium, will be measured and the potential of such detectors for the detection of coherent nucleus-neutrino scattering studied.

The point contact design of a germanium detector was first proposed by Luke et al. in 1989 under the name low capacitance large volume shaped-field germanium detector [1]. The initial aim of this detector type was to measure dark matter. The detector however suffered from strong charge trapping and was not used in actual research. Nevertheless, they reached their aim to produce a detector with a capacitance of close to 1 pF. Many years later, in 2007, Barbeau et al. [2] brought again up this design for applications in fundamental research. This time the detector they tested did not show the problematic trapping effects that Luke et al. observed in their earlier study. The design subsequently has been quickly adopted for various application in fundamental science. This will now be discussed in the next section, before the focus is shifted away from fundamental science to detector physics.

1.2 PCGe detectors as a gateway to new physics

Point contact detectors are mostly used to study neutrinos and their interactions. Neutrino properties that are or have been investigated with PCGe detectors include coherent elastic

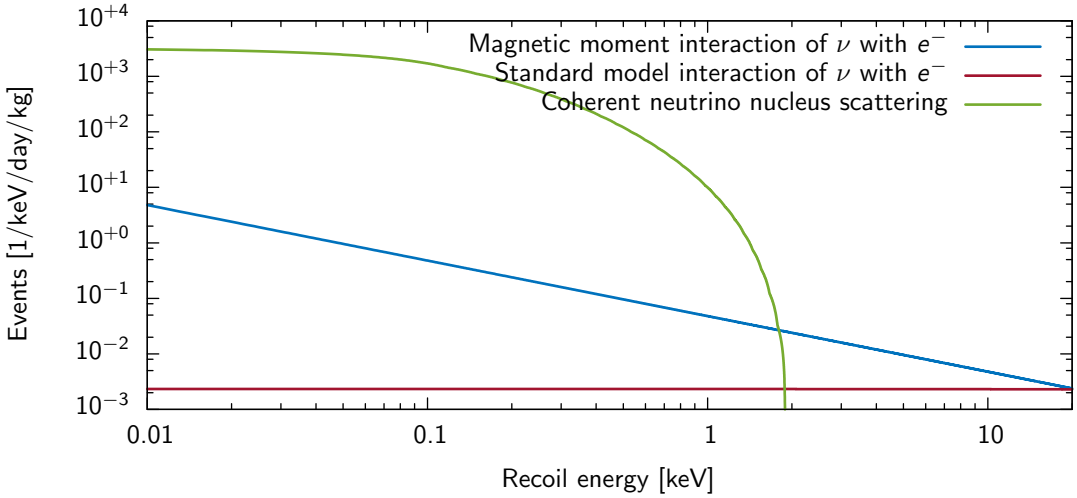

Figure 1.1: The expected signals in a germanium detector at a neutrino flux of ($10^{13}\,\mathrm{cm}^{-2}\mathrm{s}^{-1}$) close to a nuclear reactor (neutrino emission spectrum according to [3] and [4]). The magnetic moment interaction of neutrinos and electrons is represented for $\mu_\nu = 2.9\times10^{-11}\mu_B$, the current limit on the interaction. The displayed coherent neutrino-nucleus scattering spectrum must furthermore be corrected by the quenching factor, to gain the ionization energy. The calculations have been performed by Thomas Rink, Max-Planck-Institut für Kernphysik, Heidelberg.

neutrino-nucleus scattering, the neutrino magnetic moment and neutrinoless double beta decay. Neutrinoless double beta decay can be measured in detectors that are directly built from material enriched to roughly 88% in the isotope under investigation (^{76}Ge). The other effects are not dependent on germanium as a detection material, but make use of the inherent characteristics of these detectors. Furthermore, hypothetical dark matter models such as Weakly Interacting Massive Particles (WIMP) are being searched for with PCGe detector.

1.2.1 Coherent Elastic Neutrino-Nucleus Scattering

Coherence is a quantum mechanical process that considerably can enhance the cross section of an interaction. An occurrence of this phenomenon is the elastic scattering of a particle (here the neutrino) from a system that is composed of many similar constituents (here the nucleus, built of nucleons) [5]. The direction and magnitude of the momentum of the incoming particle is altered through simultaneous interactions with the constituents of the system. The total scattering amplitude is thus given by the sum of the contributions from the individual interactions. In general, they are not in phase, therefore the relative phases of the scattering amplitudes must be taken into account. If the de Broglie wavelength of the momentum transfer is large compared to the size of the system, then the relative phase factors are irrelevant and can be neglected. The total scattering amplitude can then be approximated by the number of constituents A (the number of nucleons, assumed for now all equal) times the scattering amplitude of an individual interaction. The differential cross section is given by the squared norm of the total scattering amplitude. Thus, the total cross section is enlarged thanks to the coherence by A^2. The condition relating the momentum transfer (respectively its de Broglie wavelength) to the size of the nucleus translates into a rough neutrino energy upper limit

of 50 MeV [6]. Above this energy the neutrino actually sees the constituents of the nucleus and coherence is not assured. A nucleus is built of protons and neutrons, thus the scattering amplitudes of the two types of constituent are different and they must be considered separately.

The actual differential cross section of coherent elastic neutrino-nucleus scattering is given by [7]:

$$\frac{d\sigma}{d\Omega} = \frac{G_F^2}{16\pi^2} Q_W^2 E_\nu^2 (1+\cos\theta) F^2(Q^2), \qquad Q_W = \left[N - (1 - 4\sin^2\theta_W) Z\right]. \tag{1.1}$$

The angle θ was chosen to be between the incoming and the outgoing momentum of the neutrino, E_ν is the neutrino energy and G_F the Fermi coupling constant. The weak nuclear charge Q_W depends on the number of protons Z and neutrons N in the nucleus. The weak mixing angle θ_W (Weinberg angle) is known and accordingly $4\sin^2\theta_W \approx 0.944$. This means that the number of protons in the nucleus Z has practically no impact and can be neglected: $Q_W \approx N$. The form factor F depends on the momentum transfer squared $Q^2 = 2E_\nu^2(1-\cos\theta)$ and for low values of Q^2 the form factor can be approximated to be 1. Furthermore, for small momentum transfers we can use a classical treatment. Therefore, the recoil energy is:

$$T = Q^2/2m_N = E_\nu^2(1-\cos\theta)/m_N, \qquad T_{\max} = 2E_\nu/m_N, \tag{1.2}$$

with m_N being the mass of the nucleus. The maximal recoil $T_{\max}$ is observed if the neutrino is back scattered ($\cos\theta = -1$). A germanium detector is sensitive to the recoil energy of the nucleus. In order to detect a large signal either large neutrino energies are required or the mass of a nuclei should be small. Equation 1.1 can be expressed as a function of the recoil energy by explicitly stating the solid angle $\Omega = 2\pi\cos\theta$ and using Eq. 1.2:

$$\frac{d\sigma}{dT} = \frac{G_f^2}{4\pi} N^2 m_N \left(1 - \frac{m_N T}{2E_\nu^2}\right), \tag{1.3}$$

where we used all simplifications introduced so far. The total cross section can be found by integrating this formula over all possible recoil energies:

$$\sigma_{\text{tot}} = \frac{G_F^2 E_\nu^2 N^2}{4\pi}. \tag{1.4}$$

The total cross section thus increases with both, the neutrino energy and the numbers of neutrons in the nucleus. Typical values for the cross sections of neutrinos with an energies up to 50 MeV are in the order of $10^{-39}\,\text{cm}^{-2}$. This is relatively high compared to other neutrino interactions at a similar energy. Nevertheless, coherent neutrino-nucleus scattering has not yet been observed in experiments. One of the reason for this is that the recoil energy depends on the nucleus mass, as described in Eq. 1.2. A neutrino of 10 MeV (in the upper range of a neutrino spectrum from nuclear reactors), for example, produces a maximal recoil of 3 keV in germanium. This signal is furthermore reduced by the quenching factor [8], as not all the recoil energy is converted into ionization of charge carrier. For a recoil energy of 3 keV the quenching factor in germanium is roughly 0.2. This means the actually observed signal in the detector is only 600 eV, thus below typical energy thresholds of commercial germanium detectors.

In recent years, the efforts to measure the coherent neutrino-nucleus scattering were intensified. New PCGe technologies emerged as a good candidate to measure a signal from coherently

scattered neutrinos, as they are sensitive to the energy range where these interactions actually occur. A good source of sufficiently large quantities of neutrinos ($\sim 10^{13}\,\mathrm{cm}^{-2}\mathrm{s}^{-1}$ in close proximity to the core [9]) are commercial nuclear power reactors that emit neutrinos at an average energy of roughly 2 MeV, with the neutrino spectrum dying of between 8-10 keV. Already in 2008 Barbeau et al. [2, 10] tried to measure coherent neutrino scattering with a PCGe detector at the San Onofre Nuclear Generating Station (SONGS) that was closed in 2013 and is currently being decommissioned. They were not able to measure the effect because there were high backgrounds, especially in the reactor off spectrum. At the same time the Taiwan EXperiment On NeutrinO (TEXONO) collaboration started to investigate the performance of different types of germanium detectors for use at the Kuo-Sheng Reactor Neutrino Laboratory (KSNL) [11].

The number of events expected from coherent neutrino scattering as a function of the recoil energy in germanium for a typical reactor flux are represented in Fig. 1.1. The most crucial points for the detection of the coherent scattering of neutrinos at a nuclear power plant are a high reactor flux, close proximity to the reactor (the flux falls off with the distance squared), low backgrounds ($\sim 1\,\mathrm{count/keV/kg/day}$) and a low energy threshold ($< 500\,\mathrm{eV}$).

The sensitivity could be further increased by observing neutrinos with a slightly higher energy than those from nuclear reactors. The Spallation Neutron Source (SNS) at the Oak Ridge National Laboratory completed in 2006 [12] for example can potentially be used in this regards. As a byproduct, the SNS produces a neutrino beam of $10^7\,\mathrm{cm}^{-2}\mathrm{s}^{-1}$ flux, with a sharp peak at 30 MeV of muon neutrinos and a broad peak at a similar energy of electron neutrinos. Although the flux is small compared to reactors, the higher neutrino energy turns this facility in an attractive experimental site for coherent neutrino scattering studies.

1.2.2 Neutrino magnetic moment

Neutrinos can also interact with the medium by scattering off the electrons of atoms. These interactions are described by the Standard Model and the differential cross section is given by [13]:

$$\frac{d\sigma_W}{dT} = \frac{G_F^2 m_e^2}{2\pi}\Big[\big(1-\frac{T}{E_\nu}\big)^2(1+2\sin^2\theta_W)^2 + 4\sin^4\theta_W - 2(1+2\sin^2\theta_W)\sin^2\theta_W\frac{m_e T}{E_\nu^2}\Big]. \quad (1.5)$$

The cross section is again expressed through the recoil energy T.

Neutrinos are considered massless in the Standard Model, thus with the observation of neutrino oscillations and their interpretation with finite neutrino masses, the first observation of Physics beyond the Standard Model was realized. This property introduces a new term to the total cross section that describes the electromagnetic interaction between the neutrino and an electron:

$$\frac{d\sigma_{EM}}{dT} = \pi r_e \left(\frac{\mu_\nu}{\mu_B}\right)^2 \left(\frac{1}{T} - \frac{1}{E_\nu}\right), \quad (1.6)$$

with r_e being the classical electron radius. In this expression the neutrino magnetic moment μ_ν was introduced, which is often expressed as a fraction of the Bohr magneton μ_B. The magnitude of μ_ν depends on the model that describes neutrinos, particularly if neutrinos are

assumed to be Dirac or Majorana particles. In a minimally extended Standard Model with Dirac neutrinos the neutrino magnetic moment is related to the neutrino mass m_ν and found to be [14]:

$$\mu_\nu \approx 3 \times 10^{-19} \mu_B \cdot \frac{m_\nu}{1\text{eV}}. \tag{1.7}$$

This value is many magnitudes smaller than the sensitivity of any current experiment. Some special models describing Physics beyond the Standard Model are predicting a neutrino magnetic moments up to a level of $10^{-10} - 10^{-12}\,\mu_B$ [15].

When investigating Eq. 1.5 and 1.6 it is obvious that the cross section dependence on the recoil energy is quite different for the two contributions. The Standard Model cross section is nearly constant at low recoil energies, while the electromagnetic cross section has a strong $1/T$-dependence. This difference makes it possible to distinguish both processes. Moreover, at low energies the electromagnetic contribution should be larger than the Standard Model contribution and thus should be measurable.

Usually, experiments looking for coherent elastic neutrino-nucleus scattering can also exploit their data to define new upper limits of the neutrino magnetic moment and vice versa. Although both, the TEXONO collaboration [16] and Barbeau et al. [2], published new upper limits based on their investigations at nuclear power plants, the best limit of the magnetic moment is measured by the GEMMA collaboration [17]. Their limit of $\mu_\nu \leq 2.9 \times 10^{-11}\mu_B$ (90% C.L.) was measured with a semi-coaxial HPGe detector at 13.9 m distance of a reactor core at the Kalinin Nuclear Power Plant (KNPP). At this location they expect the anti-neutrino flux to be roughly $2.7 \times 10^{13}\,\text{cm}^{-2}\text{s}^{-1}$. The spectrum that is expected from both the standard model contribution and the electromagnetic contribution of the neutrino magnetic moment with a value of the currently best lower limit is indicated in Fig. 1.1.

It is complicated to improve the experimental limits for the neutrino magnetic moment because the sensitivity roughly scales as $(B/(Mt))^{1/4}$ [16], where B, M and t are the background level, detector mass and measurement time. As all these parameters are taken to the power 1/4, improving on any of the typical characteristics of a detector setup only has a small impact on the sensitivity to the magnetic moment. Other possible ways to improve the sensitivity are by using a higher neutrino flux, lower energy threshold and higher neutrino energies that all do not show the to-the-power-1/4 behavior.

1.2.3 Dark matter detection

Although the appearance of neutrino oscillation was the first prove that there must be Physics beyond the Standard Model, there are other strong hints that our current understanding of the universe is not complete. One of the indications for this is dark matter (a short comprehensive overview is Ref. [19] or [20] and the references therein). It has not yet been detected directly but cosmological data show strong evidence for its existence. Dark matter cannot be of baryonic nature and its distribution in cosmological structures has been established through numerical simulations and lensing observations. The recent Planck data [21] furthermore shows that it makes up roughly 85% of all matter in the universe and thus roughly 25% of all energy.

Particle physicists came up with a variety of candidates for dark matter particles, of which the Weakly Interacting Massive Particle (WIMP) is the most popular one. Its mass must be in the range from 50 GeV to a few TeV and as its name suggests it should be detectable through its weak interaction with baryonic matter. The dark matter density of the Milky Way halo at

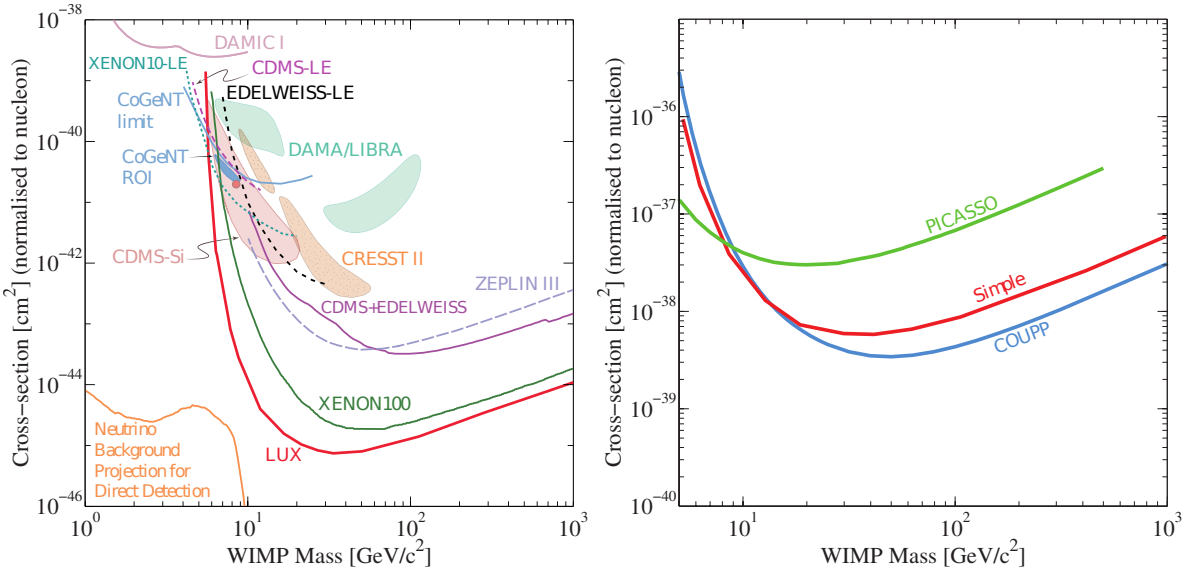

Figure 1.2: The current limits on the spin-independent cross section (left) and the spin-dependent cross section (right). The enclosed areas are regions of interest from possible signal events. The Figure was taken from Ref. [18].

the location of the solar system is assumed to be $\rho_0 = 0.3\,\mathrm{GeV/cm^3}$. Dark matter is assumed to be at rest, and the solar system therefore moves at a velocity of roughly $v_0 = (220 \pm 20)\,\mathrm{km/s}$ with respect to the dark matter [20]. Furthermore, earth moves around the sun at a speed of roughly $v_E = 30\,\mathrm{km/s}$, which slightly alters (in an annual mode) the overall relative velocity of dark matter with respect to earth. If dark matter is composed of WIMPs they would elastically scatter off nuclei in an experimental setup through the weak interaction and the recoil of the nucleus could be observed.

The differential cross section is traditionally split into a spin-independent (SI) and spin-dependent (SD) contribution. The spin independent contribution is related to an effective scalar coupling between the WIMP and the mass of the nucleus and it is coherently enhanced by the number of interacting nucleons. The spin-dependent contribution originates in an effective coupling between the spin of the WIMP and the total angular momentum of the nucleus [22]. Fig. 1.2 shows the current limits of direct WIMP searches as well as some claimed signals. The best limits on the spin-independent scattering cross section have been reached by the Lux collaboration in a few hundred kg of liquid Xenon with a minimum of $7.6 \times 10^{-46}\,\mathrm{cm^{-2}}$ [23]. These results are in conflict with the claimed observation of an annual modulation of the Dama/Libra [24] and CoGeNT (Coherent Germanium Neutrino Technology) [25] experiments. The latter operated a single modified point contact germanium diode of 443 g at the Soudan Underground Laboratory (SUL). The Majorana Low-Background BEGe at Kimballton (Malbek) experiment used a similar germanium detector of 465 g at the Kimballton Underground Research Facility (KURF) [26, 27]. They did not measure any excess of events at low energies and decided against an analysis of the annual modulation because of large noise observed in their read out electronics and pollution of their energy spectrum by slow pulses (see Sec. 3.4). Furthermore, the Texono collaboration searched with a 900 g PCGe detector

at the Kuo-Sheng Reactor Neutrino Laboratory [28] and the China Dark Matter Experiment (CDEX) with two 1 kg PCGe detectors at the China Jinping Underground Laboratory (CJPL) [29] for a WIMP signal and did both exclude the CoGeNT region. Recent new results from the XENON100 collaboration further disfavor models that tried to explain the discrepancies between the different experiments, suggesting that the observed signals might be due to unaccounted systematics [30].

Although the high resolution and low energy threshold of PCGe is very favorable, it must be considered that the detected signal is reduced by the quenching factor, as the recoil of the nucleus does not directly translate to an ionization signal. This drawback is addressed in cryogenic experiments (CDMS,EDELWEISS) that run weakly biased germanium detectors at mK temperatures, so that the phonon signal together with the ionization signal can be detected [31, 32].

The best limits on the spin-dependent cross sections are less stringent and are found primarily in bubble chamber experiments with fluorine, because the isotope ^{19}F is particularly sensitive to the spin-dependent interaction. Limits in the range of $10^{-38}\,\mathrm{cm}^{-2}$ were measured by the SIMPLE and COUP collaborations [33, 34] (see also Fig. 1.2).

1.2.4 Neutrinoless double beta decay

Neutrinoless double beta decay is characterized by a final nucleus with an increased proton number by two units and the emission of two electrons:

$$(A, Z) \rightarrow (A, Z+2) + 2e^{-}. \tag{1.8}$$

Compared to the two-neutrino double beta decay, which additionally involves the emission of two anti-neutrinos, lepton number is violated in this process. It has been noted that the observation of neutrinoless double beta decay implies the existence of a Majorana mass term of neutrinos [35]. This term however can be as small as $10^{-23}\,\mathrm{eV}$ and in this case it is too small to explain the observed neutrino flavor oscillations [36]. Therefore the two phenomena must not be directly linked and even if neutrinoless double beta decay is observed the neutrino could still be a Dirac particle. In such a scenario lepton number violation must be caused by another process that could be studied at locations such as the Large Hadron Collider (LHC). The standard interpretation of the decay is that it is mediated by two light massive Majorana neutrinos and in the following discussion only that case will be considered.

The two-neutrino double beta decay can be observed in 35 even-even isotopes that do not allow the normal beta decay. Their ground states are energetically lower than their odd-odd neighbors. They however allow two beta decays to happen simultaneously. In that case the final state is at a lower energy. The two neutrinos carry some of the energy, which currently cannot be measured. Thus only the sum of the energy of the two electrons is observable as a continuous spectrum. If it exists, neutrinoless double beta decay could also be observed in these isotopes. There are no neutrinos created in this process, thus the total energy would be seen in the electron signal and the decay would create a sharp line at the Q-value of the decay $Q_{\beta\beta}$.

The decay is characterized by its half-life $T^{0\nu}_{1/2}$, which is found to be inversely proportional to the square of the effective mass $m_{\beta\beta}$ divided by the square of the electron mass m_e:

$$\left(T^{0\nu}_{1/2}\right)^{-1} = G_{0\nu}(Q_{\beta\beta}, Z)\,|\mathcal{M}_{0\nu}|^2 \left(\frac{m_{\beta\beta}}{m_e}\right)^2. \tag{1.9}$$

The phase space factor $G_{0\nu}$ can be calculated with high accuracy, not so the matrix element $\mathcal{M}_{0\nu}$, which requires approximations and thus are strongly dependent on the underlying model and its parameters. The different models deviate by a maximal factor of 2-3, thus, at this stage from the half-life only an order of magnitude estimation for the effective mass can be gained. The effective mass or effective electron neutrino mass is:

$$m_{\beta\beta} = \sum_{i=1}^{3} U_{ei}^2 m_i. \tag{1.10}$$

U_{ei} are the electron related elements of the Pontecorvo-Maki-Nakagawa-Sakata (PMNS) matrix that translates the neutrino mass states ν_1, ν_2, ν_3 to the neutrino flavor states ν_e, ν_μ, ν_τ: $\nu_\alpha = U_{\alpha i}^* \nu_i$ (assuming there are only three generations of neutrinos). The PMNS elements appearing in the right hand side of the equation contain the two Majorana phases, and in the most unfavorable case their value is such that the expression cancels and thus the effective mass is zero.

One of the isotopes that do not allow beta decay but allow two-neutrino double beta decay is ^{76}Ge, with a Q-value of 2039 keV. It is possible to build germanium detectors from material enriched up to 88% in this isotope. These detectors have been successfully operated with a sufficiently clean environment to measure the two-neutrino double beta decay and set limits on neutrinoless double beta decay in ^{76}Ge. The most recent experiments in this category are the GERDA and MAJORANA experiments. The GERDA collaboration operated germanium detectors (semi-coaxial and point contact detectors) of a total weight of 20 kg in a 64 m^3 cryostat filled with liquid Argon in the Laboratori Nazionali del Gran Sasso (LNGS). The GERDA collaboration reported in 2013 a new limit on the half-life of the neutrinoless double beta decay of 2.1×10^{25} yr (90% C.L.) [37]. This limit can compete with other current best limits from the Xenon based experiments EXO and KAMLAND-ZEN [38, 39]. GERDA is currently undergoing an upgrade that adds 30 new PCGe detectors (of roughly 20 kg mass) and a scintillation light sensitive instrumentation of the liquid Argon to their setup [40]. The MAJORANA collaboration is currently building two large vacuum cryostats at the Sanford Underground Research Facility (SURF) that should be filled with PCGe detectors of up to 45 kg. One of their aims is to prove that this technology could be adopted for a ton scale experiment to be constructed in the future [41].

1.3 A short overview over what follows

The effect of the geometry on the performance of a PCGe detector is evaluated mainly through an experimental study: the geometry of two almost identical germanium detectors is modified in multiple steps and characterized at each stage. This section will provide a brief overview over the main subjects that are addressed. The detailed concepts behind each point will be introduced in subsequent chapters and thus are not yet discussed in detail.

Energy resolution: The energy resolution is one of the most important characteristics. The underlying physics, how it is measured and some values from actual measurements will be covered.

Pulse shape discrimination: This is a method used to differentiate signal by their temporal profile. It is one of the PCGe detectors central strength and is important for any exper-

iment in fundamental science. The discussion here will be limited to high energetic lines (MeV region) that are of importance for neutrinoless double beta decay experiments.

Low energy threshold: Point contact detectors perform especially well at low energies. The detectors performance all the way down to energies that are polluted by signals from noise fluctuations will be studied.

Sensitivity study: The sensitivity of the two PCGe detectors to coherent neutrino-nucleus scattering will be explored.

Fano factor: The Fano factor is a central characteristics of germanium. A measurement of its value will be provided.

Noise measurements: Particular at low energies, electronics noise is of importance. A new method will be presented that allows measurements of the noise properties in a data set lacking an analog pulser signal.

Analysis tools: The analysis of data requires specific software. Furthermore, simulations have been performed. The programs that have been partially developed and validated within the scope of this thesis will be presented.

Filter development and studies: Some novel and traditional filter methods will be thoroughly studied to find the most ideal filters for a given analysis.

Ballistic deficit corrections: A new method used to prevent the different temporal profiles of pulses to negatively affect the energy resolution will be described and compared to other established methods.

There are many other topics related to PCGe detector that are also of interest. However, a complete discussion of all of them would exceed the scope of this thesis and will be left to further generations of physicists.

2 Germanium detectors

Germanium detectors are semiconductor devices with a pn-junction that are run in the inverse bias mode to form a region depleted of free charged particles, that is sensitive to energy deposition from radiation. In this depleted region, incoming radiation can interact with the detection medium and free previously bound charged particles, which drift in an applied electric field and induce through their movement a current into the electrode. The current is integrated with an charge sensitive amplifier and the height of the resulting signal is proportional to the amount of charged particles created in the depleted region and thus proportional to the amount of energy deposited by the radiation. Dedicated electronic circuitry is used to measure the pulse height of these signals and therefore it reconstructs the amount of energy deposited in the detector.

The first section of this chapter will introduce different types of radiations that can be measured in a germanium detector. This discussion is then followed by a brief outline of physics of semiconductors in regards to the usage of such devices in radiation detection applications. The chapter is concluded with the presentation of some of a germanium detectors characteristics.

2.1 Radiation and its interaction with matter

Although any particle can interact with the material of a germanium detector, the most common application of germanium detectors is spectroscopy, the measurement of photons. Germanium has a density that is high compared to silicon, another very common semiconductor material and can be produced sufficiently thick (a few centimeters) to also be sensitive to high energetic photons (above 1 MeV) that penetrate through thinner and less dense materials without interacting with the medium. Germanium detectors are used to detect photons over a broad range of energies, starting from a few keVs up to tens of MeVs. Photons in this range are usually characterized as either γ-rays or X-rays, depending on their origin. γ-rays are emitted during a radioactive decay of a nucleus, while X-rays are emitted by electrons outside the nucleus. X-rays tend to be found at lower energies than γ-rays, however their typical energy range overlap. It is therefore not possible to distinguish these two radiations only by the energy of the photon or by the signal they leave in a detection system. Furthermore, the name γ-rays is also used for very high energetic photons (up to the TeV range), which are not considered in this work. Here γ-rays will only be used to refer to photons that originate from a radioactive decay and that can be detected with germanium detectors.

Photons are one particular type of radiation, however, next to it there exist other types. In total there are 4 categories of radiation that are relevant in γ-ray spectroscopy:

- Heavy charged particles: Ions and α-particles
- Electrons: β-particles
- Photons: X-rays and γ-rays

- Neutrons

Depending on the properties and energy of the penetrating radiation, each of these interact with the constituents of matter – mainly the electrons and nuclei – through different physical processes. The different processes occur with a certain probability that is governed by the laws of quantum mechanics and that are described in the framework of quantum field theory by the cross section.

In physics experiments often a large amount of particles interact simultaneously in a medium. A realistic setup thus consists of a particle beam of a flux F hitting a large target. The interaction with the target material either deflects the particles from their original path (scattering) or absorbs the particle entirely. The differential cross section, considers this by describing the number of particles N_s that are measured at a certain reflection angle per unit time, normalized by the flux:

$$\frac{\mathrm{d}\sigma}{\mathrm{d}\Omega} = \frac{N_s}{F} \tag{2.1}$$

The incoming flux must be defined as the number of particles per unit time crossing the intersecting area between particle beam and target. The total cross section σ_{tot} is calculated by integrating over all possible angles $\mathrm{d}\Omega = \sin\theta\,\mathrm{d}\theta\,\mathrm{d}\phi$.

In real situation the target is of a certain thickness, so the total cross section allows to calculate the amount of particles that are scattered or absorbed over that thickness. In the most simple case (i.e. photons) the probability of a particle penetrating a thickness x of a material follows an exponentially decaying function of the form $\exp(-\mu x)$ [42, p. 19]. The factor μ is called the attenuation coefficient and if the material is homogeneous, with a scattering site density n then the attenuation coefficient is given by $\mu = n\sigma_{tot}$. The mass attenuation coefficient μ/ρ is approximately constant for a large range of materials, as the amount of scattering sites scales roughly with the density of a material.

The total cross section is defined by different physical processes, that in turn are dependent on which type of radiation penetrates what type of material. Thus different types of radiation behave differently when traveling through germanium.

2.1.1 Heavy charged particles

Heavy charged particles primarily interact with the atomic electrons through the Coulomb force. These interactions either excite electrons to a higher atomic shell or remove them completely from the atomic nuclei. The energy required for the respective process is provided by reducing the kinetic energy of the heavy charged particle. The particle simultaneously interactions with many electrons of the medium, thus continuously losses its energy and slows down until it comes to a halt. As the number of interaction is high and the deviations from the initial path are small, the statistical fluctuations are also small and individual heavy charged particles penetrate the material in a similar fashion and are absorbed at a similar depth. Accordingly, it is practical to define the average range, a heavy charged particle penetrates into a material before losing all its initial energy (continuous slowing down approximation range). The energy dependence of this range is shown in Fig. 2.1 for germanium. As the range is small most of the radiation is absorbed very close to the surface, where the detector is not capable of detecting the radiation. Thus, this type of radiation only is marginally of importance.

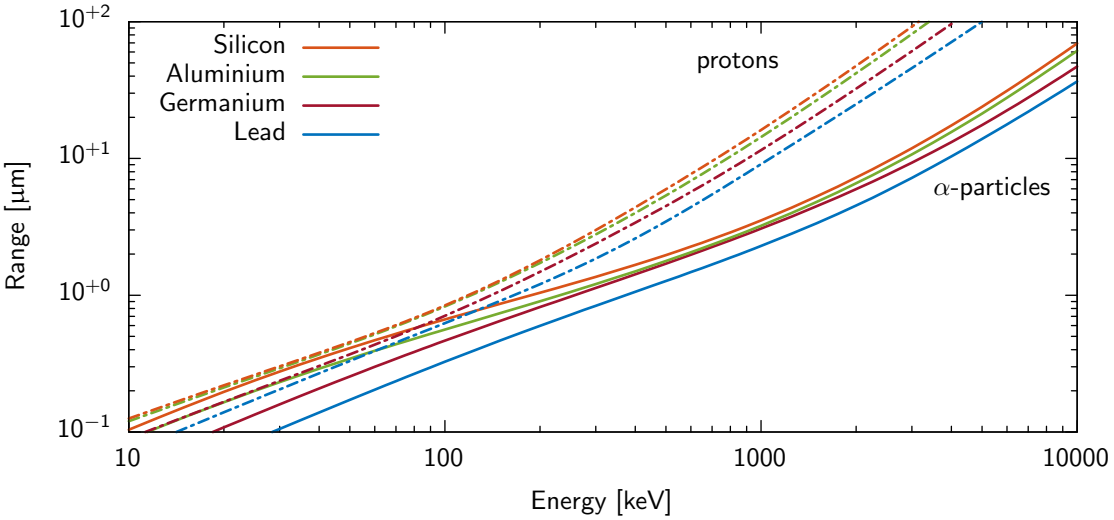

Figure 2.1: Average penetration depth (projection of the continuous slowing down approximation range on the initial particle trajectory) of α-particles (solid line) and protons (dashed line) in different materials [43].

2.1.2 Electrons

Similar to heavy charged particles, β-particles (electrons) interact mainly with the orbital electrons from atoms in the material. The mass of the incoming particle is equal to the mass of the scattering center, therefore a much larger fraction of the energy can be absorbed in a single interaction. In addition, electrons suffer repeated elastic Coulomb scattering from nuclei, each interactions resulting in a small deflection of the particle. The particles thus do not follow a straight line and the average penetration depth into the material is shorter than the average path length of a particle. It is possible that most of the electrons energy is absorbed in a few collisions, therefore even in very thin materials some of the electrons will be lost.

Fig. 2.2 represents the average path length of an electron in various materials. As the electrons are deflected in interactions with the nuclei, their path length is an upper limit to the penetration depth. As illustrated in the figure, the range bends down at very high energies which is due to additional radiative losses through Bremsstrahlung. Nevertheless, above an energy of 1 MeV electrons can penetrate a few millimeters into the material, so at these energies they can be easily detected with typical germanium detectors. Furthermore, β-particles emerge as secondary particles of photon interactions and thus take an important role in the formation of the actual detectable charge signal.

2.1.3 Photons

Compared to the interaction of charged particles by the Coulomb force, photon interactions with matter are not as likely and therefore photons penetrate further into matter before being absorbed or scattered. There are three major interactions that are of importance in the typical energy range of γ-ray spectroscopy:

- Photoelectric absorption

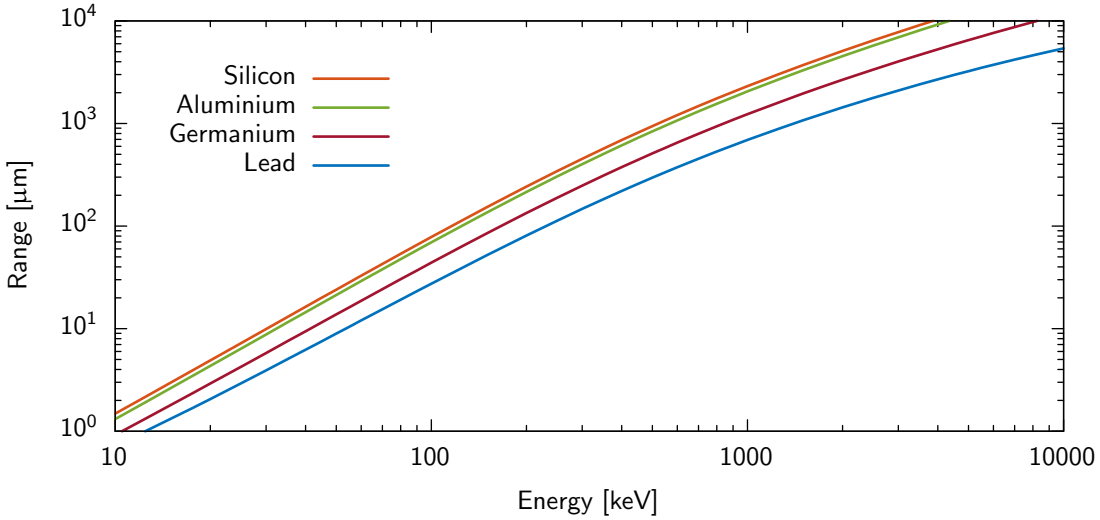

Figure 2.2: Average path length (continuous slowing down approximation range) of electrons as a function of their energy [43].

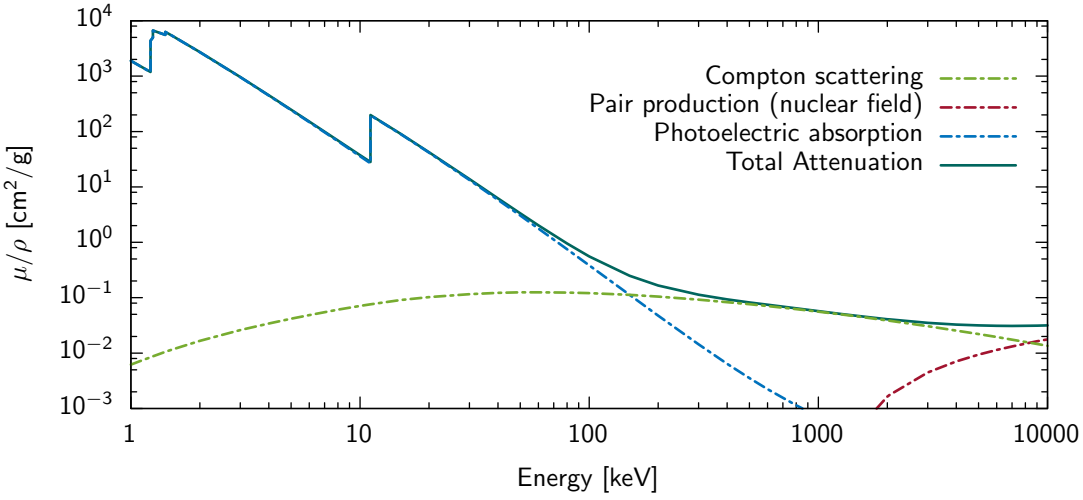

Figure 2.3: Attenuation coefficient for the most important interactions of photons in germanium [44].

- Compton scattering
- Pair production

Photoelectric absorption is the absorption of the photon by an atom and the simultaneous ejection of one of the atomic electrons. The atom must absorb the recoil momentum, hence this process only happens with an entire atom and never with a free electron. The energy conservation defines the energy of the ejected electron to be $E_{e^-} = h\nu - E_b$, where $h\nu$ is the energy of the incoming γ-ray and E_b the binding energy of the electron. The vacancy usually is filled by a free electron from the medium or through a rearrangement of the electrons in the atoms and the emission of a characteristic X-ray. The cross section of this process is complex as it must account for the entire atomic structure, particularly the energy levels of the electron shells in the atoms. The cross section thus has sharp steps at energies where the γ-energy is large enough to eject an electron from a new shell. The photoelectric effect is dominant at low energies (below 100-200 keV) and its contribution to the total mass attenuation coefficient is represented in Fig. 2.3 for germanium.

Compton scattering takes place between a γ-particle and an free or lightly bound electron (lightly bound means the energy of the photon is high compared to the binding energy). The process is well studied and the scattering angle and energy transfer can be obtained from the equations of energy and momentum conservation (see for example [45] the original paper published by Arthur Compton for more details). The differential cross section of the process (its contribution to the mass attenuation coefficient is shown in Fig. 2.3) has been calculated by Klein and Nishina and the detailed form can be found in their initial publication [46]. The Klein-Nishina equation allows to calculate the energy distribution of the recoil electron, which corresponds to the signal that can be measured in the detector for Compton scattered photons from a monoenergetic source[42, p. 57]:

$$\frac{\mathrm{d}\sigma}{\mathrm{d}E_{e^-}} = \frac{\pi r_e^2}{m_e c^2 \gamma^2}\left[2 + \frac{s^2}{\gamma^2(1-s)^2} + \frac{s}{1-s}\left(s - \frac{2}{\gamma}\right)\right], \quad E_{e^-}^{\max} = \frac{2h\nu\gamma}{1+2\gamma}, \tag{2.2}$$

with r_e the classical electron radius, $\gamma = h\nu/m_e c^2$ and $s = E_{e^-}/h\nu$. A typical example of the distribution described in Eq. 2.2 is given in Fig. 2.4 for the ^{208}Tl line at 2614.5 keV. It is apparent, that the single Compton scattered events form a continuous distributions, that is called the Compton continuum. For monoenergetic sources it is however also likely that the entire energy is deposited in the detector, thus at the energy of the incident photon a sharp peak appears – the full energy peak (FEP). The sharp cut of at $E_{e^-}^{\max}$ is called the Compton edge and single Compton scattering is not possible above this energy. The scattered photon, however can interact in secondary processes and deposit additional energy within the detector. Therefore, events can also be found in the gap between the Compton edge and the full energy peak.

For a γ-particle of more than 1022 keV (twice the rest mass of an electron) pair production, the transformation of a photon in an electron-positron pair, is energetically possible. The conservation of momentum requires this process to happen in the vicinity of a third body, usually a nucleus. The presence of the nucleus increases the complexity of calculating the cross section of the process, therefore, for different energy ranges different approximations are used. The contribution of the pair production cross section to the mass attenuation coefficient is shown in Fig. 2.3. The positron and electron normally travels only a few millimeters before

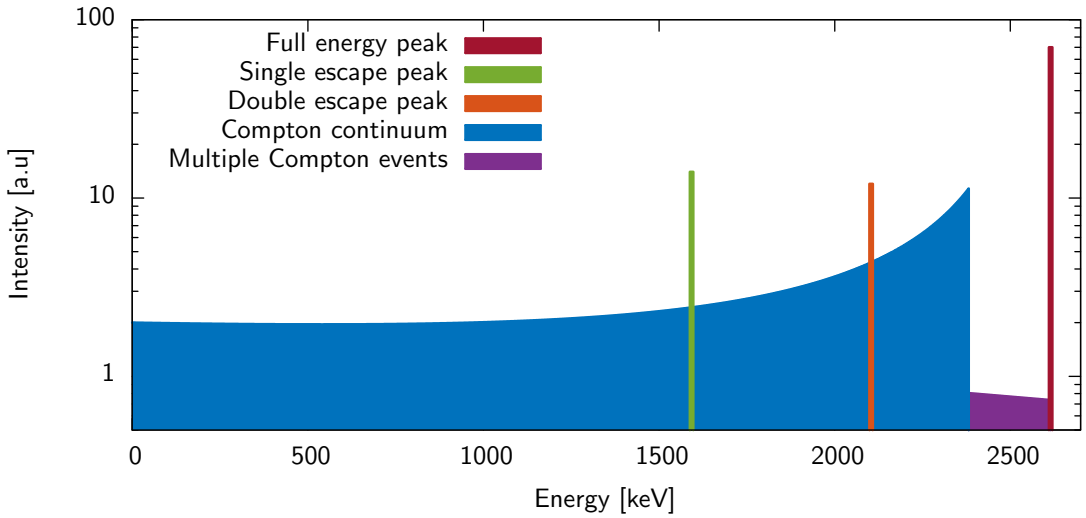

Figure 2.4: An illustration of the single Compton scattering continuum (following Eq. 2.2) created by the 2614.5 keV γ-rays of ^{208}Tl. The full energy peak an the two escape peaks are indicated in addition. Both, the precise height of the individual peaks and the strength and form of the multiple Compton event region above the Compton edge depend on the geometry and size of the detector. Their representation here does not follow a physical meaningful equation.

they loss all the kinetic energy to the surrounding material. The positron annihilates with an electron from the absorber and both disappear while two 511 keV photons are emitted. These secondary photons either escape the detector or interact by some other processes in the detector. The annihilation of the positron is particularly important for monoenergetic γ-rays, as they create additional structures in the energy spectrum. If both photons are absorbed in the detector then the entire energy of the incoming photon is deposited and the photon contributes to the full-energy-peak (FEP) of the incoming gamma-ray. However, if one or both of the annihilation photons escape the detector, their escape reduces the total energy deposited in the detector by the amount of energy (511 keV) carried away by the photon. Instead of having a single peak, additional characteristic escape peaks are formed at an energy of 511 keV (single escape peak, SEP) or 1022 keV (double escape peak, DEP) below the full energy peak (FEP). This is illustrated in 2.4 together with the Compton continuum.

The time spans over which the interaction chain of a γ-particle takes place is much shorter (a few nanoseconds) than the actual response of the detector (a few hundreds of nanoseconds), therefore it is impossible to distinguish the different forms of interactions. However, the interaction of the annihilation photons usually appear at a certain distance from the initial Compton scatter position. Some detectors have sufficient sensitivity to the location of energy deposition sites to separate these processes from others that only consist of a single energy deposition.

2.1.4 Neutrons

Neutrons are generally classified by their kinetic energy. The most common classes are thermal and fast neutrons. Thermal neutrons are neutrons in thermal equilibrium with the surrounding (usually at room temperature), thus they have lost most of their initial energy in collisions with

the medium. Fast neutrons have an energy above 1 MeV and usually originate from nuclear reactions. Neutrons interact through the strong force with the nuclei of the absorbing material. This force acts over a very small range, accordingly, the chance of an interaction is relatively small. Fast neutrons are mostly elastically or inelastically scattered and thus continuously loss kinetic energy to the medium (moderation). In an elastic scattering process, some of the neutron's kinetic energy is transferred to the recoiling nucleus which partially is converted into an ionization signal and thus can be observed in a germanium detector. In the inelastic scattering process the neutron is absorbed and re-emitted at a lower energy, leaving the nucleus in an excited state. The excited nucleus decays after a certain amount of time through the emission of some form of radiation (usually a γ-ray), that can be detected. The most common interaction of thermal neutrons is neutron capture by the nucleus, forming an isotope of an increased mass number by one unit. The final isotope often is found in an excited state, and emits a de-excitation photon. Thermal neutrons furthermore can induce fission, the break up of the nucleus, which is connected with a large release of binding energy.

2.2 Semiconductor physics

In order to understand the functioning of germanium detectors it is required to describe a few basic principles from solid state physics. The description here is very limited and will focus mainly on the physics of semiconductors. The discussion is based on Ref. [42, 47, 48] and the interested reader is referred to these references for more information on the topic.

2.2.1 Band structure

Quantum theory predicts that the wave functions of electrons, that are bound to an atom, can only be observed in electron shells, quantified energy levels. Each shell holds a fixed number of electrons; the respective quantum numbers of the system define the number of electrons in each shell and how they are divided into sub-shells. Electrons filling the outer most shell are called valence electrons and define the chemical properties of the element. In solids the wave functions of the valence electrons of neighboring atoms can overlap. The overlapping wave functions cause the energy levels of the valence electrons to be separated, therefore when atoms are combined in a periodic lattice the discrete energy levels are broadened by the overlap of many different wave functions and energy bands are formed. These bands can overlap (as in metals) or be separated (as in insulators and semiconductors) and therefore define the electrical properties of the solid.

Semiconductors need to be build of group 4 elements in the periodic table (octavalent), that means they have 4 valence electrons. The Pauli exclusion principle forces the valence electrons in group 4 elements to be split over two sub-shells (two in the s-state and two in the p-state, both with opposite spins). Therefore the valence electrons take two distinct energy levels, that are separated from each other, the p-level being the higher of the two. In a semiconductor the atoms are arranged in a diamond lattice structure and form 4 covalent bonds with their neighboring atoms. This arrangement in a sufficiently large periodic lattice will broaden the s and p-level into two energy bands: The energetic lower band – the valance band – has just enough bonding states to accommodate all the electrons of the lattice. Therefore in the absences of any excitation no higher energy states are occupied, but also no additional states

are available in the valance band. The higher energetic band – the conduction band – in this situation is empty.

2.2.2 Charge Carrier

An electron can gain sufficient energy, through thermal motion of the lattice or transferred from incident radiation, to leave the covalent bond it is forming with neighboring atoms and by doing so, be elevated from the valence band across the gap into the conduction band. In the conduction band, the electron is not bound to the crystal structure and therefore can move freely through the lattice. The excited electron leaves behind a positively charged vacancy, that can be filled by electrons from neighboring atoms, leaving behind another vacant state at a different location. Therefore, similar to the free electrons in the conduction band, this vacant state in the valance band – called "hole" – can move freely through the crystal, behaving similar to a positively charged particle. As each electron moving to the conduction band leaves behind a hole, the two particles are often referred to as electron-hole pairs or charge carriers.

An electron from the conduction band can fill up a vacant covalent bond and hence recombination between an electron and hole occurs. In a pure semiconductor the chance for this process is rather small, therefore the lifetime of the charge carrier can be in theory in the order of seconds. However, in most semiconductors there is an important amount of impurities present that form so called recombination centers, which capture both electrons and holes and trap them for a certain amount of time. If two charge carriers of opposite types are captured simultaneously they recombine. Such recombination centers are one of the main reasons why in real semiconductors the lifetime of charge carriers is less than $10^{-4}\,\mathrm{s}$.

2.2.3 Intrinsic materials and doping

The band gap in a semiconductor is relatively large (e.g. 0.7 eV in germanium) compared to typical thermal energies (i.e. at room temperature, roughly 26 meV). The probability of occupying a certain energy state is given by the Fermi-Dirac distribution, thus the probability of an electron occupying a state in the conduction band is tiny (4.4×10^{-10}). The high density of states however assures that electron-hole pairs are constantly being generated. Under the assumption, that no impurities are present in a semiconductor (intrinsic material), the number of electrons n_i and holes p_i must be equal (each electron moving to the conduction band leaves behind a hole in the valence band). The amount of charge carrier is then defined by the temperature T and the band gap E_g:

$$n_p = n_i = AT^{3/2} \exp\left(\frac{-E_g}{2kT}\right), \tag{2.3}$$

where A is a material dependent constant and k is the Boltzmann constant. As long as the electrical properties are dominated by this contribution from thermally created charge carriers and not by the amount of impurities in the detector, the material can be considered an intrinsic semiconductor. A typical value for the numbers of holes/electrons in germanium at 300 K is roughly $2.5 \times 10^{13}\,\mathrm{cm}^{-3}$.

Some residual impurities are present even in very clear materials. These materials behave according to the dominant type of impurities as either p-type or n-type material:

n-type: The impurities are dominated by group 5 elements (pentavalent), that occupy the place of a normal group 4 atom (tetravalent). This arrangement results in one of the 5 valence electrons of the pentavalent material being incapable of forming a covalent bond with the surrounding atoms, adding an excess electron to the lattice (donor). The donor electron is lightly bound to the impurity atom and very little energy is required to break the bond and release it into the conduction band. These electrons form energy levels, that lay within the band gap, close to the conduction band (only 0.01 eV below it in germanium).

p-type: In this case the impurities are dominated by group 3 elements (trivalent), and by replacing a tetravalent atom they add a vacancy to the lattice structure, which can be filled by a valence electron (acceptor). As the electrons filling the vacancy are only weakly bound to the lattice, their corresponding energy level is in the band gap, just above the valence band. By borrowing an electron from the lattice they leave behind a hole in the valence band that can move freely through the crystal structure (hole).

Due to the close proximity of the energy levels formed by the impurities to the respective bands, the thermal energy required to ionize the impurities is very small and all the impurities directly add charge carriers to the conduction band of the material. Even at relatively small impurity concentrations ($\gg 10^{13}\,\mathrm{cm}^{-3}$) these additional charge carriers dominate the conduction band. One type of charge carrier is more prominent (majority carriers) compared to the other type (minority carriers). This shifts the equilibrium between electrons and holes, especially the number of recombinations that occur. The number of electrons n and holes p is related to the intrinsic case by the relation $n \cdot p = n_i \cdot p_i$.

It is difficult to create materials pure enough to use their intrinsic properties and sometimes easier to artificially add impurities of the opposite type to compensate for the natural occurring impurities in those materials (doping). In this way, materials with properties close to intrinsic semiconductors can be created. The material used in high purity germanium detectors is of high enough purity (impurities of the order of $10^{10}\,\mathrm{cm}^{-3}$) to be considered intrinsic and no compensation is required.

Semiconductor materials can be heavily doped to create layers with a high conductivity that can be used as electrical contacts (electrodes). These layers are specifically designated as p+ or n+.

2.2.4 pn-junction

The impurities in a semiconductor can easily be controlled, so that the impurities change from n-type to p-type, forming a pn-junction. The usual technique to reach this goal is to have lithium drift under high temperature into a uniform p-type material. The lithium does not replace tetravalent atoms in the crystal structure, instead, because of its small size, it occupies the space between the atoms of the crystals (interstitial). In sufficiently large amounts the monovalent lithium then can turn the p-type material into n-type material.

At the boundary of the junction, one side is dominated by electrons from donor atoms, while the other side is dominated by holes from acceptor atoms. This situation forces the more abundant particles to diffuse naturally into the region with a low concentration of the respective charge carriers. The diffusion of charge over the boundary creates a region with a net charge on each side of the junction. The build up of this opposing charge creates an electric

potential, consequently an electric field is formed that reduces the tendency for further charge diffusion over the boundary until an equilibrium is reached.

The intermediate region, or depletion region, has very attractive properties for radiation detection. It is devoided of charge carries and thus forms a capacitor, with the depleted region being the dielectric layer and the two adjacent undepleted layers being the electrodes. The formation of an electric field over the intermediate region causes any electrons and holes entering this zone (i.e. created through ionization by radiation) to drift along the field gradient towards the n- or p-region. This motion in the electric field will cause an electrical signal being induced into the electrodes, that then can be read out.

The spontaneously formed depletion region is very thin (a few µm) and the potential created by the charge separation V_i is small ($\sim$1 V). Additionally, the capacitance of such a junction is high, so when it is connected to an external read out circuit, the noise properties are quite poor (see Sec. 4.1 for an explanation of the relationship between capacitance and noise). Therefore, such a depletion region is not very practical for radiation detection application. However, the depleted zone can be increased by applying a reverse bias voltage. This means a positive voltage is applied to the n-type side of the junction in respect to the p-type side. This attracts additional electrons and holes across the boundary and therefore enhances the naturally formed depletion region.

The depletion region extends in both direction and the actual extend can be determined in the simplest (one dimensional pn-junction, extending to infinity in the other two dimensions) case analytically from the Poisson equation (see any of the above mentioned references for the details). The depletion width x depends on the donor N_d and acceptor N_a concentrations (which here is assumed to be equal to the concentration of the respective charge carriers n and p in the individual layers) and the applied bias voltage V_b:

$$x_n = \sqrt{\frac{2\varepsilon\,(V_b + V_i)}{eN_d\,(1 + N_d/N_a)}}, \qquad x_p = \sqrt{\frac{2\varepsilon\,(V_b + V_i)}{eN_a\,(1 + N_a/N_d)}}, \tag{2.4}$$

with e being the electronic charge and ε the absolute permittivity (dielectric constant) of the material. The total width is simply formed by the sum of the two contributions. In Eq. 2.4 the voltage created by the thermal diffusion of electrons and holes across the junction V_i can be neglected then the bias voltage usually is between 1 and 10 kV and therefore much larger than V_i.

Most detectors are asymmetrically doped. This means a small part of a very lightly doped material is highly doped, for example p-type material with lithium, turning it into a n+ layer. The depletion layer then extends predominantly into the lightly doped bulk of the detector and the depletion width is given by:

$$w \approx x_n = \sqrt{\frac{2\varepsilon\,(V_b + V_i)}{eN_d}}. \tag{2.5}$$

This is valid for a one dimensional pn-junction, hence the geometry is identical to a simple parallel plate capacitor. The capacitance is given by:

$$C = \frac{\varepsilon A}{w} = A\sqrt{\frac{\varepsilon e N_d}{2\,(V_b + V_i)}}. \tag{2.6}$$

Consequently, by applying a bias voltage the capacitance is reduced, which affects the noise in a system positively (see Sec. 4.1). Furthermore, the bias voltage also increases the drift velocity of charge carrier created withing the depletion region, hence reducing the chance of charge trapping and recombination. Most detectors are of a more complex geometry and the exact relations between the above mentioned variables can only be found through simulations of the electric potentials.

A tiny residual current can even flow through a highly biased pn-junction. Some current is caused by thermally created charge carriers in the depleted region. This current thus depends on the band gap and temperature. In germanium the band gap is small, so at room temperature the thermal current is large and the detectors need to be cooled to reduce this contributions. Additional current flows over conducting paths that form between the two electrodes on the surface of the detector material. Great care is given in the fabrication process of semiconductor devices to avoid contaminations on the surface that facilitate the formation of such surface currents, but they can not be removed entirely. These currents (called leakage currents) add to the current that is observed from drifting charges in the depleted region. If leakage currents are large, tiny fluctuation in the current can be sufficient enough to corrupt the signal coming from charge carriers. The surface leakage currents grow with increasing high voltage, therefore, the bias voltage can not take an arbitrary large value. Furthermore, in high electric fields the charge carriers can gain sufficient energy to create secondary electron-hole pairs, eventually leading to a destructive avalanche.

2.2.5 Signal formation

Thermal energy causes charge carriers to move along random tracks, even when an electric field is absent. This random motion, generally identified as diffusion, causes the charge carriers to move from a region of high concentration to regions with lower concentrations. Assuming the charge carriers being confined to a point like region at $t = 0$, then after some elapsed time t the concentration profile forms a Gaussian of variance:

$$\sigma = \sqrt{Dt}. \tag{2.7}$$

The diffusion constant D is a material dependent property.

In the presence of an electric field, the charge carriers move parallel to the electric field vector. The drift direction is defined by their charge; electrons move against the field vector, holes follow the field vector. During this motion the charge carriers interact strongly with the crystal lattice creating phonons (quantized lattice excitations). This causes the charge carriers to slow down and instead of being accelerated infinitely they reach a constant velocity that depends on the strength of the applied electric field:

$$v_h = \mu_h E, \qquad v_e = \mu_e E. \tag{2.8}$$

The proportionality constant is the mobility μ of the respective particle type. The hole transport involves sequential transition probabilities, therefore they tend to move slightly slower than the electron. The mobility and the diffusion constant are linked through the Einstein equation:

$$\mu = \frac{e}{kT} D, \tag{2.9}$$

where e is the electric charge, k the Boltzmann constant and T the temperature. Typical values for the mobilities are $\mu_e = 3.6 \times 10^4\,\mathrm{cm^2/V/s}$ and $\mu_h = 4.2 \times 10^4\,\mathrm{cm^2/V/s}$ in germanium at 77 K. For high electric fields ($E > 10^3\,\mathrm{V/cm}$) the drift velocity saturates. The saturation velocity v_s is roughly $10^7\,\mathrm{cm/s}$ and reached at an electric fields of $10^4\,\mathrm{V/cm}$.

Let us consider the situation where diffusion is negligible and the electric field $\vec{E}(\vec{x})$ constant in time and known in the entire detector volume. Furthermore, a certain amount of electron-hole pairs is deposited at $t = 0$ in the detector. In this situation, the path of the electrons and holes are entirely defined through Eq. 2.8 and the position of the electrons and holes can be calculated at any point in time $t > 0$ through integration of this equation.

The presence of a moving charged particle induces a current into the electrodes, which can be monitored by an external read out system. The motion of the charge can be derived from Eq. 2.8. It remains to calculate the current induced into the respective electrode. In general this is possible through Gauss law, which relates the total charge Q in a volume to the flux of the electric field through the surface S enclosing the volume:

$$Q = \oiint_S \varepsilon \vec{E} \cdot d\vec{S}, \tag{2.10}$$

where ε is the permittivity of the medium. The above integral can be evaluated at a given time t, assuming that the charge carriers in the volume are static at that very moment. This is the quasi-steady state approximation, which is equivalent to assume, that the electric field propagates instantaneously through the detector volume. This is a good approximation as the speed of light (at which the electric field propagates) is large compared to the charge carrier drift velocity in semiconductor detectors. If the surface is chosen such that it encloses the electrode, then the above equation describes the charge Q on the electrode at each moment in time. It changes as the electric field is altered by the relocation of the charge carrier in time. The integral therefore must be reevaluated for any position of the charge carriers.

2.2.6 Shockley-Ramo Theorem

Fortunately, the calculation of the induced current in Eq. 2.10 can be simplified with the Shockley-Ramo theorem, which was discovered by W. Shockley [49] and S. Ramo [50] independently.

To derive the Shockley-Ramo theorem, let us consider a certain amount of electrodes (individually numbered by the index i) with a surface S_i and a fixed potential V_i arbitrarily distributed over a volume containing stationary space charges defined by the charge density $\rho(\vec{x})$ and a single moving charge q [51]. The potential at any point in the volume is then defined through the Poisson equation with Dirichelet boundary conditions:

$$-\varepsilon \nabla^2 \varphi = \rho(\vec{x}) + q\delta(\vec{x} - \vec{x_0}), \qquad \phi|_{S_i} = V_i \tag{2.11}$$

The permittivity ε is considered constant, however, it can be proven, that the Shockley-Ramo theorem is also valid in the case of an inhomogeneous permittivity [52]. Because of linearity φ can be be split into three distinct parts, that are defined by the following equations:

$$\nabla^2 \varphi_0 = 0, \qquad \varphi_0|_{S_i} = V_i \tag{2.12}$$

$$\nabla^2 \varphi_s = -\rho(\vec{x})/\varepsilon, \qquad \varphi_s|_{S_i} = 0 \tag{2.13}$$

$$\nabla^2 \varphi_q = -q\delta(\vec{x} - \vec{x_0})/\varepsilon, \qquad \varphi_q|_{S_i} = 0 \tag{2.14}$$

The first equation describes the electric potential φ_0, caused only by the applied voltage to the electrodes. The second equation characterizes the electric potential φ_s created by the space charge. The third equation expresses the electric potential φ_q related to the charge q. The electric field is related to the potential $\vec{E}(\vec{x}) = -\nabla\varphi(\vec{x})$, so the induced charge on electrode i can be expressed as a function of these three potentials:

$$Q_i = -\oiint_{S_i} \varepsilon\nabla\varphi_0 \cdot d\vec{S}_i - \oiint_{S_i} \varepsilon\nabla\varphi_s \cdot d\vec{S}_i - \oiint_{S_i} \varepsilon\nabla \cdot \varphi_q d\vec{S}_i. \tag{2.15}$$

The first and second term in this equation are independent of q, therefore they do not add any variation to Q_i. Variations of Q_i and thus of the induced charge are only dependent on the position of the charge q and its potential distribution in the device.

Let us consider the following fields:

$$\nabla^2\psi_i = 0, \qquad \psi_i|_{S_j} = \delta_{ij}, \tag{2.16}$$

where the second equation expresses that the field ψ_i related to electrode i is unity on its surface and zero on the surface of all other electrodes. Furthermore, Green's second identity is given by:

$$\iiint_V \Phi\nabla^2\Psi - \Psi\nabla^2\Phi d\hat{V} = \oiint_S \Phi\frac{\partial\Psi}{\partial n} - \Psi\frac{\partial\Phi}{\partial n}d\hat{S}. \tag{2.17}$$

Then, as described in Ref. [53], $\Psi = \psi(\vec{x})$ and $\Phi = \varphi_q(\vec{x})$. The volume V is consider to exclude the interior of the electrodes and its surface is accordingly the sum of the surfaces of all electrodes. With this definition, $\nabla^2\Psi = 0$, so the first integral on the left cancels and $\Phi|_S = 0$, so the first integral on the right is zero. Additionally, $\Psi|_S = \delta_{ij}$, $\frac{\partial\Psi}{\partial n} = \nabla\Psi \cdot \vec{n} = -\vec{E_q}(\vec{x}) \cdot \vec{n}$ and $\nabla^2\Phi = -q\delta(\vec{x} - \vec{x_0})/\varepsilon$, therefore the equation reduces to:

$$\iiint_V q\psi_i(\vec{x})\delta(\vec{x} - \vec{x_0})d\hat{V} = \sum_j \oiint_S \varepsilon\delta_{ij}\vec{E}_q(\vec{x}) \cdot \vec{n}d\hat{S} = \oiint_{S_i} \varepsilon\vec{E}_q(\vec{x}) \cdot d\vec{S}_i = Q_i, \tag{2.18}$$

where we moved the ε in the first equality from the left hand side to the right hand side. The sum in the second equality can be removed by evaluating the delta function. The equation of Gauss's law for the ith electrode will remain, which is simply equal to Q_i. The integral on the left hand side together with the delta function can be removed by setting $\psi_i(\vec{x})$ to $\psi_i(\vec{x_0})$. The equation therefore is:

$$q\psi_i(\vec{x_0}) = Q_i. \tag{2.19}$$

This equation is Shockley-Ramo's theorem and expresses, that the induced charge Q_i for a charge q at $\vec{x_0}$ can be found from the potential ψ_i which was defined in Eq. 2.16. This potential is commonly referred to as weighting potential. Once the weighting potential is known, it is straight forward to calculate the induced charge for any position of the charge.

Taking the time derivative of Eq. 2.19 one finally, finds the induced current $I_i = dQ_i/dt$ on electrode i to be related to the weighting field $E_{\psi_i}(\vec{x}) = -\nabla\psi_i(\vec{x})$:

$$q\vec{E_{\psi_i}}(\vec{x_0}) \cdot \vec{v} = I_i. \tag{2.20}$$

To derive the left hand side of this equation the chain rule in three dimensions was used.

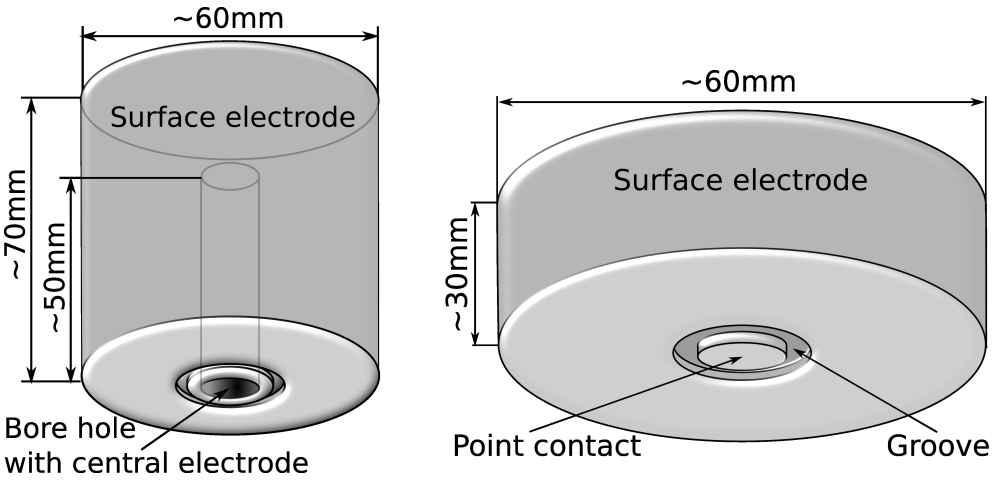

Figure 2.5: A semi-coaxial detector (on the left) and a point contact detector (BEGe, see Sec. 3.2) with a groove (on the right). The detectors are not to scale.

In reality, as discussed in the previous chapter, a charge cloud is formed, that is composed of equal amounts of electrons and holes. Electron and holes are always created in pairs, therefore at the time of creation the position of the electron and of the hole is the same, but their charge is of opposite sign, therefore at that moment they cancel each other in Eq. 2.19. Through their interaction with the electric field the electrons and holes drift in opposite directions and are separated. The weighting potential at their location differs and net induced charge appears on the electrode, that allows to derive the observed variations in current.

2.3 Characteristics of germanium detectors

It is required to produce relatively bulky detection devices from a dense material to detect at least some of the high energetic γ-rays (above a few hundreds of keV). The density of germanium ($\rho = 5.32\,\mathrm{g/cm^3}$) is twice as high as the one of silicon ($\rho = 2.33\,\mathrm{g/cm^3}$), increasing the probability of γ-rays interacting with the material per unit thickness substantially. Furthermore, the high purity that can be reached with germanium allows to produce detectors of centimeter-thickness. The slightly smaller band gap in germanium also increases the number of charge carriers, therefore it offers a slightly superior energy resolution. The downside of germanium is that the amount of thermally produced charge carrier at room temperature is large, therefore the detector has to be operated at low temperatures (usually close to liquid nitrogen temperature of approximately 77 K).

The following section will discuss the production method of germanium detectors and one of the most vital characteristics, the charge carrier statistics.

2.3.1 Production of germanium detectors

There are two main techniques to produce germanium suitable for radiation detection application. The first is the compensation of impurities through lithium ion drifting. The residual

impurities in a p-type material can be balanced in a relatively thick layer of up to a few centimeters by the lithium donor atoms. Such compensated Ge(Li) detectors have been produced from the early 1960s onward and were the first commercially available large volume semiconductor detector systems. These detectors have to be kept perpetually at low temperature, because the lithium drift continues at room temperature and finally will render the detector inoperable.

In the early 1980s sufficiently pure germanium crystals has been produced so that lithium compensation is no longer necessary. Detectors, that are produced from ultra pure (close to intrinsic) germanium are known as high-purity germanium (HPGe) detector. HPGe detectors can be stored at room temperatures for multiple years without rendering the detector inoperable, so with the emergence of this technology the production of Ge(Li) detectors ceased and most manufacturers have discontinued the production.

Ultra pure germanium is produced through the technique of zone refining [54]. The process starts with material of already high purity prepared in a similar fashion as the materials used in the semiconductor industry. The material then is locally heated and the melted zone slowly moved from one end of the sample to the other. When the material solidifies after melting, impurities more easily remain in the molten zone instead of being incorporated into the crystal structure, and thus are transferred to one of the ends of the sample as the melted zone is moved through the crystal. The process is repeated many times until impurity levels down to $10^9\,\mathrm{cm}^{-3}$ are reached. From this zone refined material large single crystals are grown to be manufactured into HPGe detectors.

p+ electrodes are usually created through boron ion implantation [55]. A monoenergetic beam of boron ions produced by an accelerator is reflected on the surface of the semiconductor, so that the ions penetrate a well defined range into the semiconductor material. The impurity profile can be control by varying the energy of the boron ion beam. With this technique it is possible to produce very thin ($< 1\,\mu\mathrm{m}$) highly doped layers. The n+ electrodes are produced most often through lithium diffusion. The semiconductor material is exposed at temperatures of 200-500 °C to a gaseous ambient or a paste (salt) of the desired dopant [56]. The diffusion process is accelerated through the high temperature, so within a short time the lithium drifts deep into the medium. The layers produced with this method tend to be thicker in the order of a few hundred of micrometers.

Any surface not covered by an electrode is at risk to develop conductive paths over the surface and enhance leakage currents. The surface of germanium oxidizes naturally when exposed to oxygen or water vapor. A thin silicone oxide or amorphous germanium layer is applied to the surface (passivation) to establish a controlled termination. Native oxides grown on the surface can attract electrons and create weak field regions and conductive surface channels [57]. Producing good passivated surfaces is one of the biggest challenges in the production of germanium detectors and the manufacturers are very secretive about their solution. If possible, detectors are fabricated in such a way, that as much surface can be covered by electrodes and as little as possible needs to be passivated.

Independent on the type of the original material, usually both, a p+ and a n+ electrode, are required to produce a germanium detector. One of the electrodes is used to provide the high voltage the other one is kept at zero potential and used for the read out of the charge signal.

The simplest configuration is the planar HPGe detector, which is formed by a high purity germanium disk, with the two electrodes covering the two flat surfaces. The maximum depletion depth of such a planar detector is limited to 1-2 cm.

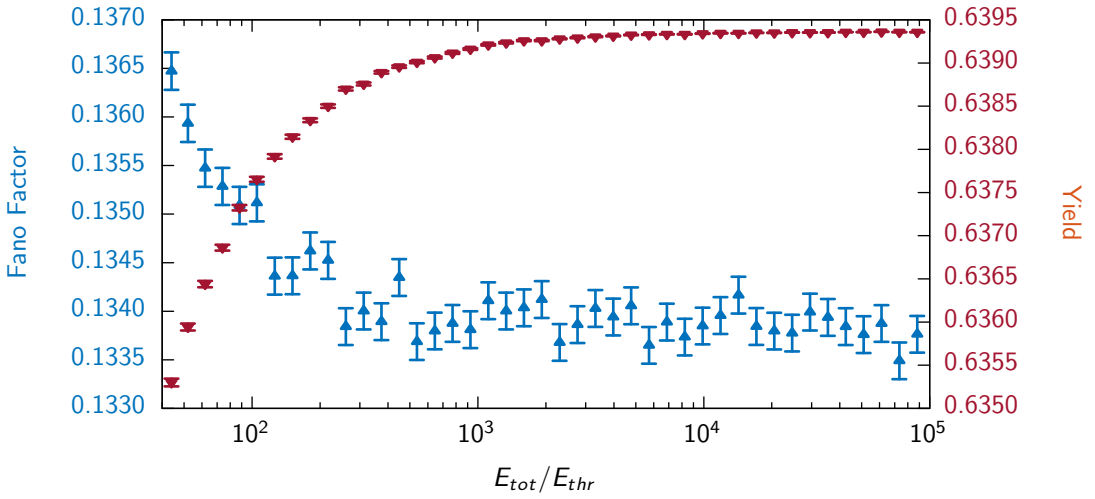

Figure 2.6: The Fano factor and yield as a function of the fraction E_{tot}/E_{thr} derived in a Monte Carlo simulation of the algorithm described in Sec. 2.3.2. At each value the algorithm was executed 10^6 and the number of charger carriers filled in a histogram. The Fano factor was then calculated by $F = var(N)/\bar{N}$ of the bin distribution and the yield was calculated by $\bar{N} \cdot E_{thr}/E_{tot}$. The error bars assume a normal distribution of the outcome of the various simulations.

The active detection volume can be enhanced by bringing the germanium into the form of a coaxial cylinder. This geometry enables the production of detectors with a mass up to 2-3 kg. Here, one electrode covers most of the outer surface of the cylinder, while the other electrode covers the central hole that passes through the cylinder. Often the hole only extends partially through the cylinder forming a closed-ended coaxial or semi-coaxial detector (see Fig. 2.5), which offers less passivation and a planar front. In this configuration the core electrode is commonly used for the data read out as the surface is smaller. The down sides of the coaxial configuration are reduced resolution caused by a large read out electrode (see Section 4.1). This limitation has been addressed with the introduction of point contact detectors. Similar to the coaxial detector, they have the form of a cylinder but are slightly smaller in diameter and height. Therefore, they don't need a central core. Instead, they contain a small circular read out electrode on one of the flat surfaces of the cylinder. The remaining surface is covered by the high voltage electrode. Their name derives from the point like read out electrode and sometimes they are also referred to as (small) point contact detector or p-type point contact (PPC) detectors. The later name indicates that these detector are in general manufactured from p-type high purity germanium. This thesis will be mostly concerned with this type of detector, so they will be covered in detail later (see Sec. 3.2).

2.3.2 Signal variance

The incident radiation interacts with the electrons in the medium and transfers part of its energy to these electrons, allowing them to move into the conduction band (band gap of 0.7 eV in germanium) and creating an electron-hole-pair that can move freely through the crystal lattice. If the initial energy transfer was large enough, these secondary particles can have sufficient kinetic energy to create free electron-hole-pairs themselves. This process initiates a

cascade of ion pairs, that only ends once the kinetic energy of the secondary particles is too low to further ionize the medium. This illustrates, that not all the energy of the absorbed radiation is available for the creation of electron-hole-pairs, but some of it appears as a residual kinetic energy of the charge carriers, that is eventually dissipates into lattice vibrations (quantized as phonons). Moreover, in germanium the highest energetic value in the valence band and the lowest energetic value in the conduction band are not found at the same value of momentum in the phase space. Therefore the transfer of an electron from the valence band to the conduction band, must coincide with a transfer of momentum to a phonon. The energy required for creating an electron-hole-pair therefore is increased by the amount of energy required for the creation of phonons.

The final number of charge carrier created by a fixed energy therefore fluctuates. If the individual electron-hole-pair creation events are independent and have a small constant probability, then the mean number of electron-hole-pairs and the variance can be calculated by applying Poisson statistics and are given by:

$$var(N) = \bar{N} = E_{tot}/\epsilon, \tag{2.21}$$

where E_{tot} is the total energy deposited in the medium by the radiation and ϵ is the mean energy required to produce a single electron-hole-pair. However, the charge carrier creation events in a germanium detector are not independent of each other. The structure of the cascade and the mechanism governing the electron-hole-pair creation in a semiconductor needs to be taken into account, causing the observed variance to be smaller than predicted by Poisson statistics:

$$F = \frac{var(N)}{\bar{N}}, \qquad 0 < F < 1 \tag{2.22}$$

The dimensionless Fano factor F was first introduced by Fano in 1947 [58], who tried to explain the resolution of gas proportional counters. His work was followed by many investigations, that primarily focused on understanding the detailed development of the ionization cascade, including thermal loss to lattice vibrations.

The appearance of a Fano factor below unity can be illustrated by considering a simple model that can be easily implemented in a Monte Carlo simulation. Although the model can illuminate some of the statistical aspects it is by no mean sufficient to calculate an exact expression of the Fano factor or explain the main physical mechanism that is responsible for the appearance of the Fano factor. Sadly, up to now the Fano factor in germanium and other semiconductors is still not well known and more efforts need to be undertaken to shed some light on the issue. The simple model that will be studied was initially proposed by van Roosbeck in analogy of cutting a board in different pieces [59]. The model partitions the total energy E_{tot} of the primary particle in a recursive algorithm and analyze the number of charge carriers that can be produced. In each step the energy of a single particle E_0 is split up into the energy required for the creation of a new electron-hole-pair E_{thr} and the kinetic energies of the initial and newly formed particles:

1. If $E_0 < E_{thr}$, then no further charge carriers can be produced, the remaining energy is lost to lattice vibration and the algorithm stopped.

2. If $E_0 > E_{thr}$, then the creation of an new electron-hole-pair is possible, the required energy for the electron-hole-pair creation is subtracted from the total energy ($E_r =$

$E_0 - E_{thr}$). The remaining energy E_r is randomly divided into two fractions, the remaining kinetic energy of the primary particle E_1, and the shared kinetic energy of the newly created electron-hole-pair E_2. The latter fraction E_2 is furthermore divided (in the simplest case equally) to form the individual kinetic energy of the electron E_e and hole E_h, such that $E_2 = E_e + E_h$.

3. The newly formed fractions E_1, E_e and E_h are considered as primaries and step 1 and 2 are applied to each piece individually until no further division is possible.

In this manner, the amount of energy deposited by the radiation in the medium is divided into individual pieces that can not be further divided and the amount of electron-hole-pairs created in the process can be estimated. The algorithm with $E_h = E_e$ has been simulated through a small program (implemented in C) and the results illustrated in Fig. 2.6 for different fraction of E_{tot}/E_{thr}. It can be seen, that for $E_{tot} \ll E_{thr}$ both, the Fano factor $F = var(N)/\bar{N}$ and the yield $Y = \bar{N} \cdot E_{thr}/E_{tot}$ are constant and do neither depend on the total deposited energy nor the minimal ionization energy. Even at small values of the ratio E_{tot}/E_{thr} the deviations from a constant value are small (in the order of 1%), thus also in that range the Fano factor and the yield can be considered as constant. The value of the Fano factor found with this simple model $F \sim 0.13$ is in good agreement with values from literature for germanium in the range 0.06 to 0.15 (see [60] for a comprehensive overview). The average energy per electron-hole-pair ϵ can be calculated from the yield Y and is $\epsilon = E_{thr}/Y$. Assuming $E_{thr} \approx 1\,\text{eV}$, this would mean that the simulated value for the yield is roughly a factor of 2 smaller than what was found experimentally (3.6 eV in silicon and 2.96 eV in germanium).

This simple model shows, that a Fano factor much smaller than unity appears naturally if a finite dispersion in the kinetic energy of the charge carrier is assumed. Apart from Monte Carlo simulations, it is possible to describe the effects in an analytic framework and to incorporate phonon losses into the model [59].

Next to this simple model, there are many other models based on similar assumptions, that try to phenomenologically describe the appearance of the Fano factor in semiconductors [60]. Unfortunately, the details of the formation of the ionization cascade, as well as some fundamental aspects of semiconductors are not yet sufficiently well understood to establish a satisfactory description of the Fano factor. Moreover, the reported values from experimental setups are found in a relatively large range and discrepancies between measurements have not yet been explained [61]. It has not even been established yet if the Fano factor indeed is a material constant or if it changes with energy and temperature as some studies with silicon would suggest [62].

In chapter 7.3.1 the Fano factor will be experimentally determined and some of the complexities that such an evaluation can create will be discussed.

3 Point contact germanium detectors

Point contact detectors are cylindrical diodes with a small point contact embedded into one of the bases. An example of such a detector is illustrated in Fig. 2.5. The most common application for PCGe detectors in fundamental research have been described in Sec. 1.2. Their wide spread use in these fields is explained by their beneficial properties: They have an exceptional energy resolution and low noise. Furthermore, as will be discussed in Sec. 3.5, they allow to distinguish certain types of events solemnly on the time profile of the current pulse. One major drawback is, that they are limited in size. The largest germanium detectors that can be produced are in the range of 2-3 kg and of a coaxial geometry. It is currently not possible to produce PCGe detectors of a similar size; the maximal size of these detectors is around 1 kg.

There are PCGe detectors available, that are produced from n-type materials, however most of the available PCGe detectors are produced from p-type materials, thus only this case will be considered in the following discussion.

3.1 Production techniques

As discussed in the previous chapter, the two most common production methods of electrodes are lithium diffusion and boron implantation. The lithium diffused layer drops gradually and the exact depth is relatively hard to control (see Sec. 3.4 for effects caused by this layer). In a typical PCGe detector the lithium diffused electrode covers most of the detectors surface and is used to apply the high voltage.

The boron implantation produces a fast drop over a few hundred of micrometers (usually roughly 0.3 µm) and is mostly used for the creation of the point contact (although other procedures are also very common). Some of the manufactures remove a thin stripe of a few millimeter thickness around the point contact to obtain a better separation between the electrodes (groove), others leave the germanium in that region intact. In both cases, the region between the electrodes is passivated to better control conductive paths along the surface.

The size of the detector is mainly limited by the methods available for crystal pulling It is possible to pull crystals with a radius of more than 4 cm. However, detectors of that size often have weak electric fields (in the corners) with increased charge carrier trapping effects. Large detectors are also more prone to high leakage currents. Typical large volume HPGe detectors are produced with a weight between 500 g and 1 kg. The same technology, however, is also used to produce detectors of much smaller size.

3.2 Existing PCGe detector designs

There are two major companies producing HPGe detectors; Canberra Industries Inc. [66] and ORTEC [67]. Furthermore, there are some smaller companies, such as Baltic Scientific Instruments, Ltd. (BSI) [68], that also have long lasting experience in the production of HPGe

	GERDA [63]	COGENT [25]	MALBEK [64]	MAJORANA [65]	TEXONO [28]	CDEX [29]
Production	Canberra	Canberra	Canberra	Ortec	Canberra	Canberra
Weight	467-827 g	443 g	450 g	∼800 g	∼ 500/900 g	∼ 1 kg
Height	23-35 mm	31 mm	30 mm	∼ 50 mm	∼ 50/60 mm	∼ 62 mm
Radius	33-37 mm	30 mm	30 mm	∼ 31 mm	∼ 50/60 mm	∼ 62 mm
Wrap around	up to G.	up to G.	up to G.	∼ 5 mm	Conf.	Conf.

Table 3.1: Different detector layouts for PCGe detectors used for particle research. Information about the point contact (P.C.) radius and the groove (G.) are often not available as they are confidential.

detectors. All the experiments mentioned in Sec. 1.2 purchased their detectors with one of these companies. Accordingly, the detectors are all rather similar.

Canberra Industries Inc. sells their PCGe detectors under the name Broad Energy detector (BEGe) and their detectors are optimized for the usage in routine γ-ray spectroscopy analysis. They normally produce diodes from p-type HPGe with a total weight of roughly 0.2-1.0 kg, a radius of 2.5-4.5 cm and a height of 2-3 cm. The point contact is produced with boron implantation on one of the bases of the cylinders. The point contact is surrounded by a groove or ditch, an indent of a few millimeter depth that separates it from the second electrode covering all the remaining surface. The second electrode is produced with lithium diffusion and can reach up to 1 mm thickness.

ORTEC has a line of p-type semi-planar detectors, which are very similar to the Canberra BEGe detectors and have roughly the same weight, radius and height. They also use boron implantation for the point contact but also offer an alternative low noise contact technology. The high voltage electrode is again produced with lithium diffusion and of a similar thickness as for BEGe's. The main difference is that ORTEC seems to not add a groove to their commercially branded detectors. Instead they implant the point contact directly into the center of the planar base of the cylinder and cover the remaining area with a passivation layer. The high voltage electrode does not wrap around onto the base with the point contact.

The producers of germanium detectors in general are very secretive about their technology and scientists often are told to not release to much information about the detector they use. Thus data on the exact detector configuration in most fundamental experiments are sparse. Table 3.1 lists some exact numbers that have been released in publications. Details about the point contact size only were found for the MALBEK detector. It has a radius of roughly 3 mm.

It is apparent that some of the experiments deviate quite a bit from the standard geometry produced by ORTEC and Canberra. The MAJORANA, TEXONO and CDEX detectors for example are higher than the standard geometry. The reason for this decision is most likely a lower surface-to-volume ratio and thus a reduction of unwanted external backgrounds. Furthermore, the TEXONO collaboration works with a 500 g n-type PCGe detector. GERDA uses a standard geometry, as the relative safe and standardized production methods in that case should assure the proper working of as many of the detectors as possible. This entails a relatively large contact size.

3.3 Capacitance

In their publication about the shape field detector Luke et al. [1] pointed out that the small size of the central electrode leads to a small capacitance, which is particular beneficial for applications where low noise properties are required. They introduced an approximation that can be used for estimating the capacitance of such a detector and that is valid as long as the outside dimensions of the detector are much larger than the central electrode. In that case the central electrode is close to be hemispherical in shape (of radius r) and the following equation can be found for the capacitance:

$$C = 2\pi\varepsilon_0\varepsilon_r r. \tag{3.1}$$

The free space permittivity $\varepsilon_0 = 8.85 \times 10^{-12}\,\mathrm{F/m}$ and the dielectric constant of the material $\varepsilon_r = 16$ are known, thus it can be calculated that the capacitance is rough 5 pF for a radius of 5 mm.

The effect of the detectors capacitance on the noise is discussed in Sec. 4.1. It is found that a lower capacitance reduces the noise contribution to the resolution. This is of importance for low energy applications, where the resolution is dominated by the electronics noise. At higher energies (MeV region) the contribution from charge carriers statistics (see Sec. 2.3.2) dominates.

The rough estimation proposed by Luke et al. is sufficient to get an order of magnitude of the capacitance. If it is required to predict the capacitance of a detector in more detail, it is possible to derive it from the simulated electric potential in the detector (see Sec. 4.4). The calculation starts from Gauss's law of electricity (Maxwell's macroscopic equations):

$$\oiint_S \vec{D} \cdot \mathrm{d}\hat{S} = \oiint_s \varepsilon_0\varepsilon_r \vec{E} \cdot \mathrm{d}\hat{S} = Q. \tag{3.2}$$

The integral in this equation describes the flux of the electric field $\vec{E}$ through the surface of a volume V, which contains a charge Q. ε_0 is the vacuum permittivity and ε_r the relative permittivity in the material. The above equation also contains contributions from the space charges, however, as it has been discussed in Sec. 2.2.6 it is possible to split Eq. 3.2 into the contributions from the geometry $\vec{E_0}$ and from the space charge $\vec{E_c}$, which in turn also allows to split the right hand side of the equation into the respective charge contribution Q_0 and Q_c. As we are only interested in Q_0 the contribution from space charges can be cancelled and we can calculate the induced charge on the electrode Q_0 from the electric field $\vec{E_0}$, without any space charges in the detector.

3.4 Slow Pulses

In a PCGe detector the high voltage is applied to the electrode covering most of the outer surface, while the signal is read out at the central point like electrode (p+ contact). The surface electrode is produced by lithium diffusion and usually chosen to have a thickness of the order of 1 mm. This helps to reduce the background from α and β-particles which can not penetrate through this layer. γ-rays usually have a penetration depth large enough, so that they easily travel through this layer and reach the depleted zone. However, at energies below 50 keV the penetration depth is less than a millimeter, therefore some γ-rays do not reach

the depleted zone and deposit their energy in this surface layer. The condition in the lithium diffused layer are different from the depleted zone. This affects the shape of these signals.

3.4.1 Lithium drift layer

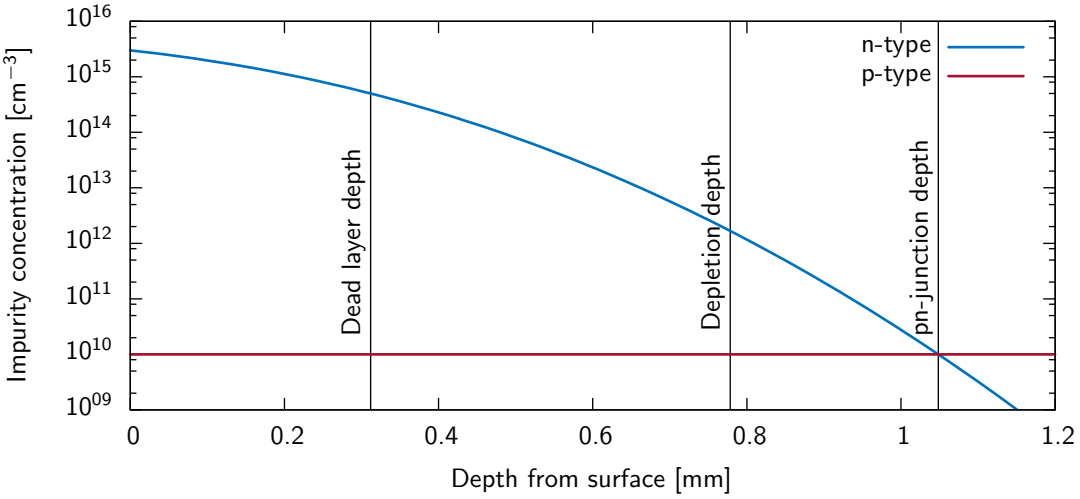

Figure 3.1: The lithium impurity concentration as a function of the penetration depth in a 1 cm thick planar p-type germanium detector of $10^{10}\,\mathrm{cm}^{-3}$ impurities (important for the calculation of the depletion depth). The profile corresponds to a diffusion of lithium at 200°C for 6 hours and an impurity concentration at the surface of $3 \times 10^{15}\,\mathrm{cm}^{-3}$. The dead layer depth was estimated to be at an impurity concentration of $10^{14}\,\mathrm{cm}^{3}$.

The production process of the n+ electrode with lithium diffusion can be described by a simple diffusion process with an infinite source at the surface. The analytic solution for the one dimensional diffusion equation with infinite source at one boundary is given by [56]:

$$c(x,t) = c_s \mathrm{erfc}\left(\frac{x}{\sqrt{4Dt}}\right), \tag{3.3}$$

where erfc is the complementary error function, c_s is the concentration right at the surface, D is the diffusion constant, which is entirely defined through the temperature [69] and t the diffusion time. The surface concentration can be estimated from the solubility in germanium which is temperature dependent and between $3 \times 10^{15}\,\mathrm{cm}^{-3}$ at 200°C and $2 \times 10^{18}\,\mathrm{cm}^{-3}$ at 500°C [70]. A typical concentration profile of lithium in germanium is shown in Fig. 3.1.

The impurity concentration in p-type germanium used for a typical PCGe detectors is in the order of $10^{10}\,\mathrm{cm}^{-3}$. The pn-junction is formed at the depth where the concentration from the n-type and p-type material are equal. From the pn-junction on the n-type impurity gradient rises fast towards the surface, thus even for large detectors the depleted region only reaches a few hundred of micrometers into the n-type material.

Between the boundary of the depletion region and the surface the electric potential is constant and therefore the electric field is zero. Charge carriers that are located in the region with zero electric potential close to the surface can not be directly detected in the read out electrode and thus do not induce a charge. Instead they follow a diffusive motion until they recombine

and are lost. Some of the charge carriers created near the depletion border however can diffuse into the depleted region, where they feel the influence of the electric field and induce a signal into the electrodes (holes for p-type material). The lifetime of charge carriers in germanium is reduced in highly doped materials [71]. Close to the surface of the diode the probability for recombination is increased and it is very unlikely that holes created in that region can reach the depletion border. The lithium diffused layer usually is divided into two regions according to the efficiency of charge collection ε from this region [65]. The dead layer or recombination layer is the region where all charges are immediately lost in recombination ($\varepsilon = 0$) and the transition layer or diffusion layer is the region where at least a fraction of the deposited charge is observable ($0 < \varepsilon < 1$). In the bulk or active layer the detector is depleted and a signal is observed at the read out electrode ($\varepsilon = 1$).

The location of the depletion border is close to the pn-junction in the direction of the n-type material and can be calculated from charge neutrality; the amount of holes moving in the influence of the reverse bias voltage to the n-type material must be equal to the number of electrons moving to the p-type material. At the depletion voltage all sites available in the p-type material are occupied, thus an equal amount of sites must be occupied in the n-type material. The number of sites in the p-type material can be estimated from the impurity density and the volume of the diode, thus for a simple geometry (i.e. planar) the position of the depletion border can be found from the impurity concentration profile.

The position of the border between the transition layer and the dead layer is not that well defined. As the impurity increases gradually it can be assumed that the recombination probability also increases gradually and thus there is no strict border between the two regions.

3.4.2 Signal formation in the transition layer

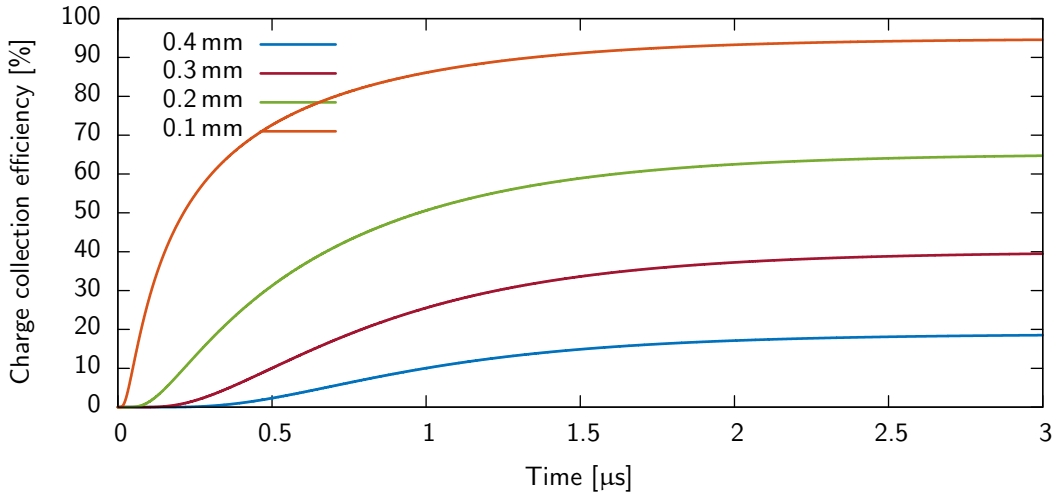

Figure 3.2: The temporal distribution of the amount of holes that reach the depletion border for a signal created at a certain distance (see color label) from the depletion border. Each signal is normalized by the total number of created holes. The total width of the transition layer was assumed to be 0.5 mm.

Electrons that are created in the n+ layer are instantaneously collected and can not induce

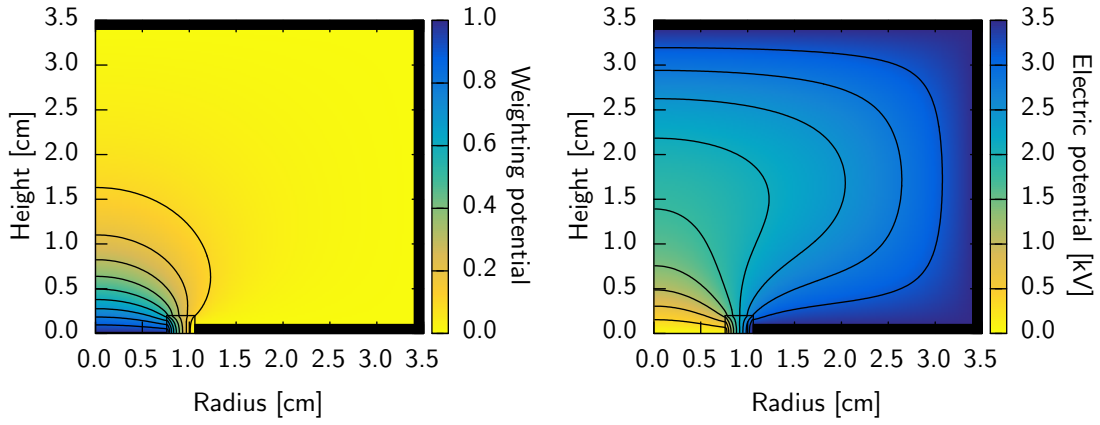

Figure 3.3: A representation of the weighting potential (left) and electric potential (right) of a typical PCGe detector (Canberra Broad Energy Germanium detector, see Sec. 3.2) simulated with ADL3 (see Sec. 4.4).

any signal into the read out electrode (p+ contact). Therefore, within the transition region only diffusion of the holes is of importance. Their movement is entirely described by the diffusion equation:

$$\frac{\partial c(\vec{x},t)}{\partial t} = D\nabla^2 c(\vec{x},t). \tag{3.4}$$

The diffusion constant is related to the charge mobility by the Einstein relation in Eq. 2.9 and can therefore be calculated from the hole mobility of $4.2\,\mathrm{m}^2/(\mathrm{V{\cdot}s})$ at 77 K [47]. The above equation can be simulated with a finite difference algorithm and the hole movement in the transition layer studied. In Fig. 3.2 such an algorithm was used to simulate the amount of holes that reach the depleted volume as a function of time for different depth of the energy deposition in the transition layer. The arrival of the holes in the depleted region is delayed and spread out over a large time span. The charge collection of a typical signal happens within a few hundred nanoseconds (see Sec. 2.2.5), thus the spread in charge caused by the diffusion in the range of a microsecond is large and dominates the signal shape (see also Fig. 3.4). This explains the origin of the term slow pulses or slow signals as their rise time is long compared to typical signals. Although recombination was neglected it is apparent that not all the charge carriers that are created are actually collected. The further away from the depletion border an interaction takes place the more of the initial charge is lost. The measured energy of these events is therefore lower than the energy of the γ-ray. For measurements near the noise threshold these slow signals are often the dominant background and good suppression algorithms are necessary.

3.5 Pulse shape discrimination

As presented in the left panel of Fig. 3.3, the weighting potential is strongest in a narrow hemispherical region around the point contact and relatively weak in the remaining volume. The electrical potential (see the right panel of Fig. 3.3) forces the positively charged holes to

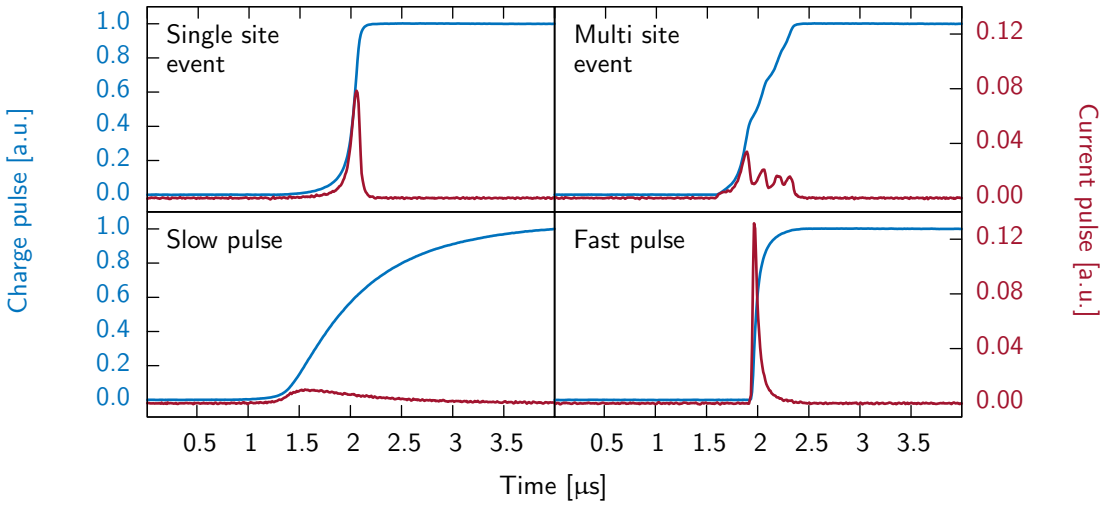

Figure 3.4: The 4 different pulse shapes that can be observed in a typical PCGe detectors (selected from a measurement).

drift inwards, towards the point contact, and the electrons to drift outwards towards the high voltage contact. As discussed in Sec. 2.2.6, the weighting potential at the position of the charge defines the amount of signal induced into the external circuit. The outwards drifting electrons only move through a weak weighting potential. Therefore, their contribution to the charge signal is small. The main contribution to the signal, comes from the holes, that drift towards the point contact and eventually pass through a region with a high weighting potential. The typical signal induced into the electrode is therefore composed of a slowly increasing initial slope (from the region with weak weighting potential), followed by a relatively sharp increase to the maximum value (from the region with strong weighting potential). This is shown in the first panel of Fig. 3.4. The signals of radiation that is deposited in the region with weak weighting potential thus all have a very similar pulse shape (funnel effect [63]).

Unfortunately, this is only valid for events with a single energy deposition within the detector (single site events). Particular at energies above a few hundred of keVs it is very common that γ-rays undergo Compton scattering and deposit energy in multiple locations within the detector (multi site events). Depending on where the holes have been created they need more or less time until they arrive in the region with high weighting potential. The signals that are induced into the electrode therefore are not aligned in time but show various sharp increases (see the second panel of Fig. 3.4). This characteristics makes it possible to distinguish multi site events from events with only a single interaction site. Backgrounds in the MeV region (e.g. multiple Compton interactions) thus can be separated from rare signals (usually single site event like) [72].

As already discussed in the previous section multi site events are not the only signal with a very peculiar form. Energy that is deposited close to the lithium contact need to diffuse into the depleted region to be collected and the measured signal rises slower compared to a typical signal of a single site event (see third panel of Fig. 3.4).

Not all the surface is covered by the lithium diffused electrode. Particles can also penetrate through the passivation layer or the point contact, which are both much thinner than the

lithium layer. As represented in the fourth panel of Fig. 3.4, these events are characterized by a fast rising pulse shape. In this case also the electron is moving through a high weighting field region and thus its contribution to the signal can not be neglected. The shape of these two singles deviates from a typical single and multi site event and can therefore be discriminated.

3.5.1 Pulse shape qualifiers

To distinguish the different classes of signals it is convenient to define qualifiers or discrimination parameters. It can be seen in Fig. 3.4 that the most distinct feature between the different pulse shapes is the time over which the charge pulse rises from the onset of the pulse to its maximum value. This is expressed as the rise time and requires to define two confining limits, usually expressed in percents of the pulse height (e.g. 10-90% or 2-70%). However for a noisy signal the pulse height is not very well defined and the limits strongly affected by the noise. For a good estimation of the rise time therefore some filtering before the measurement of the rise time is required to reduce the signal-to-noise ratio and allow a meaningful estimation of the rise time.

Another method to quantify the differences between the different pulse shapes is to normalize the current signal and measure the maximal amplitude. Figure 3.4 shows that the maximal amplitude of the current signal indeed differs considerably between the different pulse shapes. In order to normalize the current pulse often the uncalibrated value for the energy (reconstructed pulse height) is used. This explains the origin of the expression amplitude-over-energy or A/E [72]. This procedure allows to get an almost energy independent discrimination parameter for the different pulse shapes. The resolution of the amplitude measurement can be slightly improved by filtering the current pulse before measuring the amplitude (see Sec. 4.2.2).

4 Signal acquisition, analysis and simulation

The following chapter will discuss the data processing chain, from data amplification and acquisition, based on electronic components, to the filtering techniques applied to the digitized signals. New filtering methods and software will be presented in this chapter, that was developed together with collaborators within the scope of this thesis. The software and filter methods were extensively used in this work for data analysis. Furthermore, the signal formation process, that was discussed in the previous chapter can be implemented into a computational model to simulate the response of a typical germanium detector and learn more about the performance of a given system. Such a simulation tool, was adopted from previous work and was tailored for the study of germanium detector optimizations. The tool is discussed in the second part of this chapter.

4.1 Electronics

Electronic components in radiation detection systems serve three distinct purpose:

1. operation of the semiconductor detection device,
2. amplification of a detector signal,
3. shape the signal into a form to allow a measure of the investigated physical quantity with the lowest possible signal-to-noise ratio.

The first point is covered by providing the necessary voltage for depleting the detector volume, which is with a few thousand volts relatively high. The voltage supply must provide a constant high voltage, which requires a regulation mechanism to compensate for long-term drifts such as temperature and power line voltage fluctuations. Furthermore, it must be assured that low-frequency noise in the high voltage supply can not affect the read out electronics, as any fluctuation in the high voltage appears superimposed on the signal.

In the last two decades it became popular to digitize the signal and then perform an offline analysis in software, instead of altering the signal with dedicated analog electronic systems. Because of this trend the electronic chain is considerably simplified and reduced to a simple amplification stage feed into an analog to digital converter (ADC). Analog hardware implemented shaping filters thus will only be covered if necessary and the following discussion mainly focuses on the amplification of the signal. Digital shaping will be discussed in the next section.

4.1.1 Electrical components in the frequency domain

In the following discussion a system is a process that produces a characteristic response (output signal) to a given input signal. Filters are just a special type of system, that remove certain frequency components of a signal. A system is called linear if it preserves homogeneity and additivity of the signals. The first requirement implies that if the input signal is multiplied

by a constant value, the output signal is multiplied by the same constant value. The second requirement means that two signals, that are added together and fed into the system, produce the same output, as if the separate signals are passed through the system and the output added together. These two requirements are sufficient to force two successive systems to be commutative, that means they can be interchanged without affecting the output of the overall transformation.

A system in the time domain can be characterized by its impulse response function. This is simply the signal that is obtained at the system's output, if a delta function is provided to the system as an input signal. The signal measured at the system's output for an arbitrary input signal is then calculated with the convolution of the input signal and the impulse response function. The convolution can be circumvented by analyzing linear systems in the frequency domain. The description of a signal in one domain is equivalent to the other and they are linked by the Fourier transformation. In the frequency domain a signal is represented by a sum of different frequency components. The response of an arbitrary system to a generic input signal can be analyzed for a single frequency ω. A specific input signal $V_{\text{out}}(\omega)$ (represented in the frequency domain) can be multiplied with the transfer function of the system $H(\omega)$ to find the signal observed at the output $V_{\text{out}}(\omega) = V_{\text{in}}(\omega)H(\omega)$.

The impedance Z is defined to be the ratio of the voltage and the current in a system $Z = V/I$ and is a complex quantity. The impedance for a capacitor Z_C and a resistor Z_R can be derived from that definition and their respective responses in the time domain:

$$Z_C = \frac{1}{i\omega C}, \qquad Z_R = R. \tag{4.1}$$

Furthermore, Kirchhoff's first and second law are also valid in the frequency domain; at each node of a circuit the sum of all currents must be zero and the sum over all voltages in a loop is zero.

These few consideration are enough to analyze the amplification system that will be discussed in the next few sections. A more thorough discussion can be found in any introductory analog electronics book (for example [73]).

4.1.2 Amplifier

The signal induced into the electrode is tiny. A 1 MeV γ-ray for example produces roughly 3.4×10^5 charge carriers, which translates into 5×10^{-14} Cb or 50 nA (assuming charge collection within 100 ns). To capture these weak signals, an amplifier is mounted close to the detector read out electrode. Often parts (i.e. the junction gate field-effect transistor or JFET) of the circuitry are kept at cryogenic temperatures to improve their noise properties (as we will see noise in many electric components is proportional to the temperature). This first amplification stage (preamplifier) is the most crucial component of an electronics chain and defines the noise properties of the overall system.

An amplifier is a basic building block of analog systems and is characterized by its gain that relates the magnitude of the output signal to the magnitude of the input signal. Both, the input and output signals, can either be electrical current or voltage and any combination is possible. A special type of amplifier is the operational amplifier, which is a DC-coupled voltage amplifier with a high gain. An idealized operational amplifier is assumed to have infinite gain and draws no current at the two input channels (therefore the impedance of the amplifier is

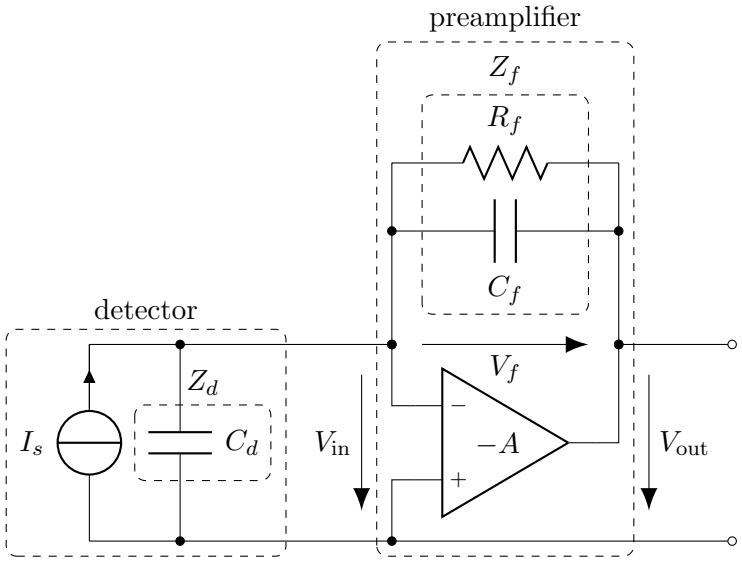

Figure 4.1: A schematic representation of a charge sensitive preamplifier setup connected to a semiconductor detector. The index d relates to components of the detector, the index f to components of the feedback loop.

infinite). By connecting the output of an amplifier to its input, a feedback loop is formed, that in the case of an idealized operational amplifier will eliminate any voltage difference that forms between the two input channels.

In reality these conditions are never satisfied. Often the gain is not only finite but also strongly frequency dependent. However, the above assumptions are very practical and often sufficient for analytical analyses of circuits.

The amplification system in most current radiation detection systems is composed of an amplifier with a capacitor feedback loop (for alternative preamplifier systems see [48]). This turns the amplifier sensitive to charge that is collected on the capacitor, thus they are known as charge sensitive (pre)amplifier.

4.1.3 Response of a charge sensitive preamplifier

A typical diagram of a charge sensitive preamplifier system is drawn in Fig. 4.1. The preamplifier is connected to a detector, that here is symbolized through a capacitor C_d in parallel to a current source I_s (representing the induced current from charge drifting in the detector). The feedback loop is formed by a capacitor C_f in parallel with a resistor R_f. The capacitor accumulates the charge created in the detector $Q_s = \int I_s \, \mathrm{d}t$; the resistor simultaneously drains the collected charge and enables to reset the output to its initial value. Usually the resistance of the resistor is large (up to a few GΩ), so that the time scales of the reset are large compared to the time scales of charge collection. The feedback loop can be reduced to a single component with an equivalent impedance Z_f of:

$$Z_f = \frac{1}{C_f} \left(\frac{1}{\frac{1}{\tau} + i\omega} \right), \qquad \tau = R_f C_f. \tag{4.2}$$

In general, all variables in the following discussion are frequency dependent. For better readability the frequency dependence, however, is not explicitly mentioned. This also applies to the transfer function of the operational amplifier $A = A(\omega)$, which in all generality can depend on the frequency.

The voltage at the output of the preamplifier is related to the voltage at its input through $V_{\text{out}} = -AV_{\text{in}}$. Furthermore, in Fig. 4.1 it can be seen that $V_{\text{in}} = V_f + V_{\text{out}}$, thus $V_f = (1 + A)\, V_{\text{in}}$. The impedance of an ideal operational amplifier is infinite so no current flows into the amplifier and the entire current observed at the input of the amplifier (coming from the detector) flows into the feedback loop $I_f = I_{\text{in}}$, thus:

$$Z_{\text{in}} = \frac{V_{\text{in}}}{I_{\text{in}}} = \frac{V_{\text{in}}}{I_f} = \frac{1}{1+A}\frac{V_f}{I_f} = \frac{Z_f}{A+1}. \tag{4.3}$$

This shows, that the feedback loop can be replaced with an equivalent impedance Z_{in} in parallel to the detector impedance Z_d at the input of the amplifier.

If the operational amplifier is near to ideal ($A \gg 1\ \forall\ \omega$) no current flows into the amplifier. Therefore all the current created in the detectors I_s has to flow through the feedback loop and be equal to I_f. The feedback loop furthermore assures that V_{in} is close to zero and thus $V_{\text{out}} = -V_f$:

$$\frac{V_{\text{out}}}{I_s} = \frac{-V_f}{I_f} = -Z_f = \frac{-1}{C_f(\frac{1}{\tau} + i\omega)}. \tag{4.4}$$

The transfer function of the system is thus dominated by components of the feedback loop and independent from the detector capacitance C_d. The transfer functions can be studied in detail by assuming a current signal $I_s(t)$ (in the time domain) positioned at $t = 0$ in the form of a delta function $Q_0 = \delta(t)$. The time dependence of the charge is then $Q(t) = \int I_s(t)\,\mathrm{d}t = Q_0 u(t)$ with

$$u(t) = \begin{cases} 0, & \forall\ t < 0 \\ 1, & \forall\ t \geq 0 \end{cases} \tag{4.5}$$

being the Heaviside step function. The current signal in the frequency domain $I_s(\omega) = Q_0$ is found through a Fourier transformation of the current signal $I_s(t)$. The output voltage in the time domain is then given by:

$$V_{\text{out}}(t) = \int_{-\infty}^{+\infty} \frac{-Q_0}{C_f(\frac{1}{\tau} + i\omega)}\, \mathrm{e}^{i\omega t}\frac{d\omega}{2\pi} = \frac{-Q_0}{C_f} u(t)\, \mathrm{e}^{-t/\tau} \tag{4.6}$$

This is an Heaviside step function with an exponentially decaying tail defined by the time constant $\tau = R_f C_f$. The rise time of the signal in a radiation detector is chosen to be small compared to the decay time, therefore this description is relatively close to real signals observed with germanium detectors. The gain of the preamplifier system $G = 1/C_f$ is controlled solely by the feedback capacitance. Accordingly a small value for the feedback capacitance must be chosen to maximize the output signal. Investigating Eq. 4.4 in more detail, it can be observed, that for the approximation to be true not only the gain of the amplifier A must be large, but also $C_d/A \ll C_f\ \forall\ \omega$. Thus for a finite gain of the operational preamplifier it must be assured that the capacitance of the detector is small enough compared to the capacitance of the feedback loop, such that this inequality is valid.

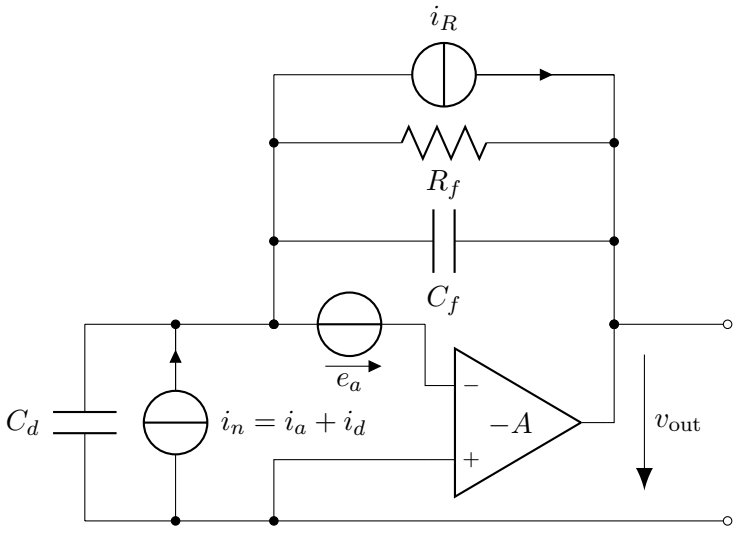

Figure 4.2: The different noise sources in a charge sensitive amplifier that are considered for the calculation of the signal-to-noise ratio: i_n the detector's and amplifier's shot noise, e_n the amplifier's voltage noise and i_R the resistors thermal noise.

4.1.4 Noise in electronics components

In the frequency domain noise is described by its spectral power density $dP/df = 2\pi dP/d\omega$. The sources of noise are treated similar to the usual current and voltage sources, however the power density is not a practical measure for the noise in such a source, instead a noise source is rather characterized by its voltage spectral density $e_n = d\Delta V/\sqrt{df}$ or the current spectral density $i_n = d\Delta I/\sqrt{df}$, where ΔV and ΔI are the root mean square deviations (or standard deviations) of the voltage respectively current fluctuations.

Thermal (Johnson) noise was discovered by Johnson [74] and first described by Nyquist [75]. The spectral noise density at a temperature T is given by $dP/df = 4kT$, where k is the Boltzmann constant. The primary source of thermal noise in an electronic circuit are resistors. For a resistor, $P = V^2/R = I^2R$, so this noise can either be described by the spectral voltage density $e_n^2 = 4kTR$ or the spectral current density $i_n^2 = 4kT/R$. The spectral density of shot noise is given by $i_n^2 = 2eI$, where I is the average current and e the electronic charge. Shot noise is caused by leakage current in the detector but also by leakage currents from the transistors gate in a non ideal amplifier. An amplifier furthermore produces voltage noise, which can be approximated by $e_n^2 \approx 4kT/g_m + A_f/f$, where g_m is the transconductance of the input transistor [48, p. 267] and the second term is the contribution from 1/f noise. The name of 1/f noise is derived from the spectral power density that scales inversely with the frequency and its origin is not well understood, a possible explanation is charge carrier trapping in the FET. A more thorough discussion of thermal, shot and 1/f noise is given in [48, p. 110-114].

4.1.5 Noise in a charge sensitive preamplifier

Let us assume that $\tau = R_f C_f$ is large enough, so that its contribution to Z_f can be neglected (in the next section it will be shown that this is true if τ is large compared to the optimal shaping time of the filter). The impedance of the feedback loop simplifies to $Z_f = 1/(i\omega C_f)$

and as before, the impedance of the detector is given by $Z_d = 1/(i\omega C_d)$. Furthermore, let us consider the three noise sources shown in Fig. 4.2:

$$i_n^2 = i_a^2 + i_d^2 = 2e(I_G + I_L), \tag{4.7}$$

$$i_R^2 = 4kT/R_f, \tag{4.8}$$

$$e_a^2 = \frac{8kT}{3g_m} + \frac{2\pi A_f}{\omega}. \tag{4.9}$$

The voltage noise of the preamplifier e_a contains the 1/f noise (reminder: $2\pi f = \omega$) and the contribution from the amplifier is expressed with the transconductance g_m. i_R is the thermal noise of the feedback resistor and i_n the shot noise created by the detector leakage current I_L and the transistor gate leakage current I_G. These noise sources were chosen according to [76], other text discussing the issue might include different noise sources according to their needs. An actual charge sensitive preamplifier is composed of many more components that each may or may not add noise, however for the purpose of this discussions the three mentioned noise sources are sufficient.

The noise sources are independent from each other, so the contribution of each noise source observed at the output of the preamplifier can be calculated separately, however the transfer function of the system to each individual noise source must be considered. The total noise at the output of the preamplifier is found by adding all the different contributions from individual sources in quadrature.

Considering only the source e_a, the two impedances act as a capacitor divider therefore the noise at the output v_{out} for this source is:

$$v_{\text{out},e} = e_n + V_f = e_n + e_n \frac{Z_f}{Z_d} = (1 + \frac{C_d}{C_f})e_n. \tag{4.10}$$

In the derivation of this equation the voltage drop over the input was assumed to be zero, which is valid for an ideal operational amplifier.

Considering now only the two current sources i_n and i_R. It can be shown, that the transfer function of the system has the same impact onto these two sources. Therefore, their contribution at the output of the preamplifier is:

$$v_{\text{out},n} = i_n Z_f = \frac{i_n}{i\omega C_f}, \qquad v_{\text{out},R} = i_R Z_f = \frac{i_R}{i\omega C_f}. \tag{4.11}$$

These three contribution are added in quadrature and the exact expression of the spectral noise densities can be inserted to find the total spectral noise density at the output of the amplifier:

$$v_{\text{out}}^2 = \frac{8kT}{3g_m}\left(1 + \frac{C_d}{C_f}\right)^2 + \frac{2\pi A_f}{\omega}\left(1 + \frac{C_d}{C_f}\right)^2 + \frac{1}{C_f^2\omega^2}\left(2e(I_G + I_L) + \frac{4kT}{R_f}\right). \tag{4.12}$$

This expression contains three terms, one constant, one proportional to $1/\omega$ and one proportional to $1/\omega^2$. Furthermore, the detector capacitance C_d also appears in the expression. This is in contrast to the signal at the preamplifier output which only depended on the feedback capacitance C_f (see Eq. 4.6). Its appearance in Eq. 4.12 is solely caused by the voltage noise of the amplifier. Finally, the noise sources depend on the feedback resistance R_f and the leakage currents I_L and I_G, so they also add to the observed noise at the output of the preamplifier stage.

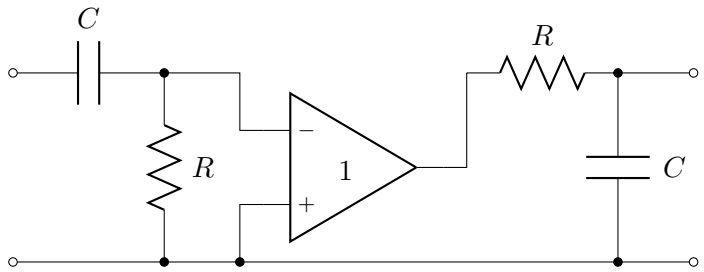

Figure 4.3: An diagram of the RC-CR shaper; the CR at the input is a simple high-pass filter, the RC at the output a simple low-pass filter. The two capacitances and resistors where chosen for simplicity to be equal.

4.1.6 Equivalent noise charge

The main purpose of a shaping filter is to improve the signal-to-noise ratio. When studying the signal-to-noise ratio it is thus inevitable to also take into account a shaping filter. For this purpose, it is possible to consider a generic shaping filter with a frequency response of $H(\omega)$, that obtains the signal from the preamplifier output. However, it is more instructive to consider an actual expression for the shaping filter. A simple band-pass shaping filter is a CR-RC shaper depicted in Fig. 4.3. The transfer function can be easily derived from that figure and is found to be [77]:

$$H(\omega) = \left(\frac{i\omega T_s}{1+i\omega T_s}\right)\left(\frac{1}{1+i\omega T_s}\right) \quad \Rightarrow \quad |H(\omega)|^2 = \frac{\omega^2 T_s^2}{(1+\omega^2 T_s^2)^2}, \qquad T_s = RC \tag{4.13}$$

The characteristic time T_s of the shaper is known as the shaping time. Assuming the detector creates the delta signal that was already used in Eq. 4.6, then at the output of the shaper the following signal can be observed (in the time domain):

$$\begin{aligned} V_{\mathrm{so}}(t) &= \int_{-\infty}^{+\infty} \left(\frac{-Q_0}{C_f i\omega}\right)\left(\frac{i\omega T_s}{1+i\omega T_s}\right)\left(\frac{1}{1+i\omega T_s}\right) \mathrm{e}^{i\omega t}\frac{d\omega}{2\pi} \\ &= \frac{-Q_0}{C_f}\int_{-\infty}^{+\infty} \frac{1}{(T_s+i\omega)^2}\,\mathrm{e}^{i\omega t}\frac{d\omega}{2\pi} = \frac{-Q_0}{C_f}\frac{t}{T_s}\,\mathrm{e}^{-t/T_s} \qquad (\text{for } t>0). \end{aligned} \tag{4.14}$$

Here it was assumed that the decay time τ of the preamplifer is much larger than the shaping time T_s, thus the $1/\tau$ term was removed from the transfer function of the preamplifier. This explains why in the previous noise discussion the decay time term could have been neglected; the noise properties are dominated by the shaping time, which in general is much smaller then the decay time, so $1/\tau$ is small compared to $1/T_s$. The function found in Eq. 4.14 reaches its maximum of $V_{\mathrm{so,max}} = Q_0\,\mathrm{e}/C_f$ at $t = T_s$. This will be important for the calculation of the equivalent noise charge.

The total noise power at the output of the shaper is found by multiplying Eq. 4.12 by $|H(\omega)|^2$ and integrating over all frequencies (the total noise power does not depend on if it is evaluated

in the time or frequency domain):

$$\begin{aligned} v_{\mathrm{so}}^2 =& \frac{8kT}{3g_m}\left(1+\frac{C_d}{C_f}\right)^2 \int_0^\infty |H(\omega)|^2 \frac{d\omega}{2\pi} \\ &+ 2\pi A_f \left(1+\frac{C_d}{C_f}\right)^2 \int_0^\infty \frac{|H(\omega)|^2}{\omega}\frac{d\omega}{2\pi} \\ &+ \frac{1}{C_f^2}\left(2e(I_G+I_L)+\frac{4kT}{R_f}\right)\int_0^\infty \frac{|H(\omega)|^2}{\omega^2}\frac{d\omega}{2\pi}. \end{aligned} \tag{4.15}$$

The transfer function in Eq. 4.15 can be replaced with the actual expression for the CR-RC shaper, which leads to three integrals that can be evaluated with the identity:

$$\int_0^\infty \frac{\omega^m\, d\omega}{(\omega^n + a^n)^r} = \frac{(-1)^{r-1}\pi a^{m+1-nr}\Gamma[(m+1)/n]}{n\sin[(m+1)\pi/n](r-1)!\Gamma[(m+1)/n-r+1]}, \tag{4.16}$$

where $a = 1/T_s$ and $r = n = 2$. The total noise at the output of the shaping filter is thus found to be:

$$v_{\mathrm{so}}^2 = \frac{8kT}{3g_m}\left(1+\frac{C_d}{C_f}\right)^2 \frac{1}{8T_s} + 2\pi A_f \left(1+\frac{C_d}{C_f}\right)^2 \frac{1}{4\pi} + \frac{1}{C_f^2}\left(2e(I_G+I_L)+\frac{4kT}{R_f}\right)\frac{T_s}{8}. \tag{4.17}$$

The equivalent noise charge is given by the relation:

$$Q_n = Q_0/(S/N), \tag{4.18}$$

where Q_0 is the magnitude of the signal at the input to the preamplifier stage and (S/N) the signal-to-noise ratio observed at the output of the shaping filter for that very signal. Accordingly, it expresses the noise level that is observed at the output of the shaping filter in units of the input signal to the preamplification stage (i.e. number of charged particles, Coulomb or eV). As the magnitude appears twice in the above expression (first in the definition of Q_0 and then in the signal-to-noise ratio) the equivalent noise charge is independent of the signal height and only expresses the actual noise level of a system. In the case of the CR-RC shaper we thus find for the equivalent noise charge squared:

$$Q_n^2 = Q_0^2 \frac{v_{\mathrm{so}}^2}{V_{\mathrm{so,max}}^2} = \frac{\mathrm{e}^2}{8}\left[\frac{8kT}{3g_m}\frac{C_t^2}{T_s} + 4A_f C_t^2 + \left(2e(I_G+I_L)+\frac{4kT}{R_f}\right)T_s\right] \tag{4.19}$$

In this equation $C_t = C_f + C_d$ is the sum of the capacitances in the system and e^2 is the Euler number squared. The equivalent noise charge has therefore three terms, one is proportional to T_s one is independent of T_s and one is inversely proportional to T_s. A similar result is found for other shapers, thus the equivalent noise is in general expressed as:

$$Q_n^2 = i_n^2 F_i T_s + e_n^2 F_e \frac{C^2}{T_s} + F_f A_f C^2, \tag{4.20}$$

where for universal validity the current noise sources are combined to i_n and the voltage noise sources are combined to e_n. The time constant T_s is defined by the respective shaping filter and its definition is not unique. The shaping factors F_i, F_v and F_f are constants and found by

Shaper	F_e	F_f	F_i
infinite cusp	1	$2/\pi$	1
triangular	2	$4\ln(2)/\pi$	2/3
gaussian	0.89	1	1.77
RC-CR	1.85	1.18	1.85
trapezoidal	2	1.38	5/3

Table 4.1: The shaping factors for a few common shaping filters. The trapezoidal filter presented consists of a rising edge, flat-top and falling edge all equal to T_s. The values are taken from [2], the columns of the infinite cusp has been flipped in the Reference, this has been corrected here.

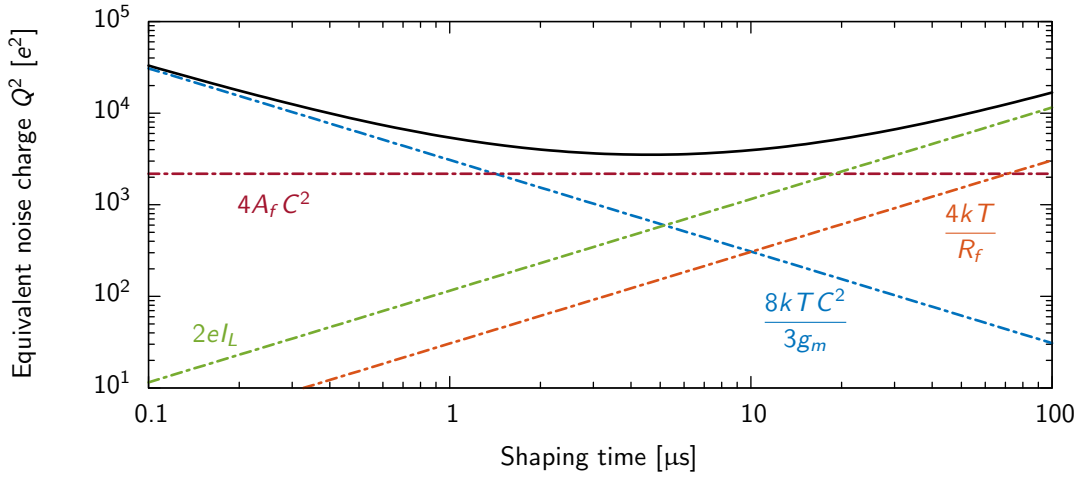

Figure 4.4: A typical curve for the equivalent noise charge of a charge sensitive preamplifier. The represented values are: g_m=1 mS, R_f=5 GΩ, I_G=0 A, I_L=10 pA, T=77 K, C_f=0.5 pF, C_d=5 pF, A_f=0.5 pV^2.

evaluating the integrals of the transfer function of the shaper. Parvel's theorem can be used to express, two of the three shaping factors in the time domain:

$$F_i = \frac{1}{T_s}\int_{-\infty}^{+\infty} [W(t)]^2\,\mathrm{d}t, \qquad F_e = T_s\int_{-\infty}^{+\infty}\left[\frac{dW(t)}{\mathrm{d}t}\right]^2\mathrm{d}t, \tag{4.21}$$

where $W(t)$ is the shaper's impulse response. The shaping factor for the 1/f noise has to be evaluated in the frequency domain. Values for the shaping factors of a few common shaping filters are summarized in Table 4.1.

In Fig. 4.4 the equivalent noise charge for the CR-RC shaper is plotted as function of the shaping time for typical values of a germanium detector read out system. At a low shaping time the noise from voltage sources dominates the equivalent noise charge, while for a large shaping time the noise from current sources dominates. The 1/f noise adds a constant offset that if sufficiently large limits the minimal obtainable noise level. The optimal value for the shaping time can be find by deriving the equation for the equivalent noise charge and setting it equal to zero. However, from Fig. 4.4 it is obvious that the minimal noise is obtained if the contribution from charge and current sources are equal. The only way to efficiently reduce

the noise, is to reduce the total capacitance of the system as it affects both, the 1/f noise and the voltage noise. Nonetheless, this will also lead to a much lower optimal shaping time, which in some cases causes new problems, thus it might be required to simultaneously increase the feedback capacitance. The current noise is usually dominated by the thermal noise of the feedback capacitor, however if R_f is chosen sufficiently large eventually the current noise will be dominated by the leakage currents (as shown in Fig. 4.4), which thus are a natural lower limit to this type of noise.

4.2 Digital signal processing

Almost every detection system, not only germanium detectors, creates some sort of electrical signal. These signals then often are converted into a digital form to analyze them with a computer. The conversion of the analog signal into a digital form is performed by a analog to digital converter (ADC). These devices, and their limitations are extensively covert in Ref. [78] and [48] and will not be discussed here. Once the signals are brought into a digital form, they can be manipulated with computational methods and algorithm studied within the field of digital signal processing (DSP). A comprehensive introduction to the field is given in Ref. [78] and most information used in this section have been taken from that book.

4.2.1 Signals and their representation

Signals describe how one parameter, for example voltage, depends on another parameter e.g. the time. Similar to a function in mathematics the parameters in a signal are usually not interchangeable.

In its digital form a signal is discrete, it is divided into samples, single containers that provide the dependent parameter for a particular value of the independent parameter. Furthermore, the signal is quantized, this means the dependent variable can only be represented by a limited set of discrete values. Often the number of levels is limited due to the technology used in the analog to digital converter (ADC). Nevertheless, the precision of any number in digital form is restricted, as it has to fit in a limited memory space.

As already discussed in Sec. 4.1.1, the signal can either be represented in the time domain or the frequency domain. Both representation are equivalent in that they contain the same information and can be converted into the other domain through a Fourier transformation. The sampling theorem links the two domains by providing a relation between the sampling rate and the maximal possible frequency called the Nyquist frequency. Claude Shannon phrased it as follows [79]:

> If a function $x(t)$ contains no frequencies higher than B [Hertz], it is completely determined by giving its ordinates at a series of points spaced $1/(2B)$ seconds apart.

The theorem therefore limits the amount of information that can be encoded in any given signal. It is particular important for the conversion of an analog signal to a digital one. If a signal is digitized at a sampling rate, such that it contains frequencies above the Nyquist frequency, a phenomenon called aliasing can appear, mimicking frequency components in the frequency spectrum of the digitized signal that were not present in the analog signal. The frequency components above the Nyquist frequency must thus be removed with an anti-aliasing filter before the signal is converted into a digital form.

4.2.2 Digital linear systems

Digital filters are digital linear systems and follow the definition given in Sec. 4.1.1 for their analog counterparts. In the time domain, these systems are characterized by the impulse response h, that allows to calculate for any input signal x the output signal y, by performing a convolution of the input signal with the impulse response (we only consider the discrete form of a convolution):

$$y[i] = \sum_{j=0}^{M} h[j]x[i-j]. \tag{4.22}$$

Although, the convolution is sufficient to calculate any response for a given input signal, it is more practical to calculate a systems response with the recursive formula:

$$y[i] = \sum_{j=0}^{i} a_j x[i-j] + \sum_{j=0}^{i} b_j y[i-j]. \tag{4.23}$$

This form not only includes the input signal but also uses the output signal calculated for proceeding samples. This expression contains the recursion coefficients a_j and b_j which define the system completely.

The most fundamental filters are the single pole low-pass, single pole high-pass and the moving average filter. Their non-zero recursive coefficients are:

- Low-pass filter: $a_0 = 1 - d$, $b_1 = d$,
- high-pass filter: $a_0 = (1 + d)/2$, $a_1 = -(1 + d)/2$, $b_1 = d$,
- moving average filter: $a_0 = 1$, $a_p = -1$, $b_0 = 1$.

The parameter d, defines the decay on a sample basis and is related to the decay time τ by the relation $d = \mathrm{e}^{-1/\tau}$. The parameter p indicates the number of samples (length) that are averaged in the moving average. The analog version of the low-pass filter and high-pass filter have been previously encountered in Sec. 4.1.6 as the CR segment (low-pass filter) and the RC segment (high-pass filter).

Shaping filters change the form of the input pulse into a form that has a better signal-to-noise ration. Thus, their main purpose is to remove undesired regions in the frequency domain.The above listed filters are not particular well suited as shaping filters, as in the frequency domain their response function stretches over a relative large range of frequencies. Nonetheless, the performance can be improved by applying a sequence of filters, one after the other.

The shaping time is the characteristic parameter of these filters and has been emerging naturally from the discussion in Sec. 4.1.6. There are different ways of defining it. Sometimes, the shaping time is the width of the moving window average filters, but more often it is the width of the shaped signal. In this thesis the shaping time T_s is defined to be the full-width-at-half-maximum (FWHM) of the shaped signal and it is related to the length of the moving average filter p by $p = \sqrt{2}T_s$.

The most popular shaping filter in radiation detection systems is composed of consecutive moving average filters of the same width. After the first moving average filter the impulse response has the shape of a rectangular function, after the second moving average filter it takes the form of a triangular function and then approaches with each further stage a Gaussian

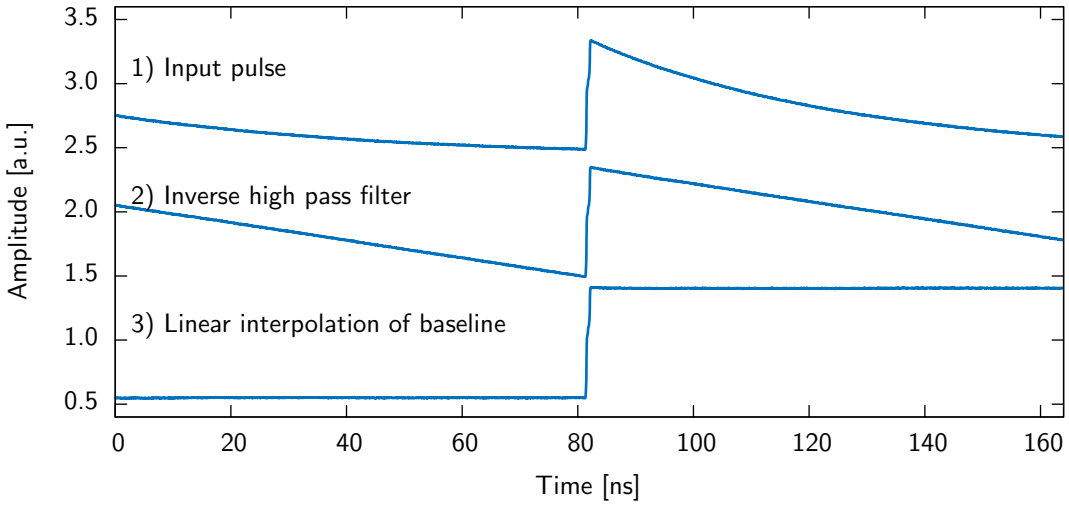

Figure 4.5: The different filter steps for a typical pile-up pulse. The upper panel illustrates the pole-zero cancellation, the lower panel the MSEC and the pseudo-Gaussian shaping filter (6 µs). The pulse heights are not drawn to scale.

shape. Because of this similarity in shape, for more than 3 successive moving average filters, it often is referred to as the pseudo-Gaussian filter. In analog electronics the pseudo-Gaussian filter is often simulated by multiple CR-RC segments.

The simplicity of the pseudo-Gaussian filter is one reason for its widespread use, another reason is that its performance is sufficient for most applications and compared to more complex filters, it is extremely fast in execution.

Next to shaping filters also other filters are required to remove signal distortions caused by the electronics.

4.2.3 Pole-zero cancellation

The charge sensitive preamplifier consists of a mechanism to reset the voltage at the output to the initial value. Some very sensitive systems use optical feedback with a switch that shorts the feedback capacitor once the output voltage reaches a certain value, causing a sharp step back to zero. However, these systems are complex and expensive, thus most of the time a feedback resistor is put parallel to the capacitor to continuously drain the charge collected on the capacitor (see Sec. 4.1).

In the theoretical discussion of Sec. 4.1.4 it was assumed that the decay time $\tau = R_f C_f$ of the signal caused by the drainage through the feedback resistor is large compared to the charge collection time on the capacitor and can be neglected. Actual signals from a germanium detector, however, must be corrected for the decay produced by the feedback loop to not introduce a bias into the pulse height measurement. This requires the knowledge of the decay time τ, which often is provided by the manufacturer of the preamplifier system. To gain a more precise value for the feedback, the decay time can also be fitted from measured signals. Once the decay time is known, it is possible to compensate the decay with a pole-zero cancellation [48, p. 177]. This correction also allows to remove deficits caused by the decaying tail of a previous event (as illustrated in Fig. 4.5).

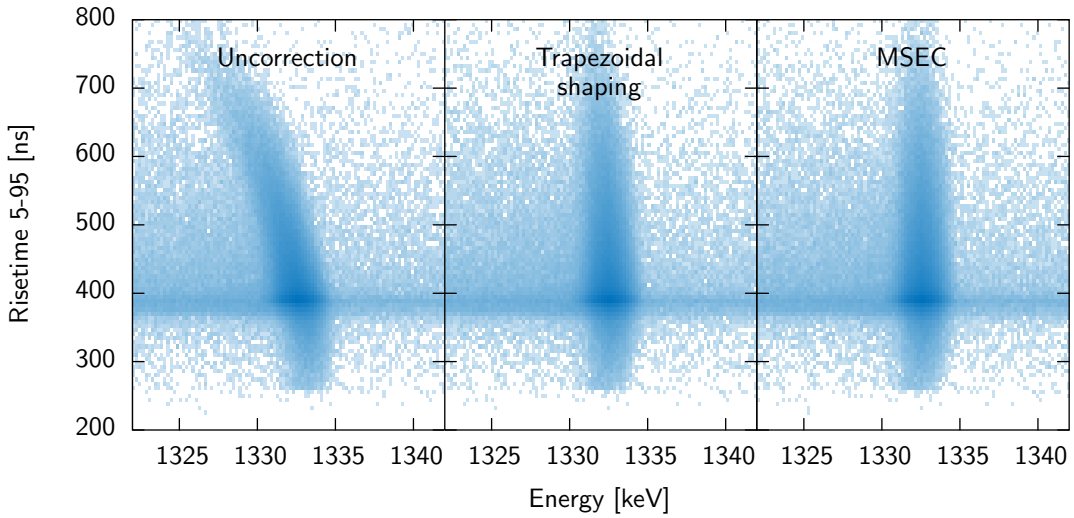

Figure 4.6: A scatter plot of the 1332.5 keV γ ray line collected with a point contact detector irradiated with the ^{60}Co isotope; left: no ballistic deficit correction (Gaussian shaping filter), center: trapezoidal shaping with a top width of half the shaping time, right: MSEC method (with Gaussian filter). The shaping time was always 6 µs. The band at 400 ns is the Compton background continuum. The blue color indicates the number of counts in the bins.

An intuitive method to perform a pole-zero cancellation can be found by studying the effect of the $R_f C_f$ feedback in the preamplifier. This is a simple single pole high-pass filter and its recursive form was given in Sec. 4.2.2. The recursive high-pass filter can be inverted and this inverse high-pass filter can be applied to the signal to eliminate the decay and return to a step-like signal. As illustrated in the second panel of Fig. 4.5, the filter is incapable of removing all effects; due to an initial offset of the baseline (the fraction of the signal before the charge pulse), the output signal will have a nonzero slope. However, this slope can be removed by a simple linear interpolation of the baseline before the charge pulse. The interpolation is performed by dividing the baseline into two segments and calculate the average. From this the offset and slope of the baseline is extracted and subtracted from the pulse.

It is convenient to have the shaping filters act on the current signal (delta-like) and not the charge signal. Thus before shaping the pole-zero corrected pulse is differentiated.

4.2.4 Ballistic deficit correction

The time required to collect all the charge carriers in a HPGe detector depends on the exact distribution and location of energy deposition sites in the detector. This dependence is reflected in strong variation of the rise time of the measured charge pulse. In point contact detectors for example, the rise time (the time the charge signal requires to rise to its maximal value) of monoenergetic radiation can take any values between 0.2 and 1 µs. If the shaping time is not much larger than the variability in the charge collection time, the amplitude reconstructed with the shaping filter underestimates the real amount of energy deposited in the detector, particular for pulses with a long rise time. This effect is called ballistic deficit and illustrated in the left panel of Fig. 4.6. The effect can be partially compensated by choosing a sufficiently large shaping time. However, at high event rates the maximal possible shaping time is only

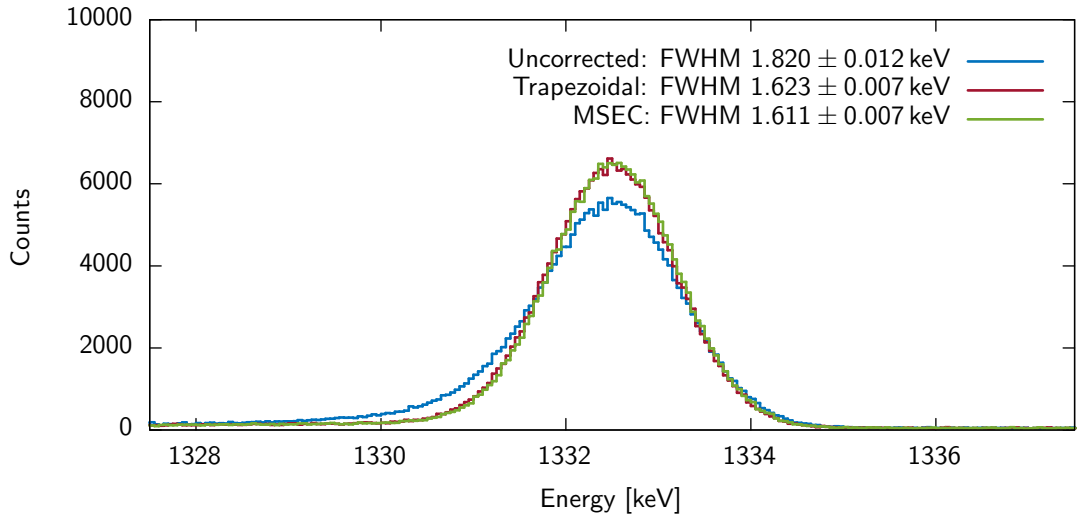

Figure 4.7: A histogram of the 1332.5 keV γ ray line represented in Fig. 4.6; for no ballistic deficit correction, a trapezoidal shaping with a top width of half the shaping time, and MSEC method enabled. The shaping time was always 6 µs. The improvement of any of the two ballistic deficit corrections with respect to the uncorrected analysis is roughly 10-11%.

a few microseconds, which is not sufficiently large to remove all effects caused by the ballistic deficit.

In the past, three different approaches were proposed to correct ballistic deficits, which mostly relayed on analog electronics. The first approach calculated a semi-empirical compensation which depended on the input signal rise time and then was added to the final output signal [80]. The second approach used a gated integrator after prefiltering the signal to integrate over the charge carrier drift time [81]. The third approach is to choose a particular shaping filter, that convert the input signal into a trapezoidal form [82]. This filter is well suited for correcting ballistic deficit effects but not optimal to minimize the signal-to-noise ratio of the pulse height reconstruction. Implementing a correction with digital methods is much simpler than with analog circuits, but usually follows the same principles.

The classical trapezoidal filter is made up of two moving average filters with different shaping times. The length of the longer moving average filter defines the shaping time of the trapezoidal filter, the length of the shorter moving average filter defines the width of the flat-top part of the trapezoidal form. The flat-top part must be chosen sufficiently large to compensate for the variability in the rise time, but should not be too large as it weights noise contribution too high. The amplitude of the shaped signal must be measured at a fixed position of the shaped signal, best towards the end of the flat-top part to be less sensitive to rise time variations. An alternative approach has been chosen in this thesis by applying an additional moving average filter to alter the top into a round shape and create a clear maximum. This method slightly reduces the filters efficiency to compensate ballistic deficits, however it is much easier to define the pulse height value. In the central panel of Fig. 4.6 this rounded-top trapezoidal filter was used. It shows that the filter still is capable of compensating ballistic deficits.

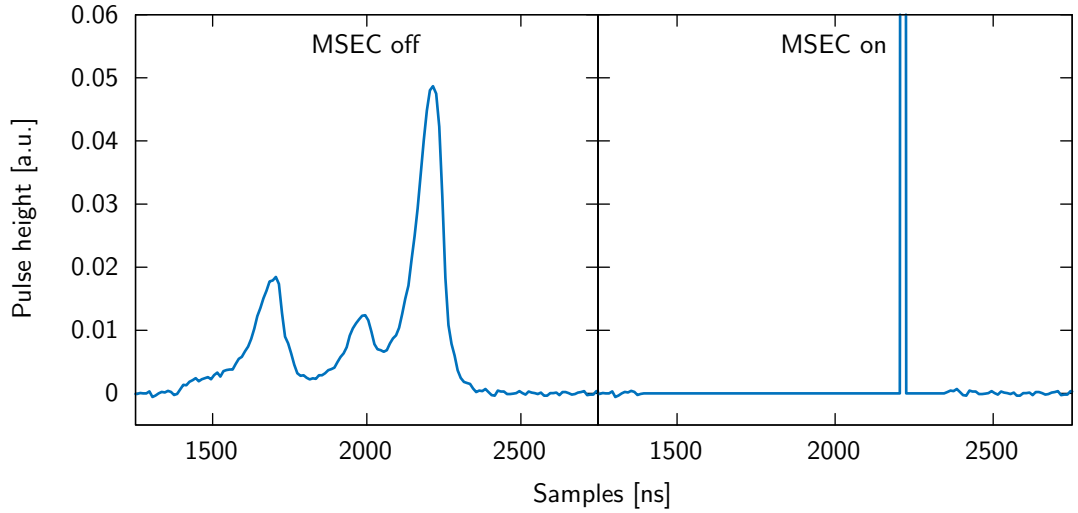

Figure 4.8: The effect of the MSEC on a normalized current pulse. All the contributions around the pulse are added up to a single sample (the size of that sample exceeds the y range up to 1.0).

4.2.5 Multi site event correction (MSEC)

Another approach proposed by Thomas Kihm [83] is described in Ref. [84] and was extensively studied within the scope of this thesis. Ballistic deficits are corrected with a multi-site event compensation (MSEC) method, a non linear, non reversible digital filter. The name MSEC refers to the filter's capability to correct for events with energy deposits in multiple locations and indicates that the filter was mainly created for signals obtained from point contact detectors.

The principle of the filter is similar to the method that uses a gated integrator, however it does not prefilter the signal. Instead, the differentiated signal (current signal) is set to zero for the duration of the charge collection process (see Fig. 4.8). The subtracted contributions are then added to the position, where the pulse previously reached its maximal value. The width of the window to which the filter is applied is found dynamically for each individual signal. This is done by starting at the maximal value of the current signal and searching for the first samples to the left and the right, that fall below a certain threshold. The threshold level is extracted from the baseline of the signal. The altered signal then can be shaped with an arbitrary shaping filter.

In the right panel of Fig. 4.6 ballistic deficits are corrected with the MSEC method (Gaussian shaping filter), resulting in the energy peak being reconstructed for any rise time value at the same position. The reconstructed energy spectrum for the three different filters discussed in this sections is shown in Fig. 4.7. The difference between the trapezoidal filter and the MSEC method is small, however if only a pseudo-Gaussian filter is used then the peak is considerably deteriorated.

4.2.6 Optimal filtering

The Wiener filter theory, established by Norbert Wiener in 1949 [85], describes a simple method to find the best filter for a given frequency distribution of the signal and the noise. A simple version of his theory states, that the optimal filter response is given by [78]:

$$H(\omega) = \frac{S(\omega)^2}{S(\omega)^2 + N(\omega)^2}, \tag{4.24}$$

where $S(\omega)$ is the signal and $N(\omega)$ the noise distribution in the frequency domain. The equation defines the shaping function to weight each frequency by the amount of signal relative to the sum of the signal and the noise. The definition requires the explicit knowledge of the entire noise and signal frequency spectra, which usually is not given. Moreover, the equation leads to a non-causal infinite pulse response in the time domain, which is unpractical for any real application. It is possible to find an alternative definition of the above equation, that forbids non-causal and infinite solutions but for a short theoretical study the above form is sufficient.

The signal and noise at the output of a typical charge sensitive preamplifier in the frequency domain was calculated in Sec. 4.1. The signal was found to be $V_{\text{out}}(\omega)^2 = Q_0^2/(\omega^2 C_f^2) = A/\omega^2$, where the preamplifier decay time was assumed to be large enough so that its contribution can be neglected. The noise was obtained in Eq. 4.12 and can be reduced to the form $v_{\text{out}}^2 = B + C/\omega^2$, where the contribution from 1/f noise was neglected. Thus the optimal shaping filter in the frequency domain is given by:

$$H(\omega) = \frac{A/\omega^2}{A/\omega^2 + (B + C/\omega^2)} = \frac{A}{2\tau B}\left(\frac{2\tau}{\tau^2 + \omega^2}\right), \qquad \tau^2 = \frac{A + C}{B}. \tag{4.25}$$

The entire frequency dependence is collected in the second factor. This expression has a simple known equation for the corresponding signal in the time domain: A two sided exponential. Thus the impulse response of the filter in the time domain is given by:

$$H(t) = \frac{A}{2\tau B}\, \mathrm{e}^{-|t|/\tau}. \tag{4.26}$$

This is the form of the so called cusp filter and as shown in its derivation it provides the best signal-to-noise ratio for a input delta signal and a system that is free of 1/f noise. The exponentially decaying tails of the cusp filter imply that the impulse response stretches to infinity, which is not practical in an actual analysis as data are only available in a very confined range. The loss in resolution, however, is small if the signal is cut of at a few decay times distant on each side. The cusp filter used within this thesis has been cut off at 5 times the decay time on each side.

In the analog to digital conversion a sufficiently large range around the signal is stored to disk and thus the filter can also make use of information that would be inaccessible in analog electronics as they happen in the future. This can be used to synthesize the cusp filter offline with simple recursive methods; the recursive form of the cusp filter is composed of two bidirectional low-pass filters.

The form of the cusp filter's impulse response has a very sharp peak at its maximum. As discussed in the previous sections such a impulse response is not capable of correcting ballistic deficits. The sharp peak of the classical cusp filter thus has been flattened with an additional moving window average within the scope of this thesis. This creates a cusp like form with a

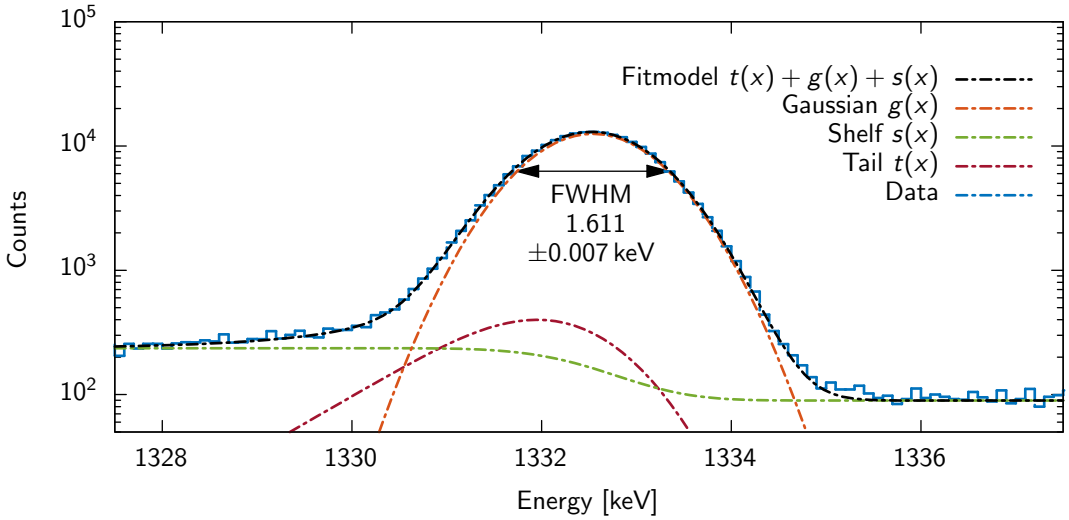

Figure 4.9: A fit to the 1332.5 keV line in the energy spectrum from a point contact detector (see Sec. 5.2.1). The different components of the fit are represented individually.

rounded-top (rounded-top cusp filter) similar to the one discussed by Kalinin and Bednyakov [86]. Although, this form is not considered optimal in theory, in a practical application such as done here, this filter proved to be very powerful to minimize noise (see Sec. 7.1).

4.2.7 Energy resolution

The signals measured with a germanium detector usually are amplified and then filtered (see Sec. 4.1 and Sec. 4.2.2) to reduce the amount of noise introduced by the read out electronic and amplification stage. The height of the signals is then analyzed and filled in a histogram (energy spectrum).

Ideally, monoenergetic γ-rays would produce a sharp line in the energy spectrum. However, no detection system is ideal. Noise induced from electronic components (see Sec. 4.1.4) and the statistical fluctuations in the ionization process (see Sec. 2.3.2) are responsible for broadening the line.

Each of the two contribution follows a normal distribution that when superimposed on each other produce again a normal distribution. The two contributions thus broaden the sharp line into a Gaussian peak, which is defined by the variance σ^2, the amount of events in the peak S_g and the peak position x_0 in the spectrum:

$$g(x) = \frac{S_g}{\sqrt{2\pi}\sigma} \exp\left(\frac{-(x-x_0)^2}{2\sigma^2}\right). \tag{4.27}$$

The detector resolution is typically either expressed as the variance of the Gaussian distribution or the full-width-at-half-maximum (FWHM). In radiation detection, the convention is to use the FWHM and this convention will be followed here. The FWHM can be found by multiplying the square root of the variance σ by $8\ln(2) \approx 2.3548$.

One consequence of the two contributions following a normal distribution is that they can

be added in quadrature to calculate the total variance σ_T^2:

$$\sigma_T^2 = \sigma_S^2 + \sigma_E^2 = F\epsilon E + \epsilon^2 Q_n^2. \tag{4.28}$$

The contribution from statistical fluctuations σ_S^2 is proportional to the Fano factor F and the energy of the incident radiation particle E. The average energy required to create an electron-hole-pair ϵ is used to convert a number of electrons to units of energy. Thus the contribution from electronics noise σ_N^2 is found from the equivalent noise charge Q_n, that usually is expressed as the number of electrons that correspond to the average noise in the system and which is independent from the energy of the radiation. The noise resolution and the equivalent noise charge are thus identical (up to a conversion constant) and will be used as synonyms.

In reality, there are additional effects that distort the shape of a typical energy peak. These contributions usually do not follow a normal distribution and should not be added in quadrature. The most important distortion is caused by charge trapping in the detector. As discussed briefly in Sec. 2.2.2, trapping sites can capture some of the charge carriers and either absorb them or release them with a certain delay. The typical time a charge carrier is trapped in such a site follows an exponentially decaying distribution. Depending on the strength of trapping, the events are reconstructed at slightly lower energies. Counts are removed from the peak forming an exponentially decaying distribution below the main peak [87]. However, this feature is also broadened by the electronics noise and charge carrier statistics – the actual form of the low energetic tail can be described by a convolution of the exponentially decaying distribution with a Gaussian function [88]:

$$t(x) = \frac{S_t}{2\beta} \exp\left(\frac{x - x_0}{\beta} + \frac{\sigma^2}{2\beta^2}\right) \cdot \operatorname{erfc}\left(\frac{x - x_0}{\sqrt{2}\sigma} + \frac{\sigma}{\sqrt{2}\beta}\right). \tag{4.29}$$

In this equation, often referred to as the Hypermet function, β is the decay constant of the exponentially decaying distribution, σ and x_0 are the parameters defining the Gaussian broadening and S_t is the number of counts in the peak. The Hypermet function was not correctly normalized in Ref. [88], however it is corrected here. The Hypermet function is also referred to as exponentially modified Gaussian (EMG) and for example used in Chromatography for peak reconstruction [89].

This distortion of the peak can be large enough so that it must be taken into account for calculating the detector resolution. This leads to an ambiguity in the definition of the detector resolution. If one is only interested how precisely the initial γ-ray energy can be reconstructed, then the FWHM is calculated including this additional distribution. On the other hand, if one is interested in material characteristics such as the Fano factor, then the tails must be subtracted to gain a unbiased value of the variance of the distribution. For most of this thesis, the detector resolution will be provided as a FWHM value that includes the spread through the tailing term. When calculating the Fano factor the resolution will be given as the variance σ of the Gaussian distribution only.

The distortion needs to be also considered when measuring the number of events in a peak. In that situation the contribution from the tail and the Gaussian must be added $S_{\text{tot}} = S_t + S_g$.

It is rarely the case, that a peak is background free. Particularly, Compton scattered event create a continuum underneath the peak. Ideally, this background component is a step function with a constant offset, but also this distribution is broadened, resulting in a function falling

over a certain width defined by the square root of the variance σ:

$$s(x) = \frac{A}{2} \cdot \mathrm{erfc}\left(\frac{x - x_0}{\sqrt{2}\sigma}\right) + B. \tag{4.30}$$

A defines the height of the step and B is the overall offset.

The three terms $g(x)$, $t(x)$ and $s(x)$ are illustrated in Fig. 4.9, representing a fit to data of the 1332.5 keV line from a ^{60}Co source. The fit has been performed with the Levenberg-Marquardt technique adopted from the C-based library MPFIT [90]. The algorithm has been implemented into a special routine for fitting the presented equations to a peak in the energy spectrum. The routine has been used for any fit that will be presented later on in this work. In Fig. 4.9 it can be see that the description presented her fits well to the data. For data of good quality, the term describing the low energetic tail is roughly two orders of magnitude smaller than the Gaussian peak and therefore has a rather small effect. However, inaccuracies in the analysis or faulty detectors can increase the term substantially.

4.2.8 Energy calibration

The reconstructed peak height depends not only on the number of charge carriers, but also on characteristics such as the preamplifier gain and pulse shaper properties. The absolute energy of a pulse height value is accordingly not computed directly but evaluated through a calibration procedure. This procedure involves the identification of structures (usually energy peaks) in the spectrum, that are known in advance, and assigns them to their original energy values. If a spectrum is obtained that does not contain sufficient features to allow a clear identification of the energy scale, then additional measurements with calibration sources are required. Standard calibration sources are well described through a few typical energy peaks that are measured at high precision; famous examples are ^{60}Co, ^{241}Am, ^{228}Th and ^{133}Ba. The energy of the used calibration peak should be as close as possible to the structures measured to avoid additional errors caused by nonlinearities of the spectrometer system. Often multiple sources are used simultaneously to cover the entire energy range evenly. Such a procedure however requires, that the detection system is sufficiently stable and does not vary between the calibration measurement and the actual measurement. A simple way to assure the stability of the system is to perform at least before and after the measurement a measurement with the same calibration sources. If many different peaks are contained in a calibration measurement, it is possible to derive the calibration curve, that relates pulse height values to energy values over a large range of energies. Most of the times a linear interpolation inbetween peaks is sufficient, but also higher polynomial least square fits are commonly used.

4.3 Germanium analysis toolkit

The GErmanium ANAlysis (GEANA) toolkit was initiated by Thomas Kihm [83] as an independent, fast analysis software for studying the data obtained in the GERDA experiment (see Sec. 1.2.4 for an introduction to GERDA). It runs on a basic Unix like system without any special dependencies and contains all the important methods for analyzing any data from germanium detectors. The existing frame was adopted from his work and extended to automatize the analysis of data collected in the scope of this thesis. Particularly, new methods for data

input/output and some new algorithm to use the program for data measured with a variety of radioactive sources (e.g. peak finding methods, rise time analysis, etc.) has been added. In the following sections some main aspects of GEANA will be presented.

4.3.1 Program organization

GEANA consists of three main blocks, first a collection of important methods organized in libraries, second a set of small programs that perform particular tasks of the data analysis chain of germanium detectors and finally a few scripts that are used for controlling the analysis chain.

The core of GEANA is an extensive set of C-style functions, that are organized in five different libraries. The libraries provide most of the functionality required for analyzing data obtained with a germanium detector, thus aside from the standard libraries available on most Unix systems there is no special dependency. The libraries can be individually build, are compatible with C/C++ and are also used for a variety of other projects that require similar methods. The methods provided by the libraries include plotting, filling of histograms, filtering of signals, reading data from and writing data to the disk, fitting peaks in histograms, finding peaks in histograms, etc.

These libraries then are used to implement five small programs, that are specialized to perform a specific task in the sequence that ultimately leads to a reconstruction of the energy of each signal. Similar to the libraries, the individual programs are all implemented in C and compatible with C++. The main task of these programs will be discussed in Section 4.3.4 and can be summarized as indicated in Fig. 4.10 as follow: data organization, filter parameter extraction and optimization, calibration, energy reconstruction.

The sequential call of the individual programs is controlled by a few additional scripts that are implemented in the scripting language BASH. The main script only requires a few fundamental information about the data set and is from there on capable of automatically perform the entire analysis of the provided data set. Some other scripts can be used for some more advanced plotting and fitting task and make heavy usage of GNUplot [91].

4.3.2 Data flow

A few basic configure parameters need to be given to the programs in order to be functional. These parameters can be defined in a header style setup file, that then is used to compile the five main C-programs. Often these parameters change slightly from one type of analysis to another, in such a case it is most convenient to use a separate version of GEANA with a particular header file. However, often analyses are similar enough, so that the same setup file can be used. It is for example possible to run the entire data set of the GERDA experiment with a single setup file.

The files produced during the analysis are most conveniently kept in a separate directory, that is consecutively updated as the analysis progresses. The folder contains initially only a file defining the detector layout (if the measurement was performed with more than one detector), but later in the analysis process other files are added. The first files that are created for example contain information about the organization of the files that need to be analyzed. Each program adds extensive logging files and a few important histograms to the folder, so that the individual steps can be checked for their validity. Each programs additionally calculates

a few new parameters that need to be passed to the next stage. These information flow from one program to the next by storing them in a configuration file that is consecutively updated by the different programs.

If requested, the final programs also produce some event based file lists. These files are organized in an ASCII format and contain all the important values of an individual event, such as time stamp, reconstructed energy of the incident radiation, veto flags, coincidences with other detectors etc. A small portion of the signal can also be added to the list to be further used to define additional background suppression parameters.

At the very end of the analysis, all important information and plots are collected on a single html web page, that is stored to the same folder and allows to easily confirm that the analysis process was performed satisfactorily.

4.3.3 Implemented methods

In Sec. 4.2 different methods to improve the pulse height reconstruction have been discussed. All of them are implemented in GEANA and can either be directly selected or automatically optimized. Before the main shaping filters are applied to the signals, the pole-zero cancellation must be performed. Then the MSEC method that was discussed in Sec. 4.2.5 can optionally be conducted to reduce ballistic deficit effects. Only at this stage the signals are filtered with the shaping filters. There are three basic filters; the pseudo-Gaussian filter composed of 4 moving window average filters of the same length, the rounded-top trapezoidal filter composed of 4 moving window average filters of different length, and the rounded-top cusp filter created from two bidirectional low-pass filters and an additional moving window average filter. After the shaping filter the pulse height is found by a simple maximum search in a confined range around the charge pulse.

These method all require that some parameters are defined in advance:

- Pole-zero: Decay time,
- MSEC: Enabled/disabled,
- pseudo-Gaussian filter: Shaping time,
- rounded-top trapezoidal filter: Shaping time, rounded-top width,
- rounded-top cusp filter: Decay of the two sided exponential, width of rounded top,
- location of the amplitude (pulse height) measurement: Time range within which a maximum search is performed.

GEANA contains mechanisms that can be used to establish the values of all these parameters automatically, even the optimal filter type. However, such a procedure is computational intensive and it is better to only search the optimal parameters from a very limited number of preselected values.

Once the filter parameters are established the peak height spectrum can be calculated and a calibration curve extracted. The calibration curve requires the knowledge of the energies of the γ-rays that were used for the calibration measurement. GEANA contains some simple methods to match these energies to the respective peaks in the spectrum in an automated manner.

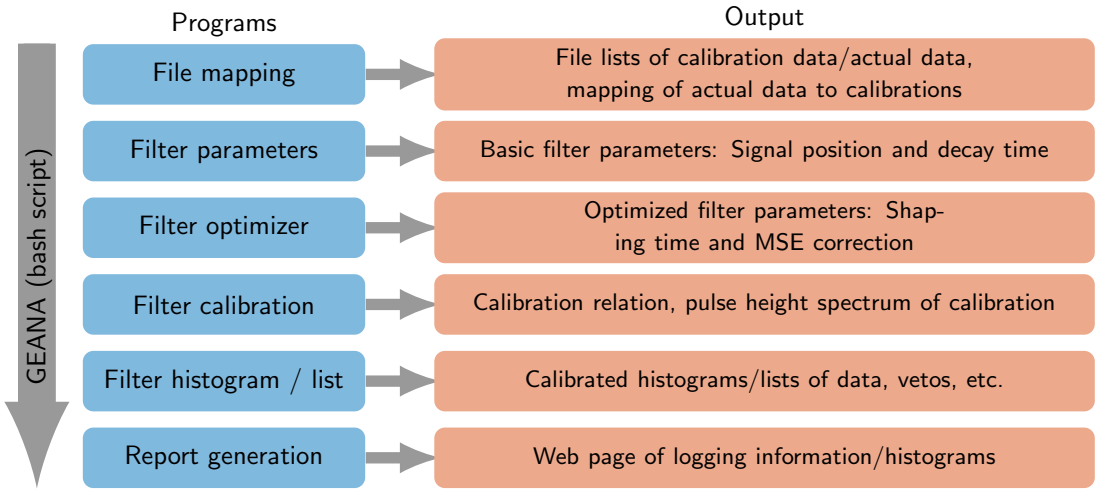

Figure 4.10: Overview of the programs in GEANA and their specific tasks.

4.3.4 Modular analysis

The division of the analysis in small programs leads to a natural sequential organization with particular tasks being performed at different stages. At each stage a specific task is executed and certain information collected, that are made available for other programs by storing them into a central configuration file. Unfortunately, this sequential structure requires that the same data will be processed multiple times as it is not possible to extract all the important information in one step. However, the required processing time can be reduced by not processing the entire data set at each level, but only gather enough statistic to evaluate the required parameters with sufficiently high precision.

The following section will give a brief explanation about the various task being performed in each stage of the analysis chain.

Mapping

In Section 4.2.8 it was discussed, that in certain situation it is inevitable to take some special measurement to calibrate the energy range in the pulse height spectrum. The two types of data, those that contain sufficient calibration information and those that do not (physics data) must be separated and organized as they will be treated differently through out the analysis process. The first category is classified as the calibration data set and each individual measurement serves as a reference point in time with a known, well defined relationship between pulse height and energy. According to some predefined rules the physics data are then assigned to the calibration data set. In GEANA this is done automatically by mapping the data set to the calibration measurement that was taken closest in time. In certain situation this is not optimal, and a manual mapping will be the favored method.

The initial steps (filter parameter search/calibration) of the analysis chain are only conducted with data that contain enough information for defining the energy range; the physics data are only used in the very last step once all the filter parameters are defined.

Filter parameters

The filters described in Sec. 4.2.2 only work if some fundamental input parameters are given. The most crucial parameter is the decay time of the preamplifier required to perform the pole-zero cancellation, which will be evaluated by the second stage of GEANA. One way to find the exact value of the decay time is to sum up a specific amount of input signals and to calculate the average signal shape. This signal will have a decaying tail with a decay constant close to the decay time of the preamplifier. However, this value can be distorted by preceding events (pile-ups). To correct this, the decay constant in the region before the pulse is additionally calculated and subtracted from the value found in the tail.

The average signal provides some additional information. The position of the rising edge of the pulse can be found to reduce the range of the following filters to a small region around this edge and define the range in which the maximum search is performed.

Filter optimization

The next stage is to find the optimal set of filters: The ballistic deficit may or may not be corrected (MSEC on/off), and the filter type and shaping time must be defined.

Thus, a method was implemented that optimizes the filter type, shaping time and MSEC by filtering a part of the calibration data set for all possible combinations of a user provided parameter list. The energy resolution of a specific energy peak is determined and the parameter set with the best energy resolution is selected. As the number of filter combinations increases quickly with an increasing number of parameters, it is beneficial to reduce the set of parameters, that need to be checked, to a minimum.

Filter calibration

The optimal set of parameters is used in the next stage to filter the calibration data set. In the mapping process calibration data sets were organized into blocks, and each calibration data set is individually filtered to take into account changes between consecutive measurements. The errors that are introduced by the nonlinear response of the data acquisition systems can be reduced by having numerous calibration peaks available. The energy range between peaks is linearly interpolated.

The matching between observed peaks in the pulse height spectrum and the γ-ray lines can be automated. A simple approach used in GEANA is to calculate ratios between the energy peaks and then compare them to ratios between γ-ray lines to look for the best match.

If shifts between two calibration measurements are too large both calibrations are rejected and the data sets taken between the two calibration measurement excluded from the analysis.

Data filtering

In the last stage, the filtering of the physics data is performed. In this process, a calibrated energy spectrum (histogram) is produced by applying the previously defined calibration relations. In addition, in that process also the event lists, that contain all the information on an event-by-event basis, are created. Often, it is also required to have calibrated histograms and event list of the calibration data sets, these data sets are thus processed again to create all required output files.

After finalizing the analysis, all relevant information will be collected from the different output files and the html web page will be created with all relevant information about a given analysis.

4.4 Pulse shape simulation

The underlying physics of signal formation can be studied by performing simulations. For this purpose an existing library (simulation toolkit), the AGATA Detector simulation Library (ADL3) was adopted [92]. The Advanced GAmma Tracking Array (AGATA) is a European large scale γ-ray spectrometer project that tries to make use of segmented high-purity germanium crystals to accurately determine the energy, time and position of every interaction of γ-rays [93]. The reconstruction of the interaction position from the pulses acquired at the different segments requires very precise simulations of pulses at different interaction positions, thus the need for such a simulation library emerged.

In ADL3, the structure and calculation of the different potentials and fields is partially based on a commercial software [94]. The simulation of the pulses from these fields then was newly implemented and is based on algorithm and physical models studied by the AGATA collaboration [95, 96].

The initial library was extended for the work presented in this thesis with field calculations that take variable permittivity in the medium into account and with geometrical models for detector types that were used for the GERDA experiment (see Sec. 1.2.4 for more information about GERDA). The field calculation is similar to an algorithm developed by part of the MAJORANA collaboration in Oak Ridge, Tennessee [97], and was tested carefully. The extended ADL3 library is currently used by other groups within the GERDA collaboration and a group of AGATA at the University of Liverpool [98].

ADL3 is implemented in C, compatible with C++ and only depends on the standard C libraries available on most Unix like systems. The main functionality is collected in libraries, that then can be used to write dedicated programs.

The library is divided in two parts, one dedicated for calculating the electric and weighting potential, the other for calculating the signal shape for given potentials and a specific interaction location. This division is usually also kept in the usage of the library, as the calculation of the potentials takes some time, but they can be conveniently stored to a file and then be reused by many different programs for the simulation of the detailed pulse shape. Furthermore, the evaluation of the potential is already sufficient to study some characteristics of the detectors, such as the depletion voltage.

4.4.1 Field simulation

The first step in simulating the pulse shape of an event is to calculate the electric potential and the weighting potential for a given detector geometry. The next sections describe a method to achieve this for any predefined detector geometry.

Electric potential and field

The electric potential is derived from the Macroscopic Gaussian Law, one of the four Maxwell equations:

$$\vec{\nabla} \cdot \vec{D} = \rho_f, \quad \text{where} \quad \vec{D} = \varepsilon \vec{E} \quad \text{and} \quad \vec{\nabla}\phi = -\vec{E}. \tag{4.31}$$

In these equations ρ_f is the free charge and ϕ the electric potential. The displacement field $\vec{D}$ is related to the electric field $\vec{E}$ by the permittivity ε, which in the most general case can be a matrix and a function of the position. In the field simulations presented here, the permittivity was considered to be a scalar, however it was not considered as constant throughout the simulation volume so that a combination of different materials can be simulated. From equation 4.31 the following equation can be derived (the position dependence of all variables is for clarity indicated explicitly):

$$\nabla^2\phi(\vec{x}) \cdot \varepsilon(\vec{x}) + \nabla\phi(\vec{x}) \cdot \nabla\varepsilon(\vec{x}) = \rho_f(\vec{x}). \tag{4.32}$$

In most situations, this equation is sufficient to evaluate the potentials in a germanium detector. It incorporates the space charges within the detector bulk, that is created by electrons and holes moving along the electric field into the highly doped medium. Moreover, it also takes into account variabilities in the permittivity and thus correctly calculates the potentials in regions that are not built from germanium. If such regions are neglected the permittivity can be assumed as constant and the equation reduced to the Poisson equation:

$$\nabla^2\phi(\vec{x}) = \rho_f(\vec{x})/\varepsilon, \tag{4.33}$$

where the permittivity usually is simplified to be $\varepsilon = \varepsilon_0 \cdot \varepsilon_r$ with $\varepsilon_r = 16$ in germanium and ε_0 being the vacuum permittivity. In certain cases the space charge is zero and the Laplace equation can be used:

$$\nabla^2\phi(\vec{x}) = 0. \tag{4.34}$$

Equations 4.32, 4.33 and 4.34 are all implemented into ADL3 in order to be capable of perform the simulations presented in later chapters. To solve the respective differential equation a method called 'successive over relaxation' [99] is used. For this purpose the detector structure is represented on a grid, with each grid point having specific attributes (a value for the permittivity, space charge and electric potential). In multiple steps, by iterating over the complete grid, the physical solution of the differential equation is approached until a certain predefined precision is reached and the algorithm is stopped. In each step, a new value is calculated at every point of the grid, by averaging the nearest neighbors and weighting this value with the last value at this position. This approach converges fast.

From the electric potential the electric field can be derived by solving the third equation in 4.31.

Weighting potential

The Shockley-Ramo theorem was discussed in Sec. 2.2.6 and the weighting potential defined that facilitates the calculation of the induced charge into an electrode. Here, a simple recipe for the calculation of the weighting potential is provided to summarize the most important findings:

- The selected electrode is at unit potential (=1).

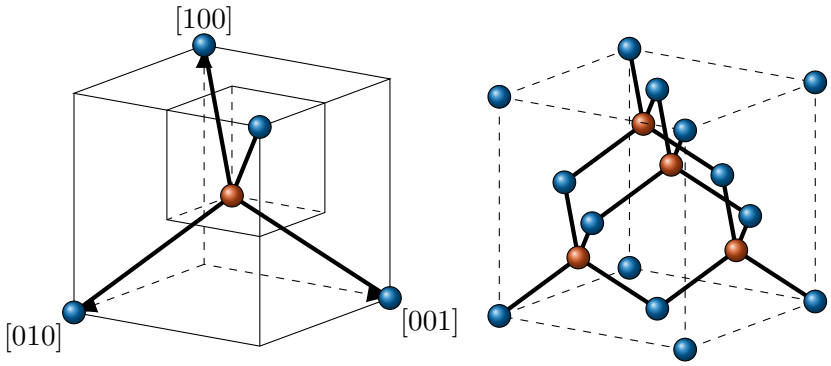

Figure 4.11: The arrangements of germanium atoms in the diamond lattice: one atom is at the center of four atoms arranged in a regular tetrahedron. The blue/red dots indicate the position of the atom, the arrows indicate the lattice directions.

- All other electrodes are at zero potential.
- All charges are removed.

The weighting field can accordingly be found by solving the Laplace Equation 4.34 with the successive-over-relaxation method.

4.4.2 Charge trajectory

In 1956 Sasaki et al. [100] observed that electrons and holes in germanium have an anisotropic mobility. This means, that the drift velocity will not be parallel to the applied electrical field, instead, it is influenced by the orientation of the field with respect to the crystal lattice directions.

The atoms in germanium are aligned in a diamond structure as illustrated in Fig. 4.11 (which is the same as for silicon and diamond). In Fig. 4.11, the coordinate system is aligned with the principal $\langle 100 \rangle$ lattice directions. The $\langle 100 \rangle$ form is part of the Miller indices notation and denotes the set of all directions that are equivalent by symmetry (such as [100],[010] and [001]). The growth method of germanium crystals in long cylindrical ingots assures that the axis along the height of the ingot is aligned with one of the $\langle 100 \rangle$ directions, the two other $\langle 100 \rangle$ directions thus must lay in a perpendicular plane.

The drift velocity can be divided into a longitudinal and a transversal part, by projecting it onto the electric field, accordingly the anisotropy can also be separated in a longitudinal and transversal anisotropy, respectively. The diamond structure is invariant under some particular rotations. The invariant rotational axes are along the $\langle 100 \rangle$, $\langle 110 \rangle$, and the $\langle 111 \rangle$ directions. If the electric field is aligned with one of the rotational axes then the transversal anisotropy must be zero, as otherwise the rotational invariance of the crystal lattice would be violated. Thus, along the symmetry axes of the diamond crystal the drift velocity is entirely defined through its longitudinal part. The longitudinal drift velocity v_l along the $\langle 100 \rangle$ and $\langle 111 \rangle$ directions was measured for different electrical field strength and a practical empirical function was derived at 77 K [101]:

$$v_l = \frac{\mu_0 E}{(1 + (E/E_0)^\beta)^{1/\beta}} - \mu_n E. \tag{4.35}$$

At low fields ($E \ll E_0$) the equation reduces to the normal proportional dependence $v_l = \mu_0 E$, at intermediate electric field strength the deviation from this dependence is modeled through the fit parameters β and E_0. A negative differential mobility [102] has been observe at high electric field (above 3 kV/cm) therefore the term $\mu_n E$ has been added to account for this effect.

In order to calculate the drift velocity for any orientation of the electric field to the crystal lattice, the details of the band structure in germanium must be studied. Only the band structure in close vicinity of the energy gap is of importance as phonon losses prohibit the population of high energetic levels. The parameters defining the shape of the energy band near the band gap for a given orientation of the electric field to the crystal lattice are the effective masses, which are known from other experimental studies [101]. Both, for electrons and holes, there exist some simplified empirical formula, that adds two more fit parameters to define these dependencies and fix the drift velocity for any orientation of the electric field and the crystal lattice [95, 96, 101]. In typical germanium detectors, the additional term for the negative differential mobility can be neglected as the field strength is below 3 kV/cm. For each charge carrier type there are 6 remaining empirical parameters, β and E_0 to define the drift velocities for a given field strength along the $\langle 100 \rangle$ and $\langle 111 \rangle$ directions respectively and two more parameters to perform a transformation to any orientation of the field and the crystal lattice. This model agrees with experimental data in that not only the magnitude of the drift velocity varies, but also a non zero transversal component appears, that points towards the axes with the highest longitudinal drift velocity.

The details of the models that define the drift velocities are implemented in ADL3 and the necessary empirical fit parameters can be either evaluated by a global fit to measurements or by assuming the detector material to be close to the one used in the publications describing the respective models.

5 Point contact optimization

A large variety of different PCGe detectors is being used in fundamental research. Some of the choices for a particular detector shape and point contact size can be found in consideration in regards to the research that should be conducted with the detector. However, also limitations in the fabrication process do affect the PCGe detector geometry.

The impact of differences in the shape and size of the point contact has not yet been experimentally investigated in detail. The largest study of variations in detectors so far was conducted by the GERDA collaboration during a characterization campaign of the 30 new BEGe detectors [63]. Furthermore, also the MAJORANA collaboration has recently released first results on the characterization of their detectors [103]. The collected data show that crystal variation are dominant and that there is practically no correlation between specific geometrical features. The reason for this is rather simple – the detectors have different impurity concentrations and not all the material could have been processed simultaneously, thus the crystal quality varies. Furthermore, it is often hard to entangle intrinsic properties of the crystal from effects caused by the design.

In order to circumvent the material and diode variability, the study presented in this dissertation tries to go into a new direction. Instead of measuring a large amount of different detectors, data from only two detectors are gathered, that are consecutively modified by varying only the least amount of parameters necessary (as discussed later on the groove and point contact size). This approach allows to study the detectors response to the geometrical modification under constant conditions in terms of intrinsic material properties. The study is performed with two almost identical detectors simultaneously to rule out systematic effects and confirm the observations with a second set of measurements.

The detectors that are study have been produced by Canberra N.V. in Olen, Belgium and follow the typical shape of their Broad Energy Germanium (BEGe) detectors, with a groove between the two electrodes. The discussion here will be limited to this type of detectors.

The first part of this chapter will describe how the design of the detectors has been defined with simulations in ADL3. In the second part the geometry of the two actually produced detectors will be described.

5.1 Simulation-based investigation of geometrical modification

In this section it is assumed that a detector of a given volume should be fabricated. The starting point is a GERDA-like detector with 3.5 cm height and 3.5 cm radius, thus a volume of 134.7 cm^2 and a weight of 717 g. This design then is consecutively altered to study how the performance can be optimized for particular applications. It must be kept in mind that this discussion is primarily aimed at applications in fundamental research. In this field the detectors require are large volumes with a low surface-to-volume ratio, low energy threshold and little noise.

The electric field simulated with ADL3 are used to study the effects of geometrical mod-

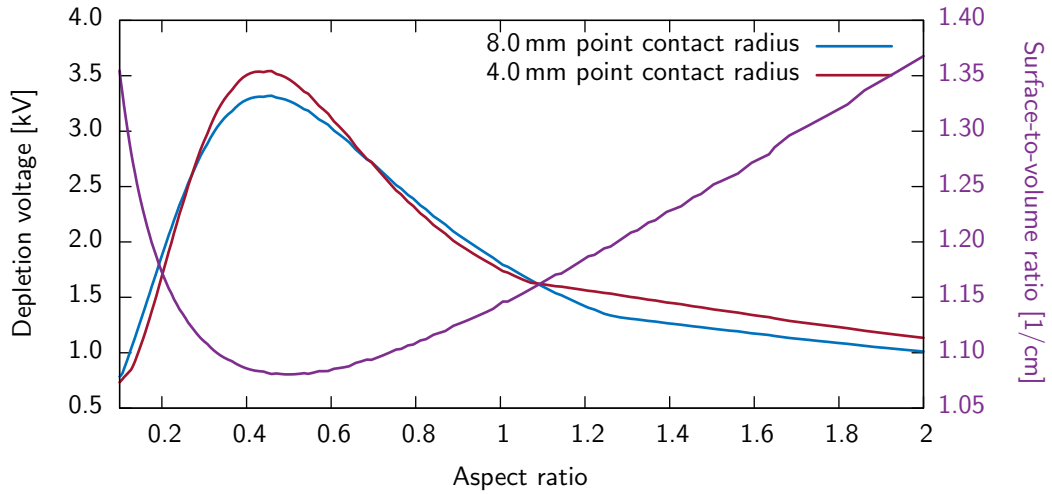

Figure 5.1: The depletion voltage of two different detector configuration are shown as a function of the aspect ratio (radius/height) for a detector of 717 g. In addition also the surface-to-volume ratio is indicated. The impurity concentration was chosen to be constant throughout the detector and at 10^{10} /cm^3. Simulated with ADL3.

ifications on detector properties. To distinguish a good geometry from a not so good one, it is necessary to define a quality factor (figure of merit). This is not straight forward. An important factor in a detector is a homogeneous electric field distribution to assure complete charge collection throughout the detector volume. PCGe detectors are relatively suboptimal in that concern, the fields in coaxial detectors are usually more homogeneous. However, PCGe detectors have other beneficial features (see Sec. 3) that must be conserved. Thus homogeneous fields are important as long as they do conserve the other features, such as low capacitance and good pulse shape properties. The homogeneity of the field can be controlled by the operational voltage of the detector, which must be well above depletion. However, the operational voltage should not exceed ~ 5 keV as effects from leakage currents more likely affect the diodes performance at high voltages. As a good homogeneity of the field for a given voltage usually coincides with a low depletion voltage, the depletion voltage is chosen to be the figure of merit for the detector geometry and can easily be simulated in ADL3 and compared for different geometries.

5.1.1 Aspect ratio

The importance of a homogeneous electric field must be weighted against a certain surface-to-volume ratio, as the geometry with the most homogeneous field most likely is not the one with the best surface-to-volume ratio. Fig. 5.1, shows the depletion voltage as a function of the aspect ratio of a detector (the ratio between the radius and the height) for two different point contact radius (8 mm and 4 mm). It can be observed that at the best surface-to-volume ratio the depletion voltage is highest, thus the field configuration not at the optimum. At an aspect ratio of 1-1.2 there is a small dent in the depletion voltage and for higher aspect ratio the depletion voltage decreases slowly. It seems reasonable to choose the aspect ratio such, that it is placed at the value of the dent in the depletion voltage. Below the dent the depletion

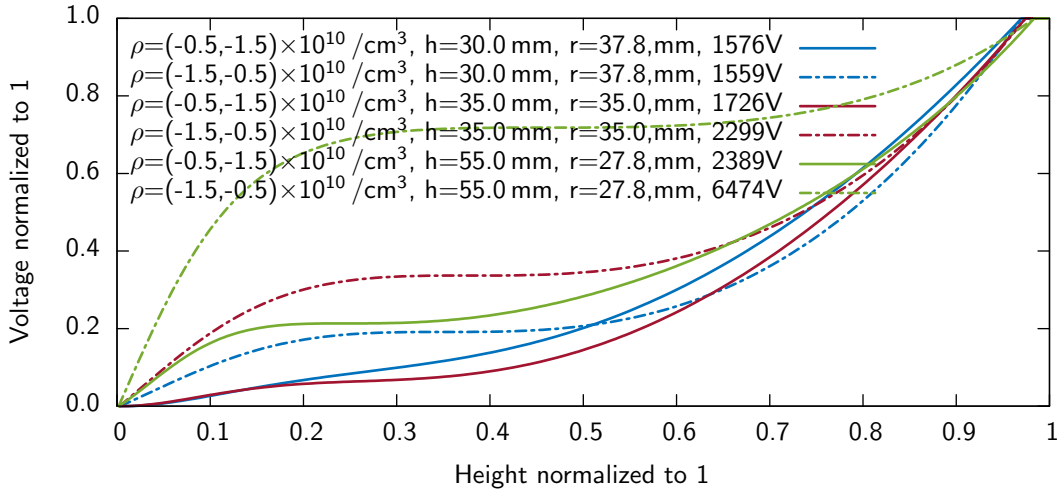

Figure 5.2: The voltage gradient at zero radius for three different aspect ratios (h for height, r for radius) with the same mass (717 g). The configuration is chosen to be at the depletion voltage and the space charge density is linear from either -0.5×10^{10} /cm^3 at the top and -1.5×10^{10} /cm^3 at the bottom (solid line) or -1.5×10^{10} /cm^3 at the top and -0.5×10^{10} /cm^3 at the bottom (dashed line). Simulated with ADL3.

voltage increases strongly thus the field configuration is less ideal while above the dent only a small improvement in the depletion voltage is gained, with a large lost in surface-to-volume ratio. The exact position of the dent is not only defined by the aspect ratio, but can also be controlled by the impurity concentration in the detector.

The dent for a 717 g detector is found at a height of 30 mm and a radius of 38 mm and the best surface-to-volume ratio is reached at roughly 55 mm height and 28 mm radius. These two geometries together with the one of an aspect ratio of 1 will be considered in the next section for studying the effect of the impurity concentrations.

5.1.2 Impurity concentration

The impurity concentration in a detector defines how much space charge is found in a certain region once the detector is depleted. As discussed in Sec. 2.2.6, the electric potential in a detector can be split up into two contributions, one that only represents the potential caused by the electrodes (zero space charge) and one that only considers the potential created by the space charge (zero voltage on all electrodes). The first potential decreases from the high voltage electrode continuously to the central electrode at zero potential and thus is by definition without a local maximum or minimum (this is equal to saying that the electric field strength is nowhere zero). The space charge potential is defined to be zero on all the electrodes and as only p-type material (negative space charge) is considered, will have a local minimum in the detector volume. In a depleted detector the total electric potential can not contain a local minimum as this would entail that the region around the minimum is not depleted. Thus the contribution from the electrodes must be sufficiently strong to eliminate the local minimum created by the space charge contribution. The strength of the electrode contribution is simply regulated by the applied bias voltage which can be considered to be a simple scaling factor for

the electric potential created by the electrodes at unit voltage. The voltage that needs to be applied to exactly remove the local minimum is the depletion voltage.

This discussion reveals the actual impact of space charge onto the electric field configuration in a diode: If the space charge is zero, which requires that there are no impurities (intrinsic material), then the diode is depleted at any bias voltage. At non zero space charge, the electric potential is modified by the space charge in that the gradient in some regions is increased, while in others reduced. In the production of PCGe detectors, low impurity concentrations are usually favored as this leads to less trapping, however impurity gradients are very practical to create a more uniform field and remove regions with low drift velocities.

The effect is represented in Fig. 5.2 that assumes an impurity concentration gradient along the height of the detector. It can be seen that for either aspect ratio the field (derivative of the potential) is more homogeneous if the space charge is chosen to be more negative on the bottom (the side with the point contact) than on the top. In all configurations but the short cylinder one (30 mm height, 38 mm radius) the depletion voltage is also lower for that configuration. The figure also highlights that the field configuration is worst (long stretches of low field strength) if the aspect ratio is chosen to be ideal in regards to the surface-to-volume ratio and is better the shorter the cylinder is chosen to be. However, choosing a very short cylinder will cause low field regions along the radial direction, which is also suboptimal.

The long straight stretches of some of the curves in Fig. 5.2 furthermore explain an observation made later in the experimental evaluation of the detectors – an undepleted bubble in the center of the detector. The curves in Fig. 5.2 are drawn just at the depletion voltage. The electric field falls off continuously from the high voltage electrode to the depletion border in the n-type material. If the applied voltage is slightly reduced the curves with long straight stretches would obtain a local minimum in the center of the detector. Such a local minimum is not physical, instead of reaching a local minimum the electric potential in that region takes a constant value. A constant potential (zero electric field) means that this region is not depleted. Instead, a local undepleted bubble is formed.

5.1.3 Point contact size and groove width

In Sec. 3.3 it has been discussed that the strength of a PCGe detector is the small capacitance related to the small size of the point contact. Accordingly, it is desirable to reduce the size of the point contact, but this should not be on the expense of a homogeneous field distribution in the detector.

Fig. 5.3 shows the relation between the point contact radius, the width of the groove (measured from the point contact to the high voltage contact) and the depletion voltage for the three geometries described in the previous sections. The left plots show that there is a small band along a particular set of parameters where the depletion voltage is minimal. Therefore, the width of the groove can be carefully selected as a function of the point contact radius to stay within the band of minimal depletion voltage. In the right plot it can be seen, that if one chooses the groove width accordingly then indeed the increase in depletion voltage is small. A maximal increase of 200 V when going from a radius of 10 mm to a radius of 0.1 mm is measured. The change is less drastic in the case of a long cylindrical shape, that shows a stable curve at a relatively high voltage compared to the other two geometries. The figure also shows, that there is an almost linear relation between the point contact radius and the optimal groove width. A large point contact radius asks for a small groove width, a small point contact

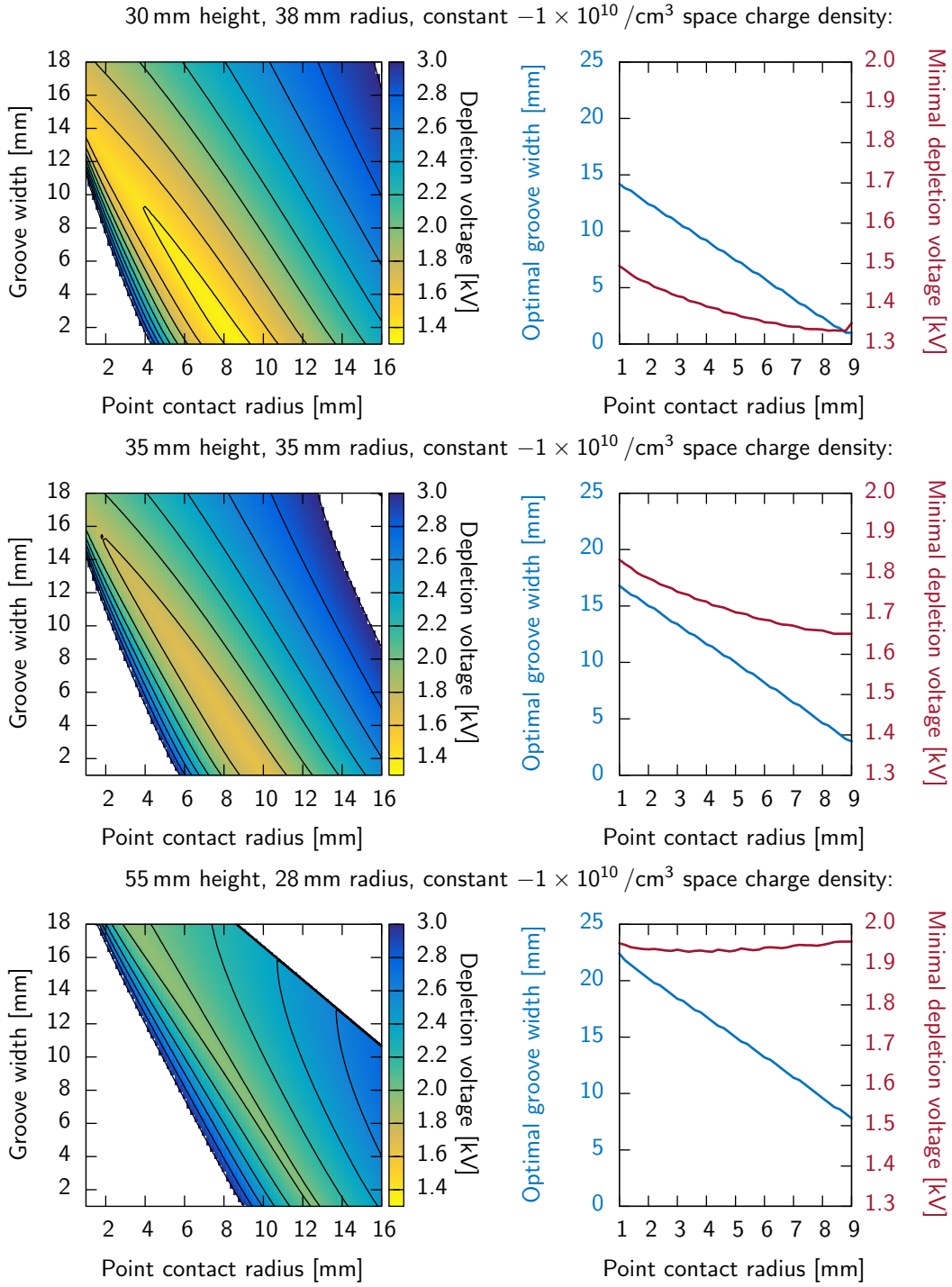

Figure 5.3: The depletion voltage dependence on the point contact size and the groove width for three different geometries. The right plot contains the configuration that minimizes the depletion voltage at a given point contact radius. Simulated with ADL3.

size for a large groove width. A large groove width, however, means a large passivated region, which is suboptimal for leakage currents.

Going from a short cylindrical shape to a long cylindrical shape the groove width also needs to be increased. At the configuration with the most optimal surface-to-volume ratio, the groove almost spans over the entire base of the cylinder. This finding is in good agreement with Table 3.1, where it can be seen that for example MAJORANA, with detectors that are more tailored to an optimal surface-to-volume ratio, have a very limited wrap around of the high voltage electrode onto the base with the point contact.

5.2 Experimental study of point contact detectors

In the previous section it was discussed how geometrical changes affect a PCGe detector. It has been found that an aspect-ratio of 1 is a reasonable choice. If an impurity gradient is present, then the point contact must be located on the side of the crystal with the more negative impurity concentration. Furthermore, for a given point contact size, the depletion voltage can be kept small if the groove width is accordingly adopted. In order to test these prediction two detector should be purchased with an initial large point contact size. In multiple steps the point contact size should then be reduced to a size that theoretically should allow to measure some of the research topics discussed in Sec. 1.2. At each configuration, the detector is characterized with dedicated measurements and a very stable experimental setup, so that systematic effects can be excluded. This procedure eliminates furthermore most systematic that are related with the germanium crystal such as a precise knowledge of the impurity concentration, the crystal dimensions and crystal defects that cause incomplete charge collection. These parameters should not be affected by a rework and thus be constant for the entire process.

The second detector is intended to further reduce systematic and allow for the eventuality of a detector breaking. The two detectors are characterized simultaneously at the same conditions. In the case that the experimental phase is successfully terminated, the total weight of the two detector would be sufficient for a measurement such as coherent neutrino-nucleus scattering and compete with the currently ongoing efforts in the related fields.

Because of the good experiences with Canberra N.V. in Olen, Belgium, it has been decided to work with this manufacturer. Its main business is standardized commercial production. The employees have therefore extensive experience with their own products and can assure a stable yield. However, the technologies available to them and their experiences beyond the standard geometries is limited.

5.2.1 Purchased detectors and their configurations

The two fabricated and stepwise modified detectors are typical BEGe detectors, up to the arrangement of the groove and point contact. An example of such a detector is depicted in Fig. 2.5. Their dimensions are listed in Table 5.1. They were named Asterix and Obelix. The name does not translate to their geometrical appearance – the two detectors have almost identical aspect ratios and mass. They have an aspect ratio close to 1 and are slightly larger than the detector geometry studied in the previous section thus have a marginally improved surface-to-volume ratio of $1.11\,\mathrm{cm}^{-1}$. Fig. 5.4 shows, that by choosing an aspect ratio close to 1 means that both detectors are slightly to the right of the bend in the depletion voltage. As previously discussed, a geometry that is located in the bend is a good compromise between a low

Name	Asterix			Obelix	
Canberra ID	14161			14158	
Weight	762 g			764 g	
Radius	3.59 cm			3.59 cm	
Height	3.58 cm			3.59 cm	
Top imp. con.	$-0.83 \cdot 10^{10}\,\mathrm{cm}^{-3}$			$-0.94 \cdot 10^{10}\,\mathrm{cm}^{-3}$	
Bottom imp. con.	$-1.00 \cdot 10^{10}\,\mathrm{cm}^{-3}$			$-1.00 \cdot 10^{10}\,\mathrm{cm}^{-3}$	
Lithium layer	~ 0.8 mm			~ 0.9 mm	
Phase	1	2	3	1	2
Cont. rad.	8.4 mm	5.0 mm	2.5 mm	8.2 mm	5.2 mm
Groove width	4.2 mm	9.0 mm	12.5 mm	4.6 mm	8.6 mm
Operational voltage	3000 V	3000 V	2500 V	4000 V	4000 V

Table 5.1: The selected parameters for the two detectors ordered from Canberra and the different point contact size configurations. The outer contact stretches all the way to the groove.

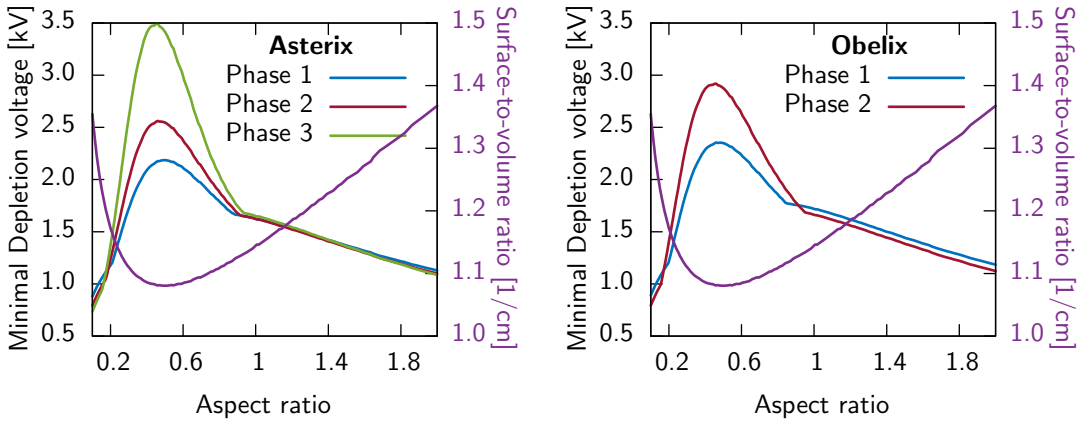

Figure 5.4: The depletion voltage of possible detector designs, with the same size and impurity concentrations as those given by Aster ix and Bollix in the respective configurations that have finally been produced. In addition also the surface-to-volume ratio is indicated, which is valid for both Asterix and Obelix as their size is only marginally different.

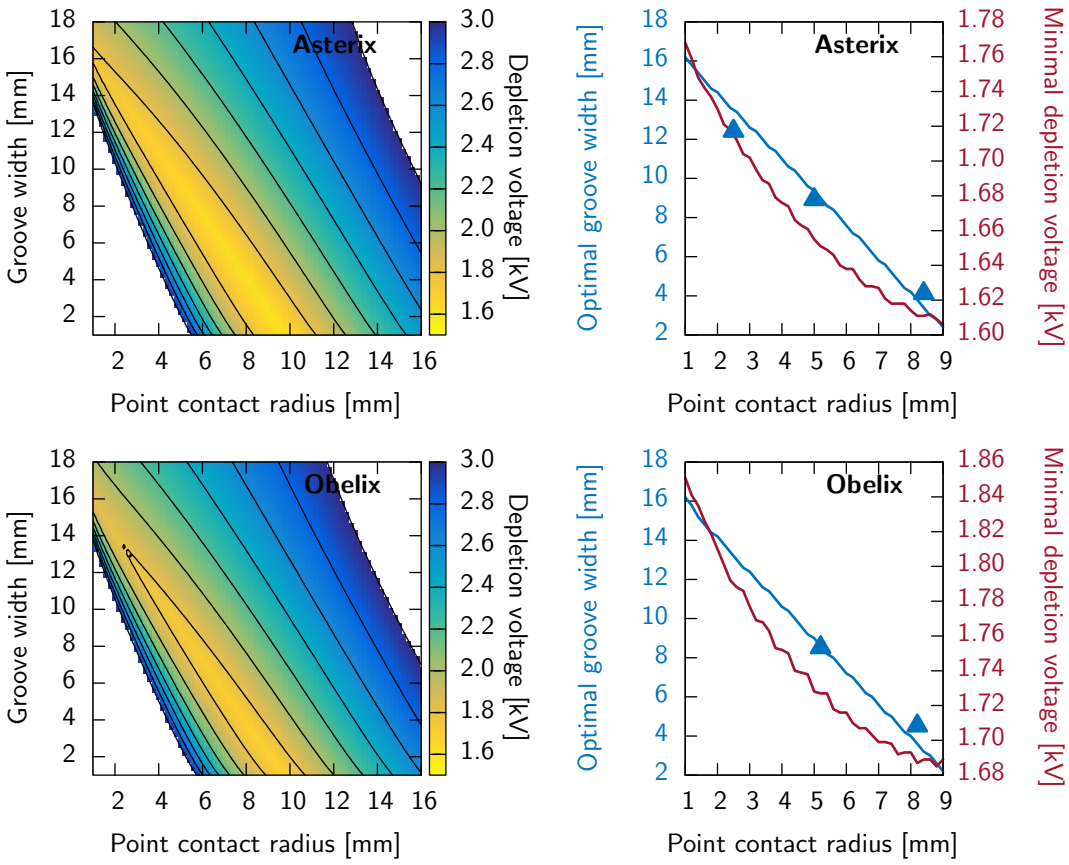

Figure 5.5: The depletion voltage dependence on the point contact size and the groove width for Asterix and Obelix. The triangles on the left plot represent the actual configurations of the detector.

depletion voltage and a good surface-to-volume ratio. The reason why the bend appears rather at an aspect ratio of 1 instead of 1.2 (see Sec. 5.1.1) is the different impurity concentration profile. The impurity concentrations in both detectors are close, however, Asterix has a slightly higher gradient. The impurity concentration was chosen to be more negative on the side with the point contact (bottom side). This choice reflects the finding from Sec. 5.1.2 and is common practice at Canberra.

The point contact sizes were chosen to start at a relatively large value and should reach in the final configuration a diameter of roughly 5 mm. The groove width was determined with the simulations according to a chosen point contact radius; the exact dependencies are shown in Fig. 5.5. The actual contact radius and groove width have been defined by the available driller sizes at Canberra and deviate slightly from the optimum (see left panels of Fig. 5.5).

6 Experimental setup and measurement protocol

In this chapter a brief overview of the experimental setup, that was especially put together for the characterization measurements of the two detectors is provided. Furthermore, also the most important measurements will be discussed.

6.1 Experimental setup

The measurements are performed on ground level. This means that the overburden is very small and most of the cosmic radiation still can reach the detector. However, the measurements used in the characterization all involve relatively strong radioactive sources, which induce a signal much stronger than the cosmic background. Thus, this location, although not optimal is sufficient.

The room is equipped with an electronics rack, a computer and two measurement tables and a picture of it is shown in Fig. 6.1.

6.1.1 Cryostat and dewar

The two detector are mounted in two separate 7500SL Canberra cryostat (see Fig. 6.2). The cryostat housing (end-cap) is made of 1.5 mm thick aluminum, that allows γ-rays above a few tenth of keV to penetrate into the cryostat and hit the detector. The housing contains a vacuum chamber with the detector and some parts of the preamplifier placed in vacuum. The vacuum chamber is connected to a long dipstick, that is insert into the neck of a 30 liter dewar filled with liquid nitrogen. The dipstick transfers heat from the detector to the liquid nitrogen and assures that the detector is kept at a constant operational temperature. The boiling temperature of liquid nitrogen is 77 K however the detector is usually kept at a slightly higher temperature.

The cryostat is equipped with a 2002CSL charge sensitive preamplifier. Parts of the preamplifier, in particular the field-effect transistor (FET), is kept at low temperature to reduce noise, while the remaining preamplifier is at room temperature. The preamplifier is equipped with a 5 GΩ feedback resistor and a 0.5 pF feedback capacitor. After the first amplification the signal is pole-zero corrected, differentiated and integrated to finally obtain a decay time of roughly 50 µs. The pulser resolution is according to Canberra 360 eV. A simplified diagram of the preamplifier setup is given in Fig. 6.3. The preamplifier has two outputs, one named 'energy' and one named 'timing'. The signal at the two outputs only differ marginally, for the characterization measurement only the energy output was used. The preamplifier has two inputs, one for the high voltage and one for a test pulser. A test point furthermore allows to measure the leakage current of the detector.

The detectors have been installed after each reprocessing step into the same cryostat to assure that there are no changes in the preamplifier setup. During the characterization measurement of the first configuration (Phase 1) the FET of Asterix broke and needed to be replaced. All measurements have been repeated after the replacement of the FET. The setup

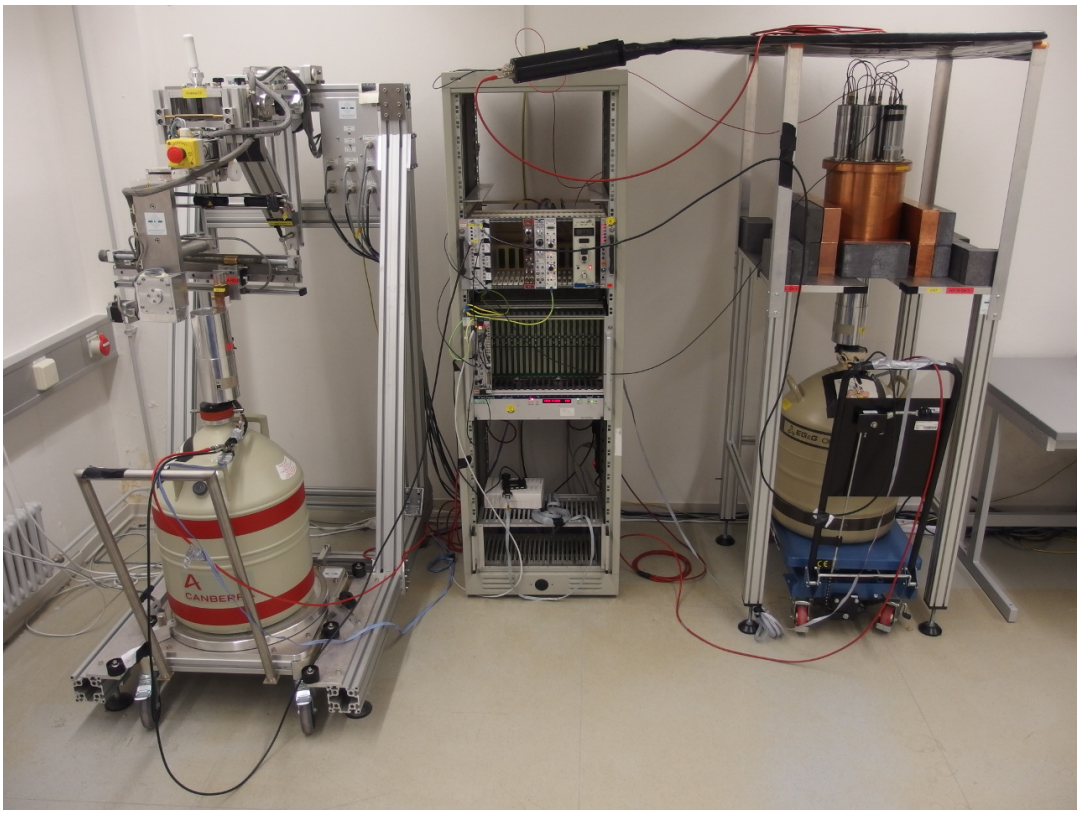

Figure 6.1: A picture of the experimental setup. To the left the automated scanning table, to the right the static table and in the center the electronics rack.

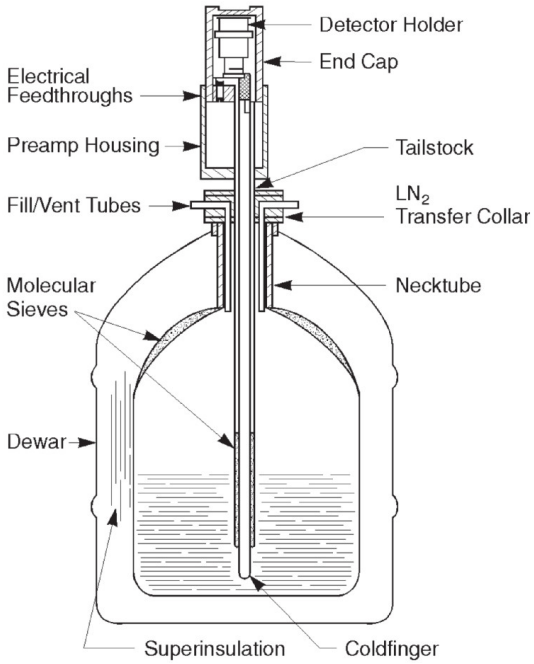

Figure 6.2: The 7500SL cryostat assembly produced by Canberra. The picture is taken from [104].

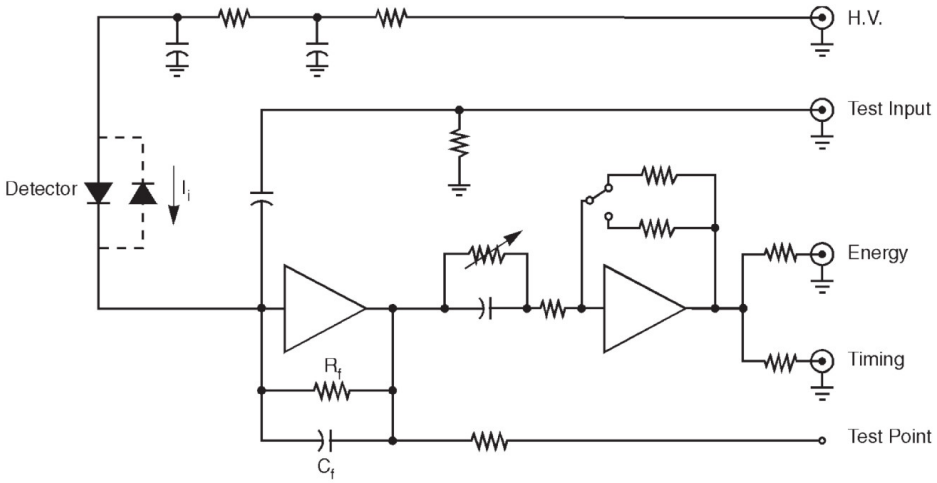

Figure 6.3: A simplified diagram of a typical Canberra charge sensitive preamplifier setup. [104].

then remained unchanged for the rest of the characterization measurements except for the removal and installation of the detector before and after the reprocessing.

6.1.2 Electronics modules

The output of the charge sensitive preamplifier is amplified with a GENIUS Shaper. the GENIUS Shaper was developed by the Max-Planck- Institut für Kernphysik, Heidelberg, and trimmed for low noise ($0.8\,\mathrm{nV}/\sqrt{\mathrm{Hz}}$) and a wide bandwidth (300 MHz-3 dB). Three different modules were used, each configured to amplify the signal so that it fits a particular energy range (0-250 keV, 0-1500 keV and 0-2750 keV). After this amplification stage, the signal is directly fed into the flash analog to digital converter (FADC).

The signal is digitized by a Struck SIS3301 VME FADC and processed with a 2 GHz VME CPU that is mounted into the same VME crate. The VME CPUs is configured to run Linux and equipped with an Ethernet connection, which allows to access the CPU over the network and to send the collected data to an external storage facility. The timing information is received from a Multi-Purpose Programmable I/O Controller (MPIC), mounted in the same VME crate. The FADC module accommodates up to eight input channels and is equipped with an integrated anti-aliasing bandwidth filter.

The signals are sampled in 10 ns steps and quantized at 14 bit resolution. For data reduction four samples are always summed up and then stored to the binary file. The length of the compressed signal is defined to be 164 µs and the rising edge of the induced pulse is in the center of the signal. Additionally in a 8 µs windows around the rising pulse edge the high frequency information at 100 MHz was stored to the same binary file. In some rare cases (for example the analysis of the noise distribution) the entire 164 µs range was stored directly at 100 MHz to the binary file.

The setup furthermore contained a single ISEG NHQ 246L module [105] that can provide a high voltage of up to 6 kV and a current of up to 1 mA for two independent channels. The relative voltage stability of the module is specified to be below 3×10^{-5}. The high voltage can be regulated over RS232 interface that was connected to the VME CPU.

For the duration of the entire characterization measurement the amplification and channel layout was kept unaltered to reduce any systematics coming from the read out chain. The HV module was found defective during the measurements of the second configuration (Phase 2) and was replaced with a similar module. No changes in the noise of the setup have been observed after the exchange. Prior to the characterization measurement possible sources of external noise have been identified and removed through a thorough grounding of the entire setup and by avoiding any unnecessary grounding loop.

6.1.3 Measurement tables

The main measurements are performed on a static measurement table (see Fig. 6.1 on the right). This is a relatively robust table like structure, with a roughly 12 cm wide gap from one edge to the center. The end-cap of the detector can be placed in this gap and a variety of radioactive sources placed on top of the end-cap. The end-cap and the source holder then are surrounded by a layer of copper and a layer of lead bricks, each having a width of 5 cm.

Next to the static table the experimental setup also consists of an automated scanning table (see Fig. 6.1 on the left). The table was designed by a subgroup of the GERDA collaboration

working at the University of Padova [106] and also used during the characterization measurements of the 30 new BEGe detectors in Belgium [63]. The scanning table is an automated apparatus to perform surface scans. In these measurements a highly collimated 5 MBq ^{241}Am source (in our case with an hole diameter of 1 mm) is pointed at different locations on the surface of a detector. ^{241}Am has one single line at 59.5 keV with a penetration depth of roughly 1 mm in germanium and roughly 5 mm in Aluminum [44]. The γ-rays emitted by that source have a good chance to penetrate through the aluminum end-cap but will be absorbed close to the surface of the detector. Therefore only a very limited part of the detectors volume is exposed to the source, which for many applications can be assumed as almost point like. The table contains a movable arm that can be rotated between 0 and 359° and brought either in a vertical or horizontal position depending on if the measured position is located on the top or side surface.

6.2 Measurement protocol

In this section the most important measurements performed for the characterization of the two detectors are quickly discussed. The list however is not complete, additional measurements have been performed for further analyses beyond this dissertation.

6.2.1 Source measurements

A set of radioactive sources have been organized to perform measurements with γ-ray lines at well defined energies.

Single source measurements

The single source measurement have been all conducted on the static table. They use a single radioactive isotope (except ^{228}Th where also γ-ray lines from its decay chain are visible) that produces a single or multiple lines in the spectra. The time a measurement requires to be run and the distant at which the radioactive source is placed depends on its strength. The count rate should not be too large as it leads to more pile-ups and thus a worse energy resolution but also not too small as then the measurement takes a long time and the peaks might be lost in the background. A count rate between 100-300 Hz was found to be a good value for most of the sources. The interesting peaks must at least contain 10'000 events to have a statistical uncertainty of a minimum of 1%, thus the required measurement time with each source can be estimated. Measurements have been performed with the following isotopes: ^{241}Am, ^{133}Ba, ^{60}Co and ^{228}Th.

Mixed source measurements

To track the energy resolution over a large energy range it is beneficial to use a combination of different sources that are placed such that the different peaks are roughly of equal height. A particular useful measurement was conducted with a mixture of ^{241}Am, ^{133}Ba, ^{134}Cs, ^{137}Cs, ^{60}Co, ^{152}Eu and ^{228}Th isotopes, which produce a spectrum with peaks in the entire energy range between 59.5 keV and 2614.5 keV.

High voltage scans

The resolution in an undepleted detector is deteriorated compared to a fully depleted detector and usually reaches an almost stable value once the depletion voltage is exceeded. To find the depletion voltage, at a variety of bias voltages a γ-ray spectrum is measured and compared to those measured at other voltages. The behavior as a function of the bias voltage was found to be more stable if one reduces the bias voltage from a value above depletion voltage towards zero Volt. The measurement was performed once for ^{241}Am and once for ^{60}Co. The detectors bias voltage was regulated from the operational voltage down to 500-1000 V in steps of 20 V and each position has been measured for 5-10 min.

Surface scans with collimated ^{241}Am source

The scanning table has been described in Sec. 6.1.3. It was decided on measuring a thin grid of points along the surface. On the top surface the measurements have been taken along rings that are aligned with the detectors center and separated by 2 mm distance. The average distance between two measurements in one ring also is 2 mm, so at small radii there are less points taken than at large radii. Along the side of the detector the measurements have been taken in rings at a specific height. The distance between measurement in the same ring is again 2 mm, the rings are separated by 4 mm distance.

The surface measurements allow to analyze in detail the signal shape from different locations in the detector and estimate the drift time of the charge carriers. It has been shown for example in Ref. [98] that such a measurement is sensitive to the anisotropic mobility of holes in the crystal that was described in Sec. 4.4.2. Each point was measured for 5 min and in total there were about 2000 points that needed to be measured for each detector.

6.2.2 Additional measurements

Some additional measurements have been performed that did not have the primary aim of measuring any particular γ-ray line but some other effects and detector properties.

Pulser measurement

The most basic way to characterize the noise of an electronic circuit in radiation detection systems is to feed a fast rising pulser signal into the test input of the preamplifier system. The received output signal does not depend on the charge collection process, but only on the rise time of the input pulse and the noise characteristics of the electronic circuitry. The measurement requires a very stable pulser signal at the test input, as small deviation in the height of the input signal will deteriorate the measurement. It was performed with a Hewlett Packard 8007B Pulse Generator with a 5 ns rise time.

Background measurements

The energy spectrum of the detector enclosed by an outer lead layer of 5 cm thickness and an inner layer of 5 cm copper was measured for 1-2 days. The trigger threshold was set into the noise so that is was possible to observe the increased rate at low energies caused by accidentally triggered noise fluctuations.

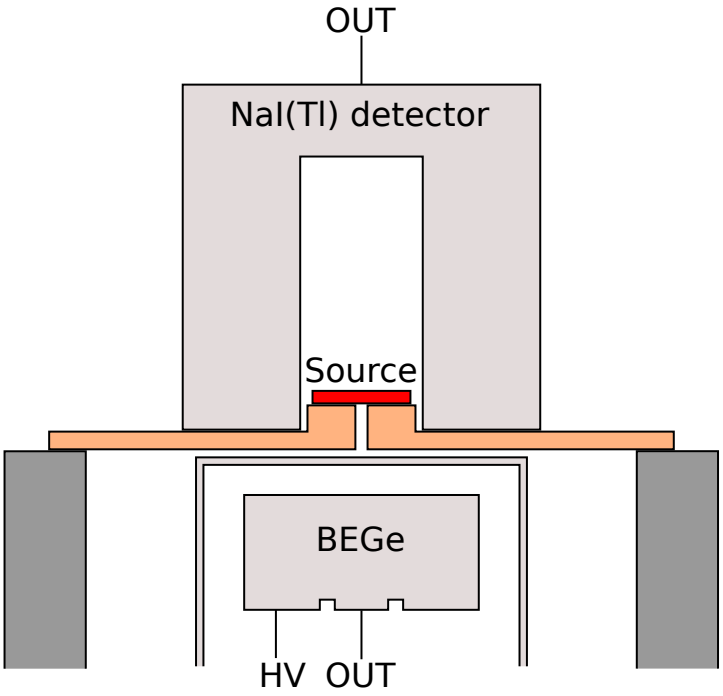

Figure 6.4: A schematic representation of the setup used for the coincidence measurement.

Neutron source

A ^{252}Cf source has been available in addition to the previously mentioned sources that emits in roughly 11% of all decays a neutron with an energy that follows a Maxwellian distribution and that has an average value of 2.3 MeV [107]. In the remaining cases it decays by emission of an α-particle at high energies ($\sim$ 6.2 MeV). Placing the source close to the detector will lead after a few days to the formation of a line at 10.37 keV. The only explanation for its appearance that could have been found in literature was proposed by the GEMMA collaboration in [15]. They suggest that the γ-line at 10.37 keV might be due to the capture of neutron by ^{70}Ge isotopes (natural abundance of roughly 21%), which creates ^{71}Ge. This is an unstable isotope that decays (half life $T_{1/2}$ = 11.4 days) by electron capture and the emission of a X-ray at 10.367 keV to ^{71}Ga. The line is particular useful to define the low energy properties of the detector. The line has been measured after roughly 3 days of irradiation with the ^{252}Cf source. Neutron capture takes place homogeneously throughout the detector volume, this distribution accordingly is similar to what one would expect from rare physics events.

Coincidence measurement

The static table has in additional a large volume NaI(Tl) detector mounted on the flat surface of the table. If required it can be moved over the cryostat end-cap that is placed in the center of the table. The NaI(Tl) detector is of coaxial shape with an external radius of 12 cm, an internal radius of 3.5 cm and a height of 30 cm (see Fig. 6.4). The NaI(Tl) detector is read out by 6 photomultiplier tubes embedded into the detector volume.

In the bore-hole of the NaI(Tl) detector a ^{133}Ba source has been placed. The emission

of a 356.0 keV γ-ray from that isotope is always accompanied by an immediate emission of an 81.0 keV γ-ray. This coincidental event can be exploited to better estimate the charge collection time in a detector. The NaI(Tl) detector has a faster detector response than a typical germanium detector (in the range of 100 ns). Accordingly if the 356.0 keV γ-ray is measured in the NaI(Tl) detector in coincident with a 81.0 keV γ-ray in the germanium detector the signal in the NaI(Tl) detector indicates the time of the energy deposition in the germanium detector close to the surface.

7 Investigation of filter performances

In order to achieve the best possible performance of a detector it is required to also use appropriate filtering methods. Unfortunately, there is no one-size-fits-all approach – the ideal filter parameters are strongly dependent on the data. In particular, the shaping filters must match the characteristics of the data otherwise the quality of the results will be suboptimal. In the following chapter some of the most vital dependencies will be addressed. The results will be used in subsequent chapters to compare the different point contact sizes. Furthermore, a detailed knowledge of the filter characteristics allows a measurement of the Fano factor, an important material property for many spectroscopy applications. This is done in the last part of this chapter.

7.1 Filter performance

A general expression for the equivalent noise charge was given in Eq. 4.20. Its form not only depends on the transfer function of the preamplifier but also the shaping filter that is used for its evaluation. The lower limit in resolution could be found by minimizing the equation describing the equivalent noise charge, however, in an experimental situation this solution rarely leads to the best result. Effects, such as ballistic deficits and incomplete charge collection, are not described within the framework of the equivalent noise charge. Thus the ideal choice of a filter strongly depends on the data that are analyzed and how well the filter performs in the presence of these effects.

Possible filter implementations have been proposed in Sec. 4.2. Most of these filters have not yet been discussed in literature and prior to using them for an analysis their most vital dependencies must be disentangled.

In order to analyze the impact of the various filter parameters, one particular measurement of Asterix in its Phase 2 configuration was selected. This measurement contains sufficient peaks in the energy range between 59.5 keV and 1460.8 keV.

7.1.1 Shaping time effects of the pseudo-Gaussian filter

The pseudo-Gaussian filter is commonly used in applications with γ-ray spectrometers and thus will be used as a reference for the discussion about filter optimization. The pseudo-Gaussian filter only has a single characteristic parameter – the shaping time. However, the filter can also be combined with the MSEC method described in Sec. 4.2.5. Therefore, a second parameter is introduced that defines if the MSEC method is enabled or not.

Fig. 7.1 illustrates how the resolution depends on the two parameters at 1332.5 keV. The energy resolution initially decreases with increasing shaping time, reaches a minimum and then increases. This behavior is due to electronics noise that was expressed in Sec. 4.1.6 as the equivalent noise charge. The equivalent noise charge is dominated by voltage noise at a short shaping time and by current noise at a long shaping time. The optimum shaping time is found at the position where the energy resolution is minimal and the two contributions are

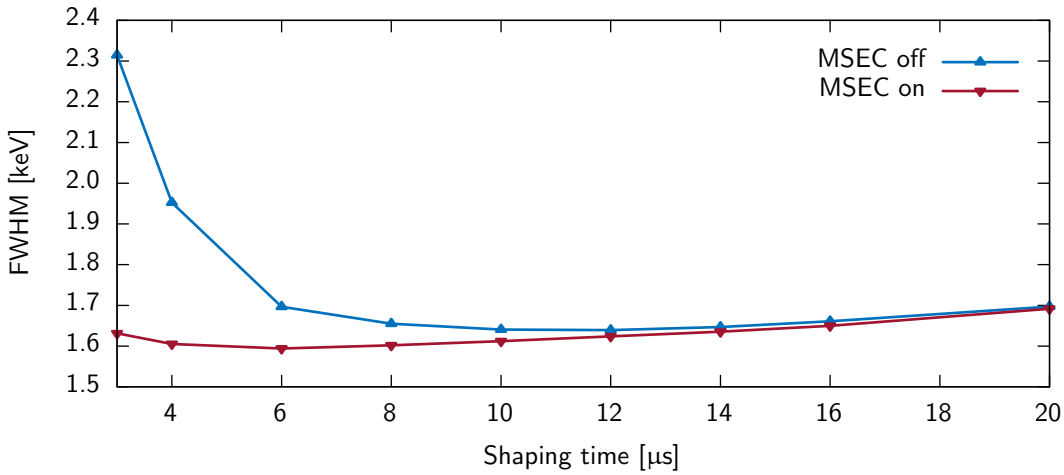

Figure 7.1: The energy resolution of the 1332.5 keV line as a function of the shaping time for the two situations MSEC enabled and disabled. The pseudo-Gaussian filter was used. Uncertainties are smaller than the markers and not indicated.

equal (the noise corner). Effects from ballistic deficits further broaden the resolution and shift the optimum shaping time and the minimal reachable energy resolution to higher values. The MSEC method corrects this effect and as displayed in Fig. 7.1 decreases the optimum shaping time from 12 µs to 6 µs. The energy resolution at 1332.5 keV also decreases by roughly 4% from roughly 1.67 to 1.61 keV. Consequently, the MSEC correction is a valuable tool to not only reduce the optimum shaping time but also decrease the energy resolution.

The top panel of Fig. 7.2 presents the curve that relates the resolution to the energy. At low energies the resolution is primary dominated by noise. With increasing energy the contribution from statistical fluctuations in the number of charger carriers increases until it dominates the energy resolution. Multi site events from Compton scattering are the most important reason for variations in the pulse shape in PCGe detectors and thus the most important cause of ballistic deficits. As has been displayed in Fig. 2.3, Compton scattering is surpassed by photoelectric absorption as the dominant interaction channel below 100 to 200 keV. With the disappearance of Compton scattering also effects caused by the ballistic deficit disappear. A correction of ballistic deficits therefore is mainly important at higher energies, which explains the differences between the curves with the MSEC enabled and disabled in the top panel of Fig. 7.2.

The bottom panel of Fig. 7.2 shows that above 400 keV the MSEC method improves the energy in average by roughly 50 eV. The improvement is not energy dependent. Below 400 keV the improvement quickly drops and below 200 keV the MSEC method actually increases the energy resolution. The summing operation of the MSEC method allows more noise to pass through the shaping filter and thus is responsible for the increased energy resolution. This increase becomes only noticeable at energies where ballistic deficit effects do not dominate. The MSEC method accordingly is not suited for the low energetic region.

A large shaping time is one way to correct for ballistic deficits. In the absence of any other correction, differences in the amount of ballistic deficit at different energies also render the optimum shaping time energy dependent. This effect is illustrated in the second panel of Fig. 7.2. The effect is reduced considerably if the MSEC is enabled, but not entirely removed.

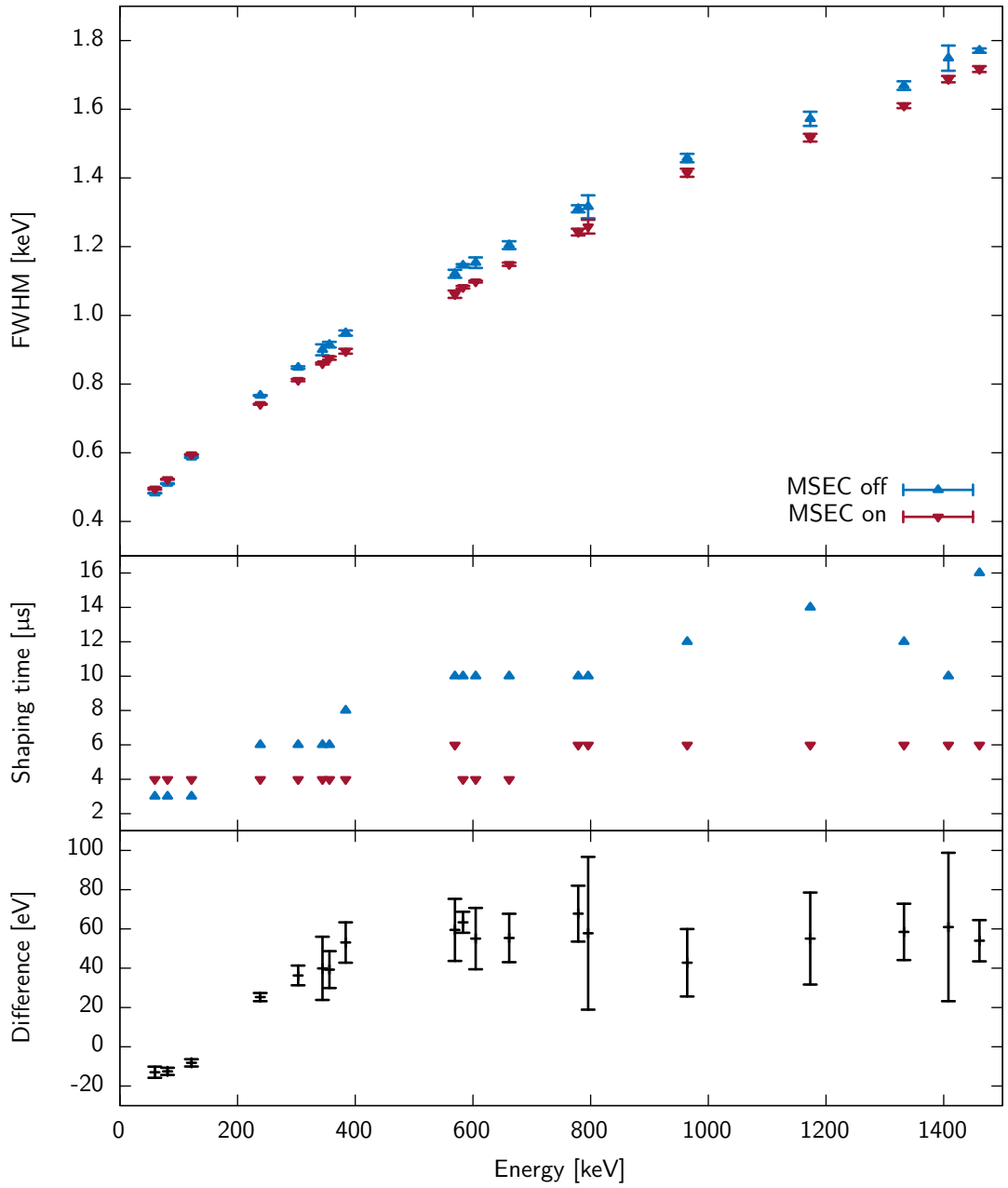

Figure 7.2: The energy resolution (top panel) and optimum shaping time (in the center) of the most prominent peaks in the measured spectrum. The pseudo-Gaussian filter is used. The bottom panel shows the difference between the resolution found with the MSEC enabled and disabled.

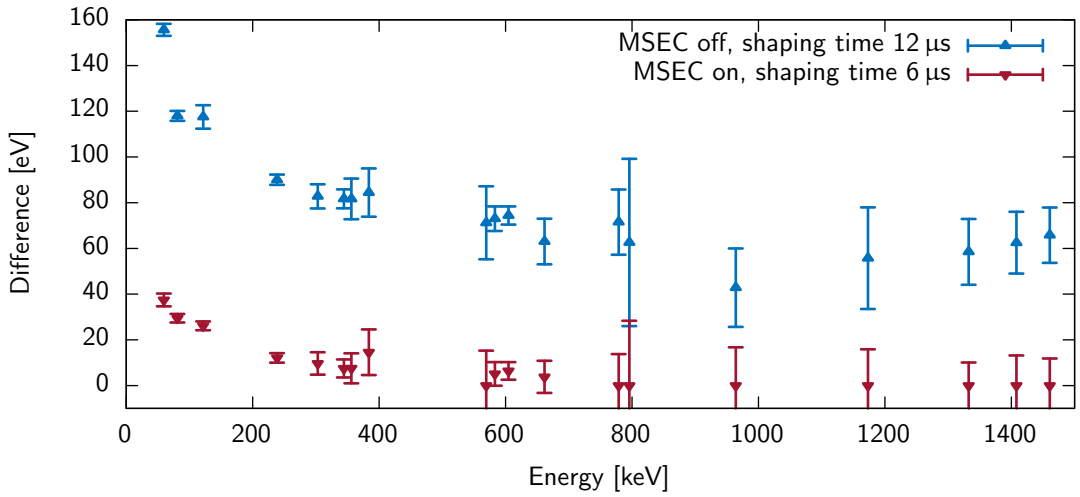

Figure 7.3: The energy resolution measured in a single spectrum processed with the pseudo-Gaussian filter (6 µs shaping time for MSEC enabled and 12 µs for MSEC disabled). The resolution displayed in Fig. 7.2 that was found with different shaping times at different energies is then subtracted from the energy found in that spectrum. This difference is indicated as a function of energy.

This suggest that the MSEC method is capable of removing an important fraction of the effects caused by ballistic deficits but not all of them.

In a typical analysis the shaping time optimization is not performed for each peak individually, but a single shaping time is chosen and the entire spectrum calculated with that shaping time. Most of the peaks therefore are not reconstructed with the most ideal shaping time and the minimum resolution is not obtained. Such an analysis has been performed for both situations, MSEC disabled and enabled. The shaping time that was used to reconstruct the spectrum was selected by finding the optimum value at 1332.5 keV (12 µs for the MSEC disable and 6 µs for the MSEC enabled). The spectra obtained with only a single shaping time is then compared to the resolution that was found when the shaping time was optimized at each peak individually. Fig. 7.3 presents the difference of the energy resolution obtained with a single shaping time and the value found with the optimum shaping time. The maximal deviation when the MSEC method is disabled is roughly 150 eV. When the MSEC method is enabled then the loss in resolution is below 40 eV. With the pseudo-Gaussian filter and the MSEC method enabled it is accordingly possible to analyze the entire energy range from 59.5 keV up to 1460.8 keV with a single shaping time without any important losses in resolution. Accordingly, the MSEC method is particularly important for an analysis that only uses a single shaping time over a large range of energies. This is the case for most applications in γ-ray spectroscopy.

7.1.2 Differences between filters

The pseudo-Gaussian filter is quite powerful, particularly in combination with the MSEC method. However, there are alternative filters that can be used. In Sec. 4.2 two additional filters have been introduced, one that is ideal in the absence of ballistic deficits and 1/f noise

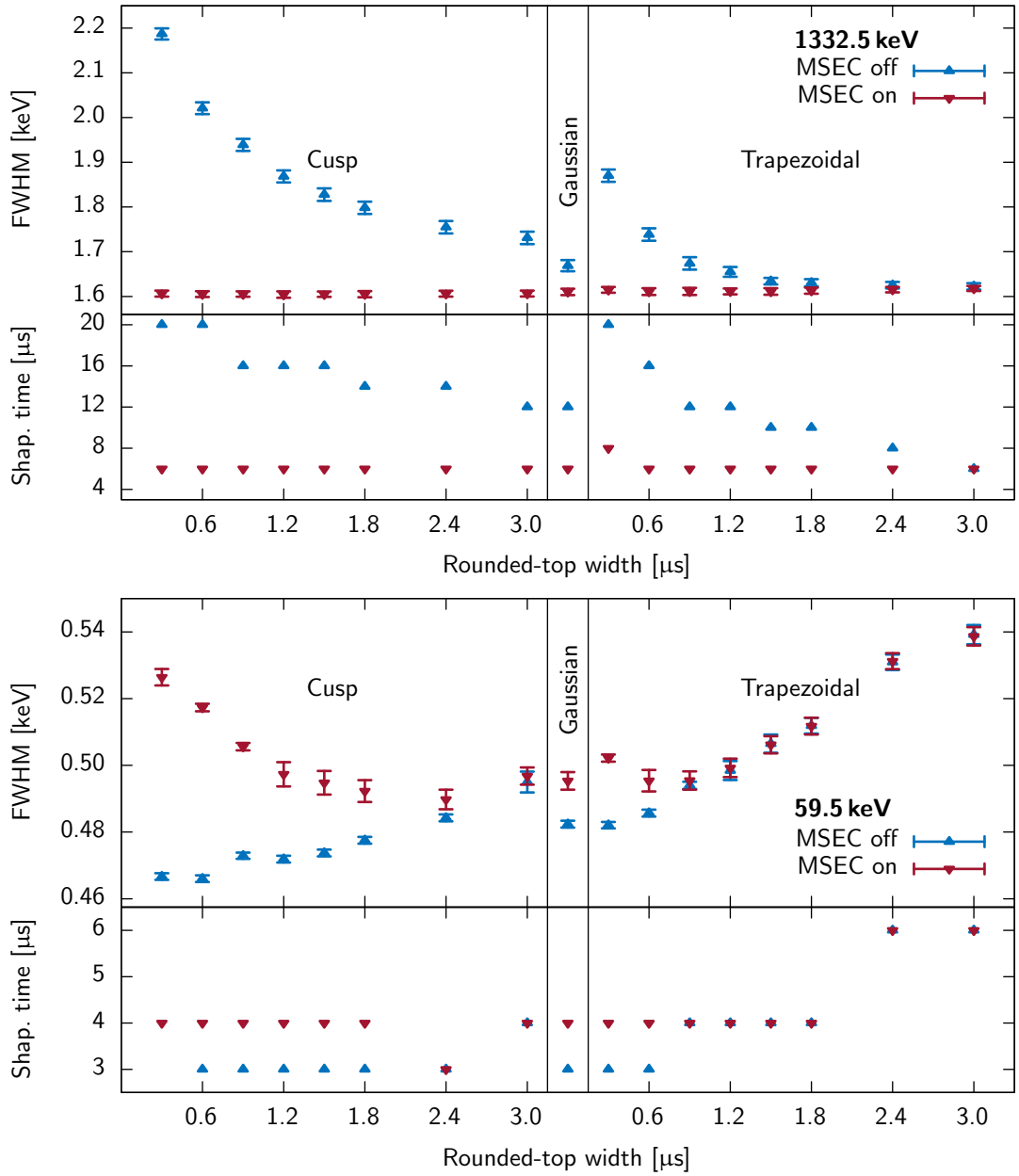

Figure 7.4: The energy resolution and the optimum shaping time of the 59.5 keV and the 1332.5 keV γ-ray lines for different filters. The x-axis value represents the width of the rounded-top. The spectrum was only analyzed for a few discrete values of the shaping time, uncertainties are thus not provided. Fluctuations in the optimum shaping time are however possible and caused by statistical fluctuations in the respective spectrum.

– the cusp filter – and one that is practical for situation with strong ballistic deficits – the trapezoidal filter. The two filters have not been proposed in their traditional form, instead additional moving average filters are used to bring the top portion of the filter into a round shape. These filters therefore have an additional parameter that controls the width of the rounded-top portion. Furthermore, these filters can also be combined with the MSEC method to improve their ability to remove ballistic deficit effects.

The lines at 59.5 keV of ^{241}Am and 1332.5 keV of ^{60}Co have been selected from the measurement used in the previous section to compare the performance of these two filters to the one of the pseudo-Gaussian filter. The respective data are presented in Fig. 7.4.

It was established in the previous section that above 400 keV ballistic deficit effects play an important role in PCGe detectors. This is expected to also be reflected in the filters performance at these energies. Indeed, at 1332.5 keV and with MSEC enabled all filters are similarly efficient and the differences between the filters are within the uncertainties. Also the optimum shaping time is found within a small range of values. In the energy range, where ballistic deficits dominate, the choice of a specific filter therefore does not matter much as long as MSEC is enabled.

The picture is different (still at 1332.5 keV) if ballistic deficits are not corrected and the real sensitivity of the filters to these effects appears. In that case, all filters require a high value for the rounded-top width to remove as much of the ballistic deficits as possible. Moreover, all filters have a tendency to slightly higher shaping times as this also helps to remove ballistic deficits. The rounded-top cusp filter is least suited to be used in the presence of strong ballistic deficit effects and even with a large rounded-top width it is not capable of matching the performance of the other two filters. The pseudo-Gaussian filter performs slightly better, however, the most ideal filter of the three is the rounded-top trapezoidal filter, which reaches a performance comparable to the situation with MSEC enabled. In this configuration, the trapezoidal filter also reaches the lowest value in the shaping time and it is thus the best choice if no MSEC can be used.

At 59 keV the situation is quite different. Here ballistic deficits are small, thus the MSEC method is not ideal and the obtained energy resolution when using the method worse or similar to the one found without the correction. With no ballistic deficits present the rounded-top cusp filter reaches its full noise reduction potential and thus the best performance of the three filters. Both filters with an adjustable rounded-top perform best when the rounded-top width is chosen small.

Some of the features that have been discussed in Sec. 4.2 on a theoretical level thus have been confirmed by data. The filter's behavior is tightly linked with the presence of ballistic deficit effects and their performance in reducing noise. When ballistic deficits are present it is vital to correct for these effects. Best suited to do this is the MSEC method, but also a rounded-top trapezoidal filter can be used. In the absence of ballistic deficits (i.e. at low energies) a cusp filter (with a small rounded-top width) should be used as this is the most ideal filter when it comes to noise reduction. It is however important to note, that because of its slow falling form, the cusp filter requires a much larger signal range and is not very suited for high count rate measurements.

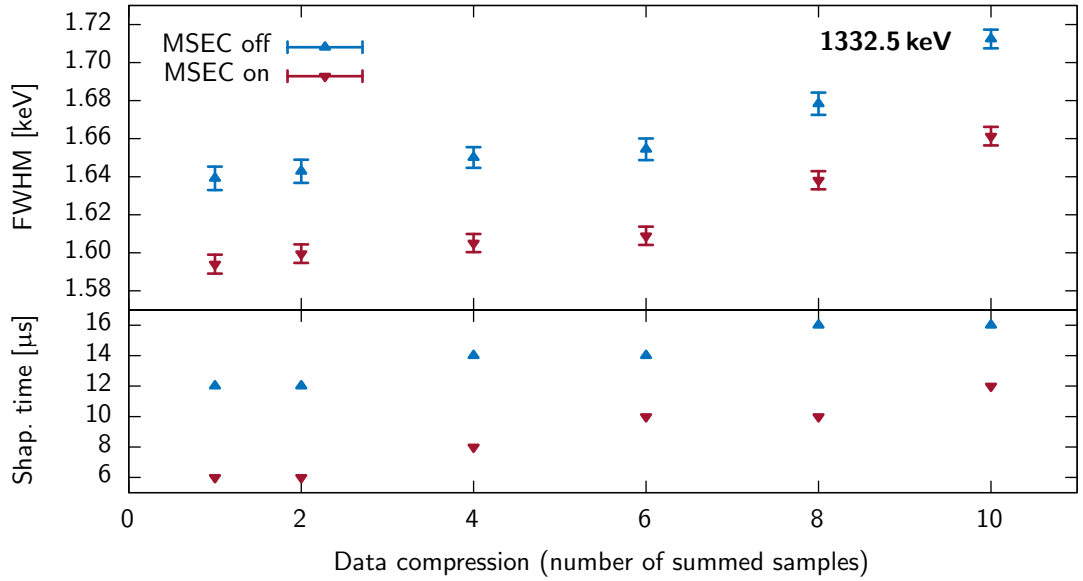

Figure 7.5: The effect of data compression on the energy resolution and optimum shaping time of the 1332.5 keV γ-ray line. The compression value describes the number of samples that are summed up prior to filtering.

compression	1	2	4	6	8	10
initialization [hours:min]	02:47	01:42	01:10	01:07	01:09	01:02
filtering [hours:min]	01:30	00:50	00:30	00:22	00:20	00:18
filter rate [events/sec]	7002	12676	21048	27691	31385	34147
data input [MB/sec]	67	121	200	264	299	325

Table 7.1: Benchmark of a typical analysis for different data compressions (compression of 1 means uncompressed). Indicated are only the CPU (user) time, the system time (used for I/O operations) is compression independent and roughly 20 min for the initialization and 17 min for the filtering. The size of the data set was roughly 355 GB which corresponds to 38 million events.

7.1.3 Data compression

There is an additional filter parameter that was not discussed so far – data compression. This parameter is not intended to improve the energy resolution of an analysis but to accelerate the analysis of large data sets. This can be done by compressing the input signals before filtering by averaging over a certain amount of samples. While most analysis programs (e.g. GEANA) perform calculation in double precision (64 bit), the data sets often have a much lower encoding defined by the FADC (i.e. 16 bit for this analysis). By summing up samples, the sampling frequency is reduced, but the number of possible quantization levels is increased. Therefore, data compression does not have to lead to a loss in energy resolution.

In Fig. 7.5 the energy resolution of the 1332.5 keV line is plotted for different compressions. It can be seen, that the loss in energy resolution for a compression of 2 - 6 is not significant for the measured data set, only for higher compression the energy resolution is increasingly degraded. The same figure also points out that there is a strong correlation between shaping time and compression: the higher the compression the larger the optimum shaping time. So, for data at a high event rate the compression factor can be of importance.

Furthermore, compressing the data before filtering also will affect the behavior and efficiency of the different filters. The effect of compression is to converge the pulse response of the different filters and thus differences in their performance are reduced. At high compression the filter thus perform similarly well.

The time required to analyze the entire data set of the mixed source measurement that was used to study the filter performance in the previous sections was measured for the analysis software GEANA at different compression parameters. The runtime was split up into the filter initialization time, which is the time required to evaluate all necessary filter parameters as described in Sec. 4.3.1 and the data filtering time, which is the time required to filter the entire data set once. For the optimization step, 10 different shaping times and 2 choices for the MSEC parameter (on/off) were tested. Event list generation was disabled for the data filtering, so that the processing time is not dominated by the write speed of the system. The analysis was run on a single Intel Xeon E5-2660 2.2 GHz CPU.

Table 7.1 lists the results of this comparison study. There is an important reduction in the execution time going from uncompressed to a compression of 2 and 4 for both the filter initialization and the data filtering. Further compression only slightly reduces the execution time. The table also points out that GEANA can process 7 k events per second on a single CPU, compressed even up to 34 k per second, once all filter parameters are defined. It demonstrates the efficiency and speed of the implemented filter methods and proves that the software meets the requirements of a fast data verification tool kit. However, the high demands on the data input (up to 325 MB/s) illustrate also the limitation of the approach taken with GEANA.

For most applications the trade off in energy resolution is negligible compared to the speed up of the program, hence compression is a powerful tool to reduce computation time, without affecting the data quality. However, in the following section it is necessary to run the analysis at the best possible filter performance, thus the data have not been compressed prior to filtering.

7.2 Measurement of the equivalent noise charge

The resolution of an electronic system usually is measured with a high resolution pulser, that is inserted into an input (often a separate test input) to the system and analyzed at the output

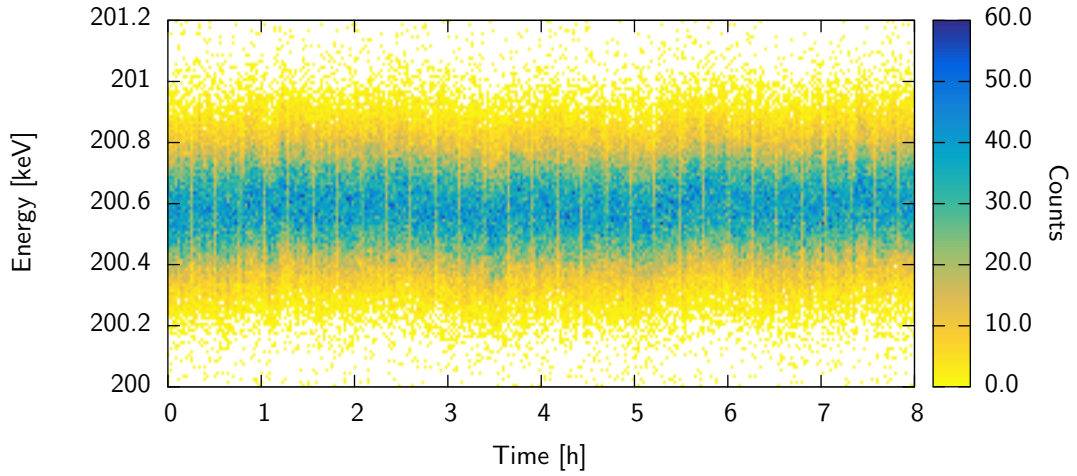

Figure 7.6: The pulser peak at roughly 200 keV in a measurement over a few hours. Some drifts are visible in the pulser peak. The breaks in the data are caused by the program saving the data to the server.

with the same procedure that usually is applied to signals from the detector. It thus is the experimental substitute to the equivalent noise charge, which has been theoretically derived in Sec. 4.1.6.

The pulser has its own intrinsic resolution, which often strongly is affected by environmental parameters and hence fluctuates in time (see Fig. 7.6). Thus the resolution measured at the output is often not only given by the resolution that can be reached with the electronic system, but also contains traces from the pulser uncertainties.

In what follows, a novel method will be introduced that allows to extract the electronics resolution (equivalent noise charge) directly from the data collected with a FADC system and thus does not require a special pulser measurement. This method is also not sensitive to uncertainties of the pulser and should therefore be more reliable than the standard analog pulser method. To the authors knowledge this method has not yet been described in literature.

7.2.1 Software generated pulser signals

A typical signal from a germanium detector is usually stored to disk in such a way, that there are sufficient samples before and after the actual charge pulse. The data taken in this work feature a range of 164 µs with the charge pulse being roughly placed in the center. The samples in front of the charge pulse (the baseline) are important to remove the DC offset of the system prior to filtering. The samples after the charge pulse (tail) are important to measure the decay time of the charge sensitive preamplifier. Most of the time there is no signal from the detector present in the baseline and the fluctuations of the samples in that region are only caused by electronics noise. Thus these samples are the perfect playground to study the noise properties of the electronics system.

The equivalent noise charge can be measured by adding a pulser like signal to the baseline. In the simplest case the added pulse consists of a fast rising edge (step function) that is followed by an exponential decaying tail. The decay time of the tail can be extracted from measured

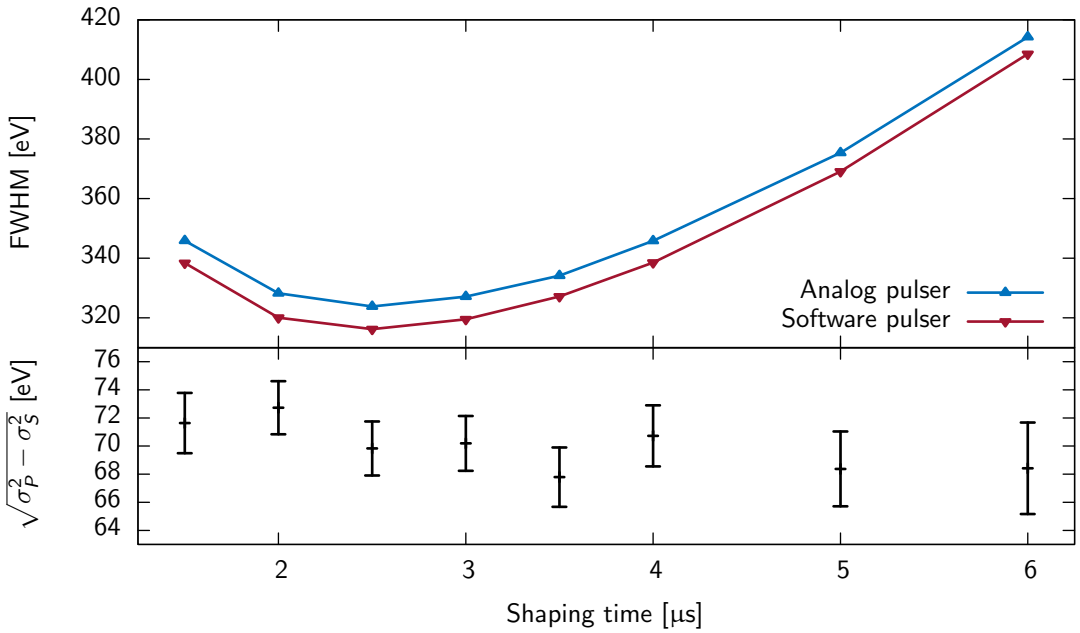

Figure 7.7: The analog pulser (at the test input of the preamplifier) and the software generated pulser compared at different shaping times. The most ideal filter at 59.5 keV has been used (cusp with 0.3µs rounded-top width and MSEC disabled). The baseline is of the same length for both the analog and software pulser. In the lower panel σ_S is the resolution of the simulation and σ_P of the pulser (FWHM). Uncertainties in the top panel are smaller than the markers and not indicated.

detector pulses and then used for the generation of a pulser like signal. This artificially created pulser signal is then analyzed with the shaping filter in analogue to the signals measured from the detectors. The width of the peak that is observed in the spectrum due to this added signal corresponds to the equivalent noise charge of a given electronics system analyzed with a particular shaping filter.

This method can not give a realistic representation of nonlinearities of the system. The pulser is only simulated at a single energy and thus only sensitive to a small region where nonlinearities can be neglected.

7.2.2 Software versus analog generated pulser

The described method was applied to a measurement with an analog pulser (at roughly 200 keV) connected to the test input while the detector was irradiated with a ^{241}Am source. A software generated pulse has been added to the baseline of the signals and the resulting resolution compared with the resolution from the pulser signal observed in the data. This can be seen in the top panel of Fig. 7.7 as a function of the shaping time. There is an offset between the two measurements, however the lower panel in Fig. 7.7 shows that the offset is shaping time independent and roughly 70 eV (0.04% of the pulse height) in size. In Fig. 7.6 it can be seen that there are some drifts in the pulser position of that measurement. The offset can be easily explained by these fluctuations of the pulser. The value found by the method is accordingly not affected by pulser drifts. Different filters and other data are in good agreement

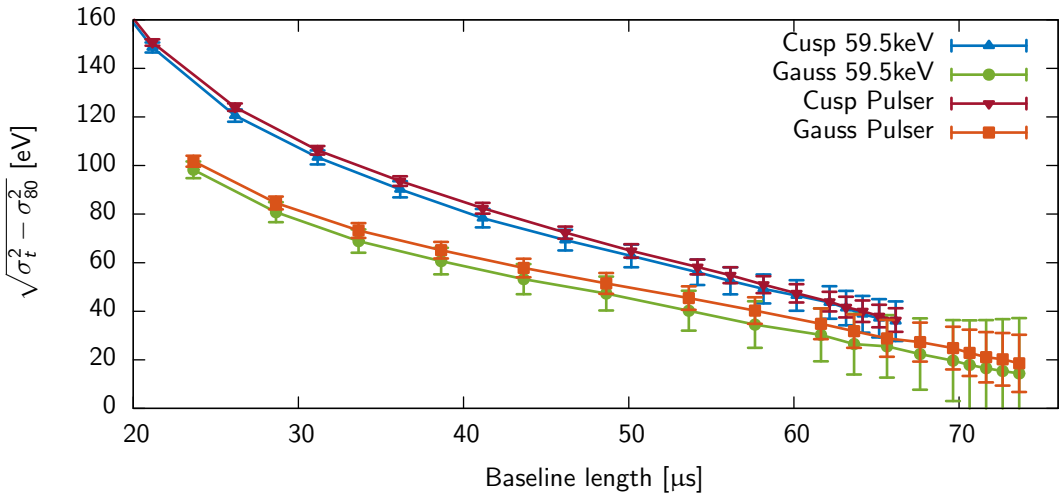

Figure 7.8: The baseline reconstruction noise as a function of the length of the available baseline. The noise that emerges because of a suboptimal baseline reconstruction is calculated from the best resolution σ_{80} at a baseline of 80 µs and the resolution at a reduced baseline σ_t. The filters are chosen with a shaping time of 2.5 µs and a rounded-top width of 0.3 µs for the rounded-top cusp filter.

with the presented plot, which means that the value is a meaningful value for the equivalent noise charge.

7.2.3 Baseline shortening

A good reconstruction of the baseline offset is an important ingredient for a good reconstruction of the pulse height of the signal (see Ref. [108] and the references therein for a detailed discussion of baseline effects). The uncertainties related to the baseline offset can be handled as an additional source of noise and it should therefore add in quadrature to the total resolution of the setup. The baseline reconstruction is performed prior to filtering, in a range before the charge pulse, thus it should not be affected by details of the pulse shape and the filter and so it can not dependent on the energy.

The method that simulates a pulse in the baseline only allows for a limited amount of baseline before the simulated signal and thus the quality of the baseline offset reconstruction will be decreased. First, the baseline available is only roughly half of the entire signal length. This is furthermore reduced as the shaping filter must be executed within a certain window around the pulse and thus the software generated pulse must be placed at a certain distance from the center of the signal to avoid overlaps. The rounded-top cusp filter requires a window of at least 8-10 times the shaping time to reach a good energy resolution (the pulse response only drops of slowly towards the edges), the trapezoidal and pseudo-Gaussian filter require 4 times the shaping time.

The effect of the baseline reduction is studied with actual data where 80 µs of baseline are available before the pulse. Fig. 7.8 shows the results for the pulser peaks at 200 keV and the 59.5 keV γ-ray line. It can be seen that, as expected, the amount of additional noise in the system increases if the baseline is reduced. The dependence of the pulser peak and the

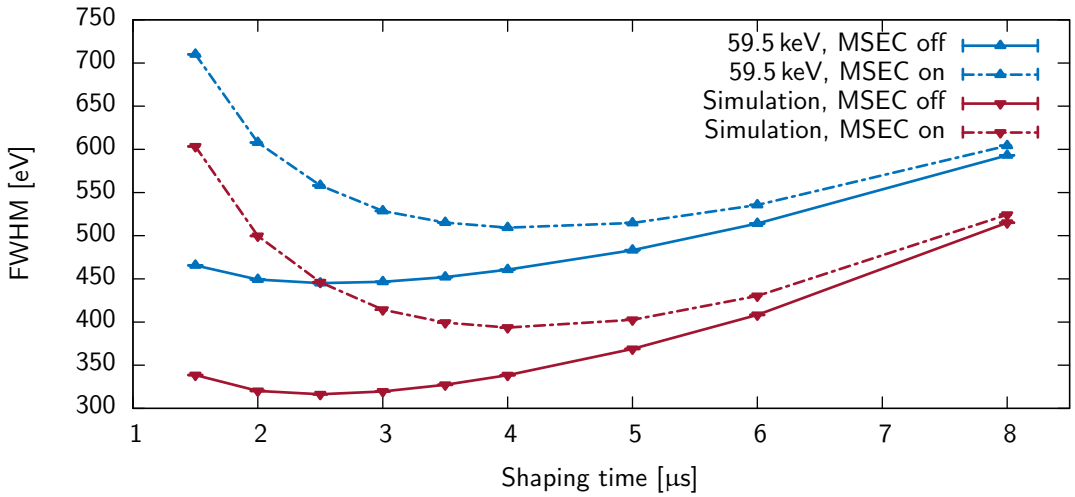

Figure 7.9: The resolution as a function of the shaping time for the 59.5 keV γ-ray line with MSEC disabled and enabled. In addition a pulse in the baseline has been simulated with an average shape of a pulse in the 59.5 keV γ-ray line.

59.5 keV γ-ray lines are very similar which shows that the noise introduced by an insufficiently reconstructed baseline offset is not affected by details of the pulse shape. Thus, if the noise that is added due to an insufficiently reconstructed baseline is known for a specified filter at one energy then the same amount of noise is induced at all the other energies as well.

The noise depends on the filter that is used. The reason for this is that the ranges used for the baseline offset reconstruction and the filtering actually overlap. The rounded-top cusp filter requires a larger filter window and therefore has a larger overlap with the baseline range and therefore is more susceptible to the baseline reconstruction compared to the pseudo-Gaussian or rounded-top trapezoidal filter. The later one was omitted in Fig. 7.8 but follows exactly the behavior of the pseudo-Gaussian filter.

As previously mentioned, the baseline noise adds in quadrature to the contributions from other sources that broaden the peak. However, none of the analysis presented within this thesis actually is affected by the additional baseline noise. The effect either is corrected by measuring the baseline noise at a certain energy and then subtracting it from the measurement, or it cancels such as in the analysis of the Fano factor, presented in Sec. 7.3.1.

7.2.4 Special consideration for the MSEC method

The MSEC method involves a nonlinear operation that sums up samples in the pulse depending on its width. This filter can not be used directly with a pulser as the response of the filter to a pulser signal is not the same as for a typical detector signal. This applies to both, an analog pulser signal fed into the test input of the preamplifier and a software generated pulser in the baseline.

The situation can be approached by finding the average pulse shape of a certain peak by summing up all pulses in that peak and then use this average pulse to simulate a signal in the baseline. The procedure was applied to the 59.5 keV γ-ray line in Fig. 7.9. It can be seen that in both cases, the simulation as well as the actual measurement, the MSEC method leads to

Croft [61]	Lowe [109]	Lepy [110]	Papp [111]	Wiens[112]	Harkness [98]
0.112 ± 0.001	0.1057 ± 0.0002	0.0953 ± 0.0005 0.1084 ± 0.0008	0.05-0.082	0.095 ± 0.006	0.099

Table 7.2: A few selected values for the Fano factor from recent measurements.

an increased resolution and a higher shaping time. This effect has been mentioned previously in Sec. 7.1.1 and is caused by the summing operation that is part of the MSEC algorithm. Fig. 7.9 shows that using the average pulse indeed reproduces roughly what has been observed for the MSEC method enabled in the data. However, at low shaping times the simulated curve increases faster than the data. This shows that an estimation of the equivalent noise charge of an analysis with the MSEC enabled must be considered with care. Studies that involve an estimation of the equivalent noise charge (either coming from actual data or a simulation) should avoid the usage of the MSEC method.

7.3 Fano factor

Above about 100 keV the energy resolution of a PCGe detector is not dominated by noise but by charge carrier statistics and thus the Fano factor. It is therefore surprising that the exact value of the Fano factor in germanium still seems to be an open issue. In 1970 Zulliger [113] considered the matter as basically settled with theoretical models and experimental measurements converging on a value around 0.05. However, with the introduction of HPGe detectors it became clear that the extrapolation to infinite charge collecting field conditions used by many earlier authors underestimated the Fano factor. In 1991, Croft measured a value of 0.11 and asked for more measurements to finally settle the matter [61]. However his call remained mostly unheard. Only recently, the interest in the Fano factor has been revived and a few new studies [98, 110, 112] published that found values in agreement with Croft (see Table 7.2). However, there are also other authors that measured much lower values, particularly in the energy region below 20 keV [111]. Some basic consideration about the origin of the Fano factor have been discussed in Sec. 2.3.2. The intention of this section is to follow Crofts call for more measurements and use a few selected data of good quality to perform such an analysis.

7.3.1 Analysis procedure

Neglecting any loss in energy resolution that is due to incomplete charge collection, the Fano factor is expressed as:

$$F = \frac{(\sigma_T^2 - \sigma_N^2)}{E\epsilon}, \tag{7.1}$$

where σ_T is the energy resolution (variance not FWHM) of a γ-ray line at an energy E and σ_N the equivalent noise charge observed with the same filter configuration as used to measure the γ-ray line. The average energy required to create an electron-hole-pair ϵ has been measured for germanium and was found to be 2.96 eV, which will be used throughout this dissertation.

Eq. 7.1 states that to measure the Fano factor at a given energy it is required to know the equivalent noise charge at a given energy. Often an additional pulser measurement is used. However, it has been seen in the previous discussion that it can not be assured that the pulser is stable over a sufficiently long time scale. Thus it is more convenient to use the procedure

describe in Sec. 7.2 that finds the equivalent noise charge directly from a given data set, not requiring a pulser being present. The equivalent noise charge must be calculated with the same method that is also used for the analysis of the data. However, it only can make use of a restricted amount of the total baseline. Accordingly, the baseline of the measured data must be restricted to the same length as the range available for the equivalent noise charge simulation. The effect of a reduced baseline affects both, measurement and extraction of the equivalent noise charge in the same way. The effect accordingly cancels when calculating the Fano factor.

Tailing effect in a peak are of different origin than the Fano factor (mostly from ballistic deficit and incomplete charge collection). The tails should therefore not be included into the energy resolution that is used for calculating the Fano factor. Instead the equation that has been described in Sec. 4.2.7 is used for fitting the peaks and only the variance of the Gaussian term taken for the analysis.

The evaluation of the Fano factor has been performed with the data set used in Sec. 7.1, however, was reduced to the most prominent γ-ray lines (more than 10^5 counts in the peak). Weak lines introduce strong uncertainties when it comes to the calculation of the Fano factor (because of the subtraction of two squared resolutions) and it is more reliable to exclude them. The entire data set has been processed for any possible combination of the pseudo-Gaussian, rounded-top cusp and trapezoidal filter (a selection of rounded-top width was used) and a variety of shaping times (2-14 µs). The MSEC method was disabled. For each combination of filter parameters the equivalent noise charge has been additionally found with the new procedure outlined in Sec. 7.2 (software generated pulser). From Eq. 7.1 it is then possible to calculate the Fano factor for a given γ-ray line.

7.3.2 Energy dependence of the Fano factor

The Fano factor is a constant defined by material properties and thus should not be dependent on the filter that is used for the energy reconstruction. Nonetheless, if the filter is not ideal it will leave artifacts in the peak shape that must be disentangle from the contributions of charge carrier statistics. Particularly effects, such as ballistic deficits, that do not affect the measurement of the equivalent noise charge in the same manner as the γ-ray line introduce systematic uncertainties. This problematic can be avoided by choosing a filter that reduces these effects sufficiently so that they can be neglected. The filter with the lowest FWHM (including contributions from the tail) has therefore been chosen for each γ-ray line separately to be used in the measurement of the Fano factor. The minimization of the FWHM assures that the filter does neither produce strong tails nor a large variance in the peak.

The evaluation of the Fano factor depends on an exact measure of the equivalent noise charge, thus the MSEC method should not be used and was disabled for the entire analysis.

The Fano factor as a function of energy is plotted in Fig. 7.10. There seems to be a slight energy dependence, thus, a function of the form $F(E) = A + B \cdot E$ was fitted to the data. Indeed this fit is slightly better ($\chi^2/\mathrm{dof} = 4.6$, with dof being the number of degrees of freedom) than if the Fano factor is assumed to be a constant ($\chi^2/\mathrm{dof} = 4.7$). The latter finds an value of 0.1076 ± 0.0005 for the Fano factor.

An energy dependent Fano factor has previously been observed in silicon [62] but not yet been confirmed by other independent measurements. Moreover, in the absence of a good model for the physics behind the Fano factor such an dependence can not be excluded. Therefore, the

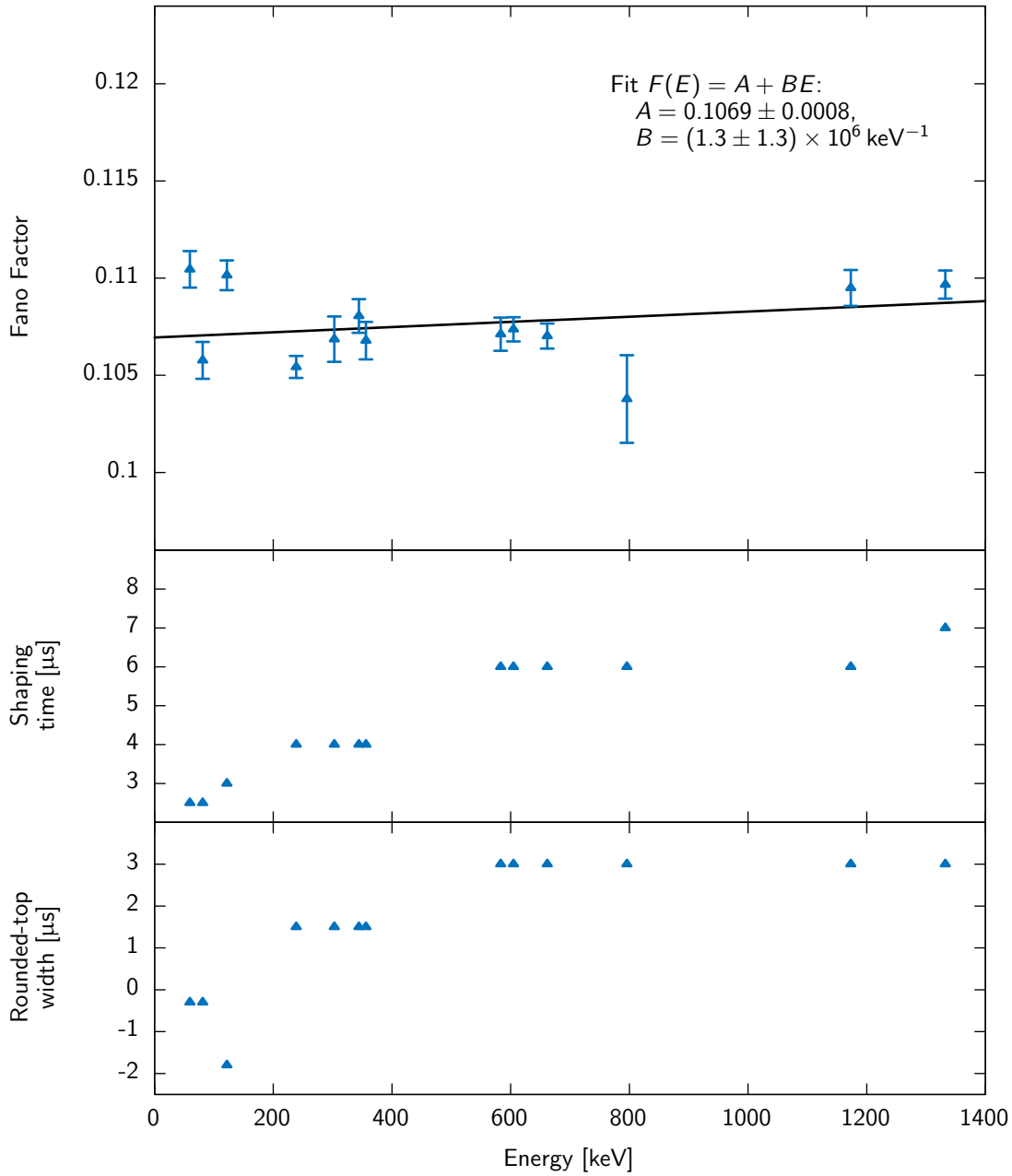

Figure 7.10: The measured Fano factor for the different γ-ray lines. The shaping time and the width of the rounded-top (negative values correspond to the cusp, positive values to trapezoidal and zero to the pseudo-Gaussian filter) are indicated for each line separately.

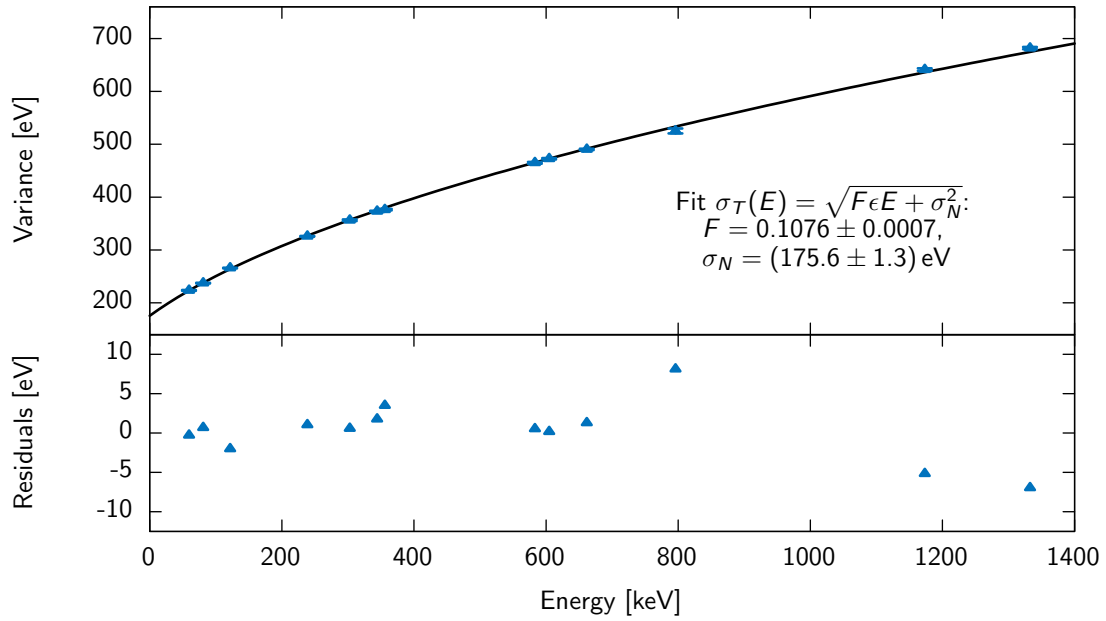

Figure 7.11: A global fit to the energy resolution (here the variance not the FWHM) of a mixed source measurement. The filter used is the trapezoidal filter with a top width of 3 µs and 6 µs shaping time (MSEC disabled).

measured energy dependence can indeed have a physical background and must not be entirely due to systematic effects. The difference between the two models however is small and thus there is no conclusive evidence for an energy dependence.

In addition, the χ^2/dof is large, which hints that there are some systematic effects that are not entirely considered. The most probable origin of unconsidered systematics is the fitmodel that has been used. This often does not perfectly describe the data, especially in the region above and bellow the peak. The spectrum in that region can be polluted by contributions from other γ-ray lines and thus not follow the model used in the fit. When it comes to finding the resolution of the peak these deviation can affect the final value considerably.

7.3.3 Global fit of the energy resolution

When the same shaping time is used for all peaks in the spectrum, then also the noise resolution at each line must be constant. The noise can then be handled as an additional fit parameter and the energy dependence of the energy resolution fitted with Eq. 4.28.

The MSEC method affects the equivalent noise charge differently for different peak, thus it can not be used in this study. Instead, the rounded-top trapezoidal filter with a rounded-top width of 3 µs is used. It has the best performance in the presence of ballistic deficit effects, however, it is not very good when it comes to noise reduction. At low energy, compared to other filter, more of the noise will remain. This however, should not effect the measurement of the Fano factor as it increases both the resolution of the noise (equivalent noise charge) and the energy resolution in the same way.

The results of a fit over the entire energy range are presented in Fig. 7.11. The value for the

Fano factor of 0.1076 ± 0.0007 is identical to the value evaluated in the previous section. The $\chi^2/\text{dof} = 3.8$ for the global fit is better as for the energy dependent fits. This measurement seems therefore to be less affected by certain systematics.

The presented study strongly suggests that a Fano factor close to the value found by Croft is most likely to be correct. Both method that have been presented found a value in good agreement with each other and close to the value found by Croft. Although there is a hint that the Fano factor might be energy dependent the trend is not compatible with a value in the range around 0.05-0.08, even at very low energies. A possible explanation for the low values, particularly at low energies, found by some studies might be a pulser measurement with slight drifts. If these effects are not carefully monitored it is easy to overestimate the pulser resolution and thus find a much lower value for the Fano factor. This is particularly true at low energy, where the resolution is dominated by noise, not the Fano factor. In the energy range that has been studied the contribution from statistical fluctuations in the number of charge carriers dominates. Thus, the a value found in that range is less prone to systematics.

8 Results from the point contact size study

This chapter will present the results from the characterization measurements of the two detectors – Asterix and Obelix – that were introduced in Sec. 5.2. These two detectors have been modified by changing the point contact size and the width of the groove. Asterix was characterized in three configurations, Obelix only in two. Some of the studied objects have been introduced in the previous chapter. The remaining topics will be briefly explained before the results on the different point contact sizes are presented.

8.1 Energy resolution

The energy resolution is one of the most important characteristics of a germanium detector. As discussed in the previous chapter, at low energies electronics noise has an important impact on the energy resolution. Thus, the reduction of the point contact size should also translate into an improvement in energy resolution. The resolution at high energies is dominated by statistical fluctuations and not electronics noise. However, the size of the point contact is affecting the pulse shape and with changes in the pulse shape the intensity of ballistic deficits changes, thus introducing variations in the resolution. This effects are small, strong deviations between different point contact sizes therefore hint that the detector is not functioning properly.

This section discusses these aspect by comparing the energy resolution of the γ-ray line at 59.5 keV of ^{241}Am, the 1332.5 keV line of ^{60}Co and the 2614.5 keV line of ^{228}Th for the different point contact sizes of the two detectors.

8.1.1 Low energy region (^{241}Am)

It has been established that at 59.5 keV ballistic deficits are small and do not need to be corrected (see Sec. 7.1.1). Therefore, the MSEC method for the analysis of the ^{241}Am data was disabled. Furthermore, in Sec. 7.1 it was found that the rounded-top cusp filter with a rounded-top width of 0.3 µs performs best of all the presented filters. This filter was accordingly selected for the analysis of the measurements presented in this section.

The optimum shaping time is fixed through the evaluation of the noise corner, the shaping time at which the resolution takes the lowest value. The respective curves are shown in Fig. 8.1 for the different detector configurations. The noise corner is shifted with each change in point contact size to a lower shaping time. This reflects a reduction in voltage noise which directly is affected by the capacitance of the detector. The energy resolution improves for both detectors between the first and second configuration. The improvement is smaller after the last reprocessing step of Asterix.

In Fig. 8.2 the shape of the 59.5 keV line in the up to three configuration is shown. Although important in number, on a logarithmic scale, the differences between the configurations are relatively small. The peaks follow nearly a Gaussian distribution, however, in the second and third configuration there are also small tailing contributions. The amplitude of the tail

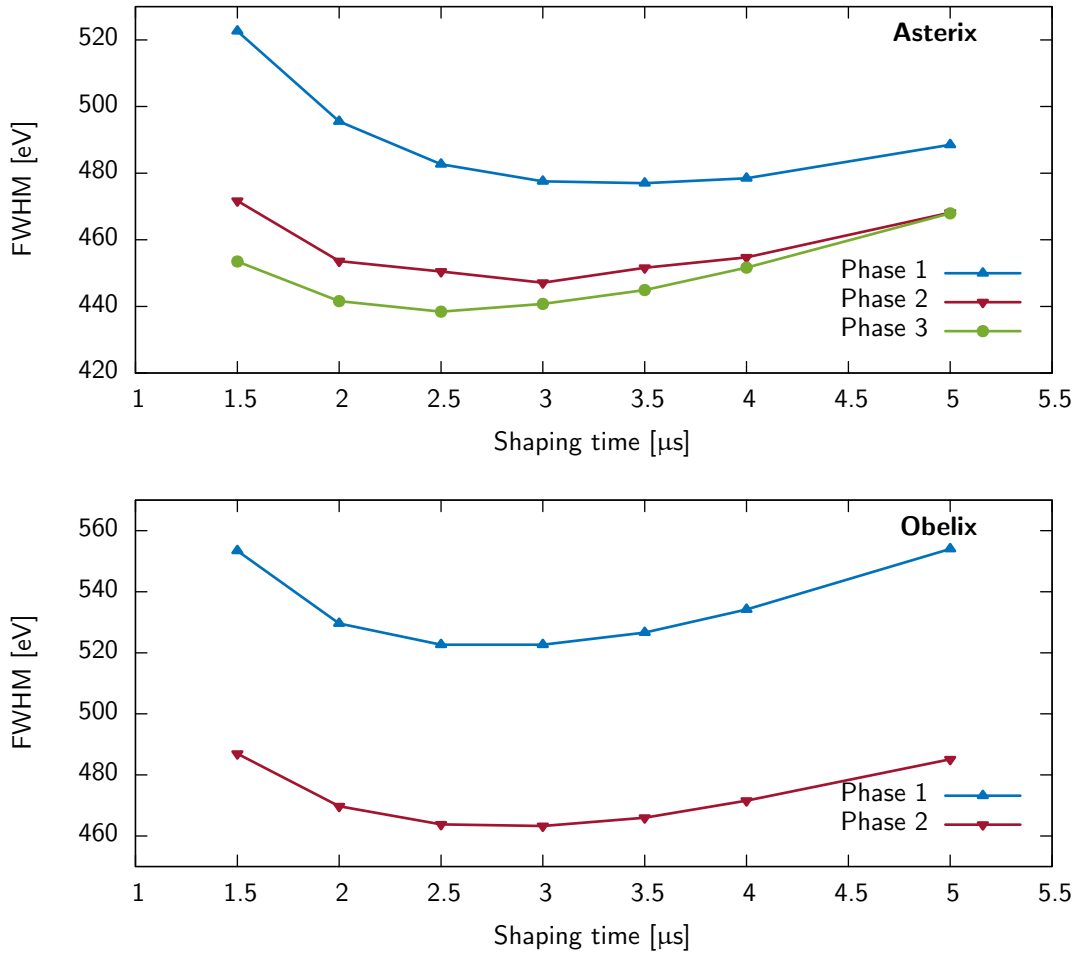

Figure 8.1: The energy resolution of the 59.5 keV γ-ray line as a function of the filter shaping time (rounded-top cusp with a rounded-top width of 0.3 µs) for Asterix (top panel) and Obelix (bottom panel). The uncertainties are small compared to the size of the markers and omitted.

Detector	γ-ray line [keV]	Config.	Filter, MSEC, top width [µs]	Opt. Shaping time [µs]	Resolution FWHM [keV]
Asterix	59.5	Phase 1	cusp, off, 0.3	3.5	0.477 ± 0.001
		Phase 2	cusp, off, 0.3	3.0	0.447 ± 0.001
		Phase 3	cusp, off, 0.3	2.5	0.438 ± 0.001
	1332.5	Phase 1	cusp, on, 1.8	4.0	$1.571 \pm 0.007 \pm 0.008$
		Phase 2	cusp, on, 1.8	4.0	$1.572 \pm 0.004 \pm 0.003$
		Phase 3	cusp, on, 1.8	8.0	$1.595 \pm 0.004 \pm 0.004$
	2614.5	Phase 1	cusp, on, 1.8	8.0	$2.370 \pm 0.008 \pm 0.008$
		Phase 2	cusp, on, 1.8	8.0	$2.326 \pm 0.008 \pm 0.003$
		Phase 3	cusp, on, 1.8	8.0	$2.330 \pm 0.008 \pm 0.005$
Obelix	59.5	Phase 1	cusp, off, 0.3	2.5	0.521 ± 0.001
		Phase 2	cusp, off, 0.3	3.0	0.461 ± 0.001
	1332.5	Phase 1	cusp, on, 1.8	8.0	$1.712 \pm 0.008 \pm 0.004$
		Phase 2	cusp, on, 1.8	8.0	$1.702 \pm 0.011 \pm 0.006$
	2614.5	Phase 1	cusp, on, 1.8	8.0	$2.637 \pm 0.007 \pm 0.015$
		Phase 2	cusp, on, 1.8	10.0	$2.586 \pm 0.007 \pm 0.009$

Table 8.1: The energy resolution (FWHM of Gaussian plus tails) for various γ-ray lines measured with the two detectors in their different configurations. The first uncertainty of the FWHM is from the fit. The second uncertainty comes from variations between different filters at higher energies that all produce very similar results (only values from the rounded-top cusp with a rounded-top width of 1.8 µs are provided). At 59.5 keV only one filter has been studied (rounded-top cusp filter with a rounded-top width of 0.3 µs) thus there is no systematic uncertainty coming from the selection of a particular filter.

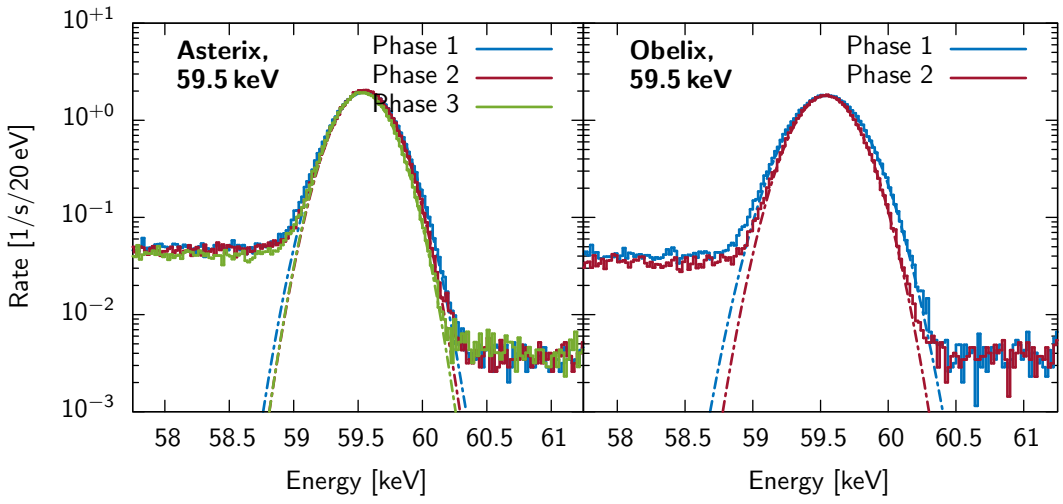

Figure 8.2: The 59.5 keV γ-ray line in the different configurations of the two detectors. The tails below the peak are below the uncertainties and thus were not considered during the fit procedure.

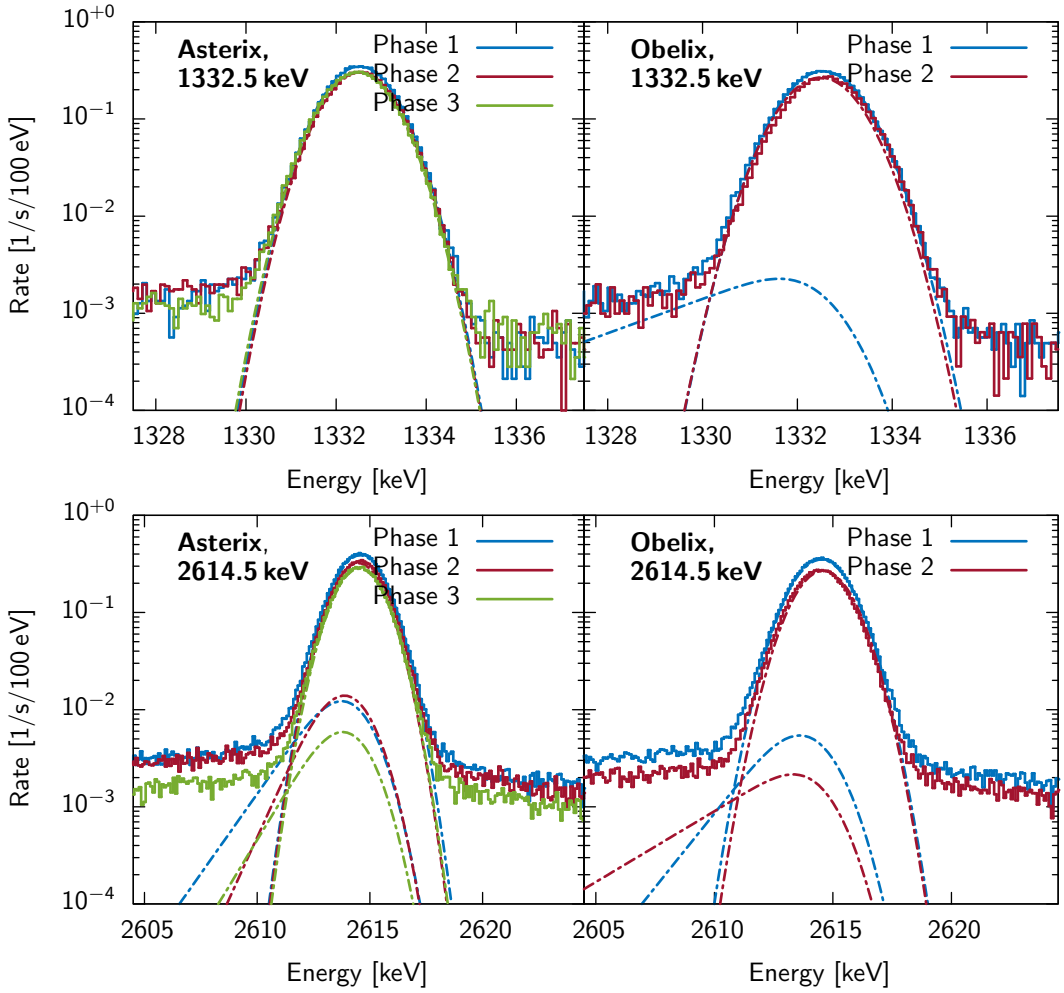

Figure 8.3: The γ-ray lines at 1332.5 keV and 2614.5 keV for the different point contact sizes of the two detectors. The tails in some of the data are smaller than the uncertainties. In these cases the tail was not drawn.

remains at least an order of magnitude smaller than the Gaussian peak. The resolution and filter configurations of the γ-ray line depicted in that figure are also summarized in Table 8.1.

8.1.2 High energy region (^{60}Co and ^{228}Th)

In contrast to the low energy region, at higher energies ballistic deficits are of importance. This not only requires the usage of the MSEC method, it also is not straight forward to define the most ideal filter at these energies. The resolution of the respective γ-ray lines is dominated by the charge carrier statistics, compared to which, both, the contribution from electronics noise and the peak deterioration caused by ballistic deficits are small (at least when the MSEC is enabled). The shaping time dependency of the resolution is therefore weak. In this situation, not physical properties or filter efficiencies are defining the ideal filter and shaping time, instead small fluctuations in the distribution of events within a peak are sufficient to

favor one configuration over another.

In order to process the ^{60}Co and ^{228}Th data the rounded-cusp filter with a rounded-top width of 1.8 µs was selected. All filters perform similar, hence this choice is rather arbitrary and might be better for a certain detector configuration than for another. The data are also processed with 6 other filters to calculate the variation between the different filters. This number is provided as a systematic uncertainty that describes the bias introduced by selecting a particular filter instead of the optimum one for each configuration. These uncertainties are indicated in Table 8.1 in addition to the uncertainties from the fit and are of the same order of magnitude. The shaping time of each filter was selected by searching the noise corner.

At high energies, the resolution improves slightly when moving from the first to the second configuration. The capacitance should only affect the electronics noise, which is a small contribution to the resolution at high energies, therefore this small improvement is predicted. Unexpected is the behavior of Asterix at its third point contact size. The resolution at 1332.5 keV is deteriorated with respect to the second point contact size while it remains constant at 2614.5 keV. It is not clear what the cause for this observation might be. Although great care is given to exclude systematic uncertainties coming from the experimental setup it is hardly possible to exclude them to this level of precision. The effect, however, seems to be consistent and not only is observed in different measurements but also for three lines in the ^{228}Th measurement that are in close proximity to the 1332.5 keV ^{60}Co γ-ray line: the 1620.7 keV line of ^{212}Bi, the DEP at 1592.5 keV of ^{208}Tl and the 1460.8 keV γ-ray line of ^{40}K. If an understanding of the increased resolution of these γ-rays is crucial to the operation of such a detector in a certain experiment further investigation would be necessary, however, this is not the case here.

Fig. 8.3 presents the peak shape of the 1332.5 keV and 2614.5 keV lines for the two detectors. None of the configurations has important tailing, the tails described by the hypermet function (see Sec. 4.2.7) is usually one to two order of magnitude smaller than the Gaussian part of the fit. Thus, neither incomplete charge collection nor ballistic deficit effects strongly impact the peak shape at any of the studied energies.

8.2 Equivalent noise charge

It has been shown that the equivalent noise charge depends on the shaping time and that for a low shaping time the voltage noise and for a high shaping time the current noise dominates. A method to measure the equivalent noise charge has been outlined in Sec. 7.2. The method is now used to extract the different noise contributions that are present in measurements of the detectors with different point contact sizes.

8.2.1 Shaping time dependency

Three measurements of a similar length (1 h) with a single ^{241}Am source at 15 cm distance from the cryostat's end cap and a dynamic range of 250 keV have been selected for this analysis. The data have been processed for a variety of shaping times (0.6-7.0 µs) once with a range adopted so that a pulser could have been generated in software in the baseline, and once with the normal range and no simulation of a pulser in the baseline. When a pulser is simulated in the baseline then filters with a large shaping time have to use a small window to reconstruct the baseline which creates additional noise (see Sec. 7.2.3). The two different analysis, one with a long and one with a reduced baseline, allow to extract the additional baseline reconstruction

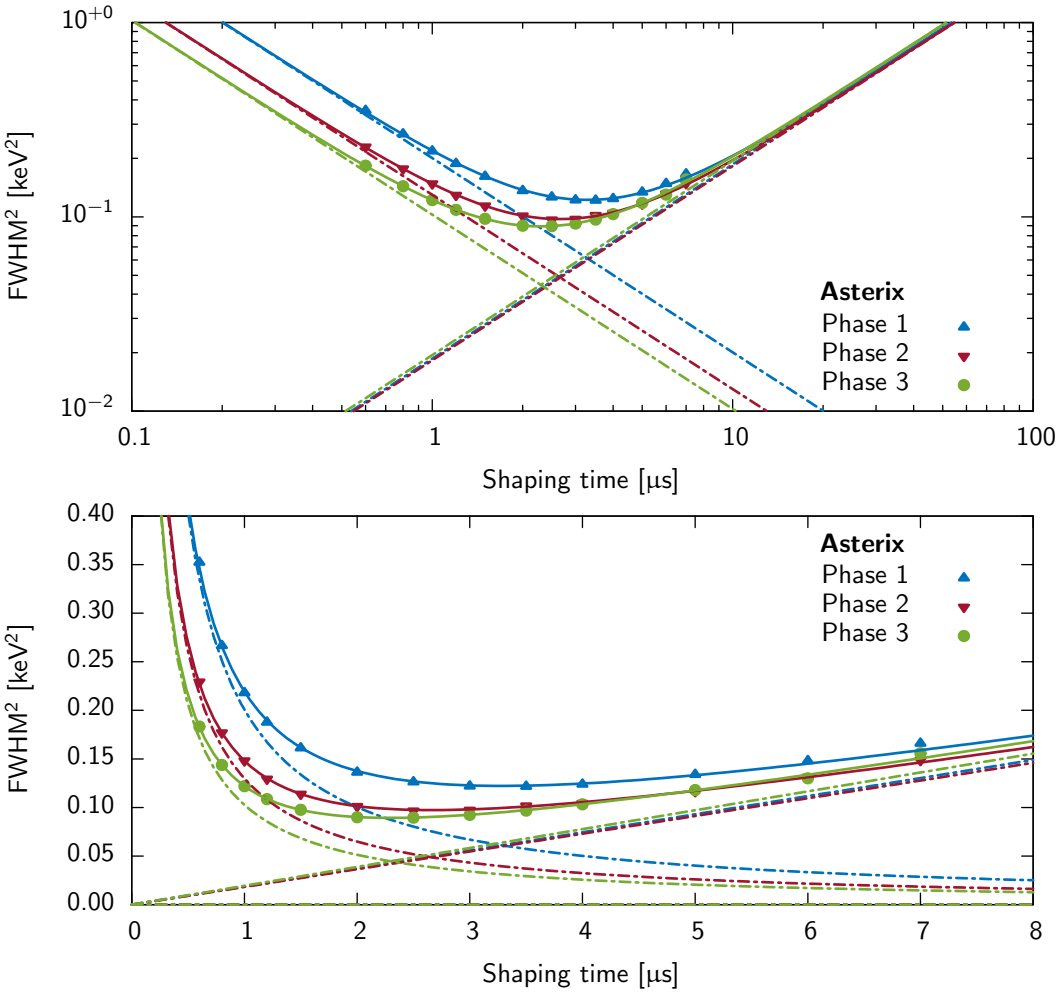

Figure 8.4: The curves of the equivalent noise charge on a logarithmic and linear scale for the different point contact sizes of Asterix. Additionally, fits to the current and voltage noise are displayed (dashed lines). The uncertainties are smaller than the markers and omitted.

Detector, Phase	Point contact Radius [mm]	Opt. Shaping Time [µs]	FWHM [eV]	Voltage noise V [keV² · µs]	Current noise I [keV²/µs]
Asterix, 1	8.4	3.5	348.8 ± 1.3	0.2007 ± 0.0003	0.0186 ± 0.0001
Asterix, 2	5.0	2.5	310.8 ± 1.9	0.1298 ± 0.0007	0.0183 ± 0.0001
Asterix, 3	2.5	2.5	299.3 ± 1.6	0.1026 ± 0.0004	0.0194 ± 0.0001
Obelix, 1	8.2	2.5	408.1 ± 1.4	0.2144 ± 0.0008	0.0332 ± 0.0001
Obelix, 2	5.2	2.5	335.9 ± 1.9	0.1458 ± 0.0019	0.0204 ± 0.0004

Table 8.2: An overview over the important parameters of the noise analysis for the two detectors at different point contact sizes. The fit parameters V and I to the voltage, respectively, the current noise are given in the last two columns.

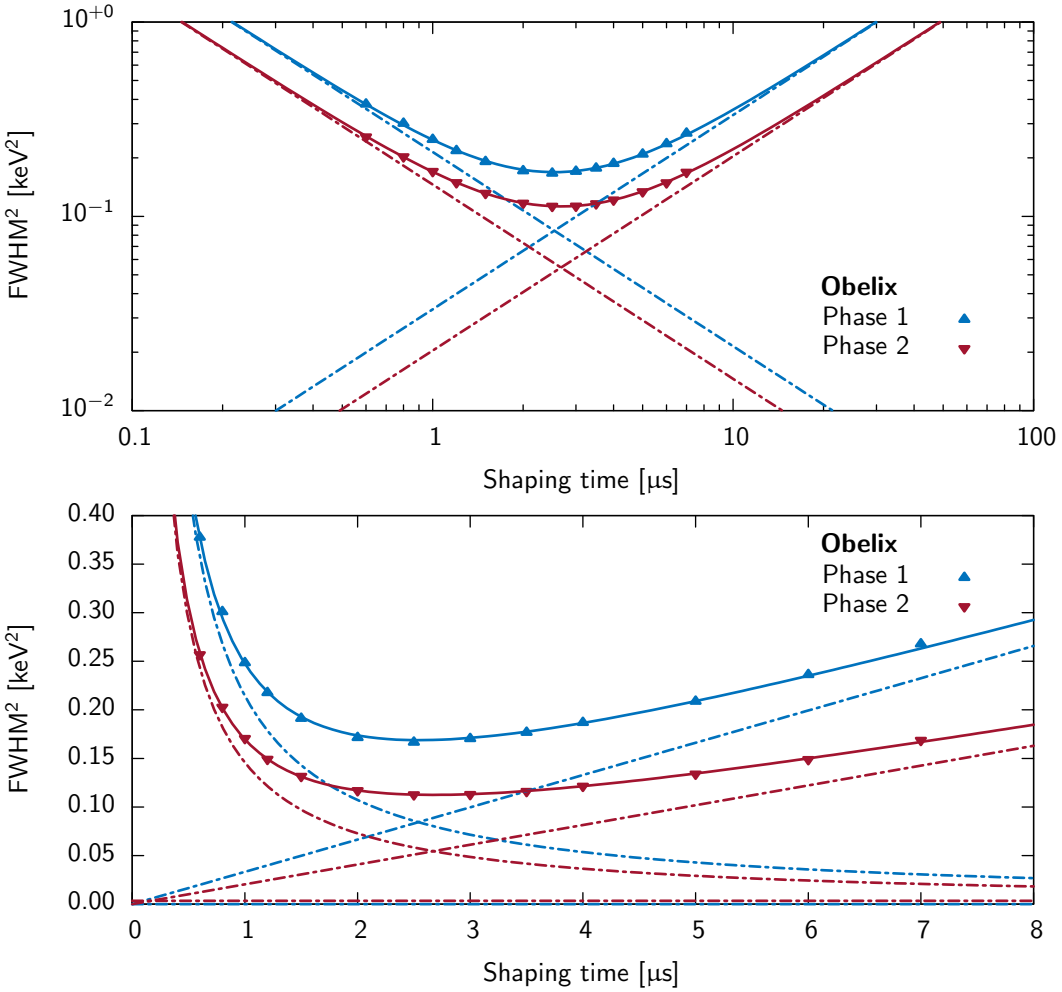

Figure 8.5: The curves of the equivalent noise charge on a logarithmic and linear scale for different point contact sizes of Obelix. Additionally, fits to the current and voltage noise are displayed (dashed lines). The uncertainties are smaller than the markers and omitted.

Detector, Phase	Radius [cm]	Leakage current [pA] Canberra	Fit
Asterix, 1	0.84	20	29.4 ± 0.1
Asterix, 2	0.50	10-20	28.8 ± 0.2
Asterix, 3	0.25	10-20	30.9 ± 0.2
Obelix, 1	0.82	50-60	55.5 ± 0.2
Obeliix, 2	0.52	10-20	32.6 ± 0.7

Table 8.3: A comparison between the leakage current extracted from the fit (assuming a 5 GΩ feedback resistor at 110 K and $F_i = 1$ for an infinite cusp filter) and the values measured by Canberra with a picoampermeter.

noise from the 59.5 keV γ-ray line. This noise can then be subtracted in quadrature from the pulser simulation to find a corrected estimation of the equivalent noise charge.

Fig. 8.4 and Fig. 8.5 present the outcome of this procedure for the three configurations of Asterix and two configurations of Obelix, respectively. As expected, the reduction of the point contact size improves the noise resolution. Furthermore, the noise corner is shifted to lower shaping times with decreasing capacitance. The resolution at the noise corner and the optimum shaping time are indicated in Table 8.2. For both detectors the value of the equivalent noise charge continuously improves when the point contact size is reduced. The best equivalent noise charge obtained is roughly 300 eV at the smallest point contact size of Asterix. This value is roughly 20% better than the manufacture's specifications of the preamplifier system.

8.2.2 Behavior of the voltage and current

The dependency of the noise resolution on the shaping time has been fitted with a function of the form:

$$Q^2(T_s) = \frac{V}{T_s} + I \cdot T_s + A \tag{8.1}$$

This formula follows Eq. 4.20 with the fitting variables corresponding to the voltage noise $V = e_n^2 F_e C_{\text{tot}}^2$ and the current noise $I = i_n^2 F_i$ at the shaping filters output. The 1/f noise has been found negligible in any of the fits and thus A was set to zero. The values found for these two variables in the fitting procedure are listed in Table 8.2.

The electronics setup has not be altered in the different configuration, thus the only value that is allowed to be changed must be related to the detector capacitance. Next to the 1/f noise which has been neglected only the voltage noise is affected by the detector capacitance. The voltage noise is proportional to the square of the sum of the capacitances in the electronics circuit C_{tot}^2 and thus with a reduction of the point contact size also the voltage noise is expected to be lowered. This behavior indeed can be observed for both detectors after the point contact size has been altered.

The entire surface between the two electrodes was refurbished in the process of changing the size of the point contact. This area is the most probable origin of leakage currents and thus any alteration of the point contact changes leakage currents. Together with the feedback resistor, leakage currents contribute to the current noise. The current noise thus is also affected by the reprocessing of the detector. According to Canberra the feedback resistor is 5 GΩ and kept at roughly 110 K, thus it is possible to calculate the leakage current from the fit. The respective values (see Table 8.3) agree reasonably well with the measurement conducted by

Canberra before shipping the detectors. The fit to the current noise for Asterix suggests that the current noise was reduced with the first reprocessing and then increased with the second reprocessing, however, the differences are relatively small. On the contrary, after reprocessing Obelix the current noise is reduced considerably. Obelix started with a relative high current noise and approached in the second configuration what was previously observed for Asterix. Still, the current noise in Obelix remained slightly worse, than what have been observed in any configuration of Asterix. Overall, the observed leakage currents are rather on the high side and currently the limiting contribution to the current noise. This must be taken into consideration to improve the resolution any further and might actually require some considerable efforts such as another rework of the groove.

The voltage noise at the output of the shaping filter is proportional to the square of the sum of the capacitances. Furthermore, the total shunt capacitance can be split up into the contributions from the detector and other capacitance in parallel to the detector $C_{\mathrm{tot}} = C_d + C_p$. The reduction of the contact size only affects the detector's capacitance C_d while the sum of the remaining capacitance C_p is constant. Although the total voltage noise can be found from the fit for each detector geometry, it is not possible to entangle the multiplication factors $e_n^2 F_e$ and the two shunt capacitances $C_d + C_p$ without any assumptions. A relation between the detector capacitance and the point contact radius has been provided in Eq. 3.1. If we assume that this form is correct for the two detectors, then the voltage noise can be expressed as:

$$V = e_n^2 F_e \left(C_p + 2\pi\varepsilon_0\varepsilon_r r\right)^2, \qquad e_n^2 = \frac{8kT}{3g_m}, \tag{8.2}$$

where r is the radius of the point contact. The shaping factor F_e can be calculated from the impulse response of the shaping filter. Its value is 1 for the infinite cusp which should be close to the filter used in this analysis. The equation does not include the conversion factors required between V and e_n which can be derived from the definition of the equivalent noise charge. Thus the equation consists of two free parameters, so if at least two configurations of the point contact size have been measured then the system of equations is determined and the individual values can be calculated. A fit of this function to the point contact sizes at which the current noise was evaluated is shown in Fig. 8.6 for Asterix. Only two data points are available for Obelix, the displayed curve corresponds to a simple calculation of the two free variables and no uncertainties are provided. In both cases, the value for C_p is larger than what is expected from just the feedback capacitance (according to Canberra $C_f = 0.5\,\mathrm{pF}$). On the other side, the value for the transconductance g_m of the order of 10 mS indeed is in the typical range of a FET.

Next to this model it was also tested if it would be more accurate to assume the point contact detector as a parallel plate capacitor. In that case the capacitance is related to the radius through:

$$C = \frac{\varepsilon_0\varepsilon_r \pi r^2}{d}, \tag{8.3}$$

where d is the separation of the two plates in the parallel plate capacitor. In order to test this model a certain value for the transconductance needs to be assumed. For simplicity the value found by the first model was used. The fit of this model to the data points of Asterix in Fig. 8.6 is a more accurate description of the observed curves. The value for C_p, however, is of the same magnitude as what was found by the first model. Still, this shows that the studied

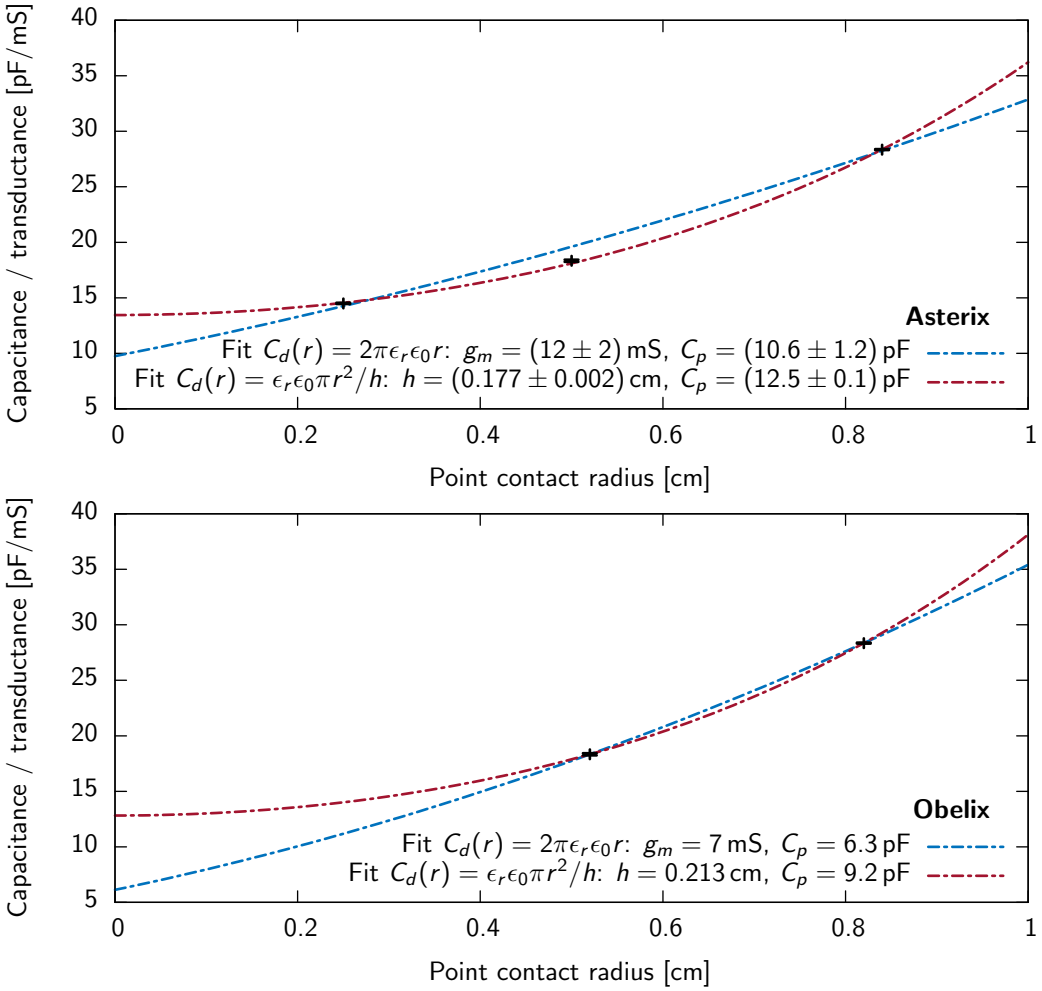

Figure 8.6: Fit of different models to the observed voltage noise. The variables are the amplifiers transconductance g_m and the sum of all capacitance C_p not including the detector's. The relation between the detector's capacitance $C_d(r)$ and the point contact radius r is modeled by the equations mentioned in the labels. The first model follows Eq. 3.1 the second assumes a parallel plate conductor and introduces in addition the distance between the two plates h. The second model uses the value found for the transconductance in the first model as a fixed value.

geometry is closer to a parallel plate capacitor and the point contact not sufficiently small so that Eq. 8.6 is a good description.

If it is assumed that no component of the voltage noise except the capacitance of the detector changed then the presented results show that the voltage noise is not dominated by the detector's capacitance, instead other capacitances in the system are dominating. Therefore, a potential improvement requires an adequate upgrade of the electronics.

8.3 High voltage scans

High voltage scans are important to establish the voltage at which a detector is fully depleted and thus can be best operated. The measurements have been performed at voltage steps of 20 V (from 700 V to the operation voltage) with an ^{241}Am source and the smallest setting for the dynamic range. An additional measurement has been taken with a ^{60}Co source and the intermediate amplification stage, however the results are almost identical. Thus, the discussion here is limited to the ^{241}Am source measurement. The data set has been processed with a rounded-top cusp filter with a rounded-top width of 0.3 µs. The measurement at the highest measured voltage has been taken as the reference measurement. The data sets have all been processed with the method that simulates a pulser in the baseline.

8.3.1 ^{241}Am and pulser resolution

The resolution of the simulated pulser and the ^{241}Am line at 59.5 keV are represented in the top and middle panel of Fig. 8.7 and Fig. 8.8 for Asterix, respectively, Obelix. For both detectors, the two configurations with the larger contact size are quite similar and also comparable between detectors. A region of a fast decreasing resolution is followed by a region of slowly increasing resolution before finally a constant value is reached. The point where the resolution reaches a constant value usually is the depletion voltage, but as the resolution increases only weakly over a relatively large voltage range it is hard to pinpoint the exact location of full depletion. A possible explanation for the intermediate slowly decreasing region is provided by Eq. 2.6. Once the p-type region is depleted also depletion into the p+ region takes place. Thus, the capacitance still decreases above the voltage where the p-type region is depleted. This further reduces electronics noise and improves the resolution. At high voltages the field configuration in the detector furthermore is more uniform, which reduces regions of low drift velocity that are prone to charge trapping. In both situations the depletion voltage would be found where the intermediate region and the region with a fast decreasing resolution meet. This is also supported by the simulated depletion voltages from Sec. 5.2.1. They were found to be approximately 1640 V for Asterix and 1720 V for Obelix in these two configuration and therefore lower than what is observed in the measurements.

In the third configuration of Asterix the intermediate region does not exist and a fast drop in resolution can be observed at roughly 1760 V. This voltage is in good agreement with the simulated depletion voltage of 1720 V. The fast drop at this voltage is most probably caused by the formation of an undepleted bubble in the center of the detector that exists just below the depletion voltage. The effect was discussed in Sec. 5.1.2. The electric field in the bubble region is zero and charge carrier displacement limited to diffusion. The pulse shape is not clearly defined and the charge collection efficiency is low which explains a sharp change in resolution once the undepleted bubble disappears.

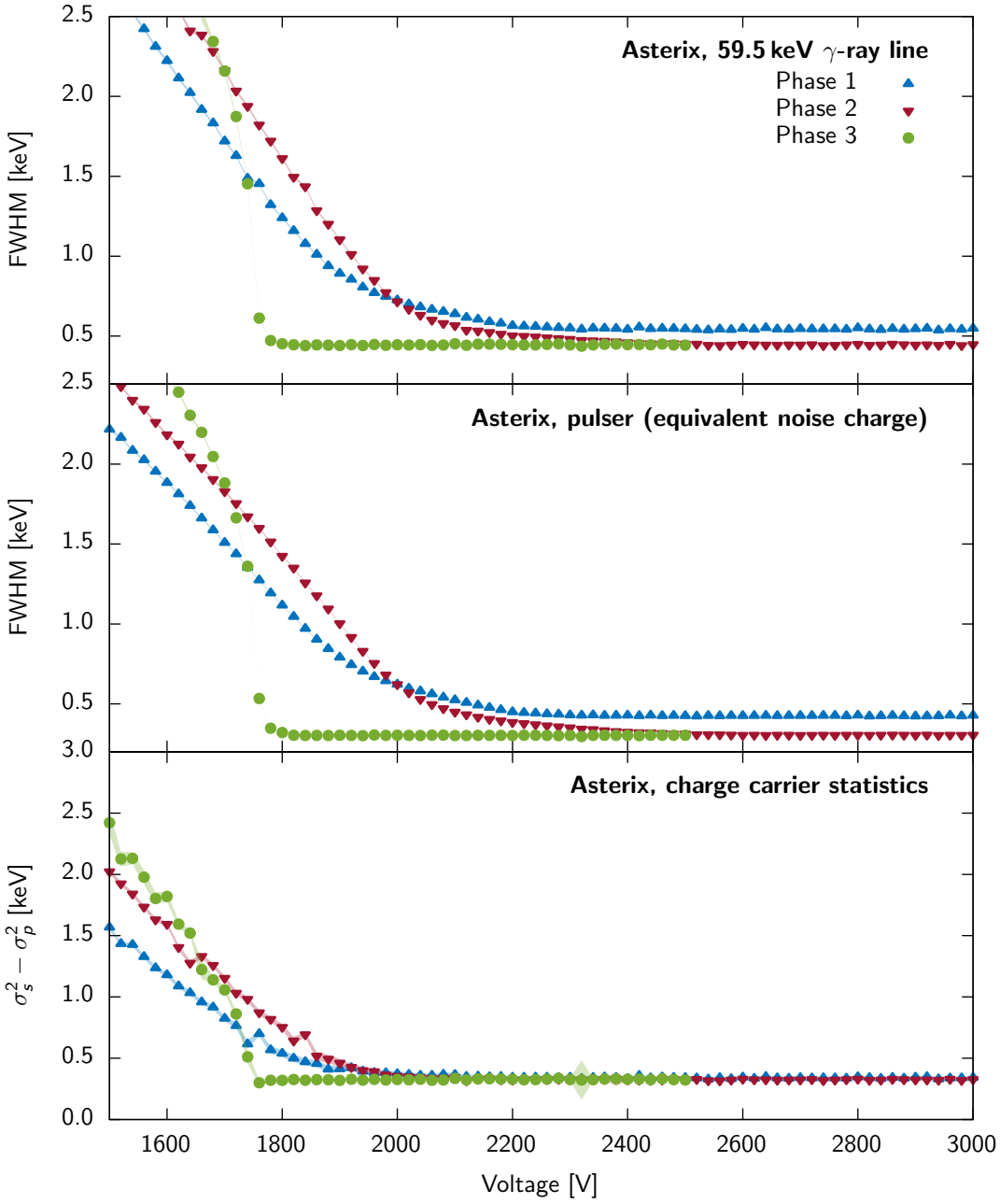

Figure 8.7: The resolution of the 59.5 keV γ-ray line, the simulated pulser (noise) and the charge carrier statistics as a function of the voltage for Asterix. The charge carrier statistics is the difference (in quadrature) of the two other curves. The transparent shaded areas are the uncertainties of the respective measurements.

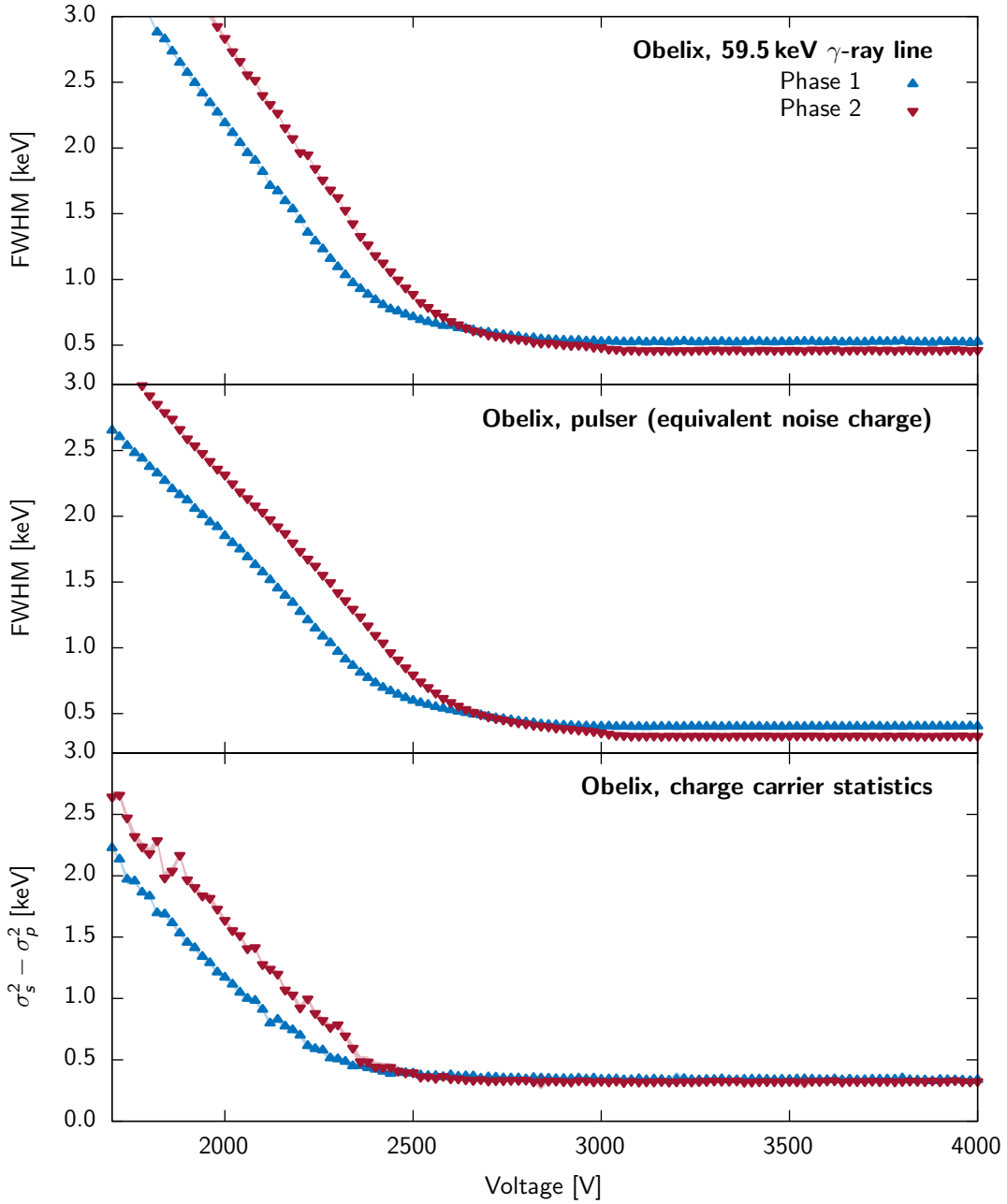

Figure 8.8: The resolution of the 59.5 keV γ-ray line, the simulated pulser (noise) and the charge carrier statistics as a function of the voltage for Obelix. The charge carrier statistics is the difference (in quadrature) of the two other curves The transparent shaded areas are the uncertainties of the respective measurements.

In the bottom panel of Fig. 8.7 and Fig. 8.8 the difference between the resolution of the 59.5 keV line and the pulser (subtracted in quadrature) is plotted as a function of the depletion voltage. This corresponds roughly to uncertainties from charge carrier statistics and is the same as the Fano factor. Above the depletion voltage it is constant, which supports the assumption of complete charge collection made in Sec. 7.3.1. Below the depletion voltage, the value increases, which means that effects such as incomplete charge collection and pulse shape variations are the main source of uncertainties. The value classifying the charge carrier statistics is still constant well into the region where the resolution slowly is increasing. This furthermore supports a depletion voltage that lays at a voltage well below the constant region.

It is possible to explain the discrepancy between simulated depletion voltage and measurements with uncertainties in the description of the impurity concentration in the detector. Next to a gradient along the height there most likely is also a radial gradient, that was not considered. Furthermore, the exact values of the impurities were given with a precision of roughly 10%. This leaves plenty of space for alternative impurity distributions that can explain the observed effects.

A specific systematics that needs to be considered for high voltage scans are hysteresis effects. The detector must not behave in the same manner when the voltage is increased than when it is decreased. In both cases, once the voltage reaches a certain level it takes a certain time for the detector to settle and reach constant operation conditions. In order to exclude these effects additional measurements with ^{241}Am and ^{60}Co have been conducted for all detectors configurations. These measurements are all consistent with what has been presented here. As previously mentioned the voltage scans have been performed from the operational voltage downwards. In that way no temporal effects (i.e. relaxations) have been observed.

8.3.2 Relative peak position and pulse rise time

The depletion of a detector furthermore can be studied through the relative position of the reconstructed peak in the energy spectrum. Fig. 8.9 shows this dependency for the two detectors. Similar to what was observed for the resolution, the curves for the first two configurations are very similar to each other. The final peak position is only slowly approached with increasing high voltage. Around 2000 V for Asterix and 2400 V for Obelix there seems to be a weak dent in the peak position, which might be related to the full depletion of the detector. Above this voltage the peak position still deviates by about 5% from the highest value. The same explanations that were given to describe the slowly increasing region in the previous section also apply here. Instead of the capacitance, in this case however the depletion width is relevant. The detector at high voltages is depleted further into the p+ region; charge carriers can drift closer to the central electron before being absorbed, will reach higher values in the weighting potential and induce a larger pulse into the electrode.

The situation is again different for Asterix at the geometry with the smallest point contact size. There is a fast drop around the depletion voltage and below the fast drop the reconstructed position increases again for roughly 50 V. The increase can be as well explained by an undepleted bubble. Such a bubble forces the charge carriers to diffuse and thus they are either lost or collected with a delay. This is furthermore supported by the average rise time of events, depicted in the bottom panels of Fig. 8.9. The charge pulse of events at this voltage takes considerably longer to rise; the pulse shape of these events is very similar to slow events originating in the transition layer. It can be assumed that the mechanics governing their shape

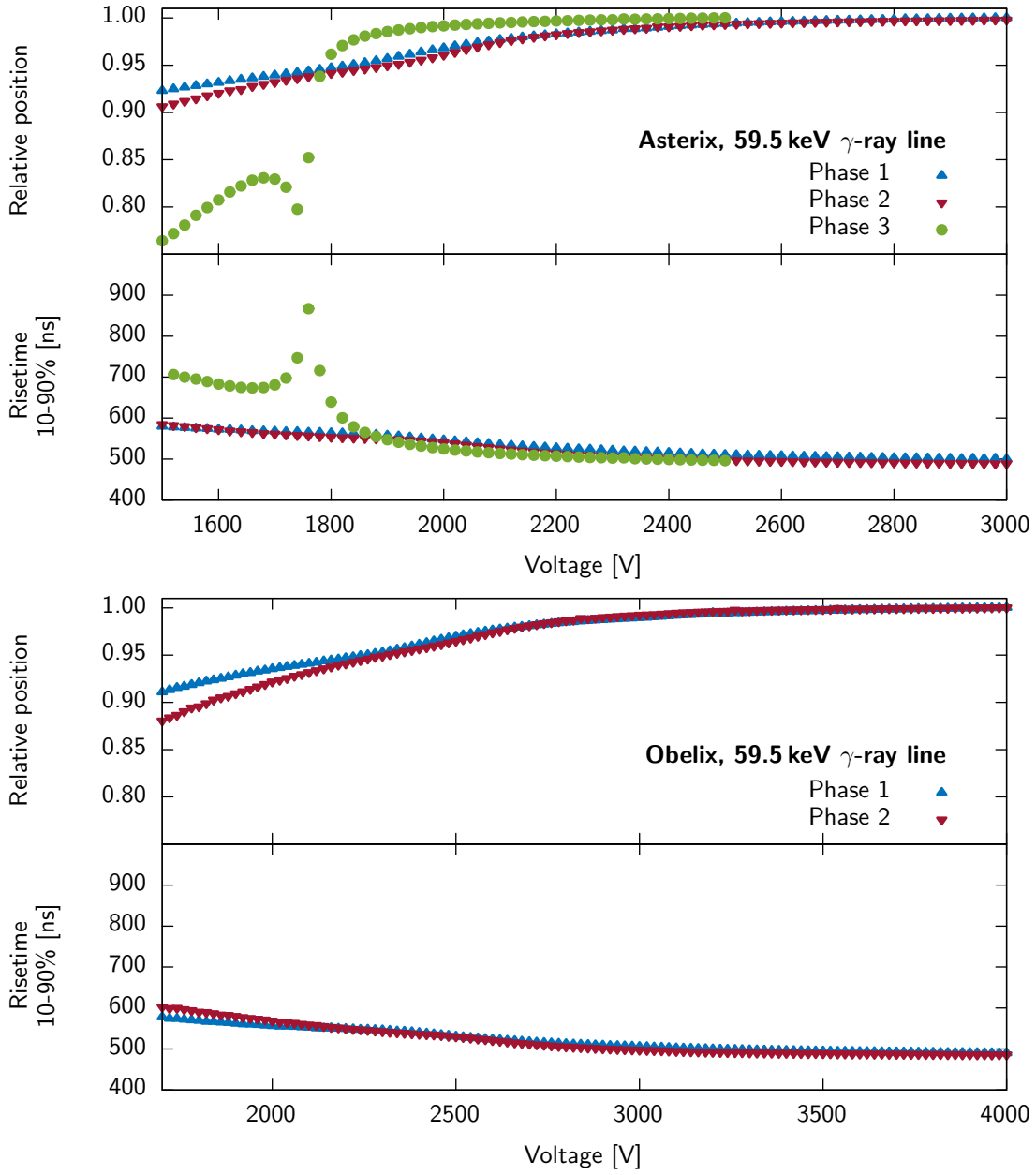

Figure 8.9: Top panel: The relative position of the 59.5 keV line for Asterix (top) and Obelix (bottom). The measurements have been calibrated in relation to the measurement at the highest voltage. The uncertainties on the position are not visible. Bottom panel: The rise time (10-90%) as a function of the high voltage. Also here are the uncertainties small.

is also alike and thus should be diffusion.

The operational voltage of Asterix was fixed at 3000 V for its Phase 1 and 2 configuration and 2500 V for its Phase 3 configuration; the one for Obelix at 4000 V for both configurations. The operational voltage, thus, is sufficiently into the plateau to exhibit a constant resolution and peak position. However, only a few hundred of Volts below the operational voltage degradations starts to play a role. Effects in the range 2-5% are easily realized.

8.4 Collimated measurements near the surface

Two sets of collimated measurements have been taken at the operational voltage of the detectors. The first set has been taken on the scanning table with an ^{241}Am source. The automated procedure allows to take measurements on a fine grid (roughly 2 mm separation between two points). The second set has been taken with a ^{133}Ba source that was placed in the bore-hole of a large Na(I) detector to track the coincidental emission of two γ-rays at energies of 81.0 keV and 356.0 keV. This measurement was performed manually and therefore restricted to a single horizontal line along the center of the detector (5 mm spacing). In both measurements the collimated γ-rays interact close to the surface in a confined space. Thus, results from measurements can be compared to simulations from ADL3, without requiring extensive Monte Carlo simulations to establish the distribution of interactions within the detector.

The simulated pulses represent the charge that is induced into the electronic circuit not the actual pulse shape that is measured. The measured pulse is affected by the electronics chain which adds some shaping and noise to the signal. In theory, the effects of the electronics can be studied by measuring the response of the system to a sharp pulser signal. Such a measurement has been performed, however, suffers from two weakness:

- The pulser feed into the test input of the preamplifier must have a very sharp rising edge to not affect the pulse response measurement through the finite rise time of the pulser signal. The Hewlett Packard 8007B Pulse Generator has a rise time of roughly 5 ns, however, it seems that this still affects the impulse response of the electronics system.

- Many pulser signals will be measured, which need to be averaged, to reduce the effect of electronics noise. The averaging procedure requires some sort of alignment. The measured signals have been aligned by the maxima of their current pulse. However, this method also adds a bias. The results would have been more precise, if the pulser signal were additionally feed into the FADC to establish a coincidence. Unfortunately, until recently, this method was not thought off, therefore such a measurement was not performed.

Furthermore, a measurement also contains traces of special pulses (i.e. slow pulses) that are explained by a simplified model and not yet implemented in ADL3. Even if it would be possible to consider all these effects it is still not assured that the electrical field in the detector can be perfectly described by the simulation. Particularly the effect of gradients in the impurity concentration on the electric field is large, however, impurity concentrations can not be measured completely throughout the detector.

As a discussion of all these problematics is complex and far beyond the scope of this dissertation only a generic comparison directly between simulated pulses and measurements will

be made and all the complications left aside. It will be seen, that the gain from a generic description is satisfactory.

8.4.1 Coincidental measurement with a NaI(Tl) detector

The radio isotope ^{133}Ba emits two coincidental γ-particles at energies of 81.0 keV and 356.0 keV. Thus, when an event is observed in the 81.0 keV peak it should coincide with an event of 356.0 keV in the NaI(Tl) detector. The energy resolution in of the NaI(Tl) detector that is used in this study is poor. However, the response is sufficient to track the onset of the signal. The position of the maxima of all peaks, that are observed simultaneously with a 81.0 keV event are located. The time difference between the position of this signal in the NaI(Tl) detector and the maximum of the current pulse is then filled into a histogram. The observed spectrum is flat except for the location where the coincidental γ-ray is detected and where a sharp peak is observe. This peak provides a rough estimation for the position-dependent drift time of the charge carriers in the germanium detector.

The results are plotted in the right panel of Fig. 8.10 at different radii. As expected, with increasing radii also the drift time increases. On the left panel of Fig. 8.10 the same effect is represented from simulation. It can be seen that the shape of the curve matches the data. Also the relative differences between the different point contact sizes is well explained by the simulation. The absolute values of the simulations and the measurements do not match: For simulations the onset of the pulse can be defined relative precisely, for the measured data the location of the maximum of the NaI(Tl) signal was used. The response time of the NaI(Tl) detector is about 100 ns, which corresponds roughly to the observed difference between data and measurement.

The coincidence measured in the NaI(Tl) detector can be used to correctly align the signals in the germanium detector. This procedure was used to find the average pulse shape of signals from a given radius represented in Fig. 8.11. The difference between the simulated signal and the measured signal comes from electronics components, which shapes the signal obtained from the germanium detector and thus brings it into the measured form. Except of these differences the signals seem to match the simulation well, particularly the drift time of the average pulse roughly matches what the simulation predicts. However, signals that originate close to the center of the diode rise slightly faster in the data while signals at a large radius rise slightly slower than simulated.

8.4.2 Relative position

Measurements with a collimated ^{241}Am source at various radius can be used to investigate regions with charge trapping within the detector. In these measurements, energy is deposited close to the surface in a very restricted area of the detector. The charge carriers then drift through the entire detection volume, to be collected at the point contact. If they encounter a region with increased charge trapping then some of the charge carriers will not contribute to the signal that is induced into the electrode and the pulse height and shape altered. Even, if charge trapping is homogeneous throughout the detector, it should be visible in this measurement, as the length of the charge carrier's trajectory depends on the initial position. With long tracks the chance for a charge carriers to be trapped increases, thus trapping effect must be stronger at large radii from the center of the detector.

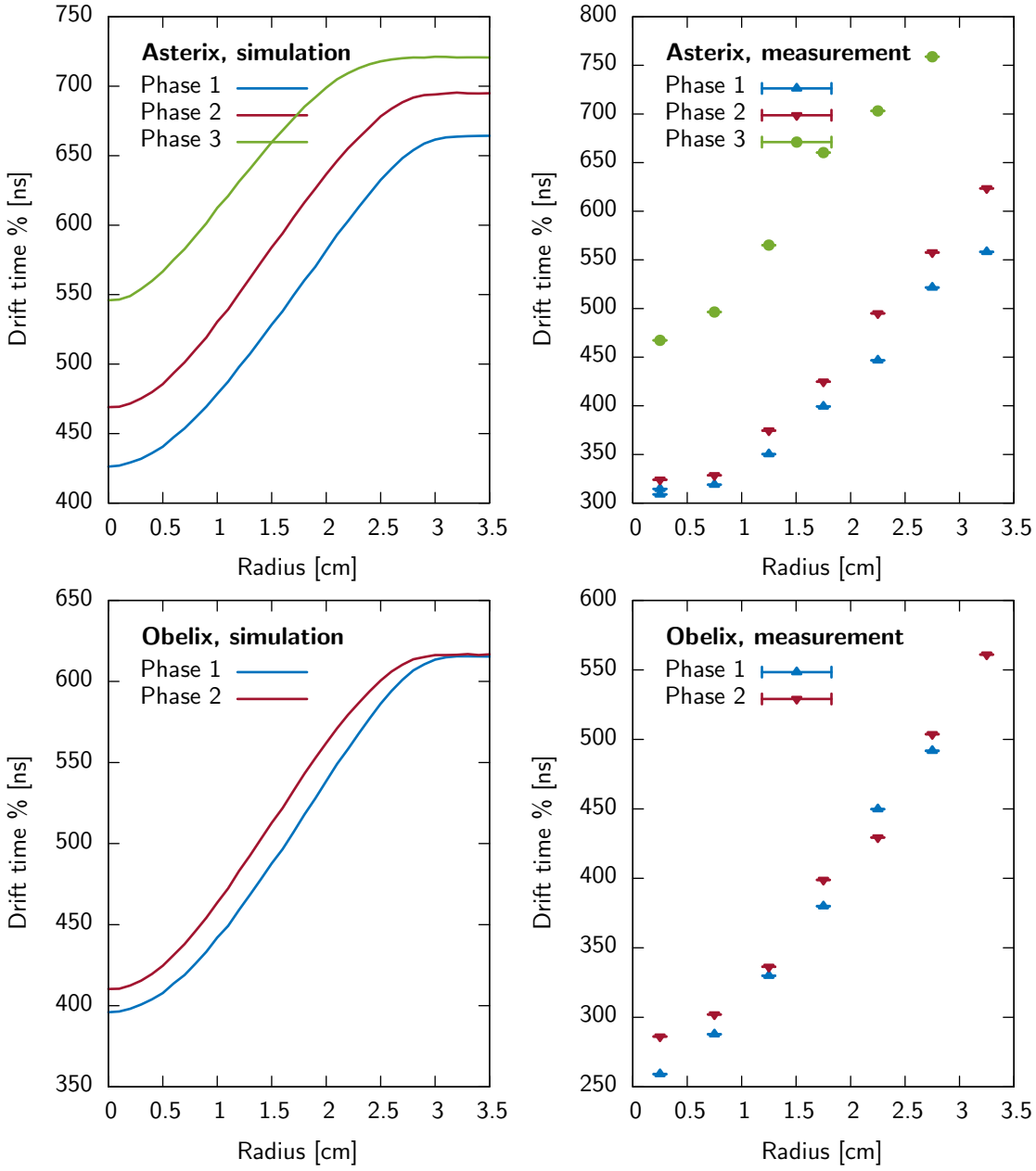

Figure 8.10: The average drift time of a signal that originates from a given radius for the two detectors at different point contact sizes. The left panel represents simulations, the right panel actual data.

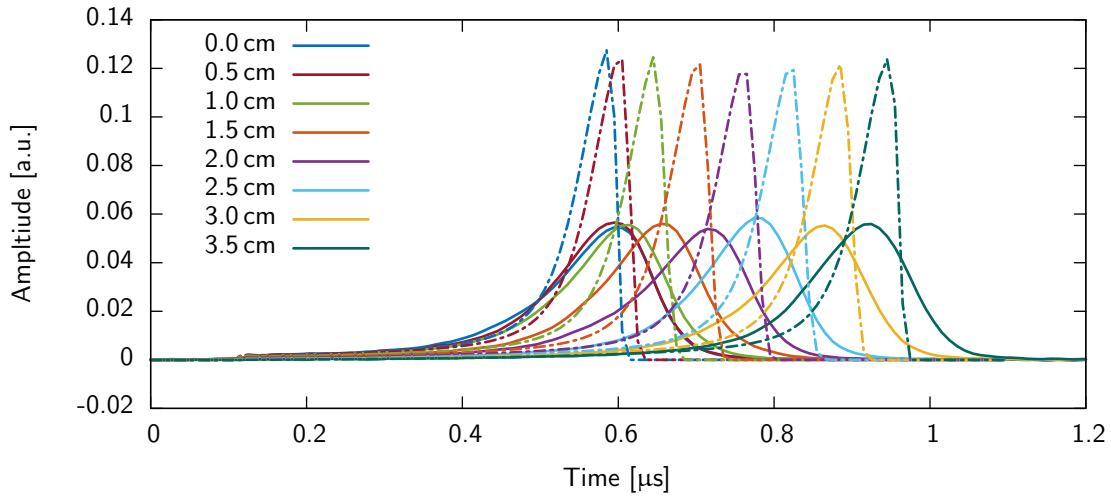

Figure 8.11: The average pulse shape from the coincidence measurement (solid lines) as a function of the distance from the center for Asterix in its second configuration is compared to simulations (dashed lines).

As discussed in Sec. 6.2.1, measurements have been taken on rings with a constant radius, with a separation of approximately 2 mm between both, individual rings and measurement positions along the ring. The uncalibrated spectra for the individual measurements along a ring were added and then the position of the peak at 59.5 keV evaluated with the peak fitting routing mentioned in Sec. 4.2.7. The relative position of the peaks is represented in the left panel of Fig. 8.12 for different radii. It can be seen, that the peak position at large radii is indeed shifted relative to the peak position at the center of the diode. Results from simulations are represented in the right panel of Fig. 8.12, which show that the measurements can be explained without including charge trapping. For the measurement the rounded-top cusp filter has been used (300 ns rounded top width), which is sensitive to variations in the pulse shape. The pulse shape of a signal changes as a function of the radius (see Fig. 8.11). This change is sufficient to introduce a ballistic deficit that is not only visible in simulations but also in the data. The shape of the effect agrees well between the simulation and the data. The effect however is more pronounced in the simulation than in the data. For the first point contact sizeof Asterix the ballistic deficit predicted by the simulation is twice as large than observed. There is no simple explanation for this effect, other than the pulse shape not being accurately modeled by the simulation. Asterix furthermore, has the strongest radial lost from ballistic deficit in its third configuration, not in its first configuration, as predicted by the simulation. Obelix is in good agreement with simulations.

8.4.3 Rise time

The collimated measurement also provides information about the anisotropic mobility discussed in Sec. 4.4.2. The electric field within a point contact detector is such that the charge carriers initially drift in a radial direction. The radial drift of charge carriers is affected by the anisotropic mobility in such a way, that depending on the orientation of the trajectory to the crystal lattice, the drift velocity changes. Thus, the time to reach the central contact depends

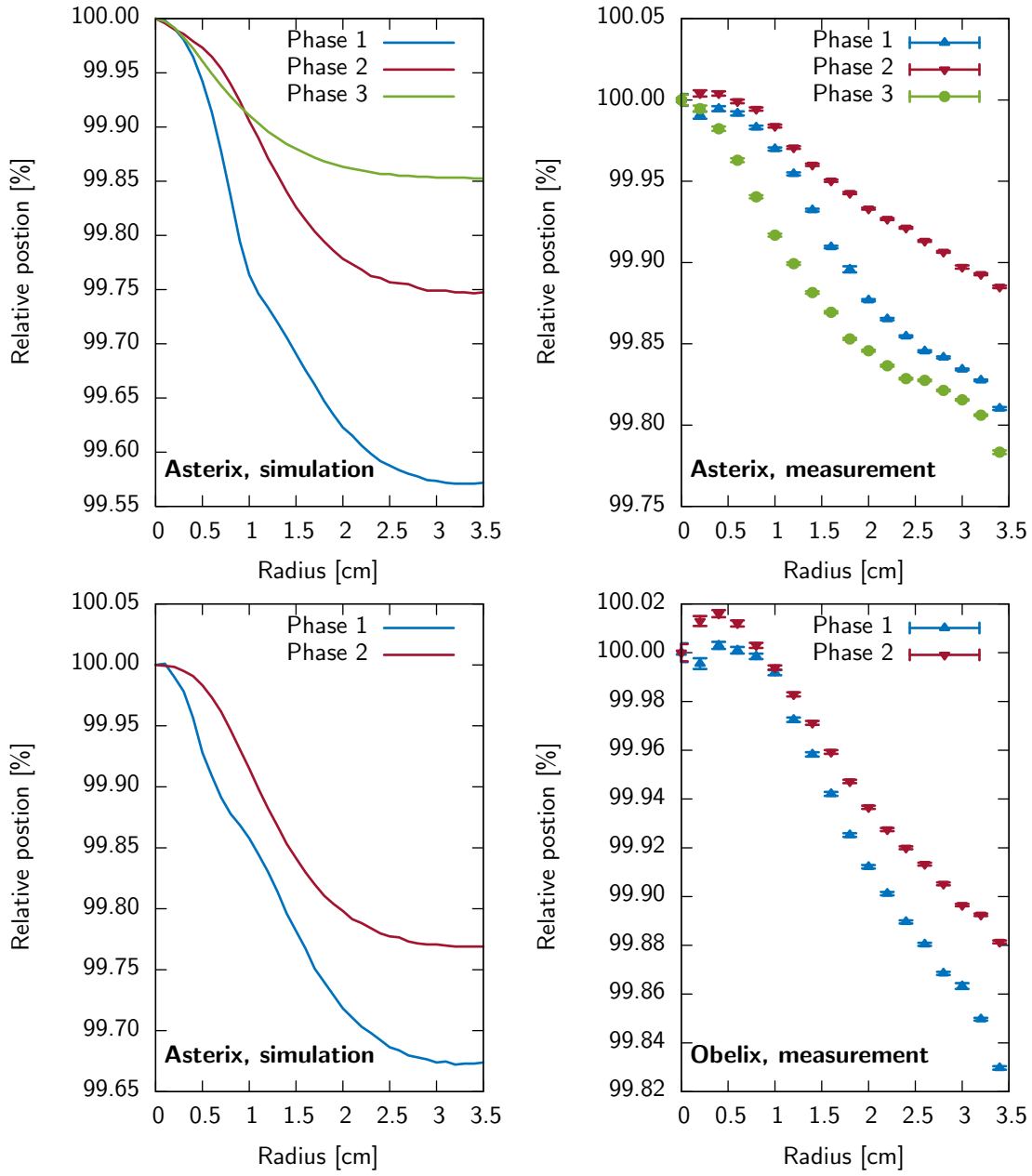

Figure 8.12: In the right panel a measurement of the relative peak position as a function of the radius is shown.The points are measured on the top surface of the respective detectors. At each radius the spectra of all available measurements are summed up to reduce statistical fluctuations. In the left panel a simulation of the same situation is given

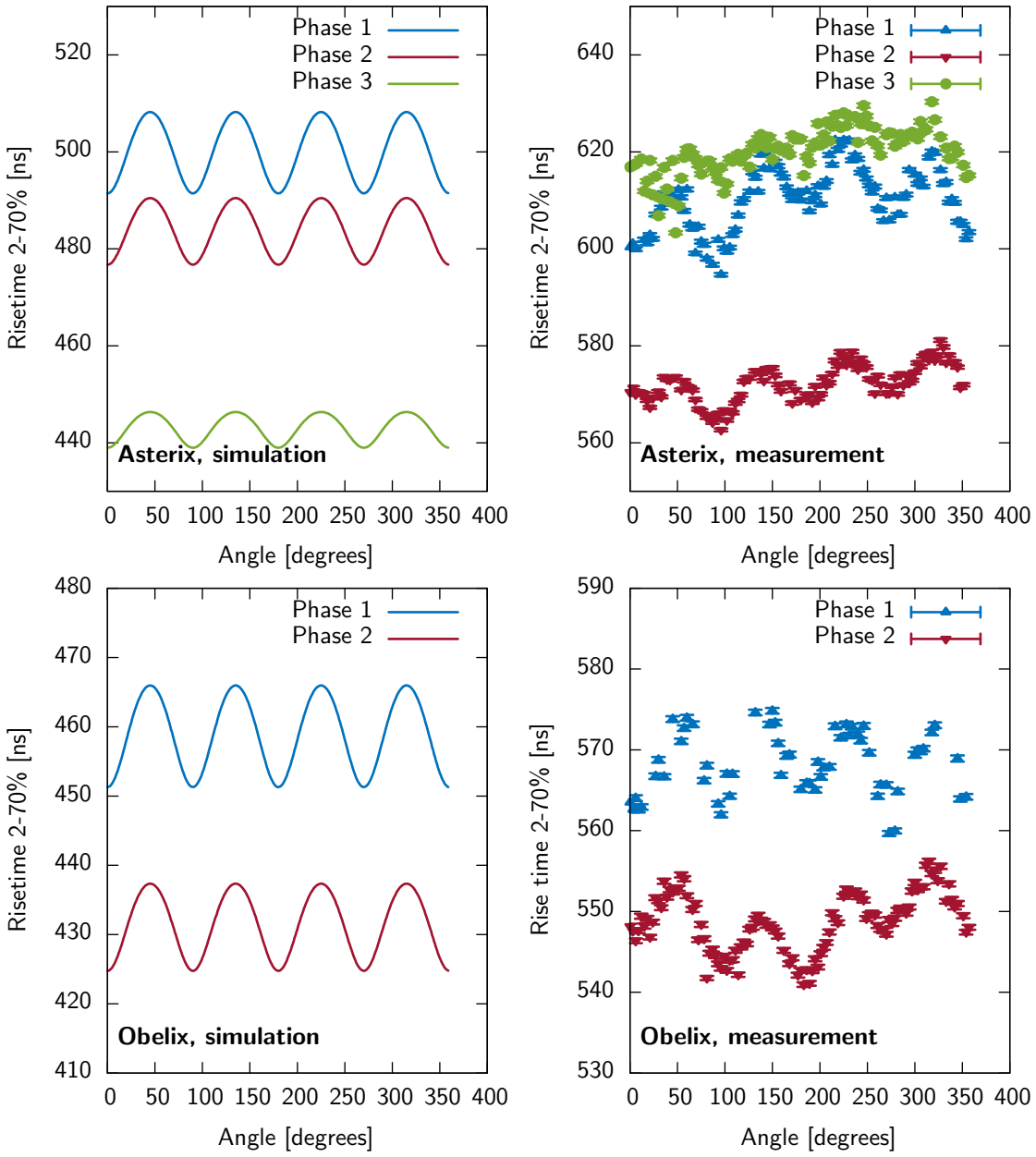

Figure 8.13: The angular dependence of the rise time. The measurements have been taken at the side surface, close to the bottom of the detector. In the left panel simulations are represented, in the right panel measurements at the same locations.

on the angle at which the charge is deposited relative to the crystal lattice. Particularly, the onset of the signal is sensitive to this effect, thus the rise time 2-70% is used to measure the anisotropic mobility. When the rise time from 2-70% is plotted against the angle, characteristic oscillations appear as represented in Fig. 8.13. The oscillations can be observed in any of the different configurations, however, for Asterix in its third configuration they are relatively weak. The oscillations are predicted by ADL3, as the anisotropic mobility is included in the simulation. However, the figure also shows that the absolute values of the rise time do not agree well between simulation and measurements. Especially, the third configuration of Asterix does not follow what was predicted by the simulation: It is in average not found at a lower rise time than the other two configurations, instead it is shifted to a higher value, similar to its Phase 1 configuration.

8.4.4 Effects observed with collimated measurements

In the previous sections it was shown that there is quantitative agreement between simulations and measurements, when it comes to the radial and angular variations between different points along the surface. However, it was also discovered that absolute measurement values do not match the predictions well. Particularly the third configuration of Asterix seems not to behave according to the simulation, while the first and second configuration of Asterix and Obelix follow the overall predictions. This agrees with the results from the high voltage scans (see Sec. 8.3), where also the third configuration of Asterix is different from the larger point contact sizes.

These discrepancies can not be easily explained as they do not show up in the simulations. The operational voltage of Asterix in its third configuration was lowered to 2500 V as leakage currents were increased. The lower operational voltage, however, can not explain the observed effects then the reduced depletion voltage was considered in the simulation.

The effect could be caused by an insufficiently precise knowledge of the impurity concentrations. It is possible, that the impurity gradient not only varies along the height of the diode but also in the radial direction. Furthermore, with roughly 10% precision (measured by Canberra), also the variation along the height could be different from the value considered in the simulation. Differences in the impurity gradient might explain both observation, an increased depletion voltage compared to simulations in the first two configurations and differences in the shape of the signal in the third configuration.

Except the odd behavior of Asterix, it has been shown, that effects that are predicted by simulations show up in the data. Even though the data and measurements do not match perfectly, most of the differences can be contributed to the effects described in the beginning of this section, especially that the electronics response function was not considered. The qualitative agreement, is sufficient to understand the physics behind the signal formation and explain why certain effects arise. A complete description of the system including all the effects that were left out in this discussion would not add a lot of new information. The overall discrepancies most likely can not be resolved in such a manner, but rather hint some systematics in the simulation. Therefore, the approach to neglect these details and mainly search for a qualitative understanding of the processes is justified.

8.5 Pulse shape discrimination

The size of the point contact alters the electric fields and accordingly the trajectories of charge carriers. This influences the funnel effect – the channeling of trajectories close to the point contact (see Sec. 3.5). Double beta decay experiments exploit the funnel effect to suppress backgrounds in their region of interest, which is typically at a few MeV. They differentiate single (signals) and multi site events (background) by their pulse shape. The methods to differentiate the signals are described in Ref. [72, 114] and use the amplitude of the current pulse divided by the uncalibrated energy (A/E) as their discrimination parameter. This discrimination parameter was previously described in Sec. 3.5.1. The method will be applied to the different configurations of the detectors to explore if there has been any change in the suppression power.

8.5.1 Calculation of suppression efficiencies

The method to calculate the pulse shape discrimination efficiency is based on two γ-ray lines in the energy spectrum of a radioactive ^{228}Th source, the double escape peak (DEP) at 1592.5 keV and the single escape peak (SEP) at 2103.5 keV. These peaks have been selected by the GERDA experiment because of their proximity to the Q-value of the two-neutrino double beta decay at 2039 keV. Events in these peaks originate from electron-positron pair production and the subsequent annihilation of the positron. The two γ-particles created in this reaction, can both deposit their entire energy in the detector and thus the event is reconstructed at 2614.5 keV, the full energy peak (FEP). If both of them escape, only the energy of the remaining electron will be registered in the detector and thus will induce a signal close to a single site event in the 1952.5 keV peak. If one of them escapes, then the second energy deposition of the annihilation photon is most likely at a certain distance from the electron and a typical multi site structure is observed at 2103.5 keV. Thus, the DEP is mostly dominated by single site events, that are signal like and the SEP by multi site events, that are background like. Hence, the two peaks can be used to define the efficiency of a pulse shape cut. Additionally to the efficiencies in these two peaks also the efficiency in the FEP of ^{212}Bi at 1620.7 keV and 2614.5 keV of ^{208}Tl will be reported to allow a comparison with the above cited works. The A/E distribution in the peaks is calculated within a range of 9 times the variance of the peaks and the background from both sides of the peak is subtracted. A lower A/E cut then is placed such that roughly 90% of the DEP events will survive and the survival fractions in the other three peaks for this cut evaluated. The A/E value is slightly energy dependent. This dependence is corrected by measuring the Compton distribution in two energy regions that are free of peaks (1200-1400 keV and 1850-2050 keV) and correcting the energy dependence with a linear interpolation according to these two regions.

8.5.2 Comparison of pulse shape discrimination performance

Table 8.4 lists the survival fractions of the different peaks in the different detector geometries. The survival fraction in the DEP is by definition close to 90% (Compton background was subtracted). The other peaks have high fractions of multi site events, thus low survival fractions are preferred. It can be observed, that with the contact size also the survival fraction decreases. This is valid for both detectors and applies similarly to all three γ-ray lines. The values found for the three configurations are in the range to those reported in Ref. [63], with the Phase

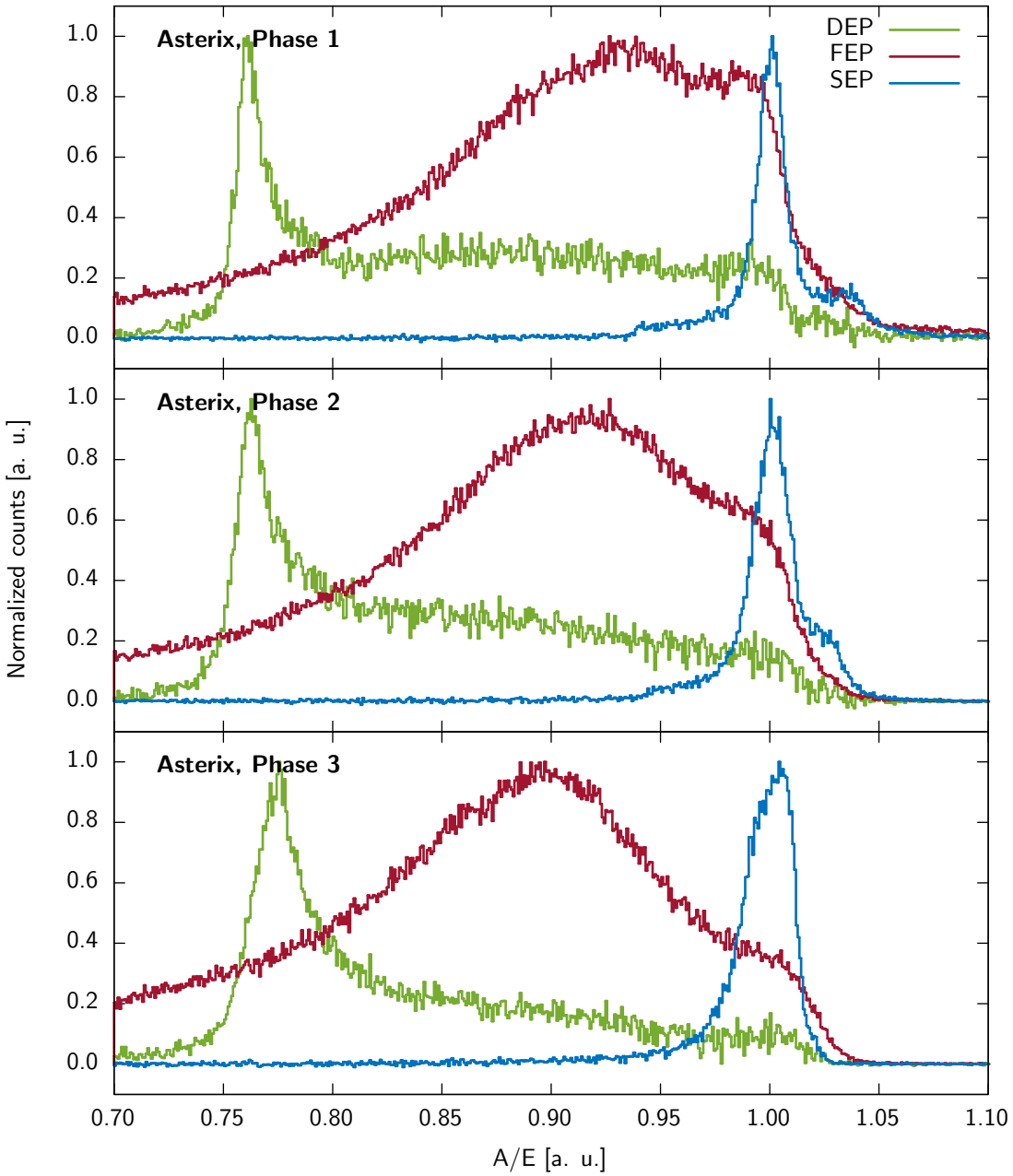

Figure 8.14: The A/E distributions in the SEP at 2103.5 keV, the DEP at 1592.5 keV and the FEP at 2514.5 keV for Asterix (all with 20 ns shaping). The height of the distributions has been fixed to 1 for better visibility.

Name, Phase	Shaping time [ns]	Acceptance (Survival fraction) [%]			
		DEP 1592.5 keV	FEP 2614.5 keV	SEP 2103.5 keV	FEP 1620.7 keV
Asterix, 1	20	89.9 ± 0.4	19.2 ± 0.5	12.2 ± 0.2	18.5 ± 0.3
Asterix, 2	0	90.2 ± 0.4	12.7 ± 0.4	7.7 ± 0.2	13.8 ± 0.3
Asterix, 3	160	89.7 ± 0.5	7.2 ± 0.1	5.2 ± 0.1	9.7 ± 0.1
Obelix, 1	40	89.8 ± 0.4	22.3 ± 0.6	14.5 ± 0.4	20.6 ± 0.5
Obelix, 2	20	90.2 ± 0.4	13.7 ± 0.4	7.7 ± 0.2	14.9 ± 0.3

Table 8.4: The survival fractions of the two detectors in their various configurations. The values have been evaluated for 6 different shaping times (0 ns, 20 ns, 40 ns, 80 ns, 160 ns, 320 ns) and the results with the lowest survival rate in the SEP are listed in the table.

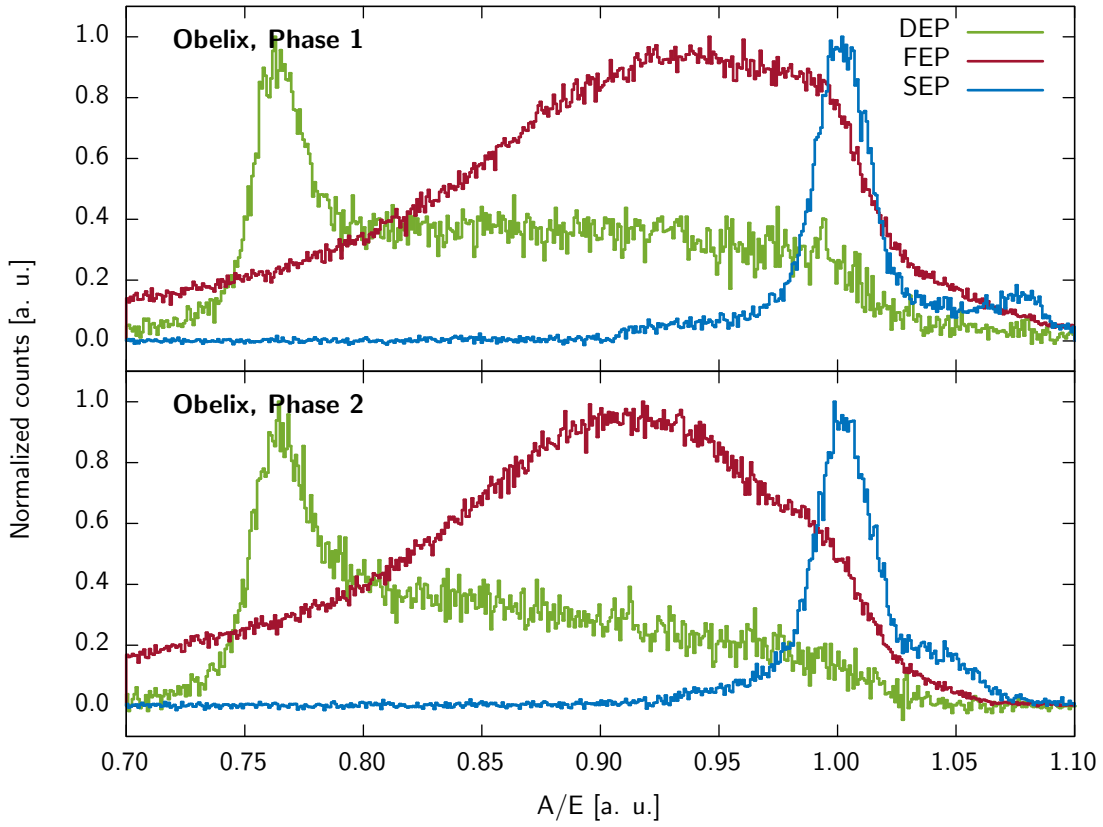

Figure 8.15: The A/E distributions in the SEP at 2103.5 keV, the DEP at 1592.5 keV and the FEP at 2514.5 keV for Obelix (all width 20 ns shaping). The height of the distributions has been fixed to 1 for better visibility.

1 configuration of Asterix and Obelix being on the high side and their respective Phase 2 configuration around the average of the reported values. The Phase 3 value of Asterix is in good agreement with the best values found in that reference.

The A/E distributions of Asterix in its three configurations are shown in Fig. 8.14 for the SEP, DEP and FEP (2614.5 keV). On the left shoulder of the DEP there is a secondary structure visible that disappears once the point contact is reduced. This non-Gaussian structure of the DEP has been also observed in Ref. [63] for some detectors. Furthermore, the SEP and the FEP distribution are shifted to the left as the point contact size is reduced which is the origin of the improve discrimination efficiency. The same observations are also valid for the two configurations of Obelix shown in Fig. 8.15.

The reduction of the point contact size increases the funnel effect by confining the weighting field to an even closer region around the point contact. The improvement is therefore expected, however, has not yet conclusively been proven. The successive improvement of the pulse shape discrimination efficiencies with a reduction of the point contact size observed in this work is a strong evidence, that a small point contact is indeed beneficial for a good pulse shape discrimination performance of a detector. The suppression power is limited as inevitably there are some single site event-like signals in both the FEPs and the SEP. However, the presented study proves, that there is still some space for improvements compared to the detector geometry of Ref. [63]. Detectors produced according to the geometry studied in this dissertation might be highly interesting for a further detector production of this or other neutrinoless double beta decay experiments.

9 Measurements near the trigger threshold

So far the measurements that have been presented focused on the range between a few tens of keVs up to a few MeV. Other than in neutrinoless double beta decay experiments PCGe detectors are mainly used for measurements at energies of a few keV or less. The potential of the two previously discussed detectors (Asterix and Obelix) for such experiments will be examined in this chapter.

9.1 Data acquisition trigger

The FADC system (SIS3301 VME) used in this dissertation samples the analog signal from the detector at 100 MHz with a resolution of 14 bits. This corresponds to 175 MB data per seconds and would require large storage facilities. However, most of this analog signal does not contain any useful information. The data thus can be considerably reduced by selecting only regions that contain signals from the detector. For this purpose most digitizers are equipped with a trigger system. This is a simple filter that searches the data stream for regions with signals and starts the data acquisition once such a region is encountered. The decision to store a signal region to disk usually is based on a limiting value (threshold or discrimination level) which must be exceeded by the signal. All the signals that do not trigger the data acquisition are irreversibly lost. Thus the lower end of the energy spectrum (energy threshold) is defined by the trigger condition.

9.1.1 SIS3301 VME trigger

The trigger condition can be calculated both, with analog electronic modules or in digital form after analog to digital conversion. The SIS3301 VME FADC system has an internal trigger. It is composed of two moving window average filters that are separated by a gap. This shapes the signal in a trapezoidal shape and thus is identical to a trapezoidal filter (without a rounded-top). The gap between the two moving window average filters is defined from the first sample of the first window to the first sample of the second window. Both the width of the moving window average and the gap can be configured individually but are limited to a maximum length of 255 samples (2.55 µs). Once the difference between the values from the two windows exceeds a certain threshold the event is stored to disk. For most of the data presented in this dissertation a window length of 120 samples and a gap of 130 samples was used. However, this size was found to be too short and was extended for the data presented in the last section of this chapter to 240 samples with a gap of 250 samples. This is close to the maximum possible value.

9.1.2 Trigger rate

The trigger threshold of the FADC can be set arbitrarily low, however at some point fluctuations of the signal caused by electronics noise will exceed the trigger level. The trigger level normally

is set sufficiently high so that these fluctuations are not of importance. However, in order to investigate physics at low energy it is required to trigger as low as possible well into the region where this fluctuations increase the rate at which noise events are triggered considerably.

The amplitude distribution of the noise is Gaussian (for small 1/f noise), thus one would expect that the amount of counts from random noise excursions above the discrimination level follows the error function. However, the trigger filter induces a time correlation between different samples. The shaped signal does not vary on a sample to sample basis but roughly on the time scale of the filters shaping time. This will affect the amount of accidentally triggered signals at a given discrimination level. The effect was extensively studied by Rice in Ref. [115, 116]. He found that at a discrimination level d the rate of accidentally triggered signals by random noise is described by:

$$N(d) = N_0 \exp\left(\frac{-d^2}{2\sigma_N^2}\right). \tag{9.1}$$

The variable σ_N is the width of the random noise distribution at a given shaping time and thus corresponds to the equivalent noise charge. N_0 is the trigger rate if the threshold level is set to zero. It corresponds to half of the number of zeros (or zero crossings) in the entire signal per second when the signal is distributed around zero. In Ref.[48, p. 171] N_0 is evaluated for a RC-CR shaper and was found to be approximately equal to $1/(4\sqrt{3}T_s)$, with T_s being the shaping time.

9.1.3 Accidentally triggered signals in the energy spectrum

In order to reconstruct the energy of a signal the acquired data are processed with the procedure described in Sec. 4.3. The final energy spectrum also contains the accidentally triggered signals that originate from electronics noise. If the trigger threshold is set at a level so that an increased rate can be observed from these events then these accidentally triggered events also appear in the energy spectrum. With decreasing energy the number of counts in the spectrum continuously increase forming a peak just above the cut off from the discrimination level.

The filters that are used in the signal processing step are more elaborated than the filters used for defining the energy threshold. Thus the distribution of the accidentally triggered events in the final energy spectrum differs from what the data acquisition has been triggered on. If the mismatch between the two filters is large unwanted artifacts in the spectrum appear. Furthermore, even for small mismatches it is almost impossible to describe the shape created by accidentally triggered signals in the energy spectrum. This, however, is required to define an energy threshold, up to which the data can be trusted and pollutions from accidentally triggered events are small.

Trigger artifacts

The discrimination level induces a hard cut off in the data selection; data not meeting the trigger condition will not be stored and hence are not available for further analysis. This cut off has no impact on a measurement performed far away from the trigger threshold, as it is improbable, that a large detector signal does not meet the trigger criteria. However, a measurement close to the trigger condition can be biased due to the cut off condition.

For a given event, the filter used for the energy reconstruction during the analysis of the data can find a different result as the filter used for evaluating if the trigger condition is met. If

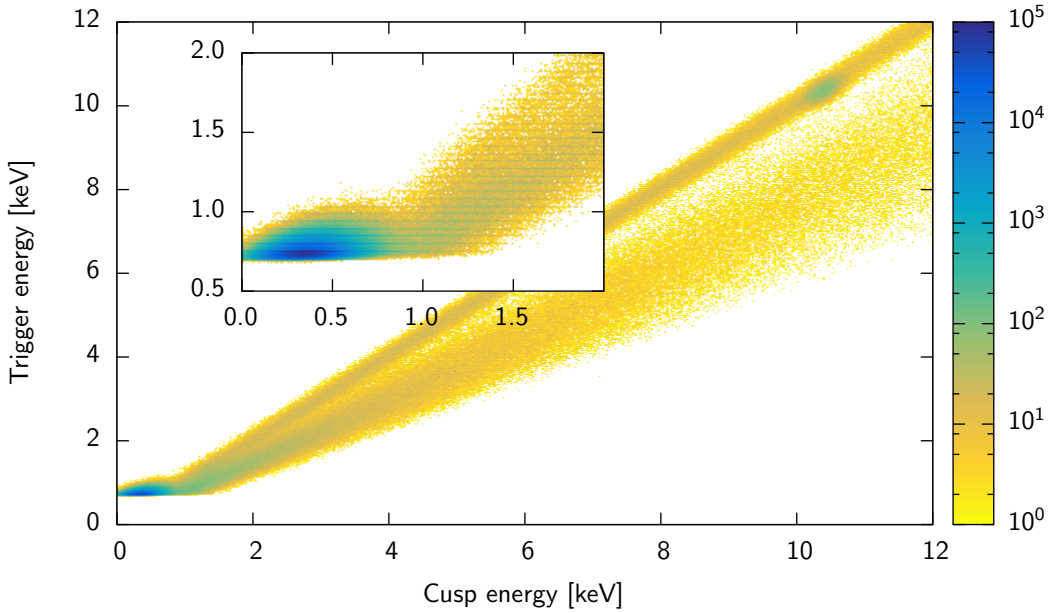

Figure 9.1: The energy reconstructed with the trigger filter vs the energy reconstructed during the analysis with a cusp filter (top with 0.3 µs, shaping time 4.0 µs) for a measurement without any sources but with the 10.4 keV line from ^{71}Ge. The measurement was performed with Asterix in its Phase 2 configuration.

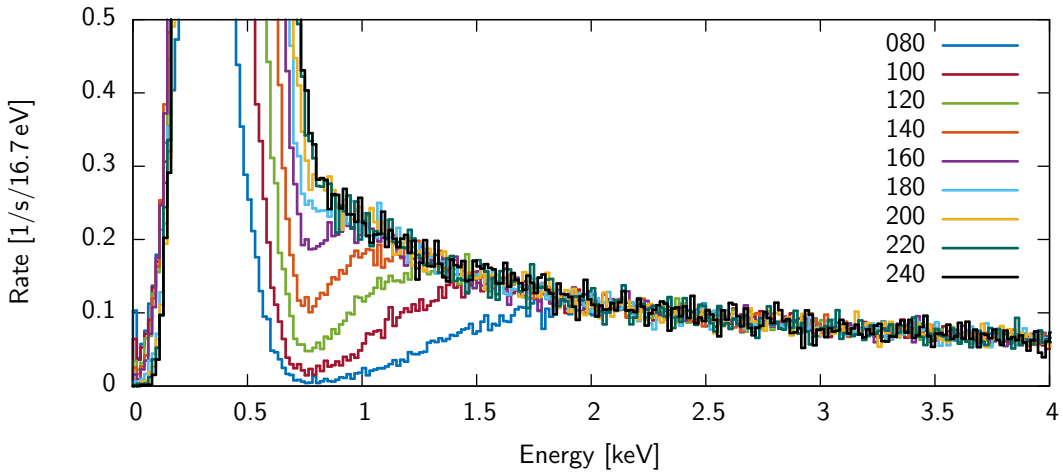

Figure 9.2: The spectra reconstructed with a cusp filter of 0.3 µs top width and 4 µs shaping time for different configuration of the trigger filter. The color of the different lines represents the shaping time (window length) of the trigger filter in samples (1 sample=10 ns). The measurements were performed with Obelix in its Phase 2 configuration.

the energy reconstructed during the analysis is lower than the one reconstructed by the trigger the event is reconstructed below the trigger cut off and instead of observing a straight cut off, the drop to zero spreads over a certain range. However, if the trigger condition reconstructs an event below the threshold but the shaping filter would have reconstructed the event above the trigger threshold then data are wrongly rejected and missing from the energy spectrum.

This effect was observed for measurements near the energy threshold and its effect caused spectral distortions up to an energy of a few keV. The effect is represented in Fig. 9.1, where the energy determined by the data analysis filter is plotted against the energy found by the trigger filter. The measurement has been taken after irradiation of the detector with the ^{252}Cf source leading to a peak at 10.4 keV from deexcitations of the isomer ^{71m}Ge. The cut off by the trigger is represented as a vertical line in the spectrum, below which no events can be found. The small deviation from a straight cut are caused by small differences in the algorithm used for reconstructing the trigger filter value in software and the actual algorithm implemented in the FADCs (the details of the algorithm were not accessible and could only be reproduced with limited precision). The energy of many events in that figure are reconstructed by the two filters at different energies. The upper band that contains the peak at 10.4 keV consists of events that were reconstructed with a similar energy in both filters. The lower band consists of events that were reconstructed at a much lower energy with the trigger filter. These events are mostly slow pulses that originate from external γ-rays depositing energy in the transition layer (see Section 3.4). The rise time of slow pulses is often large ($> 1.5\,\mu$s). These events thus can not be reconstructed correctly with a filter of only 1.2µs width. The value for the energy is accordingly underestimated. The cusp filter that was used during the signal processing on the contrary has a sufficiently large shaping time to reconstruct the energy correctly. The lower band with the slow pulses extends all the way down to the trigger threshold and is cut off by the threshold between 0.8 and 1.5 keV.

Figure 9.2 shows the spectrum that was reconstructed with a cusp filter of 4 µs shaping time for a variety of measurements taken with different trigger filter settings. It can be seen, that the smaller the shaping type of the trigger filter the more pronounced is the appearance of a fake peak in the region between 0.8 and 1.8 keV. If the shaping time of the trigger filter is chosen to be close to the maximum value (2.4 µs), the trigger filter is capable of reconstruction also the energy of slow pulses and the fake peak disappears.

In order to avoid these effects near the threshold it is thus important to already implement a sufficiently powerful filter for data triggering. For an analysis with a PCGe detector the trigger implemented in the VME FADC module might be sufficient when choosing the longest available window length. In experiments that try to perform physics measurements close to the threshold it is however beneficial to use an external trigger instead of the one implemented in the FADCs to avoid this bias at all cost.

Distribution of accidentally triggered signals

The analysis of the detailed distribution of the noise spectrum above a certain discrimination level is extremely complex on a theoretical level, and beyond the scope of this thesis. The discussion here is thus limited to some simple considerations that are used later on for fitting the spectrum of accidentally triggered events.

The simplest description of the energy distribution of accidental triggered events can be derived from the amplitude distribution of random noise, which is Gaussian. If each individual

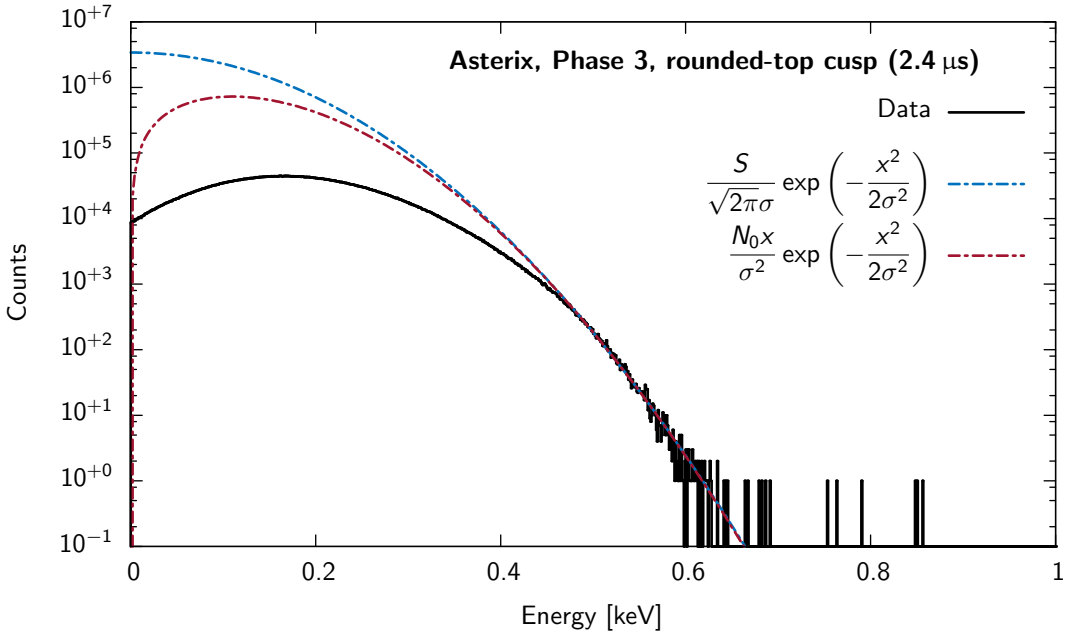

Figure 9.3: The distribution of the reconstructed energy (rounded-top cusp filter,2.4 µs shaping time, 0.3 µs rounded-top width) from baseline segments without a signal from the detector. The measurement was performed with Asterix in its third configuration.

sample (a random noise value) is filled into the energy spectrum then the amplitude distribution should directly translate into the spectral energy distribution. There are 10^8 samples per seconds at 100 MHz thus the integral of the Gaussian (the number of counts in the spectrum from noise) should roughly correspond to that number. The chance of a large excursion from the average value is small and the rate of these events small. Events observed far away from zero thus can be considered as rare fluctuations of single samples and thus should roughly follow a Gaussian distribution. This description however neglects correlation between different samples introduced by the shaping.

The correlation is considered by the rate of accidentally triggered events at a certain discrimination level in Eq. 9.1. Assuming that the energy reconstruction takes place with a filter sufficiently close to the trigger filter, then every accidentally triggered events will be reconstructed at an energy above the threshold. This must be valid for any discrimination level. Thus from Eq. 9.1 the spectral shape of accidentally triggered events can be derived. The trigger rate is the number of events above a certain threshold which is equal to the integral of the spectral distribution from the threshold to infinity. The energy distribution derived from Eq. 9.1 thus is of the form:

$$\frac{\mathrm{d}n}{\mathrm{d}E}(E) = \frac{N_0}{\sigma_N^2} E \exp\left(\frac{-E^2}{2\sigma_N^2}\right), \tag{9.2}$$

with E being the energy and $\mathrm{d}n/\mathrm{d}E$ the number of counts in a bin. If two different filters are used for the trigger condition and the energy reconstruction then this equation is no longer valid. Furthermore, all the filters used within this dissertation depend on finding the maximal amplitude in a certain range. Such a maximum search furthermore introduces a bias to the reconstructed value of accidentally triggered events to higher energies. In his paper, Rice

found that if the discrimination level is sufficiently large, the number of maxima laying above the discrimination level can be approximated by an expression that is identical to Eq. 9.1. Furthermore, as already discussed, also any sort of shaping will finally affect the number of accidental counts above a certain threshold.

The real distribution of the distribution of the reconstructed energy of the rounded-top cusp filter applied to randomly selected pieces of the baseline is shown in Fig. 9.3. It can be observed that there indeed is a strong bias to positive values coming from the algorithm that looks for a maximum in the signal. However, it is also possible that the reconstructed value is below zero. The average value of the baseline is reconstructed in a large range compared to the region where the maximum is search. Thus there indeed is a small chance that the samples in the region where the maximum is searched are all negative with respect to the average value of the baseline. The distribution is fitted with Eq. 9.2 and a Gaussian distribution close to the point where the function drops to zero on the right side. Both distribution model the actual noise spectrum far away from zero well and the differences between the two descriptions are small. In the following discussion the second model based on Eq. 9.2 is used.

It is required to model the shape of accidentally triggered events in the energy spectrum for physics measurements close to the threshold. First, if the model can be trusted then it is possible to subtract the expected distribution of accidentally triggered events from the energy spectrum and thus physics measurements into the region with an moderately increased count rate should be feasible. This procedure is limited as at some energy events will not efficiently be triggered anymore. Thus, it is important to understand the trigger efficiency curve to understand the limit of such a procedure. Second, even if the model is only an approximation of the real spectral shape then it can help to extract a lower energy threshold up to which the data can be trusted. The rate of accidentally triggered events above this energy threshold should be small.

9.1.4 Energy threshold of the two PCGe detectors

The two detectors, Asterix and Obelix, that were investigated in the previous chapter have also been measured at low energies to define the lowest accessible energies with these two detectors. Unfortunately, only data for Asterix are available with an increased trigger window.

9.1.5 Best limits on energy threshold

The last configuration of Asterix has been measured with a much larger shaping time (2.4 µs) for the trigger filter. Thus, it is possible to find the best limit of the energy threshold of the detector in its current state.

The spectra for different shaping times near the onset of the peak from accidental noise signals are displayed in Fig. 9.4 for the rounded-top cusp filter with a rounded-top of 0.3 µs. The measurement has been taken without any radioactive sources, however, the experimental setup has been installed at ground level. Even though lead and copper were used for shielding, the induced Compton background is large. Near the threshold the background level is roughly 1 event/s/keV. However, the aim of this measurement was not to reduce the background but to explore the threshold level. Thus this high count rate is acceptable. The spectral shape above the noise peak follows close to a straight line. The spectrum in the range where noise can be neglected has been split in two parts and individually summed up to find an equation

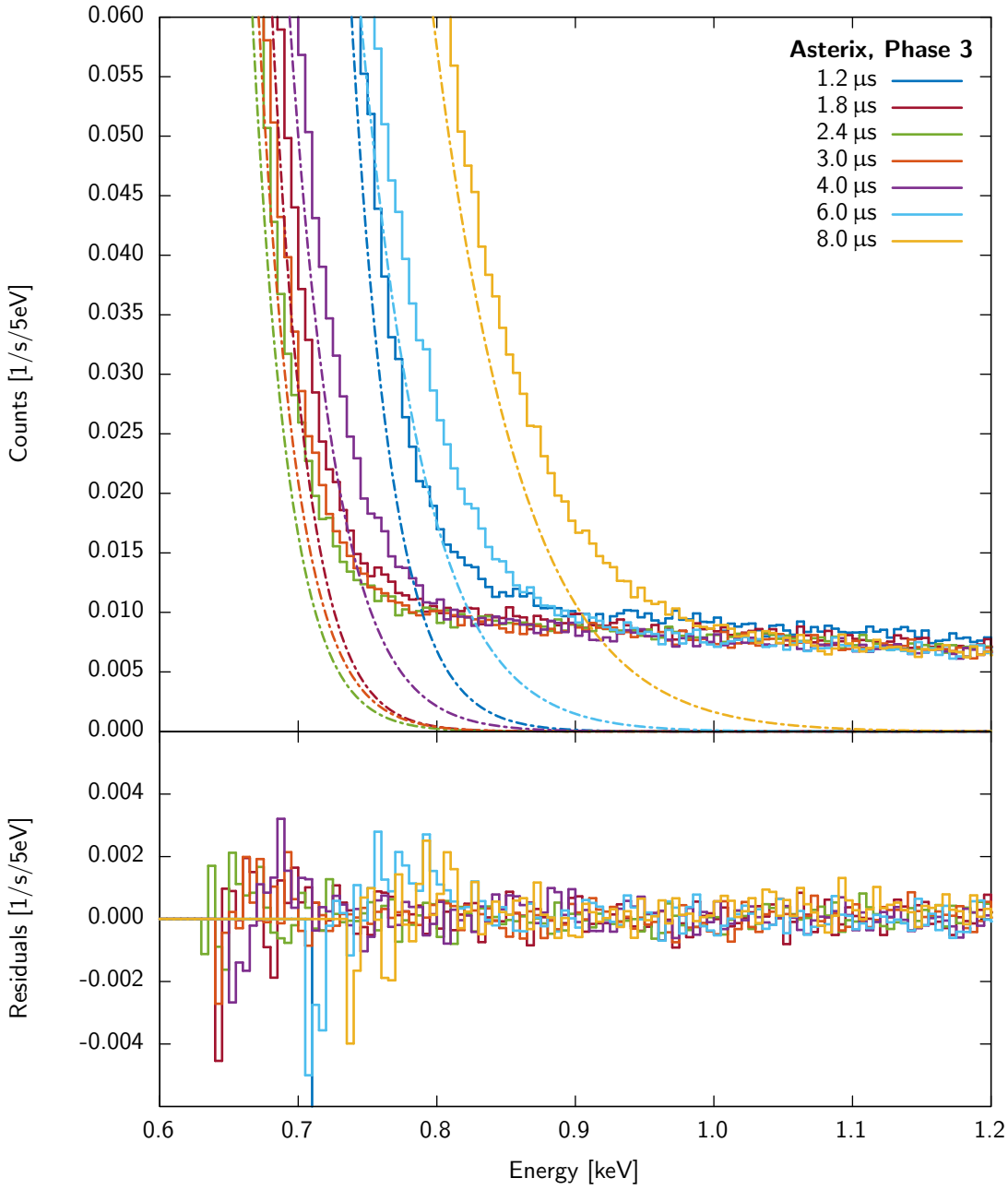

Figure 9.4: The energy spectrum around the trigger threshold at different shaping times. The spectra has been fitted with Eq. 9.2 plus a straight line; the fit without the straight line is additionally indicated. In the bottom panel the residuals of the fit are displayed.

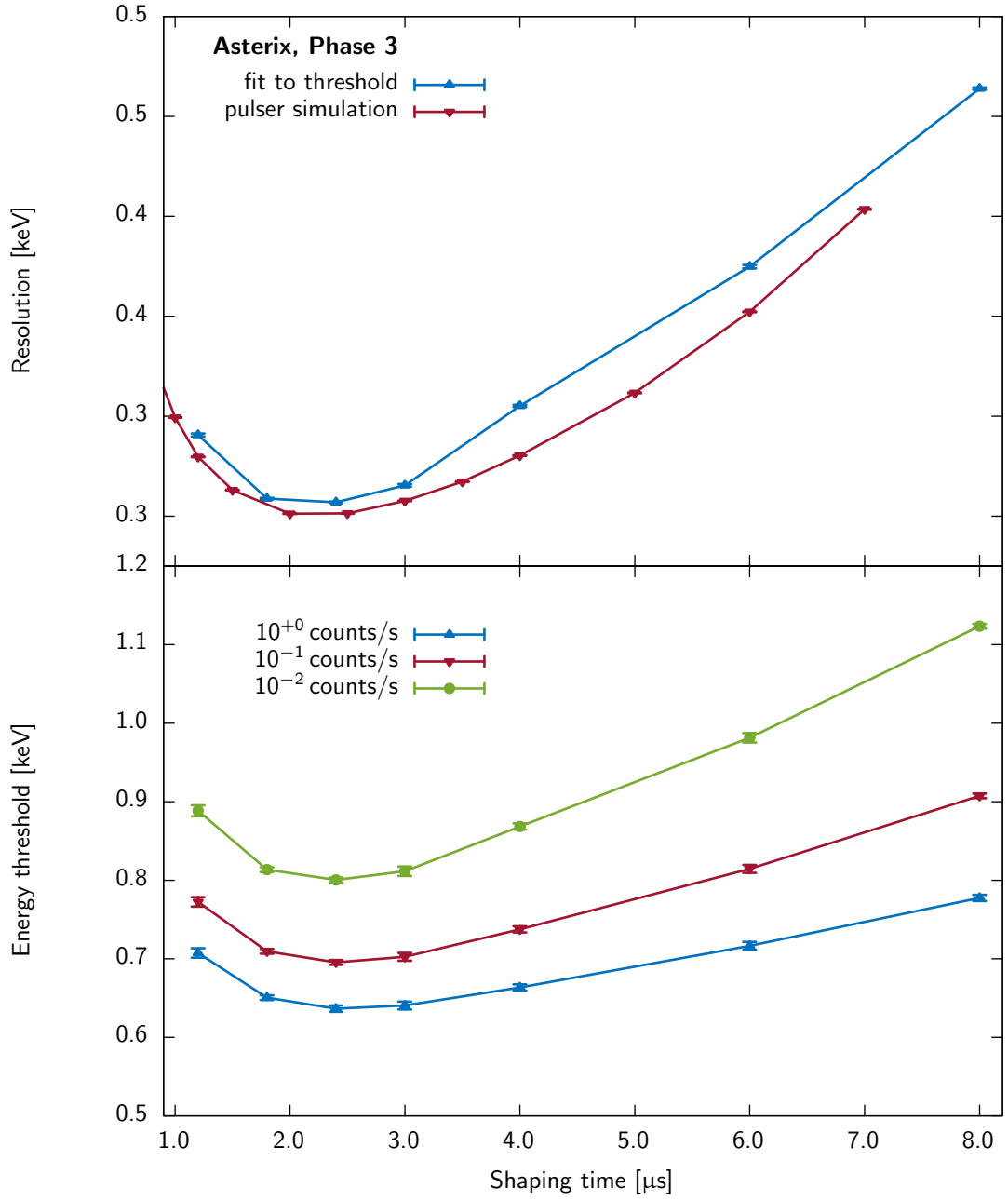

Figure 9.5: In the top panel the variance found by fitting Eq. 9.2 to the spectrum of accidentally triggered noise signals is shown together with the noise resolution found with the pulser simulation method and already displayed in Fig. 8.4. In the bottom panel the energy threshold is shown for three accepted accidental noise count rates. The data are from a measurement with Asterix.

for the straight line segment. This equation has been subtracted from the spectrum. The remaining spectrum has been fitted with Eq. 9.2. The upper limit of the fit range has been defined so that after subtraction only positive bins remain in the fit range; the lower limit of the range has been defined by minimizing the χ^2/dof of the fit result, where dof stands for degrees of freedom. The respective fits are represented in the top panel of Fig. 9.4 and the residuals between the initial spectra and the fit function indicated in the bottom panel. There is no unexpected deviation visible in the residuals. It seems thus reasonable that the spectrum follows a straight line and is surpassed by accidentally triggered events that are described by Eq. 9.2.

In Fig. 9.4 it can be seen that a shaping time of 2.4 µs seems to be close to the optimum for reaching the lowest energy threshold. The assumption of a distribution from accidentally triggered events following Eq. 9.2 seems plausible in the studied range, thus the chance of a signal being caused by a noise fluctuation even at a high discrimination level never is zero. The onset of the noise thus will be found at higher energies if the rate of actual signals from the detector is reduced. The onset of the peak from accidental triggers can be characterized by defining arbitrarily a number of noise counts per seconds that can be allowed to penetrate into the spectrum. This noise rate then will define a location in the spectrum – the energy threshold – that allows to compare different shaping times and detector geometries. The energy threshold has been plotted for different shaping times and noise rates in the lower panel of Fig. 9.5. It can be observed that the energy threshold indeed is lowest (~ 0.65 keV) at a shaping time of 2.4 µs. The energy threshold furthermore strongly depends on the allowed number of counts above that threshold.

In the top panel of Fig. 9.5 the variance in terms of FWHM ($2.3548 \cdot \sigma$) of the fit to the distribution of accidental noise events is compared to the noise resolution found with the pulser simulation method. The two curves are in good agreement, however at low and high shaping times they deviate. This indicates that indeed the shape of the spectrum close to the trigger threshold follows Eq. 9.2. However, it also shows that this is only valid in a very confined range. Even close to the onset of the noise peak the approximation of this equation is not entirely correct.

9.1.6 The energy threshold dependence on point contact size

It has been discussed in Sec. 8.2 that with a reduction in the size of the point contact also the noise from electronics is reduced. The equivalent noise charge is responsible for the width of the region with increased accidentally triggered events and thus the energy threshold should be reduced with a smaller point contact size.

It has been seen that a mismatch between the trigger filter and the data analysis filter can produce unwanted artifacts close to the threshold. Unfortunately, the measurements of the detectors in their first and second configurations have been taken with a relative small trigger shaping time (1.2 µs). The only way to avoid these artifacts hence is to also restrict the analysis filter to a similar length. It has been found that the cusp filter with a shaping time of 1.2 µs (and a rounded-top width of 0.3 µs) produces good results in restraining from introducing unwanted effects near the threshold, but still be little affected by the increased resolution of such a filter choice. It must be kept in mind that in this analysis neither the energy of slow pulses will be reconstructed correctly, nor will the energy threshold be minimized. The sole purpose of this analysis is to compare the different detector geometries.

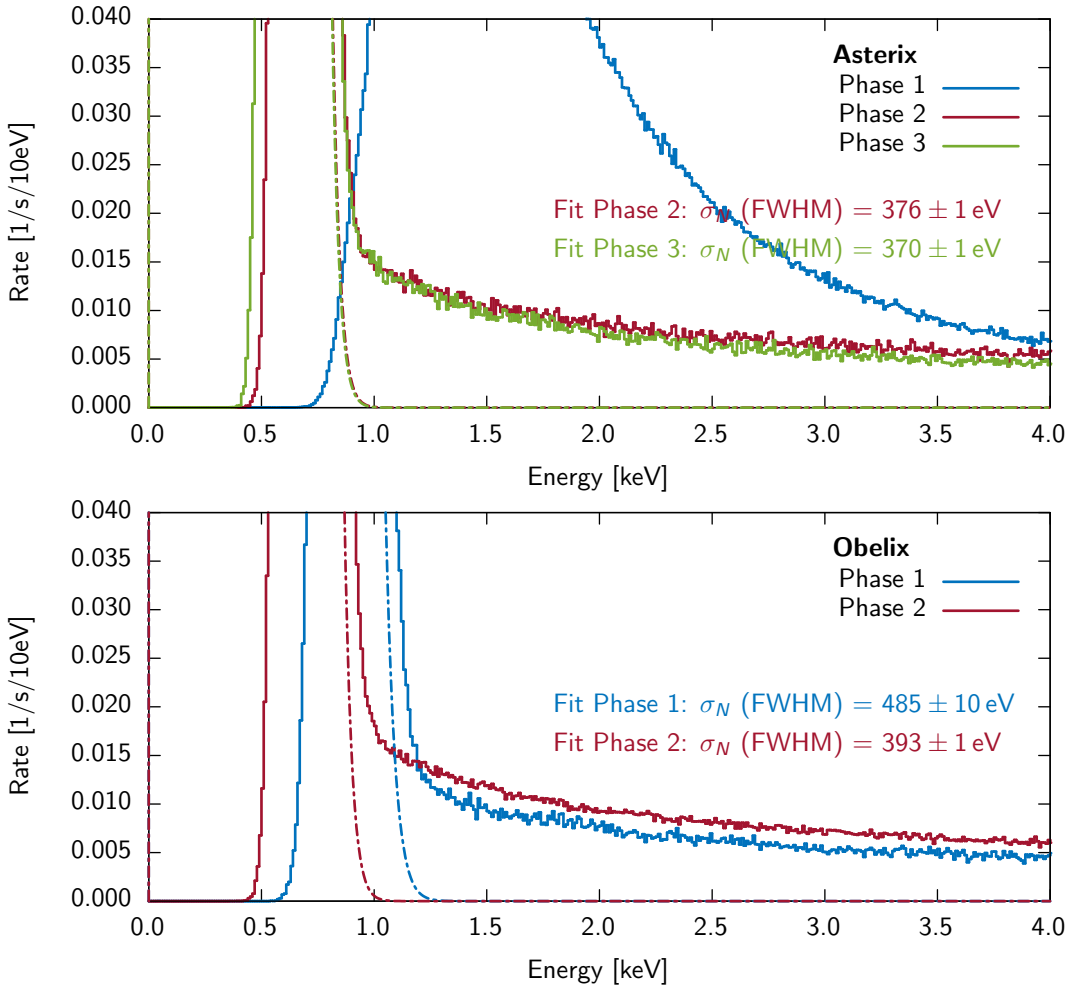

Figure 9.6: The energy spectrum for the two detectors at very low energies around the trigger threshold. The peak from accidental events is fitted with Eq. 9.2 and the variance found by the fit indicated in the label.

The energy spectra near the threshold for the two detectors in the different configurations are represented in Fig. 9.6. The spectral shape close to the threshold of Asterix in its first configuration deviates strongly from the other configurations and the count rate increases already at energies of around 4 keV. The events that make up the difference between this and the other spectra have been investigated and are not related to electronics noise, but have been found to be normal single site events. The most probable explanation, thus, is that these events originate from a contamination in the cryostat close to the point contact and penetrate through the point contact or the passivation layer into the detector. Because of the additional contribution the threshold level for this measurement has been chosen too high and the real onset of the noise peak can not be seen. Accordingly, it is not possible to compare this configuration with the later ones.

The remaining spectra follow the expected behavior with roughly constant signal level from Compton backgrounds that are surpassed at low energies by the peaks from accidentally triggered noise events. The data near the threshold have been fitted as described in the previous section and the respective value of σ_N are indicated in the figure. The values found for σ_N are close to the values for the equivalent noise charge at a shaping time of 1.2 µs indicated in Fig. 8.4 and Fig. 8.5. This explains why the difference between the second and third configuration of Asterix is basically not visible – the improvement in the equivalent noise charge between the two configuration is also small. The energy threshold for these two configurations is roughly $\sim 850\,\mathrm{eV}$ at an accidental noise count rate of 0.1 counts/s above the energy threshold.

The effect of the point contact size on the energy threshold, however, can be observed between the two configurations of Obelix. The improvement in noise between the two configurations of this detector is large enough so that also an improvement in the energy threshold can be observed. The energy threshold shifts between the two configurations from $(1105 \pm 17)\,\mathrm{eV}$ to $(906 \pm 6)\,\mathrm{eV}$ at an accidental noise count rate of 0.1 counts/s above the energy threshold. The ratio of both reflects perfectly the predictions of Eq. 9.1, from which a relation between the two configurations can be derived:

$$\frac{d_1}{d_2} = \frac{\sigma_1}{\sigma_2} = \frac{465.2\,\mathrm{eV}}{385.8\,\mathrm{eV}} \sim 1.21. \tag{9.3}$$

The improvement in energy resolution therefore indeed translates directly into an improvement in the width of the energy threshold.

9.2 Application in physics research

The experiments with the two detectors were performed at ground level and high backgrounds from cosmic radiation and the surround of the order of 2×10^5 counts/keV/kg/day are observed. In typical low background experiments this number is reduced to the order of 1 count/keV/kg/day in the low energy region. It was proven by group members [117] that background levels below this value are accessible even at a shallow depth, such as it is required near a reactor site. It thus is important to know which energy thresholds can be obtained at these background levels.

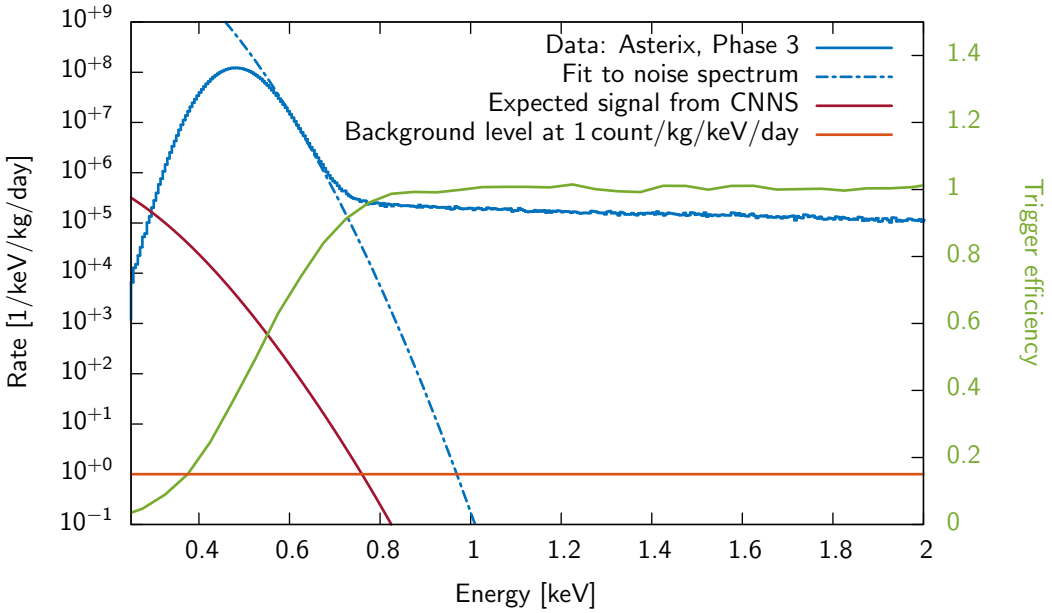

Figure 9.7: The energy spectrum on a logarithmic scale together with the Gaussian function from the fit and the expected spectrum from coherent neutrino-nucleus scattering at a reactor neutrino flux of 10^{13} neutrinos/s/sm^2.

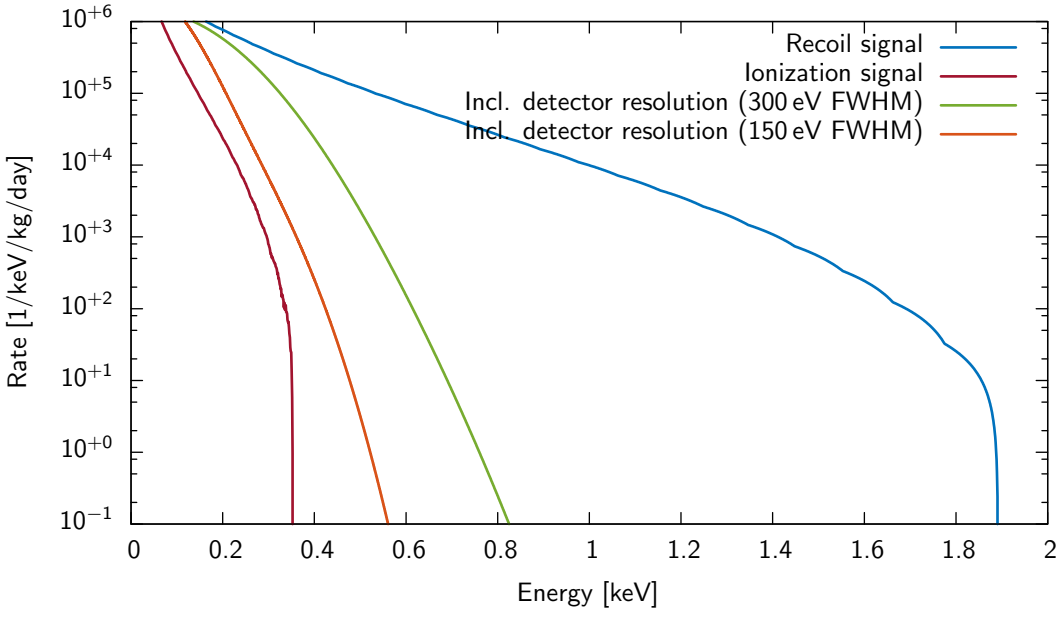

Figure 9.8: The expected recoil and ionization spectrum from coherent neutrino-nucleus scattering at a antineutrino flux of 10^{13} /s/cm^2. The ionization signal is furthermore spread out because of the finite resolution of the detector (FWHM of 300 eV is represented).

9.2.1 Extrapolation to low background levels

In Fig. 9.7 the measurement with the lowest energy threshold (Asterix) is shown on a logarithmic scale in counts/keV/kg/day. The gap between the background level from the performed measurement and the actual background levels observed in low background experiments is large. The only hint of how the number of accidentally triggered noise events scales over the five orders of magnitudes that lay between measurements and the region of interest is the fit of Eq. 9.2 to the data.

Under the assumption that the fit describes the spectrum of accidentally triggered events down to this level, an energy threshold of (1018 ± 3) eV is found for one accidental triggered event per day (only the uncertainty from the fit is considered). In a low background environment, thus, the energy threshold is found at a considerably higher value than observed at high background rates in the previous sections. However, this detector still has almost a sub-keV energy threshold at typical low background conditions.

The expected signal from coherent neutrino-nucleus scattering is additionally drawn in Fig. 9.7. It was simulated from a spectrum of the expected recoil energy that was analytically calculated by Thomas Rink (Max-Planck-Institut für Kernphysik). The expected recoil spectrum was shown at the very beginning of this dissertation and is repeated in Fig. 9.8. The spectrum is valid for a reactor antineutrino flux of 10^{13} /s/cm^2 and a neutrino spectrum that follows the distribution given in [3] and [4].

Only a fraction of the recoil energy can be observed as an ionization signal in the detector. The remaining recoil energy is transferred to lattice vibration in the form of phonons. The ionization signal and the recoil spectrum are related to each other by the quenching factor. The quenching factor is energy dependent and has been measured down to energies in the keV range. An overview over measurements and models is given in Ref. [8]. The Lindhard model that is described in that publication was used to transform the recoil spectrum into a spectrum representing the ionization signal (see Fig. 9.8). The ionization signal then can be convoluted with the detector resolution to obtain the expected signal in the detector.

The expected signal is many order of magnitude smaller than the distributions coming from accidentally triggered noise events and therefore not accessible with the current detector layout.

The trigger efficiency is in addition indicated in Fig. 9.7. It was extracted by simulating events in the baseline with a randomly selected pulse height from a flat distribution between zero and twenty keV. These event are then checked for if they would be triggered or not. At some threshold energy not all of the signals are triggered and these events are missing from the flat spectrum. The trigger efficiency measured with this method starts to drop around 800 eV thus around where accidentally triggered signals start to be recognizable. The trigger efficiency can be improved by reducing the trigger threshold, however, this will considerably increase the number of accidentally triggered events. At some point the data acquisition system can not handle the increased rate.

9.2.2 Sensitivity to coherent neutrino-nucleus scattering

With the two detectors in their current state it is not possible to measure the signal expected from coherent neutrino-nucleus scattering at a reactor site. However, all the required indigents are presented to study in which way the detectors would need to be improved for being sensitive to this signal. The following discussion is based on the ionization signal that was simulated

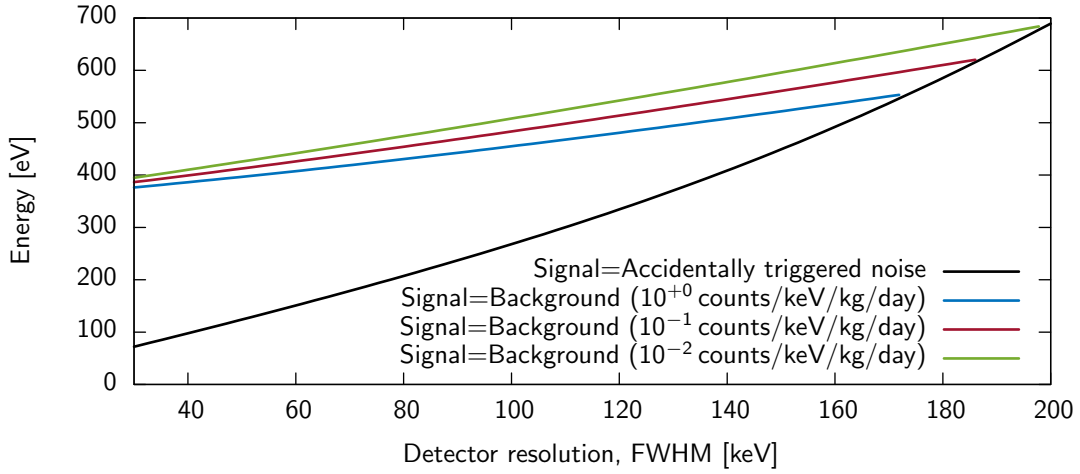

Figure 9.9: The energy at which the signal from coherent neutrino-nucleus scattering is surpassed by the accidentally triggered events as a function of detector resolution. Furthermore, also the energies at which the coherent neutrino-nucleus scattering surpasses two constant background levels.

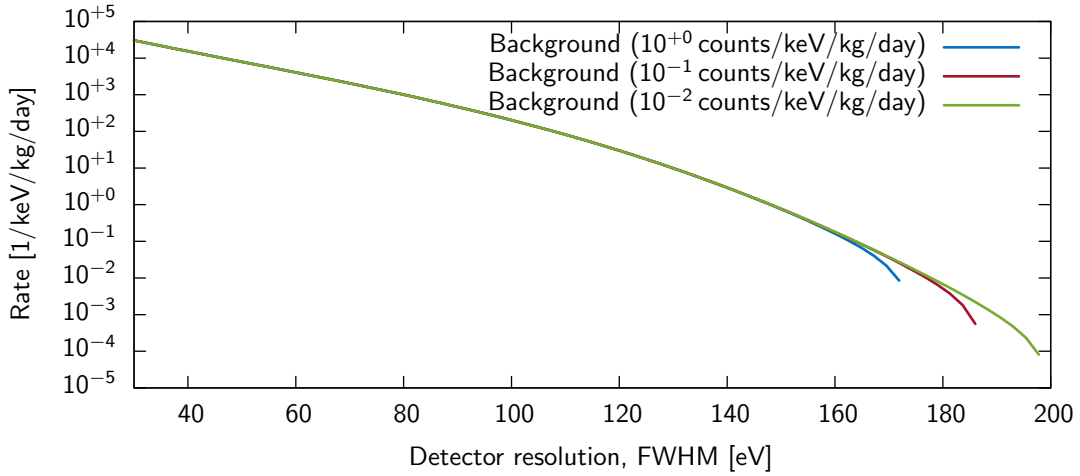

Figure 9.10: The number of counts expected in the region that is dominated by the coherent neutrino-nucleus signal for different background levels.

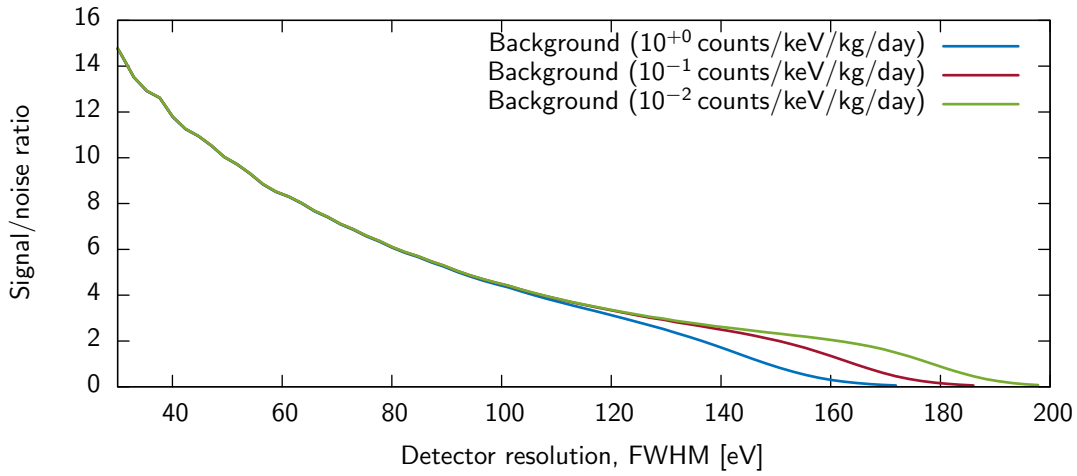

Figure 9.11: The signal-to-noise ratio in the region from 1 keV to the location where the coherent signal is surpassed by accidentally triggered events.

in the previous section and assumed a neutrino flux of 10^{13} neutrinos/cm^2/s at the location of the detector. This assumption is realistic, the GEMMA collaboration reported a flux of 2.7 as much in their experiment [17].

The ionization energy observed from coherent neutrino-nucleus scattering near a detector site ends at roughly 350 eV (see Fig. 9.8). However, it is spread out by the detector resolution to energies above this point. The location in the energy spectrum, where the signal from coherent neutrino-nucleus scattering has the same strength as the signal from accidentally triggered events is indicated in Fig. 9.9 as a function of the resolution of the detector. At energies below this value the coherent signal is lost in accidentally triggered events and thus not easily accessible. Furthermore, it is assumed that background events from external sources are constant in the range where the coherent neutrino-nucleus scattering can be observed. Different lines are indicated in the figure for the location in the energy spectrum where the signal from coherent neutrino-nucleus scattering is at the same level as the respective backgrounds. Between these two limits the coherent neutrino-nucleus scattering signal can be observed (region of interest).

The extend of the region of interests deviates only by roughly 50 eV when different background levels are considered (see Fig. 9.9). Because of this also the number of counts expected in this region (represented in Fig. 9.10) does not depend much on the background levels. However, at a detector resolution above 160 eV the region of interest is only a few tens of eV and the number of counts observed in this region low. Not only the number of events coming from the signal is reduced with the window size but also the number of counts from external backgrounds. Thus the signal-to-noise ratio remains relatively high for all values of the detector resolution. In the range from 120 eV to 190 eV the signal-to-noise ratio is between 1-4 which hints that the signal can be detected. However, the region of interest has a width of not more than 50-100 eV at these detector resolutions and thus it is questionable if a signal in such a small region can be measured.

The window can be increased beyond the range where the coherent signal dominates the spectrum. The signal-to-noise ratio in the region from 1 keV to the location where the coherent signal is lost in accidentally triggered events, which is a more realistic range for an

actual experiment, is plotted in Fig. 9.11. In this case the level of external backgrounds is of importance because in the added region these backgrounds are dominant. In order to obtain a signal-to-noise ratio of at least one, a detector resolution below 150 eV to 180 eV is required. This number is roughly half of the current value of ~ 300 eV (see Sec. 8.2).

So far, in this sensitivity study it was neglected that the accidental triggered events can be removed from the spectrum. One method to achieve this at a reactor site is to perform a measurement with the reactor turned on and one with the reactor turned off. The two spectra can be subtracted. The number of accidentally triggered events should be equal in both spectra. Thus such an experiment is sensitive beyond the point where the coherent signal is exceed by the accidentally triggered events. At some point however the high number of accidentally triggered events introduce large statistical uncertainties when the two spectra are subtracted and thus statistical fluctuations dominate over the coherent signal. Nevertheless, such a measurement has a large potential to increase the sensitivity to detectors with a noise resolution above 200 eV.

9.2.3 Possible detector improvements

In order to improve the resolution by a factor of two it is required to improve both, current and voltage noise by a factor of four. This is not easily achievable. The voltage noise can be improved by reducing the total capacitance. If the fit to the data can be trusted then the system is not dominated by the detector capacitance. The detector capacitance is roughly 1.6 pF, while the total capacitance of the system is about 10 pF. The difference between the observed total capacitance and the detectors capacitance is most likely found somewhere in the preamplifier and can thus be replaced by adjusting the circuit. An improvement by a factor of four, however, might be hard to obtain. Furthermore, there is no reason to think about a further reduction of the point contact size as it doesn't seems to be the dominant source of voltage noise.

A reduction of the current noise, however, would be more important. A reduction of the current noise not only reduces the detector resolution but also shifts the noise corner to a higher shaping time. The effect of the shaping time has been neglected in the previous discussion but it was discussed that N_0 in Eq. 9.1 should scale inversely with the shaping time. Thus the height of the peak from accidentally triggered events N_0 would be reduced. Shifting the noise corner from currently 2.5 µs to 10 µs would reduce N_0 by a factor of five. However, N_0 only has a small impact on the energy threshold. An improvement by a factor five only translates to a reduction of 20 eV.

The leakage current produced by the preamplifier usually is small. This has not been confirmed for the preamplifier system that was used for the two detectors, but it is likely that the observed current noise is indeed dominated by the detector's leakage current. The leakage current of a detector can not easily be reduced. A rework of the detector might be required but there are no guaranties that such a procedure really helps.

The current preamplifier system is optimized for a large energy range. In measurements near the trigger threshold it is not required to have a good resolution up to the MeV range. The preamplifier could be optimized to the low energy region and a small improvement might be gained.

The question remains if such improvements really will decreases the noise resolution by a factor of two. However, there are previous studies that suggest that this is feasible. Barbeau

et al. reported a PCGe detector with a resolution of 140 eV [2]. There detector is of a very similar design as those studied in this dissertation so there is no practical reason why such a resolution should not be reached.

10 Conclusion

Discourse surrounding future large scale germanium detector based experiments has gained attention in academia. Currently the largest experiments working with germanium detectors such as GERDA utilize not more than 30-40 kg of germanium. Many scientists in this field agree that an experiment of the order of several 100 kg or tons of germanium is necessary to advance research on neutrinoless double beta decay and dark matter. Thus, it is doubtful that the interest in germanium detectors, especially that for point contact germanium (PCGe) detectors, will subside. However, building an experiment of this order of magnitude is connected with many technological (electronics, radio purity, etc.) and logistical (production, storage and handling of large amounts of germanium detectors) pitfalls. Furthermore, the costs for an experiment on this scale would be extensive and it would require a minimum of a decade to obtain crucial results. Nevertheless, given that the technology is not going to disappear any time soon, it is vital to understand PCGe detectors beyond the current limitations.

The problems related to a large scale experiment do not arise in experiments near a nuclear reactor. For instance only 1-10 kg of germanium detectors are sufficient to explore the not yet observed coherent neutrino-nucleus scattering at a nuclear reactor. Such an experiment could be constructed in a foreseeable time frame and would not require a large collaboration. This dissertation mainly focuses on the potential of PCGe detectors in such an application, however, not exclusively.

The PCGe detector technology was explored with a commercially available detector type, the broad energy germanium detector (BEGe) produced by Canberra N.V., Olen, Belgium. The successive modification of a single germanium crystal removes the main systematics of a study of the point contact size – variability in the quality of the material. For this study, two almost identical detectors of roughly 760 g were used and allowed for a comparison of the obtained results. The characterization of the detectors with different point contact sizes led to the following main results:

- It has been possible to experimentally establish a link between the size of the point contact and noise from electronics. The FWHM noise resolution has been measured to be (349 ± 2) eV FWHM at 8.4 mm, (311 ± 2) eV FWHM at 5.0 mm and (299 ± 2) eV FWHM at 2.5 mm point contact radius for the first detector. Similar improvements have been observed for the second detector (from (408 ± 1) eV FWHM at 8.2 mm to (336 ± 2) eV FWHM at 5.2 mm).

- Two simple models for the capacitance as a function of the point contact radius were tested. The model, with the capacitance being proportional to the area of the point contact and not the radius, describes the data better. The detector is thus close to a parallel plate capacitor. The capacitance of the detector is then given as $C_d = \epsilon_r \epsilon_0 \pi r^2 / h$, with the vacuum permittivity $\epsilon_0 = 8.85 \times 10^{-12}$ F/m and the relative permittivity $\epsilon_r = 16$ in germanium. This model predicts a capacitance of 1.6 pF for the smallest tested point contact size.

- Thanks to an improvement in noise the energy resolution of the 59.5 keV γ-ray line improved continuously with a reduction in point contact size from (477±1) eV to (438±1) eV FWHM. As expected, the resolution at 1332.5 keV and 2614.5 keV remained unaffected for one detector ($\sim$ 1.58 keV and $\sim$ 2.3 keV FWHM, respectively) and improved slightly for the second detector (to $\sim$ 1.70 keV and $\sim$ 2.59 FWHM). This is in agreement with expectations; the dominant contribution to the resolution at high energy is from fluctuations in the number of charge carriers created in the energy deposition.

- The pulse shape discrimination efficiency is defined as the survival fraction in the single escape peak (SEP) at 2103.5 keV with respect to 90% acceptance in the double escape peak (DEP) at 1592.5 keV. A good pulse shape discrimination method removes most of the background like events (multi site events) in the SEP while signal like events (single site event) in the DEP must be conserved. The size of the point contact affects the electric fields, thus, the drift of charge carriers in the detector and the shape of the pulses induced into the electrode. The pulse shape discrimination efficiency improves from $(12.2 \pm 0.2)\%$ to $(7.7 \pm 0.2)\%$ and to $(5.2 \pm 0.1)\%$ when going from the largest to the smallest point contact size in the first detector. The second detector improves from $(14.5 \pm 0.4)\%$ to $(7.7 \pm 0.2)\%$.

- The number of accidentally triggered events from noise fluctuations above a certain discrimination level d follows, as predicted, the relation:

$$N(d) = N_0 \exp\left(\frac{-d^2}{2\sigma_N^2}\right), \tag{10.1}$$

  with σ_N being the noise resolution and N_0 the number of counts at zero discrimination level. At a typical background rate of a low level experiment (1 count/kg/keV/day) an energy threshold of approximately 1 keV is predicted.

In order to find the most optimal width between the two electrodes of a PCGe detector at a given point contact size, simulations were conducted. For this purpose, the ADL3 software [92] was extended, amongst other things, with models of the two detectors and new algorithms for the electric field calculation. The high performance of the two detectors confirmed the validity of this procedure. The library was further used during the characterization of the detectors:

- Measurements with collimated sources that induce events close to the surface of the detector are compared with simulations. Qualitative agreement has been observed between measurements from various locations and simulations in the position of the 59.5 keV γ-ray line (relative to a reference measurement) and the rise time ($2 - 70\%$). The shape of the pulse does not entirely agree and cannot be explained by simplifications used in the simulation. This suggests that the electric field within the detectors was not simulated correctly. Deviations are most likely caused by an insufficient description of the impurity concentration distribution throughout the detector volume.

Good signal processing techniques are as important as a good detector fabrication to achieve a high performance with germanium detectors. The existing program GEANA [83] was tweaked and extended to fit the requirements of the analysis presented. The program contains many

traditional but also some new filter routines. This dissertation, furthermore, carefully evaluated the performance of the different filter techniques that are implemented in GEANA. The evaluation found the following:

- The novel ballistic deficit correction method is capable of removing deterioration caused by variability in the shape of pulses at energies above 200 keV. So the γ-ray line at 1332.5 keV was improved from (1.82 ± 0.01) keV to (1.61 ± 0.01) keV.
- At energies below 200 keV a ballistic deficit correction is not required, instead, it is more beneficial to use a cusp like filter at these energies to find the best signal-to-noise ratio. The presented rounded-top cusp filter improved the resolution at these energies well beyond the specification of the manufacture of the detectors.
- A data set that ranges from a few keV to a few MeV can be processed thanks to the ballistic deficit correction with a single shaping time without any major loss in resolution. Between 59.5 keV and 1332.5 keV the loss in resolution compared to an analysis, that finds the best filter for each γ-ray line individually is less than 40 eV.
- The Fano factor is nearly constant over the range 59.5 keV to 1332.5 keV, however, it slightly increase at higher energies. Two presented methods found consistent results when the Fano factor was assumed to be constant, the better result is 0.1076 ± 0.0005. The first method consists of a constant fit to the values of the Fano factor that were calculated at individual γ-ray lines. The second method fits the function describing the energy dependence of the energy resolution to an energy spectrum that was evaluated with a single shaping time.

For the presented study a large amount of data were collected; some could not be analyzed. These data still offer some potential for interesting investigations. Furthermore, it might also be required to gather some additional data. Some further topics are:

- A careful evaluation of the details of the collimated measurements along the surface of the detectors can be used to refine the model of impurity concentration gradients in the detectors. This should finally produce a good match between the simulation and data and could also be applied to the data presented in [63].
- With a neutron source (^{252}Cf) the 10.4 keV γ-ray line from isomer ^{71m}Ge deexcitations was induced. This line is an appropriate proxy for signal like events in the low energy region. This region is dominated by slow pulses, which have a special shape that can be distinguished from those expected from coherent neutrino-nucleus scattering, neutrino magnetic moment or dark matter interactions. The 10.4 keV γ-ray line can be used to study the efficiency of different pulse shape discrimination methods at low energies. Such methods can be of particular importance to reach background level of less than 1 count/keV/kg/day that would facilitate a potential coherent neutrino-nucleus experiment. Such a study could be further extended with the purchase of a thin entrance window to measure γ-ray lines at this range of energy.
- The measurements were conducted above ground without a veto system against signals from cosmic radiation and without extensive efforts to shield the detector from external backgrounds. Contaminations from these sources in low background experiments

are roughly 5 orders of magnitude smaller. The background composition and energy threshold at these background levels have not been studied in this dissertation.

The presented results, particularly those from the characterization measurements of the two detectors, have some important implications. The results on the pulse shape discrimination of the two detectors is relevant for potential large scale experiments that try to measure neutrinoless beta decay. A small point contact size in the order of 5 mm radius or less helps to improve the pulse shape discrimination performance of PCGe detectors. This might help to control the variability observed in Ref. [63].

The obtained noise resolution is still too large to measure coherent neutrino-nucleus scattering. The sensitivity study, that was presented, shows that a FWHM noise resolution of less than $150 - 180$ eV must be reached in order to detect the coherent signal. Thus, it is inevitable to improve the detector's resolution before such an experiment can be envisioned. An upgrade or exchange of the electronics certainly is capable of slightly improving the resolution, particularly in regards to the voltage noise. However, it is doubtful that it will be sufficient. In order to reach the required resolution the current noise must be reduced. The electrical components used in the preamplifier only make up a small contribution to the observed current noise. The measured current noise must be dominated by the detector's leakage current. This noise source cannot simply be removed by an electronics upgrade as leakage currents are a property of the detectors bulk and surface. Reworking the groove might help, but ultimately the only way to efficiently remove the leakage currents is by using other detectors with a lower leakage current. The most promising way of achieving better noise conditions is to move to smaller detectors. Reducing the size to 500 g has been shown to considerably improve the noise. This dissertation has been limited to the detectors of a single manufacturer. Other companies have similar products with a slightly modified design, that might be better suited for such an application. Low background techniques are additionally vital to the successful conduction of a coherent neutrino-nucleus experiment. Background levels of 1 count/kg/keV/day need to be achieved to measure coherent neutrino-nucleus scattering. These levels of background recently have been obtained for a germanium detector operated at shallow depth of a few meters rock overburden in the energy range 40-50 keV [117]. Combined with pulse shape discrimination methods it seems reasonable to achieve the required background levels. Studying pulse shape discrimination methods in the low energy region and at low background levels is amongst the next milestones towards the realization of a coherent neutrino-nucleus scattering experiment.

Bibliography

1. Luke, P. N. *et al.* Low capacitance large volume shaped-field germanium detector. *Nucl. Sci. IEEE Trans.* **36,** 926–930 (Feb. 1989).
2. Barbeau, P. S. *Neutrino and astroparticle physics with P-type point contact high purity germanium detectors* PhD thesis (The University of Chicago, 2009).
3. Huber, P. Determination of antineutrino spectra from nuclear reactors. *Phys. Rev. C* **84,** 24617 (Aug. 2011).
4. Haag, N. *et al.* Experimental Determination of the Antineutrino Spectrum of the Fission Products of ^{238}U. *Phys. Rev. Lett.* **112,** 122501 (2014).
5. Freedman, D. Z., Schramm, D. N. & Tubbs, D. L. The Weak Neutral Current and its Effects in Stellar Collapse. *Annu. Rev. Nucl. Sci.* **27,** 167–207 (1977).
6. Drukier, A. & Stodolsky, L. Principles and applications of a neutral-current detector for neutrino physics and astronomy. *Phys. Rev. D* **30,** 2295–2309 (1984).
7. Horowitz, C. J., Coakley, K. J. & McKinsey, D. N. Supernova observation via neutrino-nucleus elastic scattering in the CLEAN detector. *Phys. Rev. D* **68,** 23005 (July 2003).
8. Barker, D. & Mei, D.-M. Germanium detector response to nuclear recoils in searching for dark matter. *Astropart. Phys.* **38,** 1–6 (Oct. 2012).
9. Oberauer, L. Coherent neutrino nucleus scattering. *Prog. Part. Nucl. Phys.* **48,** 301–304 (Jan. 2002).
10. Barbeau, P. S., Collar, J. I. & Tench, O. Large-mass ultralow noise germanium detectors: performance and applications in neutrino and astroparticle physics. *J. Cosmol. Astropart. Phys.* **2007,** 9 (2007).
11. Wong, H. T. *et al.* Research program towards observation of neutrino-nucleus coherent scattering. *J. Phys. Conf. Ser.* **39,** 266 (2006).
12. Bolozdynya, A. *et al.* Opportunities for Neutrino Physics at the Spallation Neutron Source: A White Paper. arXiv: 1211.5199 [hep-ex] (2012).
13. Beda, A. G. *et al.* Gemma experiment: Three years of the search for the neutrino magnetic moment. English. *Phys. Part. Nucl. Lett.* **7,** 406–409 (2010).
14. Beda, A. G. *et al.* Gemma experiment: The results of neutrino magnetic moment search. English. *Phys. Part. Nucl. Lett.* **10,** 139–143 (2013).
15. Beda, A. G. *et al.* First result for the neutrino magnetic moment from measurements with the GEMMA spectrometer. English. *Phys. At. Nucl.* **70,** 1873–1884 (2007).
16. Wong, H. T. *et al.* Search of neutrino magnetic moments with a high-purity germanium detector at the Kuo-Sheng nuclear power station. *Phys. Rev. D* **75,** 12001 (Jan. 2007).
17. Beda, A. G. *et al.* The results of search for the neutrino magnetic moment in GEMMA experiment. *Adv. High Energy Phys.* **2012,** 350150 (2012).

18. Olive, K. A. & Group, P. D. Review of Particle Physics. *Chinese Phys. C* **38,** 90001 (2014).
19. Bertone, G. The moment of truth for WIMP dark matter. *Nature* **468,** 389–393 (Nov. 2010).
20. Weber, M. Gentle Neutron Signals and Noble Background in the XENON100 Dark Matter Search Experiment. <http://www.ub.uni-heidelberg.de/archiv/15155> (June 2013).
21. Ade, P. A. R. *et al.* Planck 2013 results. I. Overview of products and scientific results. *Astron. Astrophys.* **571** (ed Tauber, J.) A1 (Oct. 2014).
22. Baudis, L. WIMP dark matter direct-detection searches in noble gases. *Phys. Dark Universe* **4,** 50–59 (Sept. 2014).
23. Akerib, D. S. *et al.* First Results from the LUX Dark Matter Experiment at the Sanford Underground Research Facility. *Phys. Rev. Lett.* **112,** 91303 (2014).
24. Bernabei, R. *et al.* Final model independent result of DAMA/LIBRA–phase1. English. *Eur. Phys. J. C* **73,** 1–11 (2013).
25. Aalseth, C. E. *et al.* CoGeNT: A search for low-mass dark matter using p-type point contact germanium detectors. *Phys. Rev. D* **88,** 12002 (July 2013).
26. Finnerty, P. S. *A Direct Dark Matter Search with the MAJORANA Low-Background Broad Energy Germanium Detector* PhD thesis (University of North Carolina at Chapel Hill, 2013), 304.
27. Giovanetti, G. *et al.* A Dark Matter Search with MALBEK. *Phys. Procedia* **61.** 13th TAUP 2013, 77–84 (2015).
28. Li, H. B. *et al.* Limits on Spin-Independent Couplings of WIMP Dark Matter with a p-Type Point-Contact Germanium Detector. *Phys. Rev. Lett.* **110,** 261301 (June 2013).
29. Yue, Q. *et al.* Limits on light weakly interacting massive particles from the CDEX-1 experiment with a p-type point-contact germanium detector at the China Jinping Underground Laboratory. *Phys. Rev. D* **90,** 91701 (Nov. 2014).
30. The XENON Collaboration. Exclusion of leptophilic dark matter models using XENON100 electronic recoil data. *Science* **349,** 851–854 (2015).
31. Armengaud, E. *et al.* Final results of the EDELWEISS-II WIMP search using a 4-kg array of cryogenic germanium detectors with interleaved electrodes. *Phys. Lett. B* **702,** 329–335 (Aug. 2011).
32. Agnese, R. *et al.* Search for Low-Mass Weakly Interacting Massive Particles with SuperCDMS. *Phys. Rev. Lett.* **112,** 241302 (June 2014).
33. Felizardo, M. *et al.* The SIMPLE Phase II dark matter search. *Phys. Rev. D* **89,** 72013 (Apr. 2014).
34. Behnke, E. *et al.* Improved Limits on Spin-Dependent WIMP-Proton Interactions from a Two Liter CF_3I Bubble Chamber. *Phys. Rev. Lett.* **106,** 21303 (Jan. 2011).
35. Schechter, J. & Valle, J. W. F. Neutrinoless double-β decay in SU(2)×U(1) theories. *Phys. Rev. D* **25,** 2951–2954 (June 1982).

36. Rodejohann, W. Neutrino-less Double Beta Decay and Particle Physics. *Int. J. Mod. Phys. E* **20,** 1833–1930 (2011).

37. Agostini, M. *et al.* Results on Neutrinoless Double-β Decay of ^{76}Ge from Phase I of the GERDA Experiment. *Phys. Rev. Lett.* **111,** 122503 (Sept. 2013).

38. The EXO-200 Collaboration. Search for Majorana neutrinos with the first two years of EXO-200 data. *Nature* **510,** 229–234 (June 2014).

39. Gando, A. *et al.* Limit on Neutrinoless $\beta\beta$ Decay of ^{136}Xe from the First Phase of KamLAND-Zen and Comparison with the Positive Claim in ^{76}Ge. *Phys. Rev. Lett.* **110,** 62502 (Feb. 2013).

40. Knöpfle, K. T. Upgrade of the GERDA experiment. *PoS.* TIPP2014, 109 (2014).

41. Abgrall, N. *et al.* The Majorana Demonstrator Neutrinoless Double-Beta Decay Experiment. *Adv.High Energy Phys.* **2014,** 365432 (2014).

42. Leo, W. R. *Techniques for nuclear and particle physics experiments : A How-to Approach* ISBN: 3540572805. doi:10.1119/1.16209 (1990).

43. Berger, M. J. *et al.* ESTAR : Stopping-Power and Range Tables for Electrons, Protons, and Helium Ions. *NIST.* <http://www.nist.gov/pml/data/star/index.cfm> (2011).

44. Berger, M. J. *et al.* XCOM: photon cross sections database. *NIST Stand. Ref. Database* **8,** 87–3597 (1998).

45. Compton, A. H. A Quantum Theory of the Scattering of X-rays by Light Elements. *Phys. Rev.* **21,** 483–502 (1923).

46. Klein, O. & Nishina, T. Über die Streuung von Strahlung durch freie Elektronen nach der neuen relativistischen Quantendynamik von Dirac. *Zeitschrift für Phys.* **52,** 853–868 (1929).

47. Knoll, G. F. *Radiation Detection and Measurement* ISBN: 9780470131480 (John Wiley & Sons, Inc., 2010).

48. Spieler, H. *Semiconductor Detector Systems* ISBN: 9780198527848. doi:10.1093/acprof:oso/9780198527848.001.0001 (Oxford University Press, Oxford, 2005).

49. Shockley, W. Currents to conductors induced by a moving point charge. *J. Appl. Phys.* **9,** 635–636 (1938).

50. Ramo, S. Currents Induced by Electron Motion. *Proc. IRE* **27.** doi:10.1109/JRPROC.1939.228757 (Sept. 1939).

51. He, Z. Review of the Shockley–Ramo theorem and its application in semiconductor gamma-ray detectors. *Nucl. Instruments Methods Phys. Res. Sect. A Accel. Spectrometers, Detect. Assoc. Equip.* **463,** 250–267 (May 2001).

52. Kim, H. *et al.* An extended proof of the Ramo-Shockley theorem. *Solid. State. Electron.* **34,** 1251–1253 (1991).

53. Bruyneel, B. *Characterization of Segmented Large Volume, High Purity Germanium Detectors* PhD thesis (Universität zu Köln, 2006), 137. <http://kups.ub.uni-koeln.de/id/eprint/1858>.

54. Keyser, R. M. & Raudorf, T. W. Germanium radiation detector manufacturing: Process and advances. *Nucl. Instruments Methods Phys. Res. Sect. A Accel. Spectrometers, Detect. Assoc. Equip.* **286,** 357–363 (Jan. 1990).
55. Uppal, S. *et al.* Ion-implantation and diffusion behaviour of boron in germanium. *Phys. B Condens. Matter* **308-310,** 525–528 (Dec. 2001).
56. Sher, A. H. Lithium-Ion Drift Mobility in Germanium. *J. Appl. Phys.* **40,** 2600 (1969).
57. Martin, G. N. *et al. Improving Germanium Detector Resolution and Reliability* tech. rep. (CANBERRA and Pacific Northwest National Laboratory, 2008), 7. <http://www.dtic.mil/cgi-bin/GetTRDoc?AD=ADA516274>.
58. Fano, U. Ionization Yield of Radiations. II. The Fluctuations of the Number of Ions. *Phys. Rev.* **72,** 26–29 (1947).
59. Van Roosbroeck, W. Theory of the yield and fano factor of electron-hole pairs generated in semiconductors by high-energy particles. *Phys. Rev.* **139** (1965).
60. Devanathan, R. *et al.* Signal variance in gamma-ray detectors-A review. *Nucl. Instruments Methods Phys. Res. Sect. A Accel. Spectrometers, Detect. Assoc. Equip.* **565,** 637–649 (2006).
61. Croft, S. & Bond, D. A determination of the Fano factor for germanium at 77.4 K from measurements of the energy resolution of a 113 cm3 HPGe gamma-ray spectrometer taken over the energy range from 14 to 6129 keV. *Int. J. Radiat. Appl. Instrumentation. Part A. Appl. Radiat. Isot.* **42,** 1009–1014 (Jan. 1991).
62. Perotti, F. & Fiorini, C. Observed energy dependence of Fano factor in silicon at hard X-ray energies. *Nucl. Instruments Methods Phys. Res. Sect. A Accel. Spectrometers, Detect. Assoc. Equip.* **423,** 356–363 (Mar. 1999).
63. Agostini, M. *et al.* Production, characterization and operation of ^{76}Ge enriched BEGe detectors in GERDA. English. *Eur. Phys. J. C* **75,** 1–22 (2015).
64. Aalseth, C. *et al.* Astroparticle physics with a customized low-background broad energy Germanium detector. *Nucl. Instruments Methods Phys. Res. Sect. A Accel. Spectrometers, Detect. Assoc. Equip.* **652,** 692–695 (Oct. 2011).
65. Aguayo, E. *et al.* Characteristics of signals originating near the lithium-diffused N+ contact of high purity germanium p-type point contact detectors. *Nucl. Instruments Methods Phys. Res. Sect. A Accel. Spectrometers, Detect. Assoc. Equip.* **701,** 176–185 (Feb. 2013).
66. Canberra Industries Inc. <http://www.canberra.com> (visited on 07/26/2015).
67. ORTEC. <http://www.ortec-online.com> (visited on 07/26/2015).
68. Baltic Scientific Instruments Ltd. <http://www.bsi.lv> (visited on 07/26/2015).
69. Fuller, C. S. & Severiens, J. C. Mobility of impurity ions in germanium and silicon. *Phys. Rev.* **96,** 21–24 (1954).
70. Trumbore, F. A. Solid Solubilities of Impurity Elements in Germanium and Silicon. *Bell Syst. Tech. J.* **39,** 205–233 (Jan. 1960).
71. Gaubas, E. & Vanhellemont, J. *Comparative Study of Carrier Lifetime Dependence on Dopant Concentration in Silicon and Germanium* 2007.

72. Agostini, M. *et al.* Pulse shape discrimination for Gerda Phase I data. English. *Eur. Phys. J. C* **73,** 1–17 (2013).
73. Horowitz, P. & Hill, W. *The Art of Electronics* 3rd ed. ISBN: 9780521809269 (Cambridge University Press, New York, NY, USA, 2015).
74. Johnson, J. B. Thermal agitation of electricity in conductors. *Phys. Rev.* **32,** 97–109 (1928).
75. Nyquist, H. Thermal agitation of electric charge in conductors. *Phys. Rev.* **32,** 110–113 (1928).
76. Hamamatsu. *TECHNICAL INFORMATION SD-37, Characteristics and use of Charge amplifier* tech. rep. (HAMAMATSU PHOTONICS K.K., Solid State Division, Hamamatsu City, Japan, 2001), 10. <http://www.hamamatsu.com/resources/pdf/ssd/charge%5C_amp%5C_kacc9001e.pdf>.
77. Fallot-Burghardt, W. *A CMOS Mixed-Signal Readout Chip for the Microstrip Detectors of HERA-B* Dissertation (Ruprecht-Karls-Universität Heidelberg, 1998), 254. <http://www.ub.uni-heidelberg.de/archiv/469>.
78. Smith, S. W. S. *The scientist and engineer's guide to digital signal processing* (ed Smith, S. W.) **3,** 626. <http://www.dspguide.com> (California Technical Publishing, 1997).
79. Shannon, C. E. Communication in the presence of noise. *Proc. IEEE* **86,** 447–457 (1998).
80. Goulding, F., Landis, D. & Hinshaw, S. Large coaxial germanium detectors-correction for ballistic deficit and trapping losses. *IEEE Trans. Nucl. Sci.* **37** (1990).
81. Moszyński, M. & Duchêne, G. Ballistic deficit correction methods for large Ge detectors. *Nucl. Instruments Methods Phys. Res. Sect. A Accel. Spectrometers, Detect. Assoc. Equip.* **308,** 557–567 (Oct. 1991).
82. Radeka, V. Trapezoidal Filtering of Signals from Large Germanium Detectors at High Rates. *IEEE Trans. Nucl. Sci.* **19** (1972).
83. Kihm, T. *MIZZI Computer Software GmbH* 2015. <http://www.mizzi-computer.de/home/> (visited on 07/01/2015).
84. Salathe, M. & Kihm, T. Optimized digital filtering techniques for radiation detection with HPGe detectors. arXiv: 1504.02039 [physics.ins-det] (2015).
85. Wiener, N. *The Extrapolation, Interpolation and Smoothing of Stationary Time Series* (John Wiley & Sons, Inc., 1949).
86. Kalinin, A. & Bednyakov, V. Pulse shaping for Ge-spectrometers optimized for ballistic deficit and electronic noise. *Nucl. Instruments Methods Phys. Res. Sect. A Accel. Spectrometers, Detect. Assoc. Equip.* **538,** 718–722 (Feb. 2005).
87. Phillips, G. W. & Marlow, K. W. Automatic analysis of gamma-ray spectra from germanium detectors. *Nucl. Instruments Methods* **137,** 525–536 (Sept. 1976).
88. Campbell, J. & Maxwell, J. A cautionary note on the use of the Hypermet tailing function in X-ray spectrometry with Si(Li) detectors. *Nucl. Instruments Methods Phys. Res. Sect. B Beam Interact. with Mater. Atoms* **129,** 297–299 (July 1997).
89. Kalambet, Y. *et al.* Reconstruction of chromatographic peaks using the exponentially modified Gaussian function. *J. Chemom.* **25,** 352–356 (2011).

90. Markwardt, C. B. *MPFIT: A MINPACK-1 Least Squares Fitting Library in C* 2010. <https://www.physics.wisc.edu/~craigm/idl/cmpfit.html> (visited on 01/01/2015).

91. Williams, T. & Kelley, C. Gnuplot 4.4: an interactive plotting program. <http://www.gnuplot.info> (2010).

92. AGATA Collaboration. *Detector Simulation Software ADL* 2015. <https://www.ikp.uni-koeln.de/research/agata/index.php> (visited on 07/01/2015).

93. Akkoyun, S. *et al.* AGATA—Advanced GAmma Tracking Array. *Nucl. Instruments Methods Phys. Res. Sect. A Accel. Spectrometers, Detect. Assoc. Equip.* **668,** 26–58 (Mar. 2012).

94. Scientific Instrument Services Inc. *SIMION® Version 8.1* 2015. <http://simion.com/> (visited on 05/20/2007).

95. Bruyneel, B., Reiter, P. & Pascovici, G. Characterization of large volume HPGe detectors. Part I: Electron and hole mobility parameterization. *Nucl. Instruments Methods Phys. Res. Sect. A Accel. Spectrometers, Detect. Assoc. Equip.* **569,** 764–773 (Dec. 2006).

96. Bruyneel, B., Reiter, P. & Pascovici, G. Characterization of large volume HPGe detectors. Part II: Experimental results. *Nucl. Instruments Methods Phys. Res. Sect. A Accel. Spectrometers, Detect. Assoc. Equip.* **569,** 774–789 (Dec. 2006).

97. Radford, D. *Majorana Detector Signal Generator (MJD SIGGEN)* 2015. <http://radware.phy.ornl.gov/MJ/mjd%5C_siggen/> (visited on 05/20/2007).

98. Harkness-Brennan, L. *et al.* An experimental characterisation of a Broad Energy Germanium detector. *Nucl. Instruments Methods Phys. Res. Sect. A Accel. Spectrometers, Detect. Assoc. Equip.* **760,** 28–39 (Oct. 2014).

99. Young, D. M. J. *Iterative methods for solving partial difference equations of elliptical type* PhD thesis (Harvard University, Cambridge, USA, 1950), 79. <http://www.ma.utexas.edu/CNA/DMY/david%5C_young%5C_thesis.pdf>.

100. Sasaki, W. & Shibuya, M. Experimental Evidence of the Anisotropy of Hot Electrons in n-type Germanium. *J. Phys. Soc. Japan* **11,** 1202–1203 (Nov. 1956).

101. Mihailescu, L. *et al.* The influence of anisotropic electron drift velocity on the signal shapes of closed-end HPGe detectors. *Nucl. Instruments Methods Phys. Res. Sect. A Accel. Spectrometers, Detect. Assoc. Equip.* **447,** 350–360 (June 2000).

102. Ottaviani, G., Canali, C. & Quaranta, A. A. Charge Carrier Transport Properties of Semiconductor Materials Suitable for Nuclear Radiation Detectors. *IEEE Trans. Nucl. Sci.* **22.** doi:10.1109/TNS.1975.4327640 (1975).

103. Xu, W. *et al.* Testing the Ge Detectors for the MAJORANA DEMONSTRATOR. *Phys. Procedia* **61,** 807–815 (2015).

104. Canberra Industries Inc. *Germanium Detectors* Meriden, CT, USA, 2003. <https://www1.aps.anl.gov/files/downloadables/XSD/DET/Detector-Pool/Spectroscopic-Detectors/Canberra/Germanium%5C_Detectors%5C_Manual.pdf>.

105. iseg Spezialelektronik GmbH. *iseg NHQ High Voltage Module* <http://iseg-hv.com/en/products/detail/NHQ> (visited on 06/30/2015).

106. Andreotti, E. *et al.* HEROICA: an underground facility for the fast screening of germanium detectors. *J. Instrum.* **8,** P06012 (2013).

107. Meadows, J. W. ^{252}Cf Fission Neutron Spectrum from 0.003 to 15.0 MeV. *Phys. Rev.* **157,** 1076–1082 (May 1967).

108. Bardelli, L. & Poggi, G. Digital-sampling systems in high-resolution and wide dynamic-range energy measurements: Finite time window, baseline effects, and experimental tests. *Nucl. Instruments Methods Phys. Res. Sect. A Accel. Spectrometers, Detect. Assoc. Equip.* **560,** 524–538 (May 2006).

109. Lowe, B. Measurements of Fano factors in silicon and germanium in the low-energy X-ray region. *Nucl. Instruments Methods Phys. Res. Sect. A Accel. Spectrometers, Detect. Assoc. Equip.* **399,** 354–364 (Nov. 1997).

110. Lépy, M. *et al.* Experimental study of the response of semiconductor detectors to low-energy photons. *Nucl. Instruments Methods Phys. Res. Sect. A Accel. Spectrometers, Detect. Assoc. Equip.* **439,** 239–246 (Jan. 2000).

111. Papp, T. *et al.* A new approach to the determination of the Fano factor for semiconductor detectors. *X-Ray Spectrom.* **34,** 106–111 (2005).

112. Wiens, A. *et al.* Improved energy resolution of highly segmented HPGe detectors by noise reduction. English. *Eur. Phys. J. A* **49,** 1–10 (2013).

113. Zulliger, H. R. & Aitken, D. W. Fano Factor Fact and Fallacy. *Nucl. Sci. IEEE Trans.* **17,** 187–195 (1970).

114. Budjáš, D. *et al.* Pulse shape discrimination studies with a Broad-Energy Germanium detector for signal identification and background suppression in the GERDA double beta decay experiment. *J. Instrum.* **4,** P10007 (2009).

115. Rice, S. O. Mathematical Analysis of Random Noise. *Bell Syst. Tech. J.* **23,** 46–156 (1944).

116. Rice, S. O. Mathematical Analysis of Random Noise. *Bell Syst. Tech. J.* **24,** 46–156 (1945).

117. Heusser, G. *et al.* GIOVE - A New Detector Setup for High Sensitivity Germanium Spectroscopy At Shallow Depth, 17 (July 2015).

Acknowledgements

I'm very thankful to all the people that supported me during the time I spent writing this thesis:

- First of all I'm incredible grateful to my fiancée, Nicole Vital, who supported me in every way possible. She was there to motivate me in the times when I lost hope that I would complete my thesis on time and always found a way to cheer me up. I'm so happy to have a person like her by my side and feel extremely honored I will marry her soon.
- I would like to thank my two advisers, Dr. Werner Maneschg and Dr. Bernhard Schwingenheuer, who always had a bit of spare time to give me feedback on my writing, as well as for the many interesting and enriching discussions about PCGes and my research. Furthermore, I'm indebted to Thomas Kihm, who had no obligations what so ever to help me, but was always there to discuss software and programs and inspired many of the new ideas presented in this dissertation. He also took his valuable free time to read through this thesis.
- I'm thankful to Prof. Dr. Manfred Lindner for his support and the freedom to pursue different topics I found intriguing. Furthermore, I would like to thank Prof. Dr. Norbert Herrmann who accepted the responsibility of being my second referee for this thesis. Notably, Thomas Rink for calculating some important data used in this work, Johannes Welter for reading through the theoretical section and Antoine Collin for all the inspiring discussions.
- Thanks also goes to people from the GERDA collaboration as well as the entire Lindner group at the Max-Planck-Institut für Kernphysik, Heidelberg. The exchange with people from different fields and experiments was very valuable.
- Last but not least I'm grateful to my entire family: My parents, Monika and Joseph Salathe, who supported me through my childhood and my studies. This is something that never can be paid back. My sister, Andrea Salathe, for accompany me through so many nice years and for giving me new outlooks on live. My grandmother, Bethli Furler, for always believing in me.